Loughborough University

COMPUTATIONAL FLUID DYNAMICS OF COUPLED FREE/POROUS REGIMES: A SPECIALISED CASE OF PLEATED CARTRIDGE FILTER

By

Atul Ninu Waghode

A Doctoral Thesis submitted in partial fulfilment of the requirements for the award of the degree of Doctor of Philosophy of Loughborough University

Advanced Separation Technologies Group
Department of Chemical Engineering
November, 2005

ACKNOWLEDGEMENT

Abstract

The multidisciplinary project AEROFIL has been defined and coordinated with the idea of developing novel filter designs to be employed in aeronautic hydraulic systems. The cartridge filters would be constructed using eco-friendly filtration media supported by unconventional disposable or reusable solid components. My main contribution to this project is the development of a robust and cost-effective design and analysis tool for simulating the hydrodynamics in these pleated cartridge filters. The coupled free and porous flow regimes are generally observed in filtration processes. These processes have been the subject of intense investigation for researchers over the decades who are striving hard to resolve some of the critical issues related to the free/porous interfacial constraints and their mathematical representations concerning its industrial applications.

A two-dimensional mathematical model has been developed to represent momentum and mass conservations for creeping incompressible flow in coupled free/porous flow regimes. A power law type constitutive model has been included to update the viscosity of the highly viscous non-Newtonian hydraulic fluids. The linked system of Stokes, Darcy and the continuity equations is solved using two different numerical schemes based on the standard Galerkin weighted residual finite element method in conjunction with isoparametric distorted elements.

The perturbed continuity UVP finite element scheme based on equal order approximations shows its shortcoming in generating stable and accurate results in relatively complex domains. On the other hand, the scheme using unequal order Taylor-Hood elements proves its versatility and flexibility to cope with any sort of complicated geometry without any compromise with the underlying physics. The nodal replacement scheme is found to be generic in numerical linking of free and porous flow regimes at any possible irregular shaped interface.

Two relatively newer concepts such as medium compression and pleat crowding have emerged when the cartridge experimental permeation data has been analysed against the simulated results. Incorporation of the compression permeability model into the flow model accounts for the degree of compression of the filter medium and for filtration area losses in filter cartridges. Significant over-use of media material or the need for changes to geometric or mechanical design can be identified using the procedures described.

Table of contents

List of Figures

Chapter 5

Chapter 6

xiv

Chapter 7

List of Tables

Chapter 6

Chapter 7

Nomenclature

u: Fluid velocity, $[LT^{-1}]$;

$\tilde{u}$: Fluid velocity interpolated over elemental domain, $[LT^{-1}]$;

g: Acceleration due to gravity, $[LT^{-2}]$;

p: Hydrostatic fluid pressure, $[L^{-1}MT^{-2}]$;

$\tilde{p}$: Hydrostatic fluid pressure interpolated over elemental domain, $[LT^{-1}]$;

K: Permeability of the porous medium, $[L^2]$;

Q: Volumetric flow rate, $[L^3T^{-1}]$;

Re: Reynolds number;

N: Shape functions;

W: Weight function;

J: Jacobian matrix;

U: Normalised velocity in x-direction, $[LT^{-1}]$;

V: Normalised velocity in y-direction, $[LT^{-1}]$;

P: Normalised fluid pressure, $[L^{-1}MT^{-2}]$;

t: Time variable, $[T]$;

c: Speed of sound in fluid, $[LT^{-1}]$;

n: Power law index;

Greek symbols:

ρ: Fluid density, $[MT^{-3}]$;

σ: Cauchy's stress, $[L^{-1}MT^{-2}]$;

δ: Kronecker delta;

τ: Viscous stress or extra stress, $[L^{-1}MT^{-2}]$;

η: Fluid viscosity, $[L^{-1}MT^{-1}]$;

η_B: Brinkman's effective viscosity, $[L^{-1}MT^{-1}]$;

η_0: Fluid viscosity at zero shear, $[L^{-1}MT^{-1}]$;

$\dot{\gamma}$: Rate of shear, $[T^{-1}]$;

Ω: Flow domain;

Γ: Domain boundary;

Subscripts:

p: Pressure;

v: Velocity;

x: In x-direction in Cartesian coordinates;

y: In y-direction in Cartesian coordinates;

r: In r-direction in Axisymmetric coordinates;

z: In z-direction Axisymmetric coordinates;

e: Elemental value;

f: In the free flow fluid,

p: In the porous medium;

Superscripts:

e: Over the element;

n: At time step n;

1   Introduction

1.1   Project background

Highly viscous fluids are employed to actuate the hydraulic systems in a typical aircraft machine assembly. To avoid wear of the expensive components caused by particulate contaminants, the fluids need to be filtered continuously. The highest surface area offered in the smallest occupied volume makes pleated cartridge filters a first choice of preference. Since the hydraulic filters operate at high pressures, the filtration media are required to be rigid enough to maintain mechanical integrity for the excessive fluid drag forces. If the cartridge element is allowed to exceed its dirt holding capacity, it is almost impossible and economically unfeasible to clean thoroughly and must then be discarded. In conventional filters, the cartridge is clamped between metallic flanges to maintain their integrity, which result in additional disposal problems.

The disposal of the blinded or fully loaded cartridges is a matter of serious environmental concern. Strict policies enforced by the environmental protection regulatory bodies made it mandatory for the filter manufacturer to improve the filter performance by adopting some innovative steps in the existing filter designs to reduce the environmental impact of used cartridges through their safe disposal or reuse. As the innovative design procedure involves various steps from conceptual design to final manufacture and testing, a variety of industrial groups and academic institutions collaborated in the multi-disciplinary project with their specialist research and on-field expertise. The overall efforts of the combined project teams are directed towards improved filtration performance with the use of ecologically viable manufacturing materials, which can withstand the high-pressure loads.

1.2   Aeronautical filters

Most hydraulic filters generally operate at higher pressures up to around 1000 bar or higher flow rates up to 1000 litres per minute with pumps and control valves having small clearances. A combination of high pressure and reduced clearances calls for the elimination of particles from systems, which requires protection by finer filtration. In excess of 70% of the hydraulic systems failures are

due to contamination or poor fluid conditions. Due to the pleating of the filtering media, filter cartridges offer a high effective filtration area especially for surface filtration in the compact size. Though the normal throughput for cartridge filters is lower, it is a common practice in aircraft systems to connect a number of filter modules in parallel to achieve greater dirt holding capacity and longer service life.

During operation, the pressure drop across the filter continuously rises as the particles start to deposit on the surface or in the depth of the filter and reaches the maximum limit when the cartridge gets fully exhausted. The blinded cartridge needs to be disposed off and can rarely be cleaned effectively by reverse flow for reuse. In hydraulic circuits of a typical aircraft assembly, the fluids are generally viscous non-Newtonian fluids with different types of particles with sizes ranging from 0.1 to 1 μm. Some of these particles are sticky in nature and agglomerate when deposited on the pores on the surface of medium. Though cartridge filters generally act as strainers or surface filters, deposition of such agglomerates demands disposal of blind cartridges instead of reuse.

1.3   Coupled free/porous flow regimes

In its simplest form, a cartridge filter is made up of a cylindrical metal container in which a centrally located removable filter cartridge is placed. A typical filter cartridge assembly in hydraulic circuit of aircraft machine system is shown in **Figure** 1. 1.
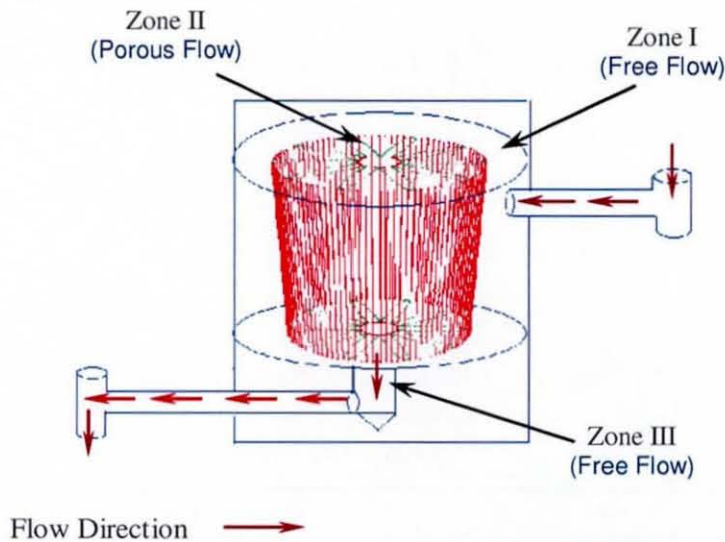
Figure 1. 1: A Cartridge Filter Assembly in a Hydraulic Circuit

The fluid enters the metal container (often tangentially), penetrates through the tubular element and leaves via the inner core except in some cases the reverse direction is used. The development of a hydrodynamic model is the primitive step towards gaining a deeper understanding of filter performance for various operating loads based on fundamental concepts of the underlying physics and representative mathematics. In terms of fluid dynamics, three distinct flow regimes are found in a cartridge assembly. Zone 1 is the free flow region enclosed between the cartridge container and the porous cartridge. The porous cartridge forms the zone 2. The inner metal core which discharges the permeate, is the free flow zone 3.

Free flow domains confined by porous walls feature in many of the industrial and natural processes ranging from biomechanics, cross-flow and dead-end filtrations, solidification of metal alloys, heterogeneous catalysis and subsurface flows. Despite the similarity between the flow regimes in these processes, their flow field characteristics may be distinct. Factors such as fluid compressibility flow Reynolds number and nature and position of the barrier separating free/porous regimes and physical properties of the permeable media may directly affect the coupled flow dynamics. Since the underlying physics of the coupled flow is very complex, its mathematical solution still poses an unresolved mystery for scientists and engineers. The mathematical representation of the interfacial constraints restricts the development of predictive model for the coupled flow problems. The commercially available software dedicated to the fluid flow simulations has exhibited their shortcoming to cope with interfacial constraints in coupled flow systems and are still in the stage of development. They are proven to be incapable towards accurate and logical solutions to the coupled flow problems in geometrically complex flow domains. Therefore, it has become essential to develop a generic mathematical model based on underlying physical concepts and logical assumptions to represent coupled free/porous flow in any complex or irregular flow geometry such as pleated cartridge filters.

A veritable plethora of research has been carried out over the decades in experimental investigations in flow through pleated cartridge filters. Although a methodology for modelling the flow behaviour in pleated cartridges has been attempted in the past (Wakeman and Harris, 1993), its geometrical complexity previously prevented construction of a generic model. The previous efforts

regarding modelling of fluid flow in pleated cartridge filters are primarily based on simplifying assumptions in the mathematical representation of the phenomena or simplified geometry of pleat structures and flow directions. However, such simplifications reduce the applicability of these models to realistic industrial situations where the flow geometry is usually complex and flow regime is multi-dimensional and highly non-uniform. In practice, a need has emerged to mathematically model the actual flow characteristics taking place in pleated cartridge filters for the qualitative and quantitative analysis of experimental results based on theoretical backgrounds.

1.4   Research Objective

The central theme behind this research lies in developing a robust and cost-effective mathematical tool for modelling the fluid dynamical behaviour of coupled free and porous regimes occurring in high performance pleated cartridge filters employed in aeronautical applications. Appropriate mathematical equations have been selected based on process characteristics and logical assumptions. The mathematical equations are transformed into the equivalent forms of the working equations to correspond to the previously selected numerical technique. Responding to the imposed boundary and interfacial constraints, the results are obtained by an iterative procedure. During the iterations, the rheological properties of the fluids such as viscosity are updated according to varying flow fields. The developed code will deliver output in a file suitable of exporting to generally available graphics packages for post processing of results in pictorial formats.

Though the overall process of model development involves mathematical computations, the principal emphasis is on adopting engineering approach. The mathematical complexity is avoided but with the scope for inclusion of mathematical theories that will be developed in future. The model is adaptable to changes in physical properties of the fluid, the filtering media and the solid contaminants. The developed tool is flexible to comply with varying geometric characteristics of pleated cartridges. The details of the generated code will be provided in the form of a detailed manual, modules and sub-modules embedded

in the software package. This will enable the design engineers to introduce any changes in them according to the process requirements without any hassle.

The overall aim of this project is to manufacture a sort of mathematical virtual machine to be operated by an ordinary worker in the industry without having any prior knowledge of its working principle. The machine will be fed with the raw materials in the form of flow and material characteristics and it will generate output in form of numbers. In this way, the appraisal of the filter operation can be achieved before manufacturing it in the workshop, which will result in considerable economy in the design process. Ultimately, it will offer a high flexibility and convenience for the tool operator without a need of detailed knowledge of fluid dynamics or numerical methods. The code will assist the design engineers in optimising the filter performance based on its geometric features and material properties as optimisation parameters. Although the present study focuses on cartridge filtration of hydraulic fluids, the approaches taken are generic and should be applicable to a range of design of cartridge filters. Ultimately, the core concept behind this work is just to provide complimentary support based on a sound theoretical basis to the experimental results.

1.5   Thesis Outline

The present thesis is composed of a total of nine chapters with additional sections for appendices and references. The hierarchy and the contents of each chapter are mentioned in brief as follows:

1. **Introduction**

   The background and scope of the project has been elaborated with its industrial concern and participation. The importance of the hydraulic filtration is explained, focussing on its application to aircraft systems. The research objective is defined in the light of the project theme, discussing the key difficulties and discriminating it against the previously reported studies on similar topics.

2. **Literature review**

   The chapter discusses fundamental concepts of filtration processes and present understanding of the project. The subject is predominantly examined keeping the pleated cartridge filtration at its centre point, reporting the past

experiences about the experimental outcomes and supporting computational analyses.

3. **Mathematical representation**

   The governing equations are given explaining the significance of the individual terms involved. The assumptions made behind selection of these equations are also given.

4. **Numerical solutions scheme**

   The ideas behind selecting the finite element method as a technique for solution of the governing equations are listed in terms of its applicability to computational fluid dynamic problems. Two different finite element schemes are given for steady-state and transient cases.

5. **Development of computational scheme**

   The transformation of the governing equations to finite element working equations is given for two coordinate systems. The necessary and sufficient boundary conditions for the governing mathematical equations are specified. A complete solution algorithm is explained.

6. **Computational results and discussions**

   The validity of the computational procedure is examined by carrying out simulations for different geometrical domains and the resulting variable profiles are discussed with the graphical representation of results. Finally, the results are presented for the special case of pleated cartridge filters.

7. **Computational analysis of experimental data**

   The simulated results obtained over the pleated cartridge domain are analysed against the available experimental data for their validity and consistency. Based on these comparisons, some conclusions are drawn suggesting innovative steps in the cartridge design procedure.

8. **Conclusions**

   This chapter consists of the concluding remarks that are drawn from the simulated results about the filter performance and the validity of the overall computational procedure and its application.

9. **Future prospective**

   This concluding chapter suggests guidelines for carrying out advanced research in this area and improvement in current algorithm.

R   REFERENCES

A   APPENDICES

2   Literature Review

The current study is an attempt to develop generic software to give an insight into the flow behaviour in pleated cartridge filters. In this context, classification criteria behind filtration equipments have been explained based on their mode of operation decided by the direction of flow. A brief summary of development of the cartridge filtration technique has been given followed by various cartridge structures. The cartridge filtration is distinguished from other conventional filtration equipments providing the details of its applicability to diversified fields of interests. Some of the previously carried out experimental procedures on cartridge filters determining its operating characteristics and optimisation criteria for their selection have been given. A few efforts taken in the past to model the flow phenomena in pleated cartridge filters are given a due consideration. On the side of the physical description of the problem, fundamentals of fluid flow in free and porous regions have been discussed with their representatative mathematical models developed to date. The major emphasis of this chapter lies in defining the interfacial phenomena occurring on the boundary separating free and porous flow regimes. Various forms of interfacial constraints derived by researchers aiming at simplifying the mathematical solution of the coupled flow problem have been discussed concisely.

2.1   Filtration Processes

Filters are generally classified according to the mode of operation, namely dead-end or cross-flow modes (Wakeman and Tarleton, 1999). In both these operations, the flow directions with respect to porous medium boundary are differentiable. These two types are again sub-divided according to the pore size in permeable media or according to the size of contaminant retained by the porous surface.

2.1.1 Dead-end filtration

In dead-end filtration, the flow field is directly obstructed by porous wall as shown in **Figure 2. 1**. Due to this unavoidable obstruction, the solids within the flow are brought to the surface of the porous walls and depending on their relative sizes with respect to pore openings either stick to the surface or trapped in the interior of the porous matrix.
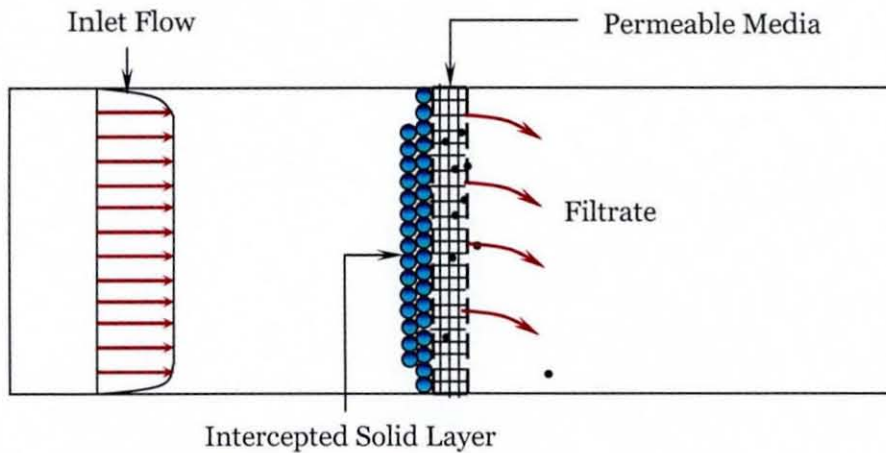
Figure 2. 1: Dead-end filtration

The continuous deposition of solids on the filter surface may culminate in the blockage of pores or in the formation of a cake. A very low permeability cake layer of deposited solids is formed on the membrane surface causing gradual decline in filtrate flow rate with time. The pressure drop across the filter medium rises to a maximum limit at which the filtrate flow rate reduces to zero due to the added resistance of the deposited solids. Deposition can be due to different mechanisms such as adsorption, depth particle interception, cake layer formation, cake layer compression etc. During filtration, all these mechanisms may occur simultaneously (Roorda, 2004). Kovintsev *et al.* (2002) modelled the dead-end microfiltration using the pore blocking model proposed by Flippov *et al.* (1994) treating it as a type of sieving process. They assumed the microfiltration process composed of three stages. The first two involve the pore blockage while the final stage is that of cake formation. The one-parameter model is cross-examined by fitting against a series of experimental data. Cartridge filters are necessarily operated in dead-end fashion.

2.1.2 Cross-flow filtration

In cross-flow filtration, the liquid entering the filter flows tangentially to the filter medium surface, as shown in **Figure 2. 2.**
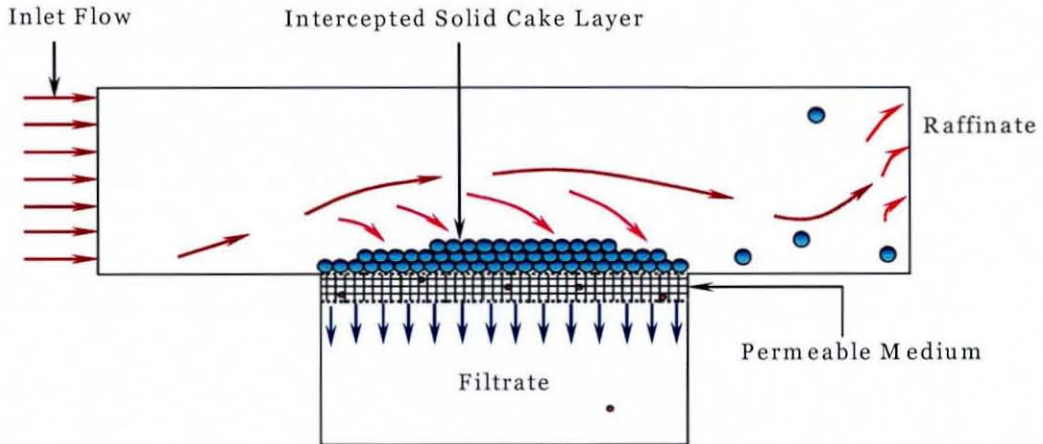
Figure 2. 2: Cross-flow filtration

In cross-flow filtration, the larger solid components from the permeating fluid form a layer on the membrane surface. Due to the tangential flow, a sweeping action takes place, which limits the build up of the cake layer. During the cross-flow filtration process, the flow becomes less developed due to fluid being lost through the permeable media.

2.2 Cartridge Filtration

Cartridge filters are generally used in applications where the main concern is the recovery of clean fluid either liquid or gas, discarding the trapped solids. The modern cartridge filtration technique is quite old and developed over the years in different phases and diversified fields of applications. In 1924, the Chrysler Corporation introduced cartridge filters for clarification of oils in automobiles. In today's sophisticated world, not a single automobile model is complete without a cartridge oil filter, cartridge air cleaner or a cartridge fuel filter. In 21st century, much of the market for cartridge filters is related to cleaning of lubricants or oils and a major portion is still contributed by the automobile sector.

Rushton *et al.* (2000) identified various cartridge constructions and geometries, some of which might be listed as,

a. Plain cylinder
b. Pleated cylinder
c. Leaf disc

and are represented in **Figure 2. 3**.

(a) Plain cylinder   (b) Plain cylinder   (c) Leaf Disc

(e) Plain cylinder multiples   (f) Pleated cylinder concentric   (g) Pleated cylinder multiples
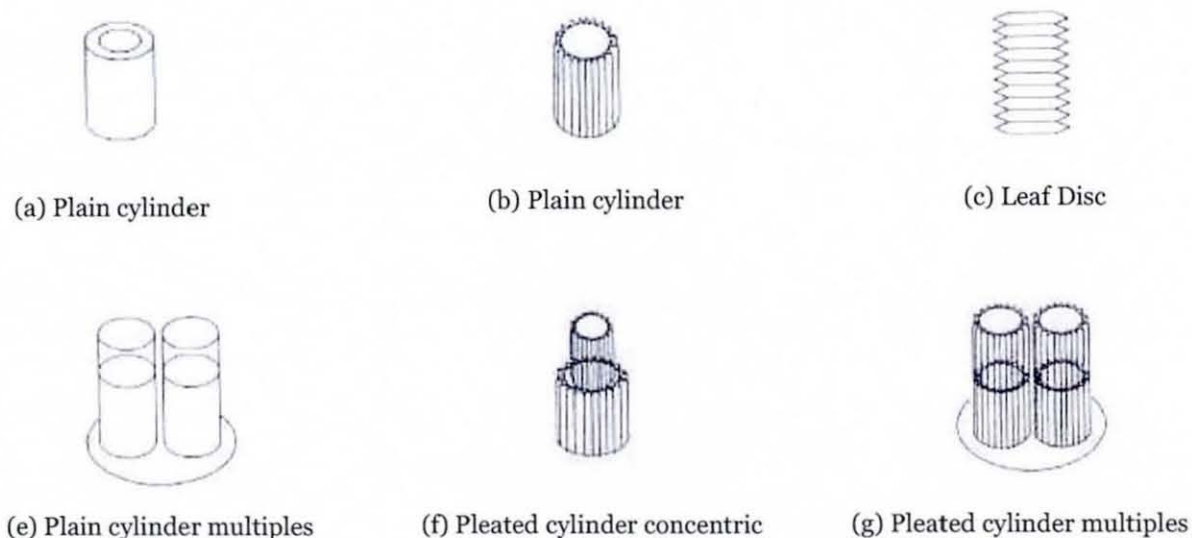
Figure 2. 3: Cartridge filter element geometries

Pleated cartridge filters are used in industrial applications where clarification or polishing of the fluid phase is required; they offer a particular advantage in enabling a large filtration area to be packed into a compact size, higher amount of material accommodated in smaller volume. The disposable cartridge is quite common when the filtration is by depth mechanism whereas in surface filtration recleanable cartridges are in general practice. The disposable cartridge can only be used once; after its dirt loading capacity has been reached or the pressure loss across it has become unacceptably high, the cartridge must be removed from the system being cleaned and disposed of by incineration, by disposal at a landfill site, or by some other means. The commonly employed filtration media are paper, felt, loose fibres such as cellulose, synthetic fibres, synthetic woven fibres, glass fibre, sintered metal powders (Purchas, 1981).

Pleated filter elements are usually constructed in cylindrical forms with the central core strongly supporting the pleated medium wound around it. The most general types of pleating configuration available are listed as,

1. Star or V-shaped pleats
2. Rectangular pleats
3. Circular pleats

(a) Triangular Pleats   (b) Rectangular Pleats   (c) Circular Pleats
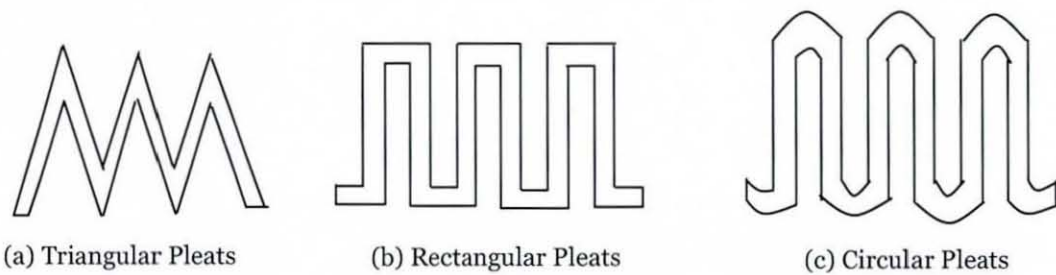
Figure 2. 4: Different pleating configurations

Pleated cartridge filters are generally dead-end filters and because of this have only limited capacity for the removal of suspended solids. This limits their application for clarification purposes but it is general practice to employ filters using many pleated cartridges in parallel, which provides greater dirt-handling capacity or extended service life. A typical pleated cartridge filter element used in aeronautic filtration circuit is shown in **Figure 2. 5** along with its design anatomy. The pleated material is a synthetic fibre medium supported by the metal wire mesh upstream and downstream to maintain its mechanical integrity.
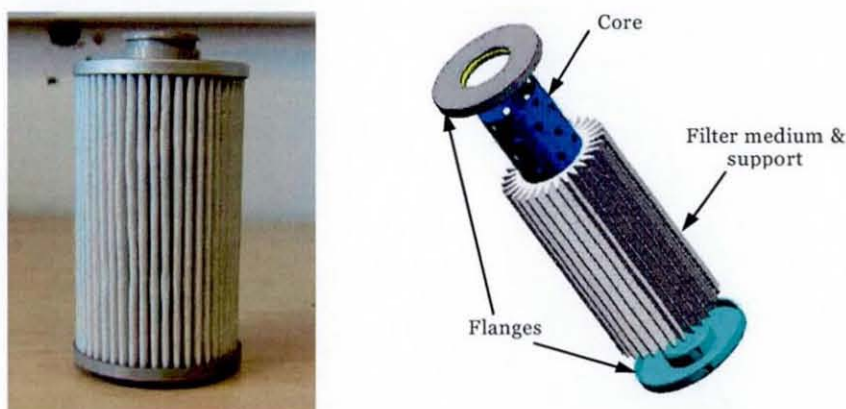
Figure 2. 5: Aeronautical pleated cartridge filter and its design anatomy

Hydraulic filters used in automotive and heavy machine applications are cartridge filters, specifically pleated cartridge filters. Paper and wire mesh are widely favoured media in hydraulic filtration systems. Glass micro fibre filter media offer better pore size distribution, higher open flow areas and greater dirt holding capacity. This makes the glass fibre medium a favourite filter medium in high-pressure hydraulic filtration in aircraft applications. Since the glass fibre medium lacks in mechanical strength, the pleats are supported on the upstream and downstream side by metal wire meshes (Dickenson, 1997). A cut sectional view of a typical hydraulic pleated cartridge filter composed of glass fibre pleats is shown in **Figure 2. 6**.
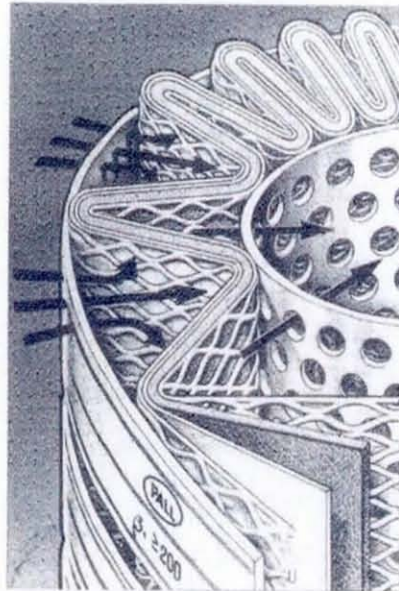
Figure 2. 6: A sectional view of high pressure hydraulic oil filter
(*Courtesy: Dickenson, 1997*)

The pleated filters are required to possess some of the following characteristics to strongly support their selection for heavy duty hydraulic filtration.

- Low weight and compact size;
- An adequate contaminant retaining capacity;
- Low pressure drop across the filter to reduce operating costs;
- Ability to withstand high pressure differential to maintain the integrity of pleated structure.

In a commercial sense, hydraulic filters may be described as high pressure, medium pressure and low pressure filters. High pressure filters operate in the excess of 400 bar working pressure and flow up to 400 litres per minute. Medium pressure hydraulic filters are suitable of variety of pressure and return line applications and can operate up to 250 bar operating pressure and flows up to 800 litres per minute. Low pressure filters are typically designed for operating pressures of 30 bar with flow rates up to 1200 litres per minute. They find particular applications in industrial, automotive and mobile applications.

2.2.1 Application Areas

Fochtman (1973) explained the historical perspective behind development and innovations in cartridge filtration technology along with design and testing procedures. During Word War II, various defence organisations were conscious about investigating the performance of cartridge filters in military vehicles to avoid breakdown of equipments from dust attack. The attempts were extended in designing air filters taking to account the major concerns over increasing chemical, biological or nuclear warfare threats. Parallel to these, increasing air pollution in industrial and domestic sectors increased the need for innovating newer filtration techniques with varying volumetric capacities. In biological and medical applications, newer cartridge designs have emerged to maintain cleaner environments protecting against the bacterial and viral infections. Increasingly stringent requirements for hygienic processing conditions have led to adoption of membrane cartridges in pharmaceutical industries. The wide variety and diversity of applications makes it somewhat difficult to prepare overall performance specifications for cartridge filtrations. Fochtman (1973) estimated at least 15% yearly growth in cartridge filtration industry.

Nickolaus (1974) describes the range of filter cartridges used in industry and defines the terms to differentiate the performance of various types of cartridges. He gives commonly available filter cartridges, which fall under the category of disposable as well as reusable categories. The particle removal efficiency of each type of filter cartridge is expressed in terms of its micron ratings. Depth and surface cartridges are differentiated based on their suitability in

removing varying types of contaminants and range of contaminant concentrations. The parameters on which the filter performance is rated such removal ratings and dirt holding capacity are discussed. He describes the production testing procedures and in-plant testing procedures to decide the reliability of filter cartridges.

Pointon *et al.* (1974) describe various filters such as pressure filters, leaf filters, centrifuges etc. used for clarification and screening in chemical industry. They discussed in detail the types of cartridge filters used in chemical industries and their respective selection procedure on the background of filtration economics. Accordingly, the cartridge can be judged based on three criteria i.e. the size of smallest particle to be trapped, the resistance to flow and the dirt holding capacity. The low capital and installations cost strongly supports the choice of cartridge filters, even though they may be expensive in terms of high running costs particularly in cases of disposable cartridges. Concluding the article, he lists some speciality applications of cartridge filters. In some cases, cartridge filters are used to avoid manual handling and physical contact with toxic solvents and highly coloured chemicals. In number of cases, cartridge filters are employed to protect conventional filtration equipments to avoid expensive re-treatment. They are being used to remove unwanted impurity from reactant streams prior to feeding the reactor. Cartridge filters are also used for protecting automatic reflux valves of distillation columns.

Viruses causing transmittable diseases exist in natural water and tap water in dilute concentrations and even are capable of causing diseases when ingested. Farrah *et al.* (1976) presented a method for the efficient concentration of viruses from large volumes of tap water in short time span over a pleated depth fibre glass cartridge filter by adsorption mechanism. In their successive attempt, Farrah *et al.* (1977) reported adsorption of enteroviruses from estuarine water on pleated cartridge filter. Sobsey and Glass (1980) reported a simple and reliable method for concentration of poliovirus from tap water on pleated cartridge filter composed of electropositive filter media. An ample amount of research articles are still being published in the environmental and medical journals related to trapping of viruses from drinking water sources on pleated cartridge membrane microfilters.

Scanlon (2004) explains the importance of cartridge sterile filtration in brewing process to achieve microbial stabilization of beer to remove spoilage

mechanisms such as bacteria and yeast prior to packing. Since the operating conditions in beer brewing process are harsh with high liquid flow rates and high pressures, filter systems must be designed to handle these process conditions as well as any process upsets. Two main design parameters for cartridge filters in the beer brewing are the optimal pleat density and novel-end cap design to achieve robustness and integrity of cartridge structure.

2.2.2 Experimental investigations and computational analysis

Gollan and Parekh (1985) considered mathematical modelling of several hydrodynamic phenomena of fluid flow in semi-dense pleated structures in cartridge filters. The pleat was assumed to be composed of a membrane sandwiched between two supportive layers, one upstream and one downstream, of different permeability values. Four different cases of semi-dense pleated configurations were considered: constant and pressure-dependent downstream layer permeability with time-variant and time-dependent membrane permeability. The relationship between pleat physical properties, fluid flow rate, pressure drop and overall efficiency was evaluated, and they considered an "optimal" (*sic*) or effective membrane area of a pleated cartridge to be a product of the actual area multiplied by pleat efficiency. Longer pleats and a thinner downstream supportive layer were claimed to increase the actual area, but there may be an adverse effect on efficiency primarily because of lower downstream layer permeability.

Yu and Goulding (1992) presented a mathematical analysis and design optimisation for ultra high efficiency inlet air pleated filter panels for modern aero-derivative combustion turbines. Though the flow through the filter media is not uniform along the depth of the pleat, the pleat height is subdivided into infinitesimal finite element and flow through the walls of the element is assumed to be constant. A closed form semi-analytical/numerical approach has been adopted for the solution of the Navier-Stokes equation for air flow between pleat spacing with uniform mass addition and subtraction applied to each finite element along the pleat channel. The problem can be considered as coupling of two separate problems, one with mass subtraction and second with uniform mass addition with sharing the common wall with specific filter media characteristics. An integral form of solution is obtained for the pressure differential between the

inlet and any location along the length of the pleat. The pressure drop is observed to be proportionate only to the air velocity in the channel confined by the pleats. In the upstream pleat channel the effect of momentum change is more significant than the viscous drag and there is a net gain in pressure in the flow direction. The coupled equations for the upstream and downstream pleats are in the form of finite difference formulae. They can be solved simultaneously for all the finite elements by a simple iterative scheme using the pressure drop versus face velocity characteristic curve for each filter media used. The results generated gives pressure drops and velocity profiles in the upstream and downstream pleat spacing and through the filter media along the length of the pleat.

It is also deduced that for a particular pleat height, there exists an optimal pleat density in the filter corresponding to minimum pressure drop in the panel. At low pleat density, high pressure drop values are observed for high flow velocity values. On the contrary, at a higher pleat count, higher panel pressure differential is obtained due to high pressure losses between the pleat spacing. The optimum ratio of pleat height to pleat spacing is independent of the media face velocity and is a function of filter media characteristics.

Wakeman and Harris (1993) developed a methodology for modelling pleated cartridges, in order to predict magnitude and direction of fluid and particle velocities, the pressure distribution, permeability of the filter cake or a measure of particle deposition. If cake starts building during filtration, the volume of the flow region upstream of the pleat will change, posing extra complexity to the problem. It was assumed that there was no formation of cake, which is the practical case when filtering low concentrations of smaller particles. The model was developed specifically for "star" pleat configurations, which were considered to have symmetry in radial direction, therefore requiring only half of the pleat to be modelled. The free flow was modelled by the unsteady state Navier-Stokes equation and the pressure drop in the porous region was calculated by the Darcy equation. The governing equations were solved using a classical finite difference scheme. The number of particles trapped in the porous medium was related to the magnitude of flow through medium and its history at a particular point. The flow was radial in the free flow region upstream of and far from the filter medium, and flow deviated as it approached the pleat surface in order to pass through the porous structure. A smaller amount of fluid flows through about 50% of pleat face

with most of the flow through the area between the inner tip of a pleat and centre of the pleat face before the stage of solids deposition. The pressure differential developed over a pleat was primarily dependent on the porous medium permeability in the initial stages of filtration (before deposition of particles). After the solids start to deposit, the pressure loss is a function of the overall permeability (which decreases with time) of the medium and the deposited solids. The work stresses a need to develop a three-dimensional model to generate a better representation of the cartridge filter. The need to use depth filtration equations as well as the classical Darcy equation to account for internal deposition of solids was also recognised.

Chen *et al.* (1995) developed a finite element numerical model to optimise the design of pleated filter panels. Although filter panels have a linear rather than cylindrical configuration, similarities in that both are pleated point to the development of similar modelling procedures. The optimization parameters considered were pleat count, pleat height, pleat configuration and filter media characteristics. The pleats were rectangular in shape. Uniform velocity profiles were assumed in the upstream pleat channel and sinusoidal in the downstream channel. It was assumed that the fluid penetrates the porous medium only at the top and bottom regions of the pleat, with any penetration along the length of the pleat being negligible. This was a major assumption that is unjustifiable in the absence of either numerical or experimental modeling, and which has later been shown to be fully quantifiable (Ruziwa *et al.*, 2004). Chen *et al.* (1995) modelled the free flow using the Stokes equations and the porous flow using the Darcy-Lapwood-Brinkman equation to compensate for simplified velocity profiles and neglected viscous effects. This equation is a modification to the Darcy equation by adding a convective term applicable to high flow rates, and viscous stress term to account for fluid-porous media interactions. It was found that the flow in the upstream pleat channel became fully developed in a very short distance. There was a small fraction of the flow that passed through the back end of the filter, the amount of which decreased with pleat spacing or increased with pleat height.

The total pressure drop across the pleated filter was a result of flow contraction in the upstream panel region, viscous drag between the fluid and porous surface on both the upstream and downstream channels, the pressure drop across the filter medium and flow expansion in the downstream region. For a

certain pleat height, there was an optimal pleat count corresponding to a minimum pressure drop. At a lower pleat count (smaller filtration area), the filter medium face velocity was higher, resulting in a greater pressure drop. At a higher pleat count, the pressure drop due to the viscous drag in the porous medium became more significant, resulting in a high pressure drop. An optimal pleat count occurred when the combination of viscous drag and medium resistance was a minimum. The numerical results were compared with the analytical results obtained by Yu and Goulding (1992). Optimization was carried out for six different filter media. The results showed that for a given pleat height, the optimal pleat count increased if the permeability of the filter media decreased. The optimal pleat count occurred when the magnitude of the viscous drag became critical relative to media pressure drop.

Lücke and Fissan (1996) proposed an algorithm to calculate filtration performances of pleated filter elements directly from the geometry of the pleats and filtration performances of plane filter media. Filtration performances of filter media include particle penetration probability and pressure drop across the medium. A model for velocity field and overall pressure drop of a filter element is developed based on approximate solutions of the two-dimensional Navier-Stokes equation along with equation for overall particle penetration. Based on their previous experimental investigations, the authors assumed that the flow entered and left from the medium perpendicular to the surface. The effective filter medium coefficient model which represents particle penetration considers velocity dependence of diffusional deposition mechanism of submicron particles as well velocity independence of interception diffusion mechanism in the bulk of porous matrix. Since the obtained general formulae are complicated, they are simplified for special cases for rectangular pleat spacing.

The velocity field obtained for rectangular channels within the pleats is compared with the perturbation solution obtained by Berman (1953) and lie in their close vicinity. The pressure drop values obtained from the model are analysed against the numerical solution previously obtained by Chen *et al.* (1995) and are in remarkable agreement. When the pressure drop values are plotted against the pleat spacing for varying pleat lengths, the curves are observed to be passing through a minimum, which will allow minimizing the pressure drop of a filter element down to a theoretical limit. The proposed approach is tested for

different filter media through experimental procedures. It was found that for high efficiency filters the calculated results are closely matching with the experimental values. It is concluded that the proposed algorithm would help to optimise the filter equipment to minimise the pressure drop for a given particle penetration intensity and need to be extended to pleated filter cartridges.

Del Fabbro *et al.* (2000) attempted the modelling of airflow in high efficiency pleated filters made up of nuclear and car type media and their clogging by the solid particulates. The variation of filter efficiency and pressure drop due to deposition of solid particles are analysed with experimental procedures and computational modelling. The experiments were performed using particle tracers of known diameters. The airflow through the pleated system is modelled by the Navier-Stokes equation, which contains an additional viscous drag term within the porous media. These viscous forces are expressed according to the Darcy's law in which the resistance of the filter medium is taken as a function of mass of the particulates deposited. The model was examined against the experimental results to determine the pressure drop of the filter and distribution of airflow for a mass of particles deposited. The filter performance was tested against operating parameters such as filtration velocity, geometric parameters of the pleating assembly such as pleat height and pleat spacing along with the size of particles deposited. It was observed that for pleated filters of identical geometrical properties and for a given mass of solids trapped on the media, the pressure drop across the filter is the highest for particles with the smallest diameter and this effect is noticed in each such filter irrespective of the type of filter media used. As the pleat spacing is increased, an increment in filter pressure drop is observed independent of the type of the filter media. The combined effect of the height of the pleat and the filtration velocity is having a great influence on the relationship between pressure drops versus mass of particles deposited. For a given mass particle deposited per unit area the pressure drop is higher for the car filter media than the nuclear media.

Baléo *et al.* (2000) simulated the pressure drop in pleated cartridge modules made of activated carbon cloth for removal of VOCs from air. The steady state hydrodynamic behaviour of the filter was analysed where the pressure drop is independent of time due to negligible deposition of particles, keeping the filter efficiency constant. The mass and momentum balance equations and coupled

transport equations linked to turbulent nature of flow were solved using a finite volume method. Attention was paid mainly to the possibility of predicting accurately and quantitatively pressure losses in different module configurations. The flow was considered steady, isothermal, axisymmetric and turbulent. The Navier-Stokes equation was augmented by a source term to account for the additional pressure gradient in the porous region. The classical k-ε model or Reynold's stress model was incorporated to account for turbulence. The experimental pressure drop was related to the to the mean flow velocity in the single module by a polynomial expression which contained viscous and inertial terms. The pressure losses were mainly found to occur in the porous region in the radial direction. Possible improvements were suggested for the filter geometries to suppress dead zones and to reduce singular pressure losses along with producing a more uniform distribution of the feed flow rate.

Caeser and Schroth (2002) derived the steps for calculating pressure drop when air flows through a zig-zag or V-shaped deep pleated filter element. It is based on the assumption that the pleat geometry is unaffected by the air flows and therefore the pleats can be regarded as completely rigid. The total pressure drop in a deep pleated filter element can be attributed to the pressure difference inside the pleat due to frictional losses and dynamic pressure gain, pressure drop during the entrance and exit of the pleated system and pressure drop due to the resistance to flow from the filter medium. The pressure drop occurred inside the pleat is calculated by one-dimensional Navier-Stokes equation whereas the pressure drop contribution by the filter medium is calculated by the Darcy equation assuming that the volumetric flow is evenly distributed on the filter surface. The fundamentals of calculations derived are implemented in a computer code. The influence on pressure drop in deep pleated cassette filters are analysed against varying pleat shapes, pleating depths and pleat distances. The geometrical component of pressure drop is calculated from the discrepancy between total pressure drop across the filter element and pressure drop across the permeable medium.

It was observed that the filter area reduces by keeping the pleats closer, thereby decreasing the contribution of porous media pressure drop. Simultaneously, the geometric component of pressure drop exhibits over proportionate influence resulting an increase in the total pressure drop. It can be

concluded that a large filtering area cannot be always advantageous for deep pleated cassette filters. When the flow characteristics in two different pleat geometries, namely V-shaped and rectangular pleats are compared, it was observed that the pressure drop in rectangular pleated filters are always greater than those obtained in V-shaped pleated system. With V-shaped pleat geometry, the filter medium is at the same angle to direction of flow at every point resulting in uniform flow through the medium. However, any deviations from this geometry such as a curvature in pleat facing to the direction of flow can have seriously adverse effects on pressure drops. The results showed that the pleat geometry in deep pleated cassette filters, exhibits higher impact on the pressure drops in the filter elements than the filter media of high air permeability.

Subrenat et al. (2000) studied cylindrical pleated filters made from activated carbon cloth (ACC) and polypropylene layers using a laboratory pilot plant. Experimental pressure drops were measured as functions of the geometrical configuration of the filter and properties of its constitutive material. The experimental study presented measurements of pressure drops through planar media. The permeability of this set of experiments was studied as a function of the number of planar medium layers. The experimental pressure drop data were then fitted using a classical model consisting of viscous and inertial resistance terms. The pressure drops of systems of multiple layers of porous media were considered to be additive and correlated using

$$\Delta p = a_1 v + a_2 v^2 \qquad\qquad (2.1)$$

It was found experimentally that this assumption was only valid up to two layers of porous media. The pressure losses through the pleated filters were analysed as a function of the number of pleats, and it was found that the developed surface of the pleated medium might not be the actual area through which the feed flows. Therefore, the pressure drop through the pleated domain was considered as a function of volumetric flow rate (whereas velocity was used for planar media) as

$$\Delta p = a_{1,N} Q + a_{2,N} Q^2 \qquad\qquad (2.2)$$

It was observed that as the number of pleats in any filter module was increased, the thickness of the pleat increases at both its ends due to overlapping of media – which was said to thereby reduce the effective cross-section for the flow. Therefore, the global pressure drop normally rises. If the number of pleats

were increased further, a maximum is reached where the pleated geometry behaves as a homogeneous porous medium due to extensive overlapping of pleats. The thickness of this homogeneous medium equals the pleat height and the fluid only flows through head of the pleat. These two phenomena, decrease in effective cross-section and local increase in media thickness due to overlapping, were decoupled to introduce parameters controlling the evolution of pressure drops through pleated filters as a function of number of pleats. Two parameters were considered in modelling the aerodynamic behaviour of the filter (the equivalent section and the thickness) to ensure pressure losses of airflow through a given filter as a function of the number of pleats. The equivalent section was defined as the area of the planar medium for which the same pressure drop at the same flow rate would be obtained with the pleated filter. Equivalent thickness was defined as the thickness of a zero pleated filter that would give the same pressure drop as the pleated filter. The total area offered to flow by a pleated filter was reported to increase with the number of pleats. The numerical correlations for the equivalent thickness and sections were only valid for the particular filters used in the experiments. The authors found that for identical operating conditions of inlet concentration and interstitial velocity, the adsorption capabilities of pleated and planar filters were the same.

In their later work, Del Fabbro *et al.* (2002) examined experimentally and numerically air flow distributions and pressure drop variations with velocity in two types of clean pleated filters, namely High Performance Particulate Air (HEPA) filters used in nuclear applications and Low Performance Particulate Air Filters (LEPA) employed in the automotive industries. A fluorescent tracer is introduced in the filters to characterise the flow distribution. The variables considered during experimentations were air flow velocity, pleat height and pleat spacing. For the study of clean filters two parameters are analysed namely the pressure drop and flow distribution function calculated from the mass of fluorescent aerosols trapped. The experimental findings are validated against the numerical solutions obtained from a CFD computer code based on Navier-Stokes equation for steady and isothermal airflow. The Navier-Stokes equation contains an additional sink term given by the Darcy's law to account for the pressure drop in the filter medium. All the simulated results indicate that in the case of LEPA filters, the geometric characteristics of pleats have a great influence on pressure

drop variations than in the case of HEPA filters due to heterogeneous airflow distribution in the former case. These differences in air flow distributions between the two pleated filters are mainly attributed to the air flow resistance of the filtering media. The numerical studies exhibits that the Darcy's law is valid globally in HEPA pleated filters so that they behave practically like flat filters with equivalent surface area. Based on information gathered from experiments and CFD calculations, they developed an analytical dimensionless model to directly calculate pressure drop in clean pleated filter over a wide range of operating parameters. This model could be readily used to optimise the pleating filter design corresponding to a minimum pressure drop value.

Park *et al.* (2003) carried out some experiments with several dozen pleated cartridge filters having varying geometrical features in order to find out the effect of pleating variables such as pleat depth, pleat count and filter length on the flow field. The studies were carried out on pleated cartridge filters only. Park *et al.* (2003) were able to show experimentally that when the filtration velocity is maintained unchanged, the pressure drop developed across the filters having the same pleat depth and pleat count, increases. The authors also noted that as the pleat depth and pleat counts are increased, the pleat channel becomes deeper and narrower, resulting in higher pressure drops across the filter elements. These results are important in the design and construction of pleated cartridge filters.

Subrenat *et al.* (2003) extended the work by Baléo *et al.* (2000) to 3-dimensional simulation of flows in cylindrical pleated cartridge filters packed with activated carbon cloths for removal of VOCs from air by adsorption. The pleated medium was modelled as a porous region taking into account the medium permeability and pleating effects. It allowed the study of preferential flow directions in the pleated medium in order to avoid premature breakthrough of the filter. The design and analysis of the filter was carried out considering the optimisation in terms of pressure drop, residence time of fluid in the porous medium, porous medium properties and geometrical characteristics of the pleats. In the vicinity of the solid walls a no-slip condition was applied with the assumption of an equilibrium turbulent boundary layer. At the exit of the filter, the diffusion flux normal to surface was assumed to be nil. The numerical computational procedure was based on the finite volume method with quadrilateral control volumes and structured meshes. When the simulated

pressure drop values were compared with the experimental ones, satisfactory agreement was claimed with discrepancies always less than 200 Pa, which is significant in low volumetric flow rates. The pressure differential developed over the porous medium was less than 10% of the total pressure drop in the filter system indicating that all pressure losses due to singularities and wall friction are well estimated. The pressure in the device was observed to decrease from inlet to exit except for the upper part of the bottom wall where the kinetic energy of the fluid is converted to static pressure. The ranges of local velocity of fluid at the surface of the porous medium were observed to be around 10 times higher than average velocity over the whole developed surface of the filter. This discrepancy was attributed to the overlapping of pleats at the upstream sections creating a dead zone. To improve the efficiency of filtration, the best flow direction for the fluid was found to be from outside to inside of the pleated cylindrical filter. It was found that as the number of pleats was increased the pressure drop went down due to an increase in the surface area, and at a higher number of pleats the pressure drop started to rise due to an increase of the presence of dead zones due to overlapping. Therefore, for a given value of the flow rate an optimum pleat count could be deduced where the pressure differential is a minimum.

Tronville and Sala (2003) describes an experimental procedure to determine the operating characteristics of pleated air filter panels containing commercial filter medium intended to use in air handling within air conditioning systems. Pressure drop was measured in a clean minipleated filter panel in steady state conditions as a function of face velocity. The fluid flow in the whole pleated system is investigated through numerical analysis using a commercial CFD code based on finite volume method. In simulations, a three-dimensional computational domain of three small pleats is considered to avoid the boundary effects. In CFD analysis, the panels are considered to be made of three porous elements in series two of air: entering and exiting channels upstream and downstream of the filter medium and the third one being the filter medium itself. In the free flow channel, upstream and downstream of the filter medium the flow is turbulent and the incompressible Navier-Stokes and continuity equations govern the flow field. The turbulence is represented by three models namely the Reynolds stress model, standard k-ε model and renormalization group k-ε model. Results using the standard k-ε model showed unrealistic and poor predictions compared to the experimental data

whereas the Reynolds stress model is observed to be better describing the experimental pressure drop values when a nonisotropic turbulence is assumed. The result was also confirmed on simplified two-dimensional domain.

The overall resistance to flow is contributed by the resistance from the free flow air channel and the filter medium. Both of these resistances are expressed as functions of pleat count per unit length and the face velocity. An empirical two-parameter correlation is developed relating pressure drop across the panel to its geometry including pleat spacing and permeability of the filter medium. The model parameters are found by quadratic regression and the results showed good agreement with the experimental values. The overall pressure drop is made of the values attributed to free flow channels and by the porous medium according to the Darcy's law. For the minipleated panel, the air and the filter permeability were found be of the same order of magnitude. Curves obtained from the model predictions representing the pressure drop across the panel as a function of pleat count per unit length are found to pass through minimum for each value of face velocity considered in this study. It was concluded that with increase in pleat count, the opening width decreases causing an increment in viscous drag in the free flow region in upstream and downstream channels. The resistance offered by the filter media decreases with increase in pleat count due to reduction in seepage velocity through the medium. The influence of the air resistance on pressure drop becomes significant at higher values of face velocity. This study provides the air filter manufacturers a way to determine the optimum pleat count per unit length that minimizes the pressure drop across the minipleated panel and further in full-scale filter.

More recently, Oxarango *et al.* (2004) found solutions to the one-dimensional Navier-Stokes equations for a laminar fluid flow in a channel with wall suction or injection. The approach is based on integration of Navier-Stokes equations in accordance with the perturbation analysis and averaging techniques. The developed model is validated successfully against the result obtained from the commercial CFD code. The authors claimed their model to preserve the inertial terms that could affect the wall suction and growing particle cake layer at the wall in the filtration process. The model has been examined for validity for flow through a single porous channel of rectangular or circular cross-sections. The model is then applied to a two-dimensional multi-channel system consisting of a

large number of adjacent entrance and exit channels connected by a porous filter medium. Finally, the approach has been extended to pleated filters by a two-dimensional model using a unit element of pleated filter with periodic boundary conditions. The pleats considered are simply rectangular in shape and the intrusion of the fluid in the porous medium is assumed to be unidirectional. It has been shown that the developed model is capable of analysing the effect of non-uniform boundary conditions and the influence of heterogeneous geometrical characteristics on the heterogeneity of fluid flow structure.

Most of the literature listed in previous paragraphs is concerned with the experimentation or modelling attempts in pleated cartridge air filters used in automobiles or gas turbines to achieve high air quality standards. The major emphasis was towards optimum design of pleating configurations to yield a minimum pressure drop, which would lower down their operating costs. In practice, the aeronautical pleated cartridge filters are intended to filter highly viscous generalised Newtonian fluids whose rheological properties changes with the operating conditions and hence influence the flow distributions and pressure drop variations to a greater extent. Some of the work performed in the past related to this topic covers the pleated filter channels, which differentiate significantly from the pleated filter cartridges in their design and flow characteristics. An ample amount of research has been performed using simplified forms of pleat geometry such as rectangular or triangular pleat shapes which deviate greatly from real pleating configurations used in modern types of pleated cartridge filters where the pleats are having circular crests and troughs and which makes their modelling a difficult task to undertake. The operating parameter such as fluid velocity lies in the range of 0.25 to 3 m/s in the case of air filtration, which causes the flow to be nearly turbulent, and presents a need for the inclusion of turbulence model in the flow modelling. In the liquid filtration, the fluid velocity values are very low enough to assume the flow regime to be creeping and laminar.

Most of the experimental data obtained from the pleated filters was used to develop analytical models to generate optimisation procedures for the pleated filter designs. It puts a question mark on validity of these models since they lack some sort of theoretical validation that could be obtained from the flow modelling based on actual physical phenomena taking place during filtration. In the modelling attempts, many of the researchers have simplified the physics

underlying the filtration in pleated systems using modified forms of Navier-Stokes or Darcy equations to achieve simplicity in their solution procedures. On one hand, some of them have solved the free and porous flow equations individually without any proper linkage between these two distinct flow regimes whereas on the other side, some of them solved just the free flow equations with the porous terms embedded in them in form of source or sink terms. Though these models generate valid results, they exhibit inflexibility in varying design and operating parameters of the pleating system. In reality, there exists a coupled free/porous flow phenomenon in the pleated cartridge filters which needs to be modelled using appropriate forms of the flow equations applicable to all the geometries and operating conditions encountered in the pleated cartridges.

2.3   Fluid dynamical behaviour of incompressible fluids

Basically, the laws of conservation of mass and momentum represent the fluid flow behaviour in transient as well as steady state modes of operation. Though the generalised forms of these conservation laws are same, their mathematical representation varies depending on the nature and geometry of the flow domain and physical and chemical properties of the fluid. In the subsequent discussion, various forms of mathematical models for free and porous flow dynamics are presented. As the interfacial constraints play a crucial role in modelling the coupled free/porous flow dynamics, different forms of interface conditions developed by researchers either experimentally or conceptually, forms the core section of this discussion.

2.3.1   Free and porous flow dynamics

The conservation of linear momentum equation is represented by the Cauchy's equation of motion (Nassehi, 2002) containing viscous and convective transport terms. Combining Cauchy's equation with an appropriate stress equation yields well-established models used in free flow computational fluid dynamics. In the case of generalised Newtonian fluids, the Cauchy's stress tensor is considered to a function of instantaneous rate of strain and is independent of memory of deformation. In these cases, the Cauchy's equations take the form called as the Navier-Stokes equations of motion for generalised Newtonian fluids

(Bird *et al.*, 2000). In some highly viscous fluids, the Reynolds number is small enough to neglect the contribution to the flow by convection mechanism and the Navier-Stokes equations gets transformed into the Stokes equations for creeping flow.

The processes featuring flow through a porous medium commonly encounter in chemical, mechanical, aerospace, hydro-environmental, geothermal, petroleum and reservoir engineering. Examples include the manufacturing processes of advanced composites, oil recovery and underground water flow (Das and Nassehi, 2001). An understanding of fluid flow relative to a swarm of permeable particles is frequently occurred in chemical engineering such as flow through fixed bed of catalyst pellets (Sutherland and Goodarz-Nia, 1971). Vankan *et al.* (1997) performed the quantitative analysis of blood perfusion with a hierarchical mixture model of blood perfuse biological tissue. The important industrial process, which is solely based on the concept of flow regime bounded by porous walls, is filtration separation (Wakeman and Tarleton, 1999; Rushton *et al.* 2000).

The porous medium is a material consisting of a solid structure with an interconnected void and on the pore scale i.e. microscopic scale the flow quantities such as velocity and pressure will be irregular (Nield and Bejan, 1992). In real time experiments, the flow quantities are measured as an average over area or volume occupied over a number of pores (macroscopic level). The general way of deriving laws of governing macroscopic flow variables is to adopt standard fluid flow equation averaging over area and volumes occupied by a large number of pores. There are two ways of averaging called as spatial and statistical. In the spatial approach, a macroscopic variable is defined at the centroid of a representative elementary volume and is calculated as a definite mean over that volume. In statistical approach, the macroscopic variables are obtained from the flow through individual pores, which are macroscopically equivalent.

Darcy (1856) carried out experiments on hydrology of the public fountains of Dijon and presented a proportionality between pressure drop through a uniform permeable medium and a one-dimensional flow velocity as,

$$\nabla p = -\frac{\eta}{K} \cdot u \qquad\qquad (2.3)$$

where, ∇p is the pressure drop across the permeable media, η is the viscosity of the fluid, K is the permeability of the medium and u is the velocity of flowing fluid. Lage (1996) described the theory and origin of Darcy Equation. The validity of Darcy's equation in representing flow through porous media is widely accepted (Beavers and Joseph, 1967; Gartling *et al.*, 1997). The validity of the Darcy equation is subjected to assumptions such as low Reynolds number and no fluid-porous media interaction. Darcy's law faces severe criticisms regarding the order of the differential equation and the corresponding inability to specify no-slip boundary conditions at solid walls and impose the standard mass continuity restrictions at porous, open fluid interfaces. In addition the Darcy's law is only valid for the value of Reynolds number close to unity. To ameliorate these limitations, various researchers came forward with different modifications to conventional Darcy equation.

To comply with the requirement of no fluid-porous medium interaction, Brinkman (1947) added extra viscous diffusion terms to the standard Darcy equation to the formed so called the Brinkman equation.

$$\nabla p = -\frac{\eta}{K}\cdot u + \eta_B \nabla^2 u \qquad (2.4)$$

where, η_B is the effective viscosity of the fluid and the porous medium which is assumed constant everywhere in the flow domain equal to the fluid viscosity. However, the hypothesis about constant effective viscosity was not proved theoretically or experimentally as reported by Kaviany (1991) and Givler and Atobelli (1994). Theoretical studies by Lundgren (1972) followed by Kim and Russel (1985), including mixture and averaging studies, exposed its ability to represent flow behaviour only in very high porosity medium generally greater than 0.6. Rudraiah and Rao (1982) reported a similar attempt and they referred these equations as Darcy-Lapwood equations. In addition, to account for the fluid-porous medium interaction, Katto and Masuoka (1967) modified the Darcy-Lapwood equation with the inclusion of viscous force terms and named it as Darcy-Lapwood-Brinkman equation.

To enhance the applicability of the standard Darcy's law to the high Reynolds number flow, Wooding (1957) performed modifications with the addition of convective-acceleration terms. This equation then represents the

momentum balance in porous region obtained with an analogy with the Navier-Stokes equation as,

$$\nabla p = -\frac{\eta}{K} \cdot u + \eta_B \nabla^2 u + \rho (u \cdot \nabla) u \qquad\qquad (2.5)$$

where, ρ is the fluid density.

However, it is apparent that in the case of the very low permeable medium, the boundary layer formed in the vicinity of free/porous interface breaks down and hence there is negligible effect of the inertia forces induced by the convective acceleration terms. Beck (1972) pointed out that the addition of a convective-acceleration term has raised the order of the differential in the standard Darcy equation and made it cumbersome to impose the slip boundary conditions. In the case of viscous fluid flow in open channel, the fluid carries all the stress when displaced from one point to another in the absence of applied forces. However, in case of viscous flow through a stationary solid permeable medium, the porous matrix carries most of the viscous stress imposed on the fluid and therefore the convective transport mechanism plays a negligible role in momentum transfer through porous medium.

In the case of compressible fluids such as gases at low pressures, there is a slip flow between the fluid and the porous medium resulting in the whole of the stress being carried away by the fluid. In these cases, The Darcy's law is inappropriate in the porous medium (Chen *et al.*, 1995). In the porous region, the Reynolds number is characterised as,

$$Re_p = \frac{\rho u \sqrt{K}}{\eta} \qquad\qquad (2.6)$$

At very low value of Re_p, the non-linear drag is negligible and it holds true for the range of Re_p between 1 and 10. However beyond the maximum limit of 10, the form drag due to the solid structure becomes comparable with the surface drag due to friction between the fluid and the porous medium. In such cases, the Darcy's law is observed to be inadequate in representing the flow behaviour completely and calls for amendments in this regard. According to Nield (1991), the appropriate extension to Darcy equation to account for this non-linear drag is the Forchheimer's correction given as,

$$\nabla p = -\frac{\eta}{K} \cdot u - \rho \hat{c} \sqrt{K} \|u\| \cdot u \qquad\qquad (2.7)$$

where, $\hat{c}$ is the dimensionless inertia coefficient or form-drag constant. A number of arguments have been made in the past regarding the selection of the non-linear drag term and the non-linear convective acceleration term suggested by Wooding (1957). The experimental data given by Bear (1972) proves the validity of this non-linear Forchheimer drag term. Over the years, various mathematical formulae and correlations have been developed to get the value of this drag coefficient (Beavers *et al.*, 1973; Coulaud *et al.*, 1988). Taking into account the scale and geometry of the aeronautical filters, all the models discussed here, are mainly concerned with the macroscopic approach with the description of the phenomena as a fluid continuum averaged over a large volume composed of a number of microscopic pores. Despite this fact, some of the recent efforts reported on porous flow modelling on microscopic scale are also given a due justice in this discussion.

Imdakm and Sahimi (1991) developed a Monte-Carlo simulation model for a class of particle transport processes in flow through a porous medium including macromolecular transport, fines migration, flow of stable emulsions deep bed filtration and size exclusive chromatography. Two distinct approaches, namely a continuum approach and a statistical approach, were adopted in their work. The model developed takes into account the effects of various phenomena, which can change morphology of porous medium. The model was reported to be in well agreement with experimental data and would allow knowledge of particle transport at pore level to include all relevant feature of the process at network level.

Sabiri and Comiti (1994) analysed the flow of non-Newtonian purely viscous fluids through packed beds of different structures. The proposed a model taking into account the structure of porous media in order to predict pressure in creeping flow and transition and a general procedure based on capillary model was suggested. The model was tested on beds densely packed with spheres, long cylinders and flat plates. The scatter between model predicted and experimental values was reported to be less than 10% for all the porous media of different structures considered.

Smit *et al.* (1998) used a unified modelling theory of flow through porous media to quantify pressure gradients in homogeneous porous medium. The

framework for the analytic modelling procedure was presented with the way of inclusion of problem dependent specifications such as morphology, length scale, tortuosity, anisotropy of porous medium, fluid rheology and interstitial Reynolds number.

Alda *et al.* (1999) simulated the flow through permeable media using particle models. To avoid complexities in fluid flow, two models namely microscopic molecular dynamics and macroscopic dissipative particle dynamics were adopted. The velocity of fluid flow due to density of porous material and applied external pressure was investigated.

Itoh *et al.* (2002) developed real coded lattice gas automata (RLG) method with a special boundary condition and Lattice-Boltzman method for simulating three- dimensional fluid dynamics in complex porous geometry. Those models are capable to simulate pore scale fluid dynamics that is an essential part for understanding mass transport in porous media precisely. Simulation results of porous regime flow by Lattice-Boltzman method with variable pressure drops conditions showed quantitative agreement with macroscopic relation of Darcy's law and Kozeny-Carman equation.

2.3.2 Interfacial Constraints in Coupled/Free Porous Flows

On the level of pore fluid continuum, individual pore flow is one type of free flow bounded by solid impermeable walls. On the macroscopic scale of reference, the porous medium is composed of an ensemble matrix of millions of pores. Therefore, the flow behaviour in the free channel flow regime and ensemble porous regime are distinct. The significance of the flow variables, especially the velocities, are distinguishable in these regimes and needs to define a means of maintaining a physical continuity at the interface separating them. Several correlations based on experimental findings and mathematical fundamentals have been developed over the years to pacify the difficulty of combining free and porous flow regimes.

Though Darcy's law is a simple empirical or semi-empirical equation to describe the porous flow, its validity is questionable in certain situations. In these cases, various modifications or extensions to original Darcy equation are required as discussed in the previous section. The selection of Darcy's law or any of its

extended form is still a hot topic of debate and involves not only the fundamental issues of its appropriateness but also facts arising in linking of the porous and free flows across the interface between the two domains.

The first and which can be referred as classical work by the scientific community was carried out by Beavers and Joseph (1967) who proposed hydrodynamic boundary conditions at interface between porous flow and free flow regime bounded by impermeable solid wall. They performed experiments measuring the mass efflux of a Poiseuille flow over a naturally permeable block and concluded that the resultant velocity profile will take the form depicted in **Figure 2. 7.**
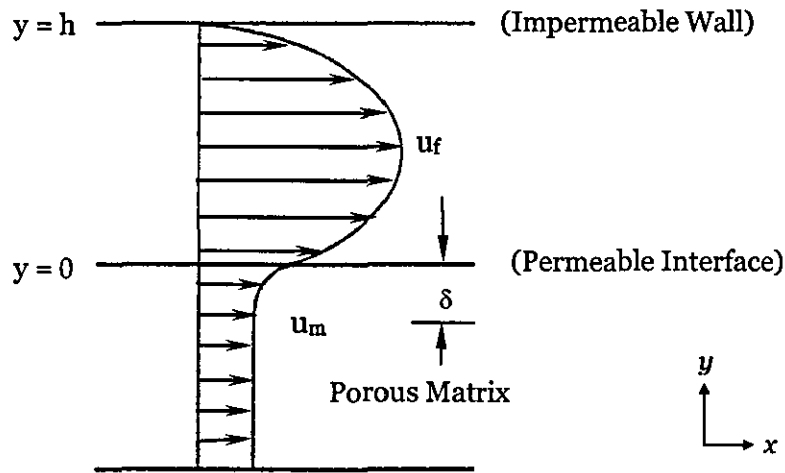
Figure 2. 7: Velocity Profile in parallel flow channel bounded by impermeable solid wall and permeable wall

The experimental results show a boundary layer region formed within the porous material. They objected the validity of the Darcy's law near the boundary separating the free and porous regimes but confirmed its validity in the interior porous region. They proposed that the interfacial velocities of the freely flowing fluid and the fluid velocity in the porous matrix could be related by an *ad hoc* boundary condition,

$$\frac{\partial u_f}{\partial y} = \frac{\alpha}{\sqrt{K}}\left(u_f - u_m\right) \qquad\qquad (2.8)$$

Where, u_f is the velocity of flowing fluid calculated at $y = 0^+$ and u_m is the seepage velocity measured at small distance the interface showing the existence of thin

layer just inside the porous medium over which transition in velocity takes place. The dimensionless slip wall coefficient α is independent of fluid viscosity and apart from permeability depends on the structural parameters of the porous medium in specific on the interface.

Saffman (1971) proposed that the precise form of the Beavers-Joseph boundary condition was particular to the planer geometry considered in their experimental work and was not correct to the order of permeability of medium *K*. He considered the problem as special case of flow through non-homogeneous porous medium with porosity and permeability changing discontinuously from values of unity and infinity to the values of porous medium forming boundary. The boundary conditions can then be obtained by standard boundary layer technique to equations describing non-homogeneous porous media. The boundary condition for tangential component of velocity was suggested as,

$$u_f = \frac{\sqrt{K}}{\alpha}\frac{\partial u_f}{\partial n} + O(K) \tag{2.9}$$

Where, *n* is the direction normal to the boundary surface.

Neale *et al.* (1973) studied viscous flow relative to an isolated permeable sphere. They stated that the meaningful solution for this situation cannot be solely obtained by applying Darcy's law in its simple form unless some empirical parameters are introduced in it. It was demonstrated that the internal permeation within high-porosity permeable particles would not frequently be significant to neglect. They concluded that by adopting Brinkman's extension of Darcy's law fully predictive solution can be obtained. As an extension to this work, Neale and Nader (1974) found that for the problem of flow in a channel bounded by a thick porous wall, one gets the same solution with Brinkman's equation as obtainable from Darcy's equation together with Beavers-Joseph condition when the non-dimensional parameter α in that condition is replaced by the term, $\sqrt{\frac{\eta_B}{\eta}}$ in which

η_B is Brinkman's effective viscosity. They objected to the validity of a slip velocity at the interface and stated that both the velocity and shear stress must be continuous across the interface as,

$$u_x = v_x \tag{2.10}$$

$$\eta_B \frac{\partial u_x}{\partial y} = \eta \frac{\partial v_x}{\partial y} \tag{2.11}$$

Haber and Mauri (1983) obtained a complete analytical solution for the problem of viscous flow relative to an isolate permeable sphere with an impermeable core. Both Brinkman's equation and Darcy's equation are utilized to derive general forms of velocity and pressure fields. A boundary layer region is created at the edge of porous medium and a consistent approximate solution for the flow inside a porous medium can be attainable only when the Darcy solution is matched with the boundary layer solution. An extension in the boundary condition is required in a manner that the Darcy solution satisfies its asymptotic value on the boundary. A boundary condition equivalent to that derived by Beavers and Joseph (1967) is postulated as,

$$\vec{u} \cdot n = \sqrt{K} \nabla_t \cdot u_t \qquad\qquad\qquad (2.12)$$

where, u_t is the tangential component of the velocity vector $\vec{u}$, ∇_t is the tangential component of the operator ∇.

Vafai and Thiyagaraja (1987) analysed fluid flow and heat transfer at porous interface bounded by free flowing fluid, impermeable medium, and another porous medium. The analytical results obtained are in close agreement with the numerical results gained by using central finite difference method. An explicit theoretically derived expression for interface velocity between free fluid and porous medium is compared against the numerical and analytical results and are in narrow vicinity.

Sahraoui and Kaviany (1992) studied the flow at the free/porous interface by direct simulation of flow in porous medium made of cylindrical structure using the slip boundary condition given by Beavers and Joseph (1967), and the no-slip wall condition by using the Brinkman's extension to Darcy's law. Unlike the previous studies in this field, the full Navier-Stokes equation was solved to study the inertial effects at the interface even for the cases where the flow in porous medium away from the interface is Darcian. Parallel and longitudinal flows were considered in order to examine the effect of two dimensionality of the flow on the slip coefficient α in Beavers-Joseph boundary condition. By experimental investigation they found that,

$\alpha = \alpha\,(\varepsilon, R_e, h, y, bulk\ flow\ direction, surface\ structure\ of\ the\ porous\ medium)$

Where, ε is the porosity of the medium, Re is the fluids Reynolds number, h is the width of channel, y is distance from the interface.

For the accurate estimation of local velocity near the interface (inside the porous medium), the Brinkman's effective viscosity η_B must vary within the porous matrix, which is contradictory to Brinkman's assumption of uniform η_B. By examining the Brinkman's treatment of the interfacial hydrodynamics they concluded that the parameters $\eta_B(y)$ and $K(y)$ can nor be expressed in a generalised form.

Ochoa-Tapia and Whitaker (1995a) presented a boundary condition to correct the Darcy's law with Brinkman's equation in the porous regime to be analogous to the Stokes equation for a homogeneous fluid flow. The momentum transfer hybrid condition is proposed as a jump condition based on non-local form of volume averaged momentum conservation equations. Outside the free/porous boundary region, the volume averaged form of momentum conservation equation reduces to individual flow equations of the respective regimes such as Darcy or Stokes equations. Unlike the past work carried out on similar lines, a jump in shear stress is assumed at the interface region which makes the velocity averaged velocity field continuous across the interface. The jump in shear stress is inversely proportional to the permeability of the porous medium expressed as,

$$\langle u_x \rangle = \langle v_x \rangle \qquad\qquad (2.13)$$

$$\frac{1}{\varepsilon}\frac{d\langle u_x \rangle}{dy} - \frac{d\langle v_x \rangle}{dy} = \frac{\beta}{\sqrt{K}}\langle u_x \rangle \qquad\qquad (2.14)$$

where, β is an empirical constant and $\langle u_x \rangle$ and $\langle v_x \rangle$ denote the components of velocity within the free flow channel and porous medium respectively in the direction of the flow.

In the continuation of this study, Ochoa-Tapia and Whitaker (1995b) compared their theoretical results obtained by using the stress jump condition with the experimental data reported by Beavers and Joseph (1967). The comparison yields good agreement between theoretical and experimental investigations constrained to the adjustable parameter β in Equation (2.14) which desires experimental analysis for its realistic determination.

Alazmi and Vafai (2001) mentioned five different kinds of interface conditions between the porous medium and adjacent fluid layer all of which are described before. A systematic analysis of variances among different boundary conditions has been established with the convergence and divergence among

competent models. The influences of the model parameters such as the Darcy number, inertia effect, Reynolds number, porosity and slip coefficients have been analysed. All the model variances are showing significant impact on the velocity field. Finally a set of correlations have been generated for interchanging the interface velocities.

In the recent work reported by Seonghyeon *et al.* (2002), a boundary condition is put forward at the interface between a permeable block and turbulent flow channel. An investigation was carried out in characteristics of turbulent channel flow in vicinity of permeable block. The boundary condition suggested is just an extension of laminar boundary conditions suggested by Beavers and Joseph (1967) to two dimensional turbulent flow. Since the parameters α and K in Beavers-Joseph are solely dependent on porous material properties, it supports the investigation done by Seonghyeon *et al.* (2002) for turbulent flow system. Since the effective length inside the porous medium is diameter of a single pore, flow in porous domain is still laminar even though flow in adjacent channel is turbulent.

All the references listed previously mainly concern the two domain approach in which the free flow channel and the adjoining porous medium are considered as two different domains exhibiting distinct flow characteristics. In one domain approach, the porous layer is assumed to be a pseudo-fluid and the combined free flow and porous regimes are considered as a one flow domain. The two separate domains collapse to one composite domain by reposing the governing equations (Basu and Khalili, 1999) and no interface conditions need to be considered. In this situation, the Navier-Stokes equation is modified incorporating the Darcy term as,

Error! Objects cannot be created from editing field codes.

(2. 15)

where, ρ is the density of the fluid, $\vec{u}$ is the velocity vector, p is the pressure, $\vec{g}$ is the gravitational force per unit volume, η_B is the effective viscosity of the fluid and the porous medium, η is the dynamic viscosity of fluid and $\vec{\vec{K}}$ is the permeability tensor of the porous medium.

The transition from the free to porous flow regime or vice-versa takes place through spatial variation of properties such as the permeability (Beckerman *et al.*, 1987 & 1988). In free flow regime, $\eta_B = \eta$ and the permeability is infinite and the

contribution by the Darcy term is ignored. In porous regimes, for a particular value of permeability, all of the terms involving velocity in Equation (2. 15) are formally retained but the term corresponding to Darcy's law predominates.

The Brinkman equation contains Laplacian terms and it's of the same order as Stokes equation. Therefore, through the use of Brinkman equation at the free/porous interface and in the bulk of porous matrix, the boundary conditions in both Stokes and Darcy equations become compatible. However, theoretical studies by Lundgren (1972) and Kim and Russell (1995) pointed out that the applicability of Brinkman equation is restricted only to the high porosity domain where the curvatures of the streamlines in the bulk porous medium adjacent to the interface are generally greater than the pore diameter. Durlofsky and Brady (1987) through their fundamental solution of Brinkman equation pointed out the limits of its applicability based on the porosity of the medium. The term "effective viscosity" in the Brinkman equation can neither be measured by the experimental means (Nield and Bejan, 1992; Parvazinia et al., 2005) nor can be calculated by relating it to any other physical parameters of the porous domain/fluid system. Therefore, in most of the cases, the Brinkman effective viscosity is assumed to be equal to the fluid viscosity (Hsu and Cheng, 1985; Vafai and Thiagaraja, 1987). However, in filtration of suspensions, the effective viscosity of the feed stream can not be equal to the clean filtered fluid viscosity and may lead to wrong interpretation of actual process. Secondly, in the case of porous media of very low permeability of the order of 10^{-12} m^2 or greater, the possible occurrence of boundary layer inside the porous medium in the vicinity of interface is almost impossible.

The slip boundary conditions like the classic Beavers- Joseph constraints require continuation of velocity and tangential components of shear stress. In this case, the interfacial velocities of the fluid in the free flow regime and in the porous regime are related by an *ad hoc* matching condition, which admits a discontinuity in their tangential component. This is an empirical approach deduced from a simple one-dimensional situation and its extension to multi-dimensional cases is not well understood. The imposition of slip boundary condition at the free/porous interface includes calculation of slip-wall coefficient, α. As stated earlier, the value of α depends on the physical parameters as well as geometrical features of the flow domain. Though the actual prediction of α by any experimental or analytical procedures appears to be simple and straightforward for the domains with

simplified shapes, its calculation for the complex and irregular shaped free/porous interface is practically impossible.

In the context of importance of the current problem on industrial scale, a two-dimensional model is developed representing the fluid dynamical behaviour in the combined system of low permeability porous flow regime adjacent to freely flowing viscous fluid in a confined channel. Reviewing the above discussed slip and no-slip boundary conditions, it can be inferred that the imposition of these so called "artificial" interface conditions become impracticable for the specific cases of combined free and low permeability porous flow regimes encountered in the industrial filtration processes. To circumvent these complexities, a nodal replacement scheme has been devised in light of the finite element method in which the Darcy equation can be effectively imposed as a boundary condition for the free flow regime and vice-versa.

2.4   Closure

The background phenomena and interactions between clear fluid and adjacent porous medium are diverse and complex. Mathematical modelling of such coupled flow system requires real time physical representation of interfacial effects to yield convergent and accurate values of field variables by numerical analysis that can be justified on an experimental basis. Various interfacial constraints derived theoretically over the years, experimentally, or in conjunction have been elaborated in concise manner in the previous section. It will be appropriate to conclude that all of the boundary conditions can be classified into two categories, slip and no-slip. Slip interface conditions such as that of Beavers and Joseph require evaluation of a slip coefficient which depends on physical and geometrical properties of porous medium. There is no theoretical derived formula or correlation for the slip coefficient that can be applied to any free/porous interface of any arbitrary shape. The only possible way to calculate the value of these slip coefficients is by an experimental procedure, which is nearly impossible for complex flow geometries. On the contrary, the no-slip interface conditions such as the Brinkman equation alleviates the mathematical complexities arising due to the different order of differential equations in free and porous flow regimes.

Besides, they are accompanied by a parameter such as the effective viscosity which cannot be experimentally measured or theoretically defined accurately. Most of these interfacial conditions look lucrative on mathematical grounds to represent the underlying physical concepts but they pose severe hurdles when applied to the numerical analysis of real life engineering problems in practice. The present work presents a novel numerical scheme for the solution of linked free/porous flow problem without imposing any so called "artificial boundary condition" in terms of velocity or stress continuation across the interface which will circumvent the difficulty of calculating any slip interface coefficient. In turn, the main focus of the present work is development of a scheme for the imposition of permeable wall condition in viscous flow domains which can resolve the difficulties associated with existing techniques of coupling the free flow and low permeability porous flow regimes.

3.   Mathematical representation

In computational fluid dynamics, the velocity and pressure fields are calculated by solutions of the conservation of mass and momentum equations after transforming them into a format suitable to the numerical method. Before undertaking any computational procedure, the equations are required to be expressed in the most generalised form to describe all the possible transport mechanisms. Various types of mathematical equations can be derived from these generalised forms depending on the physical nature of the problem and geometry of the problem domain. Based on the selection of the mode of operation on time scale, transient as well as time-invariant equations can be adopted. In many cases, the physical properties of the fluid and the medium undergo changes with variations in process variables. In such cases, complementary equations are desired to account for these changes in main governing equations. Depending on the geometrical features of the problem domain, the equations may take alternate forms when resolved spatially.

Considering the practicability of modelling an actual problem, the appropriate selection of governing equations also relies on some kind of assumptions and approximations made to simplify the complexities involved with the problem. Some of these assumptions are related to simplification in the physical phenomena whereas some are linked to smoothening of the underlying mathematics to ease the computations.

The discussion in the present chapter begins with assumptions and approximations related to modelling of coupled free/porous fluid dynamics in pleated cartridge filters. The assumptions are followed by the mathematical models expressed in general as well as modified forms suitable to the study cases discussed in the present work. Finally, necessary and sufficient boundary or interface constraints which emerge physically and required mathematically to enhance the solutions of the equations are described.

3.1   Assumptions and approximations

The flow of highly viscous fluid through a hydraulic circuit in a typical aircraft machine system is assumed to be isothermal. The hydraulic fluid is assumed to be an incompressible so that the density of the fluid is independent of pressure. The fluid exhibits a generalised Newtonian behaviour. It doesn't retain any memory of deformation and the stress-strain relationship is considered to be accounted for by variations in rheological properties. Though the unclean fluid in an actual situation is accompanied by solid contaminants, the fluid/solid mixture is assumed to be a single fluid continuum due to the low concentration of solids.

The permeable medium is considered to be a solid matrix with interconnected pores and the porous body is assumed to be rigid so that any deformations caused during operations can be neglected. The porous structure is taken to be homogeneous and isotropic in all flow directions. There is no possible interaction between the fluid and the porous medium, neglecting any viscous forces arising due to these solid-liquid contacts. There is no reaction or adsorption or absorption of fluid in the bulk of the porous matrix.

The pleated cartridge filters operate in a specific range of flow rates depending on the desired rate of filtration. In these ranges, the flow is assumed justifiable to be creeping and laminar which will be justified by the Reynolds number calculations based on flow areas in free as well porous flow regimes. All the inertial effects are neglected and the convective mechanism is assumed to be playing no role in the momentum transfer.

In the light of a microscopic approach towards the problem, pore level fluid dynamics has to be considered and the same methodology should be extended to millions of such pores forming a porous continuum. Though, with the advent of high speed supercomputers, the problem can be attacked at first with mere enthusiasm, it doesn't seem to be feasible taking into consideration the computational economy. Problems like this at the submicron level may appear attractive to researchers. When the industrial relevance and concern of the current problem is taken into consideration, there are still issues that lack qualitative and quantitative attention for their industrial implementation. "In the present study a macroscopic process is considered, described and analysed on practical grounds."

3.2   Governing equations

A reasonable description of a process involving flow of fluid in free flow channels confined by porous walls would be as follows,

- ✦ Hydrodynamic Model
- ✦ Rheological model

The hydrodynamic model follows the basic laws of the conservation of mass and momentum. The rheological property of fluid such as viscosity is updated continuously by a constitutive equation and supplements the governing hydrodynamic model.

3.2.1   Equation of continuity

The equation of continuity simply represents Newton's first law of conservation of mass. It describes the rate of change in density of fluid resulting from changes in mass velocity (Anderson, 1999). For an incompressible fluid, it takes a divergence free form given as,

$$\vec{\nabla} \cdot \vec{u} = 0 \qquad\qquad (3.1)$$

where, $\vec{u}$ is the velocity vector.

In two-dimensional Cartesian system, the equation of continuity can be resolved spatially as,

$$\frac{\partial u_x}{\partial x} + \frac{\partial u_y}{\partial y} = 0 \qquad\qquad (3.2)$$

where, u_x and u_y are the components of the velocity vector $\vec{u}$ in x and y-directions, respectively.

3.2.2 Equation of Motion: Free Flow Regime

The equation of motion is based on law of conservation of momentum written for steady state case as,

$$\vec{\nabla} \cdot \vec{\vec{\sigma}} + \rho \vec{g} - \rho \vec{u} \cdot \vec{\nabla} \vec{u} = 0 \tag{3.3}$$

where, ρ is the density of the fluid, $\vec{\vec{\sigma}}$ is Cauchy's stress tensor and $\vec{g}$ is the gravitational force vector per unit volume (Bird *et al.*, 2000). For incompressible flow of a Newtonian fluid these equations are termed as the well-known Navier-Stokes equations (Aris, 1989). The second term on the left hand side of the equation (3.3) represents convective transport and for a creeping laminar flow of a highly viscous fluid is usually small and can be ignored. In absence of any gravitational forces, the equation of conservation of momentum for a creeping incompressible laminar flow can be derived from Equation (3.3) as,

$$\vec{\nabla} \cdot \vec{\vec{\sigma}} = 0 \tag{3.4}$$

The Cauchy's stress tensor is resolved as,

$$\vec{\vec{\sigma}} = -p\vec{\vec{\delta}} + \vec{\vec{\tau}} \tag{3.5}$$

where, p is the hydrostatic pressure, $\vec{\vec{\delta}}$ is the Kronecker delta tensor and $\vec{\vec{\tau}}$ is an extra stress tensor. The extra stress tensor $\vec{\vec{\tau}}$ represents the rheological behaviour of fluid. The highly viscous fluids used in aircraft hydraulic systems are inelastic, time-independent fluid which does not retain any history of deformation. In this category, for generalised Newtonian fluids, the extra stress tensor can be expressed as,

$$\vec{\vec{\tau}} = \eta \vec{\vec{\Delta}}(\vec{u}) \tag{3.6}$$

where, η is the apparent viscosity of the fluid, $\vec{\vec{\Delta}}$ is the rate of deformation tensor which can be expressed in a two-dimensional Cartesian coordinate system,

$$\Delta(u) = \begin{bmatrix} 2\dfrac{\partial u_x}{\partial x} & \dfrac{\partial u_x}{\partial y} + \dfrac{\partial u_y}{\partial x} \\ \dfrac{\partial u_y}{\partial x} + \dfrac{\partial u_x}{\partial y} & 2\dfrac{\partial u_y}{\partial y} \end{bmatrix} \tag{3.7}$$

Resolving equation (3.4) in two-dimensional Cartesian system and substituting equation (3.7),

$$-\frac{\partial p}{\partial x}+\frac{\partial}{\partial x}\left(2\eta\frac{\partial u_x}{\partial x}\right)+\frac{\partial}{\partial y}\left[\eta\left(\frac{\partial u_x}{\partial y}+\frac{\partial u_y}{\partial x}\right)\right]=0 \tag{3.8}$$

$$-\frac{\partial p}{\partial y}+\frac{\partial}{\partial y}\left(2\eta\frac{\partial u_y}{\partial y}\right)+\frac{\partial}{\partial x}\left[\eta\left(\frac{\partial u_y}{\partial x}+\frac{\partial u_x}{\partial y}\right)\right]=0 \tag{3.9}$$

A set of equations (3.8) and (3.9) is termed as the Stokes equation of conservation of momentum in free flow regime.

3.2.3 Equation of motion: Porous flow regime

In absence of any gravitational or body forces, for a two-dimensional creeping laminar flow of an incompressible fluid, the conservation of momentum in porous regime can be expressed by the empirical Darcy's law (Darcy, 1856) as,

$$\vec{\nabla}p+\frac{\eta}{\vec{\vec{K}}}\cdot\vec{u}=0 \tag{3.10}$$

where, $\vec{\vec{K}}$ is the permeability tensor of the porous medium. For a homogeneous permeable medium, this permeability tensor can be expressed in its directional components as,

$$K=\begin{bmatrix} K_x & 0 \\ 0 & K_y \end{bmatrix} \tag{3.11}$$

In two-dimensional Cartesian coordinate system, the individual components of the Darcy equation is written as,

$$\frac{\partial p}{\partial x}+\frac{\eta}{K_x}\cdot u_x=0 \tag{3.12}$$

$$\frac{\partial p}{\partial y}+\frac{\eta}{K_y}\cdot u_y=0 \tag{3.13}$$

As the flow Reynolds number in low permeability pleated porous cartridge is relatively small such that $Re<<1$, the inertial effects are neglected and selection of the Darcy's equation is well justified.

3.2.4 Constitutive equation

A constitutive equation expresses the extra stress τ as a function of the rate of deformation of the flowing fluid. The hydraulic fluids in aircraft machine system are usually typified as generalised Newtonian shear-thickening fluids. The apparent viscosity of these fluid increases with increase in the rate of shear and can be expressed by a power law equation proposed by Ostwald (1925).

$$\eta = \eta_0 \dot{\gamma}^{n-1} \tag{3.14}$$

where, η_0 is the viscosity of the fluid at zero shear or consistency coefficient, $\dot{\gamma}$ is the rate of shear and n is the power law index which for a shear-thickening fluid is always greater than unity. It is clear that a fluid with a power law index value of unity represents a purely Newtonian fluid. The rate of shear can be calculated as,

$$\dot{\gamma} = \left[2\left(\frac{\partial u_x}{\partial x}\right)^2 + \left(\frac{\partial u_x}{\partial y} + \frac{\partial u_y}{\partial x}\right) + 2\left(\frac{\partial u_y}{\partial y}\right)^2 \right]^{\frac{1}{2}} \tag{3.15}$$

Depending on the rheological nature of fluids, other viscosity models can be incorporated in the main hydrodynamic model. In case of non-isothermal operation of the filtration device, thermal effects can be included in equation **(3.1)** by an Arrhenius type exponential formula (Pittman and Nakazawa, 1984).

3.3 Boundary constraints

The partial differential equations in the hydrodynamic models may have infinite solutions when general solutions are attempted. For a specific problem, the boundary conditions are provided by the underlying physics of the problem when the finite domain is the actual physical domain. These boundary conditions restrict the spatial variations of field variables within boundaries of the problem domain. Besides the physics, the nature of boundary conditions to be specified is also decided by the mathematical nature of the governing differential equations. In cases where the physical domains are truncated to reduce the computational costs, fabricated boundary conditions are required at the artificial boundaries formed due to this truncation. In case of transient problems, initial values of the

boundary constraints are required to start the computations on time scale. In the ongoing discussion, a brief introduction of the boundary conditions specific to the present problem has been given. The detailed implementation of these boundary conditions in the solution scheme will be explained in later chapters.

3.3.1 Inlet boundary conditions

Based on the desired volumetric flow rate, Dirichlet type velocity boundary conditions are imposed at the flow inlet. Depending on the angle of contact between the entering fluid and the inlet boundary, the individual velocity components can be resolved as shown in **Figure 3.1**.
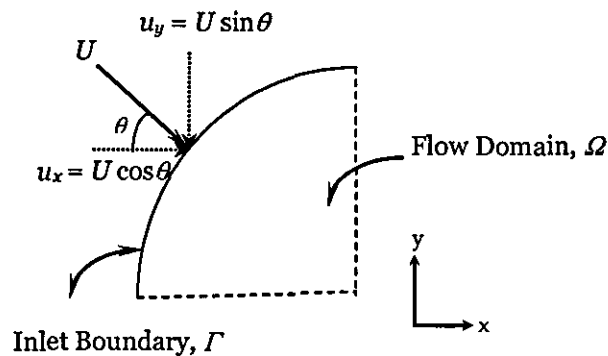
Figure 3. 1: Inlet boundary conditions

In the case of rectangular flow inlets, depending on the nature of problem, plug flow or fully developed parabolic velocity profile is specified at the inlet as shown in **Figure 3. 2**.
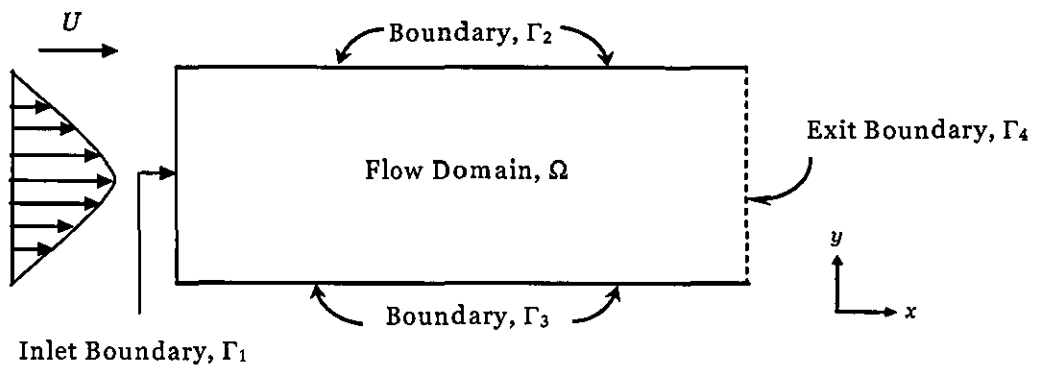
Figure 3. 2: Parabolic inlet boundary conditions

In these circumstances, the inlet boundary conditions can be written as,

$$
\left.
\begin{array}{l}
u_x = U(y) \\
u_y = 0 \\
\sigma_{xx} + \sigma_{xy} = 0
\end{array}
\right\}
$$

(3. 16)

3.3.2 Impermeable and permeable wall boundary conditions

If we consider the domain Ω in **Figure 3. 2** to be in free flow regime with the solid boundaries Γ_2 and Γ_3 to be impermeable, there should not be any relative velocity between the boundaries and the adjacent viscous fluid. If the solid boundaries are stationary, with a flow moving past it then,

$$u_x = u_y = 0 \quad \text{on solid walls, } \Gamma_2 \text{ and } \Gamma_3$$

(3. 17)

These are called as the no-slip wall boundary conditions. However, due the order of differential, The Darcy equation for the porous regime is not compatible with these no-slip wall boundary conditions.

Therefore, if the domain Ω in **Figure 3. 2** is permeable region, then the only boundary conditions imposed on the bounding walls Γ_2 and Γ_3 are,

$$
\left.
\begin{array}{l}
u_y = 0 \\
\dfrac{\partial u_x}{\partial y} = 0
\end{array}
\right\}
$$

(3. 18)

The bounding walls and the adjacent viscous fluid are moving with different velocities in the direction of flow.

3.3.3 Line of symmetry boundary conditions

If the domain is symmetric along any of its axis parallel to the coordinate axis, only half or quarter of the physical domain can be selected as the finite domain to achieve computational economy.
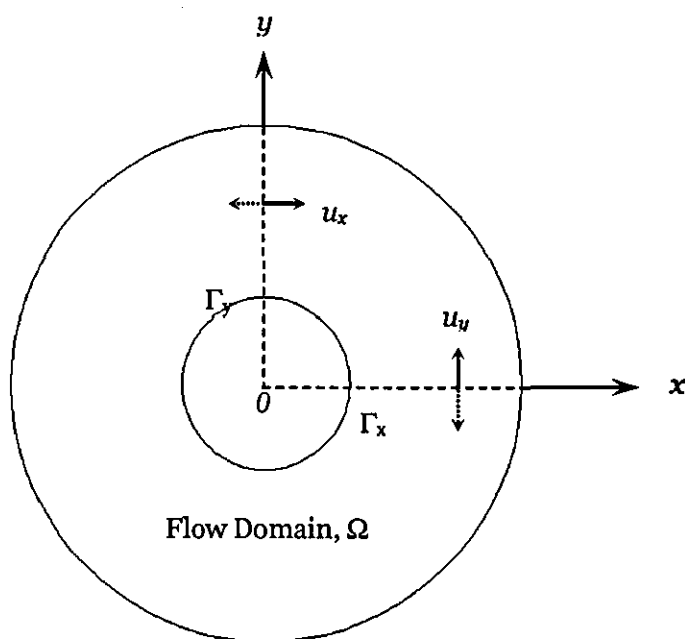
Figure 3. 3: Line of symmetry boundary conditions

As shown in **Figure 3. 3**, the flow domain Ω is symmetric along both the co-ordinate axes. To take the advantage of the geometrical symmetry, artificial boundary conditions are imposed on the fictitious boundaries Γ_x and Γ_y as,

Dirichlet boundary conditions:

$$\left.\begin{array}{l} u_y = 0, \quad \text{on } \Gamma_1 \\ u_x = 0, \quad \text{on } \Gamma_2 \end{array}\right\} \qquad (3.19)$$

These conditions are kinds of slip-wall boundary conditions and imply that there exists a finite domain beyond the line of symmetry.

Neumann boundary Conditions:

$$\left.\begin{array}{l} \sigma_{xx} + \sigma_{xy} = 0, \quad \text{on } \Gamma_1 \\ \sigma_{yy} + \sigma_{yx} = 0, \quad \text{on } \Gamma_2 \end{array}\right\} \qquad (3.20)$$

Equation (3.20) leads to elimination of flux terms along the lines of symmetries. In many circumstances, the axis of symmetry is not parallel to any of the co-ordinate axes. For such problems, the physical nature of these boundary conditions still remain intact i.e. across the line of symmetry $\vec{u} \cdot \boldsymbol{n} = 0$.

3.3.4 Exit boundary conditions

If the exit velocity in the flow domain is unknown a *priori* and is calculated by solving the mass and momentum conservation equations, essential type velocity boundary conditions cannot be imposed at the outlet. At the outlet of the long domain, fully developed velocity boundary conditions can be applied. The imposition of correct fully developed velocity profile at the outlet relies on many physical, geometrical and numerical factors. It is well known that the stress-free boundary conditions applied at the outlet result in unacceptable numerical oscillations in flow simulations.

Papanastasiou *et al.* (1992) suggested that for the realistic solution of Stokes equations no outflow boundary condition should be specified. They observe that in the Stokes limit, this free boundary condition appears to be equivalent to natural, stress-free constraint. Renardy (1997) proved that the no outflow boundary condition of Papanastasiou *et al.* (1992) actually implies an effective boundary condition. Therefore in the present study, the same approach has been adopted for the Stokes flow simulations.

3.3.5 Free/porous interface conditions

Mathematical models which justifiably represent coupled free/porous flows under specific conditions provide useful predictive tools for design and analysis of important classes of industrial processes involving combined flow situations. From the mathematical point of view, the prime hurdle in coupled flow simulations is the formulation of fluid flow equations which can reliably represent interfacial phenomena and flow through porous bulk matrix in all the cases of combined flow systems. In the present work, the Darcy equation is assumed to be valid in representing both, the interface and the bulk porous medium. Therefore, in the present study, the Darcy equation is imposed effectively as the boundary condition for the free flow equations at the free/porous interface. This will circumvent the difficulty of linking differential equations of different mathematical orders at the interface. The mathematical details of this numerical linking technique will be provided in the subsequent chapters.

In the flow simulations, pressure is calculated from the continuity equation. When the pressure field is specified as a boundary constraint at any

single grid point of the computational domain, the continuity equation corresponding to that point should be discarded from set of the equations to avoid numerical inconsistency. Therefore, pressure as a primitive variable cannot be imposed as an effective boundary condition like velocity. In general, imposition of a pressure datum at the exit may appear to be a sort of a natural or Neumann type boundary condition (Nassehi, 2002).

3.4 Closure

The hydrodynamic model for the combined free/porous flow situation encountered in pleated cartridge aeronautical filters has been presented. Every individual term in the mathematical model has been attempted to elaborate on the physical grounds. The selection criteria for the mathematical equations have been discussed taking into account their physical relevance and mathematical compatibility to the problem. The boundary and interfacial constraints required for the theoretically consistent and accurate solutions to the model equations have been listed.

4. Numerical solution schemes

The mathematical equations describing the incompressible fluid dynamics in free as well as porous flow regimes represent the system of simultaneous partial differential equations in which the field variables are continuous functions in both space and time domain. Analytical solutions of these differential equations will provide closed formed expressions for the dependent variables as functions of spatial as well as temporal position of any discrete point in the flow domain. However, the analytical solutions are possible for a particular category of partial differential equations and computationally feasible only for simple flow domain geometries. Therefore, numerical methods based on some kind of approximation, are the most reliable alternatives to achieve stable solutions and their accuracy is reasonably comparable to the analytical solutions. The numerical methods assume the flow domain as a set of finite number of discrete points, areas or volumes, generally termed as the grids. In physical sense, though the dependent variables are continuous throughout the domain, the solutions gained by numerical techniques prescribe the values of field variables on the grid points. The differential equations are weakened to lower order equations approximated or interpolated strictly in terms of the flow field variables at two or more of the discrete grid points.

Depending on the level and mode of approximations, a wide variety of numerical methods have been developed over the decades. The present chapter discusses in short possible merits and demerits of some of these numerical methods which have proven their versatility for solving the incompressible fluid dynamics equations. The selection criteria for a specific numerical technique have been explained in the context of the present problem. Various forms of transient and spatial approximation techniques have been elaborated related to the selected numerical methods. Finally, some of the noted references dealing with application of the selected numerical method to the coupled free-porous hydrodynamics computations.

4.1   Selection of Computational Method

When discussing about computational methods in simulating fluid flow and heat transfer, generally denoted by a common term *computational fluid dynamics*, finite difference methods (FDM), finite element methods (FEM) and finite volume methods (FVM) emerge in mind by default. Every corner of the literature concerning computational fluid dynamics is somehow covered by these three widely renowned numerical techniques utilised to obtain solutions to partial differential equations. A veritable plethora of research articles could be found discussing their background history, fundamentals, mathematical derivations and addressing their possible merits and demerits when applied to a particular set of equations.

In the FDM, the domain is approximated by interconnected points or grid points and it yields point approximations to the governing differential equations (Peyret and Taylor, 1983). The partial derivatives in the governing equations are replaced by approximate algebraic quotients which are expressed strictly in terms of flow field variables. The partial differential equations are totally replaced by a system of algebraic equations which can be solved for the values of the flow-field variables on discrete grid points only (Patankar, 1980). Though the formulation of the finite difference working equations is simple and straightforward, the order of magnitude of error introduced due to the difference approximation is quite considerable. In addition, for multi-dimensional problems, the finite difference methods show their inability with unstructured grids.

In the FEM, the solution domain is approximated by small discrete elements either line segments, surfaces or volumes interconnected by grid points or nodes. The variation of the field unknowns within the element domain is approximated by a simple interpolation method using their values at the nodal points corresponding to the element (Segerlind, 1984). The governing differential equation containing approximated values of field variables is weighted followed by integration over the elemental domain. This method utilises an integral formulation to generate a system of algebraic equations which is minimised to reduce the error introduced due to the approximations. The weakened differential equations are therefore transformed into simple algebraic equations derived over each node of each element and are assembled together over the overall domain.

Thus, the FEM formulations generate piecewise variations of the field unknowns anywhere within the elemental domain. The FEM exhibits its suitability in approximating curved boundaries of any kind of complex and irregular domains. In addition, unstructured adaptive meshing can be accommodated in a versatile manner in the FEM formulations.

FVMs can be placed under both the categories FDM and FEM as appropriate since FVM can be formulated using either of them (Chung, 2002). FVM utilises the control volumes and control surface to discretise the geometrical solution domain. A variety of finite difference type approximations are substituted in the governing differential equations integrated over the control volume converting them to a system of simultaneous algebraic equations (Versteeg and Malalasekera, 1995). Unstructured meshes along with enforcement of natural boundary conditions typically featured in FEM can be conversantly utilised in finite differences through the FVM formulations. Either finite differences or finite elements are used in FVMs where in some cases better accuracy and efficiency can be achieved.

Besides these widely used numerical techniques, numerical methods such as the boundary element method (BEM) (Brebbia, 1978), coupled Eulerian-Lagrangian methods (CEL) (Noh, 1964) and Monte-Carlo methods (MCM) (Binder, 1984) are also found to be used in simulating flow dynamics. These techniques are beyond the scope of this discussion and their detailed descriptions are therefore omitted.

The pleated cartridges considered in the present work are employed in hydraulic machinery of aircraft system usually operated at excessive high-pressure loads. About 70% of the hazards occurring within the hydraulic systems are attributed to failure of their filtration equipment. As 200-300 cartridge elements are used simultaneously either in series or parallel network in aircraft assembly, their design and analysis methods play a crucial role in the high-pressure filtration performance. In this context, point accuracy is expected in design computations without any compromise with the personal safety of on-board human lives in passenger as well as commercial aircrafts.

Referring to the past literature on the coupled flow dynamics discussed in Chapter 2, the geometrical characteristics of the interface separating the free and porous flow regimes plays a crucial role in their fluid dynamical behaviour. In the

pleated cartridge filter assembly, the free-porous barrier is highly curved and complex which is well imagined from the schematic representation of the cartridge assembly in **Figure 1. 1.** In such curved regions of the solution domain, the variations in the field variables are generally significant and unstructured grid generation is an obvious requisite.

As previously described, finite element technique has proven to be very versatile in dealing with curved geometries of the solution domain without any lack in stability and accuracy of the solutions. This makes smooth imposition of boundary conditions especially the derivative type natural boundary conditions in simplified manner. Adaptive meshes are easily compliable within the finite element formulations to compensate for steep variations in the field variables generally encountered in the curved regions of solution domains. Numerical procedures based on FEM can be easily extended to multi-dimensional problems with the same order of accuracy, stability and convergence in the solutions. Though the FEM formulations are mathematically rigorous in their underlying principles and need comparatively longer computational times, it is the most suitable numerical technique for obtaining solutions to the fluid dynamics of coupled free-porous regimes found in pleated cartridge filters.

4.2   Finite element method in fluid dynamics

Courant (1943) demonstrated the use of piecewise approximations within triangular regions. He examined different geometric regions, used separate approximation functions and assembled individual solutions into a global solution. By the early 70's, FEM was mainly used for solving the problems relevant to structural mechanics (Thomas, 1980). Finite element modelling was limited only to expensive mainframe computers generally owned by aeronautics, defence and nuclear industries. In the same time, Zienkiewicz and Cheung (1965) reported the applicability of FEM to all field problems that can be transformed into variational form and it received broader interpretation in the engineering community. They made applications of FEM to simple flow problems followed by Oden and Welford (1972) and Chung (1978). Gartling (1976) described the developments in the use of FEM in fluid dynamics. The applications of the method

to problems of viscous incompressible flows were reviewed. The analysis of coupled flow problems was also discussed and problem formulations, solution methods and examples of typical finite element calculations were presented. Significant contributions in computational fluid dynamics began with Streamline Upwind Petrov-Galerkin (SUPG) method (Heinrich *et al.*, 1977) applied to convection dominated flows.

Nassehi and Petera (1996) described a two-dimensional finite element model for describing tidal hydrodynamics in estuaries within Lagrangian framework. Jurjenic (1999) gave a Galerkin weighted residual finite element numerical solution method with velocity material time derivative discretisation to solve a classical fluid mechanics system of partial differential equations and modelling two-dimensional stationary incompressible Newtonian Fluid Flow. De Sampaio and Moereira (2000) gave a new finite element formulation for both compressible and nearly incompressible fluid dynamic equations. The formulation combined conservative and non-conservative dependent variables. The main feature of the method was derivation of a discretised equation for pressure where pressure contributions arriving from the mass, momentum and energy balances were taken implicitly in time discretisation. New approaches and various methodologies are preponderant in literature. Zienkiewicz and Codina (1995) developed for the past decade the concept of Characteristic Galerkin Methods (CGM) which produce results similar to Taylor-Galerkin Method (TGM) in dealing with convection dominated problems. Some of the textbooks that contribute to the fundamentals, developments and applications of FEM in fluid dynamics and heat transfer can be listed as Baker (1983), Girault and Raviart (1986), Gresho and Sani (1999), Heinrich and Pepper (1999), Reddy and Gartling (2001), Nassehi (2002) and Zienkiewicz and Taylor (2002).

The Control Data Corporation sold first commercial finite element software in 1964, without any pre-processing and post-processing facility. The computational time required for simple problems was in hours and only linear equations could be handled. Interactive graphics were practical and availability of computer power to solve problems on dedicated basis was achieved. The introduction of personal computers was powerful enough to run finite element software providing extremely cost-effective problem solving. Today, we have hundreds of commercial software tools containing pre-processing, processing and

post-processing modules in one single unit, offering wide range of choices. Some of the most commonly used software packages for fluid flow problems are ABAQUS, ICEM-CFD, COSMOS and newly introduced FEMLAB by the COMSOL Corporation (Zimmerman, 2004). However, most of these commercial packages show their inability in modelling Navier-Stokes/Stokes equations coupled with low-permeability Darcy equations with accurate representation of interfacial physics and mathematical compatibility of the equations.

Finite element formulations of engineering processes can be based on different methodologies. Unlike the common case with the structural analysis, it is not a general practice to model fluid flow processes using the principle of minimisation of variational statements. Weighted residual methods, such as the Galerkin, least-square and collocation techniques are directly applicable to achieve solutions to engineering problems in conjunction with the finite element approximations (Nassehi, 2002). These weighted residual methods are distinguished based on the nature of the weighting functions used in the integral formulations. The standard Galerkin weighted residual method utilises weight functions in the integral formulation, identical to the shape or interpolation functions used for approximating the field variables. The simplicity gained by choosing identical weight and interpolation functions has made the standard Galerkin method the most widely used technique in finite element solution of differential equations and many finite element models for flow problems are variations of this basic formulation. The solution procedure using the finite element technique can be arranged into the following basic sequential steps,

✦ Discretisation of the solution domain into finite elements numbering the nodal points and specifying their coordinates;

✦ Specification of the approximating functions writing the governing equations in terms of unknown nodal values of the field variables;

✦ Derive weighted residual integral statements for each nodal point;

✦ Modify the system of equations imposing the boundary conditions discussed in Chapter 3;

✦ Assemble the system of simultaneous algebraic equations and solve to obtain the values of field variables on each nodal point;

✦ Perform additional calculations to calculate other systems parameters if requisite.

In the ongoing discussion, we will consider the domain discretisation with the description of some of the most commonly used finite elements. The types of interpolation functions used in the present work are explained in short with their mathematical background and suitability to the system of governing equations.

4.2.1 Domain discretisation

Domain discretisation denotes division of the problem domain into number of smaller sub-regions called elements without any gap as well as any kind of overlapping between them. The assembled system of interconnected finite elements is commonly termed as a finite elements mesh. In a particular structured mesh, the elements can be of different sizes but an exactly identical geometrical basic shape and an equal number of nodes associated with each of them. The finite elements should have nodes located on their boundaries and in some cases in their interior also. Considering their geometrical shapes, triangular and quadrilateral elements are intensely popular in finite element modelling of two-dimensional fluid flow problems. Representatives of these families of finite elements are shown in **Figure 4. 1** and **Figure 4. 2;**

(a) 3-Node　　　　　(b) 6-Node　　　　　(c) 10-Node
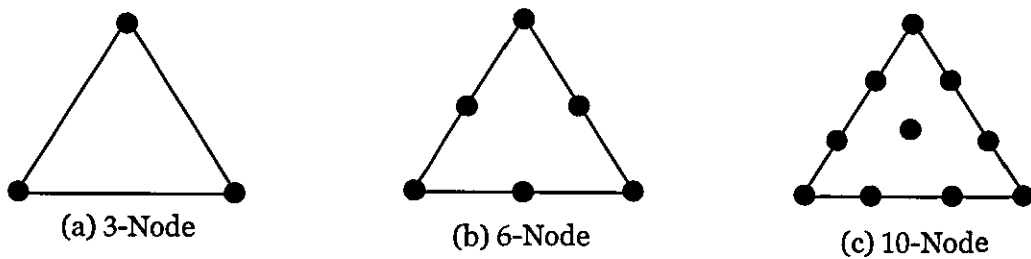
Figure 4. 1: Triangular finite elements

(a) 4-Node　　　　　(b) 9-Node　　　　　(c) 16-Node
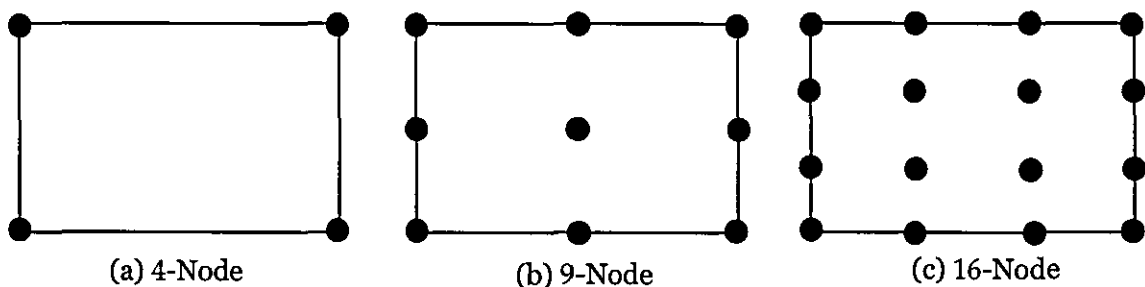
Figure 4. 2: Rectangular finite elements

In most of the engineering problems, the domain is bounded by curved segments. Discretisations of domains having curved boundaries with elements having straight sides incur a possible error in the approximation. In such cases, transformation is essential from global system to local system of coordinates for the interpolation functions to remain invariant (Zienkiewicz and Morgan, 1983). The coordinate transformation could be in some nominal sense smoother for the rectangular shaped finite elements used in this work compared to the triangular shaped finite elements.

The solution domain is tessellated into finite element mesh and the discretisation procedure is expressed mathematically as,

$$\Omega = \sum_{i=1}^{e} \Omega_i \tag{4.1}$$

where, Ω is the overall problem domain and e denotes the total number of finite elements in the mesh.

The domain boundary Γ can be represented as,

$$\Gamma = \sum_{i=1}^{e} \Gamma_i \tag{4.2}$$

The field variables generally associated with the incompressible fluid flow problems are velocity components and pressure. Within each elemental domain, these primitive variables are approximated by interpolation methods as,

$$\begin{cases} \tilde{v}_x = \sum_{j=1}^{k} N_j(x,y) v_{xj} \\[2mm] \tilde{v}_y = \sum_{j=1}^{k} N_j(x,y) v_{yj} \\[2mm] \tilde{p} = \sum_{j=1}^{k} N_j(x,y) p_j \end{cases} \tag{4.3}$$

Where, $\tilde{v}_x, \tilde{v}_y$ are the interpolated values of velocity components and $\tilde{p}$ is the interpolated value of pressure approximated over the domain of element e. k is the number of nodes associated with the elements similar to e.

The fact that should be kept in mind in any finite element modelling attempt of the flow processes is that the finite elements just represent an integral part of geometrical flow domain and does not resemble any parts of body of the flowing fluid (Nassehi, 2002).

4.2.2 Choice of interpolation functions

The general forms of interpolation functions or shape functions corresponding to finite element are based on its shape and number of its associated nodes as shown in **Figure 4. 1** and **Figure 4. 2**, where figures (a), (b), (c) represent linear, quadratic and cubic order of approximations respectively. In most of the types of commonly used finite elements, these interpolation functions are polynomials of lower degree than the governing differential equations. One of the most important subjects of research in finite element approximations of incompressible Navier-Stokes/Stokes equations involves the velocity-pressure interpolation. When the standard Galerkin formulation is incorporated in conjunction with the finite element approximations, the approximating spaces chosen for all the primitive variables are bounded by the classical inf-sup or Ladyzhenskaya-Babuška-Brezzi alias LBB criterion (Ladyzhenskaya, 1969; Babuška, 1970; Brezzi, 1974) as a necessary and sufficient constraint to achieve stable solutions (Brezzi and Fortin, 1991). The LBB condition states that velocity and pressure spaces cannot be chosen arbitrarily. If Q^h and V^h are the approximating spaces for pressure and velocity respectively, the sufficient condition is that,

dim $Q^h \leq$ dim V^h (Donea and Huerta, 2003).

The sufficient condition for linking the velocity and pressure approximating spaces is provided by the LBB compatibility criterion which states that,

the existence of a stable finite element approximate solution (u^h, p^h) to the steady incompressible flow problem depends on choosing a pair of spaces V^h and Q^h such that,

$$\inf_{q^h \in Q^h} \sup_{w^h \in V^h} \frac{\left(q^h, \nabla \cdot w^h\right)}{\|q\|_0 \|w^h\|_1} \geq \alpha \geq 0, \qquad (4.4)$$

where, α is independent of mesh size h.

In the context of finite element method, different schemes based on various strategies have been developed which satisfy the LBB stability condition. They range from the least-square Galerkin technique (Hughes *et al.*, 1986) to the use of elements generating unequal order interpolation functions for the field unknowns and schemes which depend on perturbed continuity equation (Zienkiewicz and

Wu, 1991). The least square Galerkin finite element method depends on utilisation of sophisticated C^1- continuous Hermite elements. These elements lack flexibility and their application in geometrically complex domains involves elaborate schemes (Nassehi and Petera, 1994).

Much of the efforts have been invested in developing the methods using equal order velocity and pressure interpolations assuming it as the simplest choice from computational point of view. Numerical schemes for incompressible flow problems based on such types of approximations are found in the work by Brezzi and Douglas (1988), Douglas and Wang (1989). The perturbed continuity method based on equal order interpolation functions depends on inclusion of temporal derivative of pressure in the continuity equation which in physical terms amounts to considering the fluid to be slightly compressible (Zienkiewicz and Wu, 1991). This inherently forces the addition of temporal derivative terms such as $\dfrac{\partial \vec{u}}{\partial t}$ in the Stokes and the Darcy equations.

An alternative technique to satisfy the LBB stability criterion is the use of non-standard elements with unequal order approximating functions for velocity and pressure fields. In this context, among the first methods of FEM approximation of incompressible flow problems is the mixed interpolation method (Hood and Taylor, 1974). In such cases, the velocity interpolation functions are of higher order than the pressure approximating functions. The most popular element of such type is a confirming isoparametric quadrilateral with 9-node biquadratic interpolation for velocity and 4-node bilinear for pressure (Nickell *et al.* 1974; Huyakorn *et al.*, 1978, Bercovier and Pironneau, 1974;). Crouzeix-Raviert elements makes pressure discontinuous on the elements and which generate different order interpolation functions for velocity and pressure (Crouzeix and Raviert, 1973).

In the present work, the finite element formulations have been derived using both equal and unequal order approximating functions for the velocity and pressure field. C^0-continuous 9-noded quadrilateral Lagrangian elements have been chosen with biquadratic approximation functions for velocity and pressure generating total of 27 degrees of freedom per element consisting of 18 nodal velocity components and 9 nodal pressures. To devise a Galerkin finite element

scheme with mixed interpolations, Taylor-Hood elements are used with continuous piecewise polynomials of degree 2 for velocity approximations and piecewise bilinear approximations for pressures. Taylor-Hood element is the lower member of the bubble element family (Arnold *et al.*, 1984; Brezzi and Falk, 1991). Total of 22 numbers of degrees of freedom corresponds to these Taylor-Hood elements consisting of 18 velocity components over all the 9 nodes and 4 nodal pressures calculate over the vertices of quadrilateral elements. **Figure 4. 3** shows both these elements with their corresponding number of degrees of freedom.

(a) Biquadratic Lagrangian Element   (b) Taylor Hood

● : Velocity and pressure

△ : Velocity
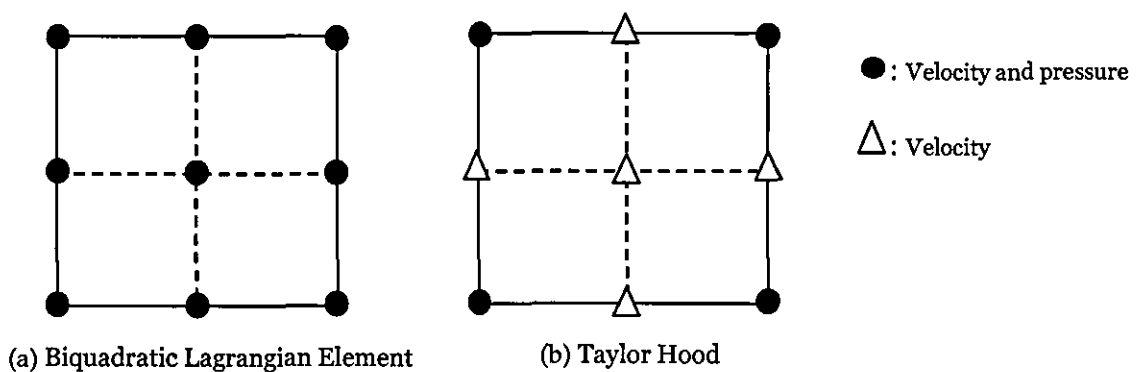
Figure 4. 3: 9-noded biquadratic and Q2/Q1 Taylor-Hood element

4.2.3 Time stepping techniques

The solution obtained from the finite element approximation should be uniquely accurate and should exhibit the property of stability. Accuracy of a numerical scheme is a measure of the closeness between the approximate solution and exact solution whereas stability defines measure of the boundness of the approximate solution with time in case of transient problems. As mentioned in the previous chapter, the governing equations for viscous incompressible free as well as porous flow equations contain first order differentials in time domain. A proper balance between the temporal and spatial approximations must be maintained to achieve overall stability in the solutions to transient problems. Usually, in finite element analysis of unsteady state problems, the spatial and temporal terms are not formulated to weak forms in parallel. Instead, the equations are discretised

first with respect to spatial variables therefore obtaining a system of coupled ordinary differential equations in time. The first-order differential system is integrated with respect to time in forward direction to trace temporal variations in field variables starting from a known value at initial time. This is the most convenient method for solution of time-dependent partial differential equations by finite element procedures and is named as 'partial discretisation' technique. Single-step methods such as θ-time methods and Taylor Galerkin methods are the most frequently used partial discretisation procedures for solution of transient problems by weighted residual finite element scheme.

4.2.3.1   θ-time-stepping method

Consider a function ϕ varying between time interval $[t, t+\Delta t]$ corresponding to time steps n and $n+1$ respectively as shown in **Figure 4. 4**.
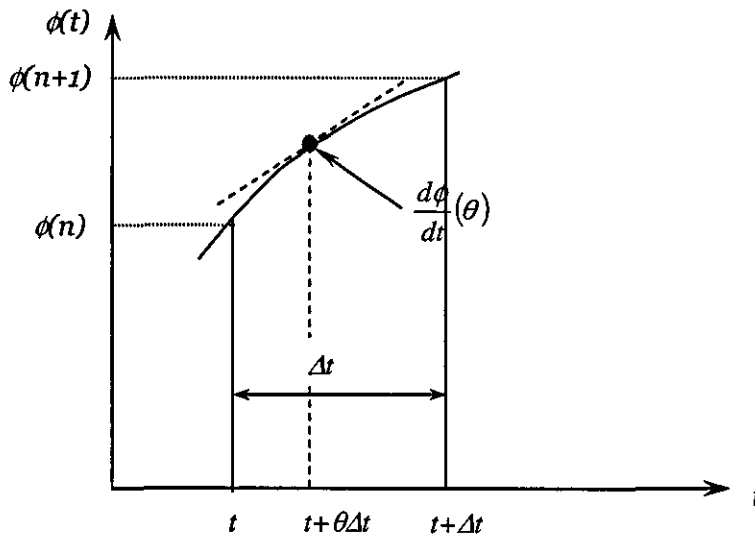
Figure 4. 4: Time stepping method

At any point θ between the time interval t and $t+\Delta t$, the variation in ϕ is expressed by the mean value theorem as,

$$\left.\frac{d\phi}{\partial t}\right|_{\theta} = \frac{\phi|_{n+\theta\Delta t} - \phi|_n}{\theta\Delta t} = \frac{\phi|_{n+1} - \phi|_n}{\Delta t} \qquad (4.5)$$

where, $0 \leq \theta \leq 1$

The variable ϕ at point θ can be approximated using linear interpolation as,

$$\phi\big|_\theta = \theta\phi\big|_{n+1} + (1-\theta)\phi\big|_n \qquad\qquad (4.6)$$

Several well-known methods are obtained for different values of θ parameter. These choices and their associated names are,

1. $\theta = 0$,   Forward difference or Euler method

2. $\theta = 1/2$,   Central difference or Crank-Nicholson method

3. $\theta = 2/3$,   Galerkin method

4. $\theta = 1$,   Backward difference method

For values of $\theta > 1/2$, the method is unconditionally stable and the only method which is second-order accurate is Crank-Nicholson (Johnson, 1987).

Besides the Crank-Nicholson method, the second-order accurate explicit time schemes that can be generally employed in unsteady state finite element formulations are Lax-Wendroff method and the Leap-Frog method (Donea and Huerta, 2003).

4.2.3.2   Taylor-Galerkin method

In certain cases, the time-stepping methods such as θ, Lax-Wendroff and Leap-Frog method show unsuitability when applied in conjunction with the standard Galerkin finite element method with linear interpolations (Donea and Quartapelle, 1992). In such cases, the Taylor-Galerkin methods proposed by Donea (1984) generate improved approximations to temporal differential terms by the use of Taylor series expansions including the second and third order time-derivatives.

Consider a partial differential equation,

$$\frac{\partial\phi(x,t)}{\partial t} + f[\phi(x,t)] - c = 0 \qquad\qquad (4.7)$$

Where, f is a linear differential operator with respect to x. Taylor series expansion of variable ϕ within the time steps n and $n+1$ gives,

$$\phi^{n+1} = \phi^n + \Delta t \frac{\partial\phi}{\partial t}\bigg|^n + \frac{1}{2}(\Delta t)^2 \frac{\partial^2\phi}{\partial t^2}\bigg|^n + \ldots \qquad\qquad (4.8)$$

The temporal derivatives in equation (4.8) can be substituted from the parent differential equation (4.7) evaluated at that time level.

Hence,

$$\left.\frac{\partial \phi(x,t)}{\partial t}\right|_n = -f[\phi(x,t)]_n + c \tag{4.9}$$

Similarly, the second order derivative at time step n can be replaced as,

$$\left.\frac{\partial^2 \phi(x,t)}{\partial t^2}\right|_n = \frac{\partial}{\partial t}\{-f[\phi(x,t)]_n + c\} \tag{4.10}$$

All the temporal differential terms arriving in the right hand side of equation (4.8), are found using the original differential equation (4.7) providing a differential equation exclusively in terms of spatial variables which can be discretised by the standard Galerkin method. The order and accuracy of the time-stepping scheme in Taylor-Galerkin method principally relies on the highest order of temporal derivative term retained in the expansion equation (4.8). Though the Taylor-Galerkin methods are easy to formulate even for the multi-dimensional problems, repeated differentiation and substitution of temporal derivatives may prove to be difficult.

4.2.3.3   Time-splitting method

In the original Taylor-Galerkin method proposed by Donea (1984), the Taylor series is truncated to the required order of accuracy and is used to evaluate time derivatives in terms of spatial derivatives. A more efficient form of this scheme is termed as time-split scheme which uses multiple time steps within two successive time levels. The value of variable evaluated in one time step is used to calculate its value at the successive time step using a simple difference formula.

We consider an intermediate time step $j+\frac{1}{2}$ within two successive time levels j and $j+1$ at a time interval of Δt as shown in **Figure 4. 5.**
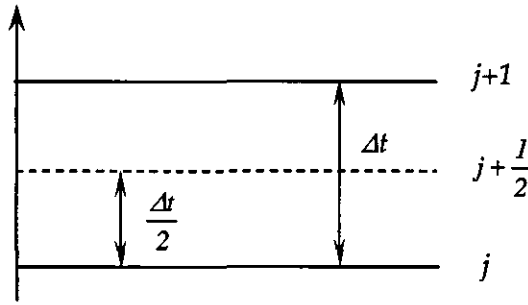
Figure 4. 5: Two step time-splitting procedure

At time level *j+1*, the value of function ϕ can be expressed in form of Taylor-series expansion as,

$$\phi^{j+1} = \phi^j + \Delta t \left.\frac{\partial \phi}{\partial t}\right|^j + \frac{(\Delta t)^2}{2} \left.\frac{\partial^2 \phi}{\partial t^2}\right|^j \tag{4.11}$$

If we consider a function,

$$F(t) = \frac{\partial \phi}{\partial t} \tag{4.12}$$

Then, the Taylor series expansion of function *F(t)* within time levels *j* and $j+\frac{1}{2}$ can be evaluated as,

$$F^{j+\frac{1}{2}} = F^j + \frac{\Delta t}{2} \left.\frac{\partial F}{\partial t}\right|^j + \left(\frac{\Delta t}{2}\right)^2 \left.\frac{\partial^2 F}{\partial t^2}\right|^j \tag{4.13}$$

Maintaining the first order temporal accuracy,

$$F^{j+\frac{1}{2}} = F^j + \frac{\Delta t}{2} \left.\frac{\partial F}{\partial t}\right|^j + O(\Delta t)^2 \tag{4.14}$$

Substituting for *F* from equation (4.11) into equation (4.14) followed by multiplication by Δt,

$$\Delta t \left.\frac{\partial \phi}{\partial t}\right|^{j+\frac{1}{2}} = \Delta t \left.\frac{\partial \phi}{\partial t}\right|^j + \frac{(\Delta t)^2}{2} \left.\frac{\partial^2 \phi}{\partial t^2}\right|^j \tag{4.15}$$

Comparing the terms in equation (4.11) and (4.15), it can be concluded that,

$$\phi^{j+1} = \phi^j + \Delta t \left.\frac{\partial \phi}{\partial t}\right|^{j+\frac{1}{2}}$$ (4.16)

Therefore, the awkward situation of calculation of second-order temporal derivatives in the original Taylor-Galerkin method can be relaxed by substituting first order time differentials evaluated at intermediate fractional time steps between two successive levels maintaining the same order of accuracy (Townsend and Webster, 1987). The two step time-split procedure is also termed as a predictor-corrector method in which the value calculated in the predictor step at $j+\frac{1}{2}$ is substituted to calculate its value at corrector step *j+1*. In the similar way, the stability and order of accuracy for equations having higher order temporal derivative terms can be improved by using multiple step time-splitting procedure (Nassehi and Bikangaga, 1993).

4.3   Isoparametric elements and coordinate transformation

In cases like the flow domains having curved boundaries, the finite element discretisation error can be minimised by utilising elements themselves having curved sides. A regular element called as the master element is chosen and a local finite element approximation based on this master elemental interpolation functions are carried out. Two independent elements can be used in the finite element analysis, one for approximating geometry and the other for interpolation of field variable. The master element is mapped into the global coordinates to generate required curved irregular element. The transformation of global coordinate system to a local coordinate system proves to be convenient in constructing the interpolation functions and calculating the integrals using simple quadrature formulae. When the one-to-one transformation between the global and natural coordinate system has been established using polynomials of the order equal to that of the interpolation functions, it is termed as an isometric mapping technique (Ergatoudis *et al.*, 1968). The derivatives of the interpolation functions can also be evaluated in the generalised space of transformed curved element. The

isometric mapping of irregular rectangular elements takes place as shown in **Figure 4. 6.**

(a) **Distorted element**   (b) **Master element**

Figure 4. 6: Isoparametric mapping of quadrilateral elements

The coordinate transformation can be expressed as,

$$\begin{cases} x = \sum_{i=1}^{n} N_i(\xi,\eta)x_i \\[2mm] y = \sum_{i=1}^{n} N_i(\xi,\eta)y_i \end{cases}$$

(4. 17)

The transformed derivatives of the interpolation functions are expressed in matrix form as,

$$\begin{bmatrix} \dfrac{\partial N_i}{\partial x} \\[2mm] \dfrac{\partial N_i}{\partial y} \end{bmatrix} = [J]^{-1} \begin{bmatrix} \dfrac{\partial N_i}{\partial \xi} \\[2mm] \dfrac{\partial N_i}{\partial \eta} \end{bmatrix}$$

(4. 18)

where, J is the Jacobean matrix expressed as,

$$[J] = \begin{bmatrix} \sum_{i=1}^{n} \dfrac{\partial N_i}{\partial \xi} x_i & \sum_{i=1}^{n} \dfrac{\partial N_i}{\partial \xi} y_i \\[2mm] \sum_{i=1}^{n} \dfrac{\partial N_i}{\partial \eta} x_i & \sum_{i=1}^{n} \dfrac{\partial N_i}{\partial \eta} y_i \end{bmatrix}$$

(4. 19)

For the coordinate transformation it is required that the Jacobean matrix is non-singular. The magnitude of error in this approximation depends on the degree of irregularity of parent distorted element to be mapped. The details of the

coordinate transformation procedure are elaborated in the textbooks like Reddy (1993).

The weighted residuals in the finite element formulations are calculated by the means of numerical integration technique. Elementary integration formulae such as trapezoidal rule assumed equally spaced data in most of the cases and somewhat lack in accuracy therefore have limited applicability. To circumvent these problems, Gaussian quadrature techniques are in common use where the points of subdivision are not equidistant but are placed symmetrically with respect to the mid-point of the interval of integration. The Gauss quadrature technique evaluates an integral as,

$$I = \int_a^b f(x)dx = \sum_{i=1}^n w_i f(x_i)$$ (4. 20)

The Gauss-Legendre quadrature formula has the interval between –1 and 1 which is easily compliant with weighted residuals converted to the natural coordinate system discussed before.

Consider an integration of a function $\phi(x, y)$ over a quadrilateral element in two-dimensional finite element mesh as,

$$I = \int_{x_1}^{x_2} \int_{y_1}^{y_2} \phi(x, y)dxdy$$ (4. 21)

The transformation between global and local coordinates gives,

$$dxdy = |J|^e \, d\xi d\eta$$ (4. 22)

and,

$$I = \int_{-1}^{+1} \int_{-1}^{+1} \Phi(\xi,\eta)|J|^e \, d\xi \, d\eta$$ (4. 23)

After algebraic manipulation,

$$I = \int_{-1}^{+1} \int_{-1}^{+1} G(\xi,\eta) \, d\xi \, d\eta$$ (4. 24)

Using the Gauss-Legendre quadrature formula,

$$I = \int_{-1}^{+1} \int_{-1}^{+1} G(\xi,\eta) d\xi d\eta \approx \sum_{i=1}^m \sum_{j=1}^n G(\xi_i,\eta_j)W_i W_j$$ (4. 25)

Where, ξ_i and η_j are the quadrature point coordinates. W_i and W_j are the corresponding weighting function values and m & n are the number of quadrature points. For n sampling points, a polynomial of the order of *(2n-1)* can be integrated exactly (Zienkiewicz and Taylor, 2002).

4.4   Axisymmetric problems

Axisymmetric domains posses symmetry about an axis of rotation and variations in field variables within such 3-dimensional domains can be obtained using two-dimensional finite elements. The axisymmetric element is obtained by rotating a two-dimensional element about z-axis to obtain a torus as illustrated in **Figure 4. 7.**

(a) Triangular ring   (b) Quadrilateral ring
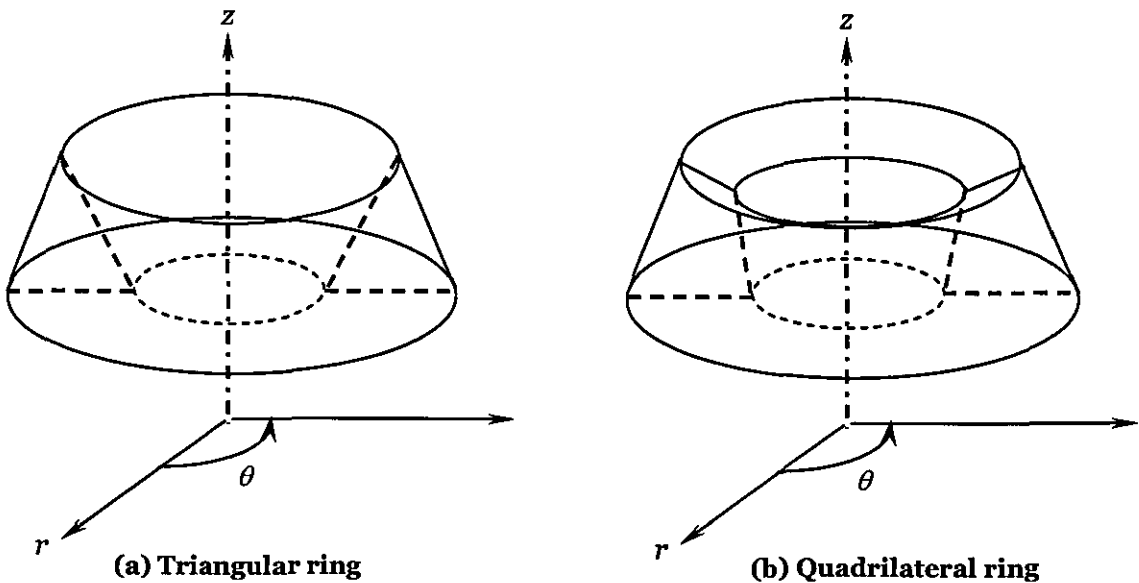
Figure 4. 7: Axisymmetric elements

The governing equations pertaining to the free and porous flow dynamics i.e. equations (3.1), (3.4) and (3.9) are resolved in axisymmetric coordinate system as,

Equation of continuity:

$$\frac{\partial u_r}{\partial r} + \frac{u_r}{r} + \frac{\partial u_z}{\partial z} = 0 \tag{4.26}$$

Stokes equations:

$$\begin{cases} \rho\frac{\partial u_r}{\partial t} = -\frac{\partial p}{\partial r} + \frac{\partial}{\partial r}\left(2\eta\frac{\partial u_r}{\partial r}\right) + \frac{2\eta}{r}\frac{\partial u_r}{\partial r} - \frac{2\eta}{r}\frac{u_r}{r} + \frac{\partial}{\partial r}\left[\eta\left(\frac{\partial u_z}{\partial r} + \frac{\partial u_r}{\partial z}\right)\right] = 0 \\[3mm] \rho\frac{\partial u_z}{\partial t} = -\frac{\partial p}{\partial z} + \frac{\partial}{\partial z}\left(2\eta\frac{\partial u_z}{\partial z}\right) + \frac{\eta}{r}\left(\frac{\partial u_z}{\partial r} + \frac{\partial u_r}{\partial z}\right) + \frac{\partial}{\partial r}\left[\eta\left(\frac{\partial u_z}{\partial r} + \frac{\partial u_r}{\partial z}\right)\right] = 0 \end{cases} \tag{4.27}$$

Darcy equation:

$$\begin{cases} \rho\frac{\partial u_r}{\partial t} + \frac{\partial p}{\partial r} + \frac{\eta}{K_r}\cdot u_r = 0 \\[3mm] \rho\frac{\partial u_z}{\partial t} + \frac{\partial p}{\partial z} + \frac{\eta}{K_z}\cdot u_z = 0 \end{cases} \tag{4.28}$$

In axisymmetric flow problems, the boundary conditions and domain geometry are essentially required to be independent of the circumferential direction. Therefore the governing flow equations can be analytically integrated with respect to this direction to reduce a 3D model to two-dimensional form as in equations (4.27) and (4.28). The three dimensional spatial integral in weighted residual statement is replaced by,

$$\iiint\phi(x,y,z)\,dx\,dy\,dz = \int_0^{2\pi}\iint\phi(r,z)\,r\,d\theta\,dr\,dz \tag{4.29}$$

where, $\iiint dx\,dy\,dz = \iiint r\,dr\,d\theta\,dz$

For isoparametric quadrilateral element the residual integral in local coordinate system can be expressed as,

$$\int_0^{2\pi}\int_{-1}^{+1}\int_{-1}^{+1}\phi(\xi,\eta)\,rd\theta\,|J|\,d\xi\,d\eta = 2\pi\int_{-1}^{+1}\int_{-1}^{+1}\phi(\xi,\eta)\,r(\xi,\eta)\,|J|\,d\xi\,d\eta \tag{4.30}$$

Where, J is the Jacobian matrix of coordinate transformation.

Using Gauss-Legendre quadrature with algebraic simplification Equation is written as,

$$2\pi\int_{-1}^{+1}\int_{-1}^{+1}G(\xi,\eta)d\xi d\eta = 2\pi\sum_{i=1}^{k}\sum_{j=1}^{k}w_i w_j G(\xi_i,\eta_j) \tag{4.31}$$

4.5   Finite element simulation of couple flow dynamics

Consider a flow model consisting of the following equations,

$$A\,\vec{u} + \vec{\nabla}p = \vec{f} \tag{4.32}$$

$$\vec{\nabla}\cdot\vec{u} = 0 \tag{4.33}$$

in domain Ω.

where, $\Omega \subset \Re^2$ is a bounded domain with a continuous boundary Γ, $\vec{u}$ is the velocity vector, $\vec{f}$ is the body force vector and p is the pressure. Depending upon the choice of operator A we obtain two different flow models,

a. $A(\vec{u}) = \vec{\bar{I}} \cdot \dfrac{\eta}{\vec{\bar{K}}}\vec{u}$, where $\vec{\bar{I}}$ is the identity tensor, η is the fluid viscosity,

$\vec{\bar{K}}$ is the permeability tensor for the porous media, which is the Darcy equation

b. $A(\vec{u}) = -2\vec{\nabla}\cdot\eta\vec{\bar{D}}(\vec{u})$, where $\vec{\bar{D}}(\vec{u})$ is the symmetric part of the velocity gradients tensor, which is the Stokes equation.

To obtain an accurate and stable solution for the coupled problem of Stokes-Darcy flow, the following problems are resolved. As mentioned earlier, in modelling the incompressible flow, the LBB stability condition must be satisfied which in turn poses severe restrictions on the choice of the approximating spaces that can be used.

In addition to the requirement of LBB criterion, it is also known that due to the incompatibility of operators in the Stokes and the Darcy equations, the approximating functional spaces used for the numerical solution of these equations need to be different. In essence, the Darcy equation should be treated as an elliptic Poisson equation where the degrees of freedom should be kept as low as possible. However, the corresponding approach for the Stokes equation which would in some minimal sense be to use a piecewise constant (discontinuous) approximation for pressure and linear (continuous) approximation for the velocities, results in an over-rich pressure space generating trivial solutions for the velocity accounting to "numerical locking". In the following discussion, some of

the previously reported studies pertaining to simulation coupled free–porous flow dynamics in particular; by finite element technique is considered.

Salinger *et al.* (1994) presented a finite element procedure to solve large scale, coupled free/porous steady state flows encountered in spontaneous ignition of coal stockpiles. This study presented a coupled system of chemical reaction, mass transport and natural convective flows within the stockpile, which is modelled as a porous medium and the surrounding ambient air. Two formulations for the coupled flow phenomenon are derived one with the Darcy's law and the second with the Brinkman equations to represent the porous flow behaviour in the stockpile. In both the approaches, the free flow behaviour is expressed by the Navier-Stokes equations. In the formulation, which uses Darcy's law, the extended version of the Beavers-Joseph slip wall boundary condition (Beavers and Joseph, 1967) proposed by Jones (1973) is imposed at the interface between the porous coal pile and the surrounding air. A weighted residual Galerkin finite element method using triangular elements is used to solve the system of partial differential equations in axisymmetric coordinate system. A mixed order P2/P1 formulation is adopted to approximate the field unknowns namely concentration, temperature, velocity and pressure. For the same finite element mesh used, the solutions obtained using the Darcy-slip formulations are found to be much more stable than that obtained from the Brinkman formulation. The Darcy-slip formulation derived in this work requires only the pressure discretisation in porous medium rather than velocity unlike the Brinkman method. The solutions obtained for the Brinkman formulations on more refined mesh are found to be stable in the bulk of the porous matrix but consists of oscillations near the free/porous interface. The computations were observed to be totally insensitive to the values of slip coefficient employed at the interface which minimizes the effect of empiricism involved in Beavers-Joseph slip interface condition.

In finite element formulations of coupled Stokes-Darcy problem using C^0 continuous elements, inter-element flux terms arise when Green's theorem is applied to reduce the second order differential in Stokes equations to first order differentials. In combined flow regimes, these flux terms can not be ignored due to the absence of approximately equal magnitude opposite fluxes on the other side of free/porous boundary. To alleviate this awkward situation, Nassehi and Petera (1994) presented a novel scheme for coupling Navier-Stokes and Darcy equations

along a porous boundary in a flow regime representing an axisymmetric slurry filtration system. The scheme is based on least-square finite element formulation in conjunction with C^1-continuous Hermite elements which posses an inter-elemental continuity for the second order differentials. Therefore, The scheme doesn't encourage formation of the inter-elemental flux terms and can be advantageously used to model combined Navier-Stokes and Darcy flow regimes directly without making unrealistic assumptions. However, these elements lack flexibility, in general and their application in geometrically complex domains involves enormous complications.

Gartling *et al.* (1996) presented a numerical formulation for the conjugate problem involving the incompressible flow adjacent to a saturated porous medium. The major emphasis was on development of a generally applicable finite element scheme for simulation of Navier-Stokes equation coupled with both Darcy and non-Darcy type porous flow equations using mixed interpolations for the field unknowns. The continuity of physical entities across the free-porous barrier has been addressed by conditions such as those given by Beavers and Joseph (1967). The developed formulation is applied to two different practical problems having fixed free-porous interface and emerging free-porous interface in alloy solidification. The performance of mixed finite element formulations towards the Darcy equation proves to be marginal. In constructing the finite element formulations, the only difficulty arise is the evaluation of boundary integral terms along the porous, clear fluid interface. The coupling of Navier-Stokes and Darcy model exhibited the drawback of handling stress boundary conditions at the interface. The linking of Navier-Stokes equations with the Brinkman equation seems to be uncomplicated except the evaluation of accurate value of the Brinkman effective viscosity, η_B.

Nassehi (1998) analysed the fluid flow behaviour of combined free and porous flow regimes observed in cross-flow membrane filtration systems. Modelling of axisymmetric porous tube and shell system is based on Darcy equation and Navier-Stokes equations, respectively. The existence of viscous stress terms in the Navier-Stokes equations which are expressed in terms of second order differentials of velocity, makes its straightforward linking to Darcy equation impossible. To circumvent this problem, Nassehi (1998) developed a novel finite element solution scheme in which the porous wall condition expressed by the

Darcy equation is imposed as the effective boundary condition for the free flow regime at the free-porous interface. A perturbed form of continuity equation is used enhancing the use of equal-order interpolation functions for velocity and pressure. The computational results generated using the developed scheme proves preservation of the mass continuity in complex branching flow domains. The flexibility of the scheme has been analysed by performing numerical experiments with different values of inlet fluid velocity, porous wall permeability and exit conditions.

Burman and Hansbo (2002) proposed a unified approach for the solution of the coupled Stokes and Darcy problem using an edge stabilisation technique in a finite element environment using mixed P1/P0 elements. The edge stabilisation technique resolves the viscous stress term associated with the Navier-Stokes equations into its tangential and normal components at the free-porous interface. The normal stress component is then equated to the pressure differential across the interface. The concepts illustrated are mathematically complicated for their suitability for practical situations where the interface may have geometrically complex shape. However, the so called "numerical locking" occurring due to the discrepancy between the gradient operator from both the equations at the interface can be avoided by using lowest order mixed finite elements such as P1/P0 combination of approximation.

Mardal *et al.* (2002) considered a single perturbation problem describing both the Stokes and the Darcy equations. The value of the perturbation parameter lies within the bounds of 0 and 1. The system represents approximately a linear Stokes problem when the perturbation parameter is large while it gets transformed into a mixed formulation of Poisson's equation or Darcy equation for a homogeneous porous medium as the perturbation parameter tends to zero. A finite element solution procedure has been developed for the perturbation problem with convergence and stability properties that are uniform with respect to the perturbation parameter. The relative error in the velocity was obtained using P2-P0 element, nonconforming Crouzeix-Raviart element, mini element and Raviart-Thomas element which illustrated that none of them exhibit convergent solutions with respect to the perturbation parameter. Finally, robust non-conforming finite element discretisation is proposed which is uniformly stable with uniform velocity error estimates in the perturbation parameter.

Discacciati *et al.* (2002) presented some fruitful results for coupled system of free and porous flow equations for surface and subsurface flows. All the suitable interface conditions between the free and porous flow regimes are discussed in the context of coupled Navier-Stokes and shallow water equations for surface flows and Darcy equation for groundwater flow. A finite element numerical scheme has been devised for the solution of coupled equations based on domain decomposition method (Quarteroni and Valli, 1999) emphasizing on Neumann-Dirichlet iterative procedure. The 3D shallow water equations are solved by the multi-layer approach and for the porous region, mixed finite element formulation has been employed. The spatial discretisation for both free surface and porous region has been carried out by 3D prismatic finite elements. In each of these coupled flow formulations, the results are noted to be insensitive to the mesh parameter h.

Miglio *et al.* (2003) extended the same methodology of coupling free surface and sub-surface motion of fluid using the Beavers-Joseph continuity condition at the interface. The pressure term in the 3D shallow water equation includes hydrostatic pressure and hydrodynamic correction. The hydrostatic pressure in the Darcy equation is accompanied by the potential energy per unit weight of water. Finite element discretisations of the governing equations are carried out adopting the lowest order Raviart-Thomas finite elements. The temporal discretisation is achieved by the implicit theta scheme. Two different water channels are considered as solution domains with a homogeneous porous medium. The numerical results showed that the iterative scheme is convergent and the accuracy and stability of the results are confirmed by the preserved continuity of the mass.

Discaccitati and Quarteroni (2003, 2004) followed by Discacciati (2004) introduced a differential system based on the coupling of the Navier-Stokes/Stokes and Darcy equation for the modelling of interactions between surface and groundwater flows. They proposed an iterative subdomain methods based on domain decomposition approach to solve the coupled flow problem using finite elements. At the free/porous boundary, the normal component of the Cauchy's stress from the Stokes region is equated to the pressure from the Darcy region. The tangential component of Cauchy's stress is related to the seepage velocity in the porous region at the interface by a slip-wall condition similar to

Beavers and Joseph (1967) or Payne and Straughan (1998). The interface conditions have been split conveniently so that at each iterative step of the solution procedure two subproblems are required to be solved. A scalar interface variable is defined differently for these two subproblems and its value has been updated at the end of each iteration by means of an implicit-θ method. The finite element discretisations have been carried out by using P2/P1 mixed order Taylor-Hood elements for the Stokes equations and P2 Lagrangian elements for the Darcy equation. The dependence of the rate of convergence on the mesh parameter h and the physical properties has been accessed. The critical value of time step, Δt required for stable solutions is found to be dependable on the fluid and porous region Reynolds numbers.

Layton *et al.* (2003) discussed the transport of substances back and forth between surface water and groundwater. The seriousness of the problem has been discussed in the context of prediction of pollutant concentration discharged into natural aquifers making its way to the underground water supply. The mathematical model consists of Stokes equations in the fluid region and the Darcy equation in the porous region coupled at the polygonal interface. The normal boundary condition at the free/porous interface is imposed by equating the Cauchy stress in the fluid region with the pressure from the Darcy region. The continuity in the tangential components of the velocities in the individual regions has been achieved by using the Beavers-Joseph-Saffman boundary condition (Jager and Mikelić, 2000). A complete finite element numerical analysis along with its mathematical background have been explained to solve this coupled flow problem in uncoupled steps involving porous media and fluid flow subproblems.

All the cited references concern the finite element modelling and simulations of combined Navier-Stokes and Darcy equations with their detailed mathematical insights, physical concepts relating the free-porous interface phenomena and their suitability towards applications to realistic situations. Besides these appreciable efforts, some researchers attempted to achieve solutions to the coupled flow problems using different numerical techniques. Damak *et al.* (2004a & b) developed a new Navier-Stokes-Darcy's law combined model for fluid flow in a cross-flow filtration tubular membrane. Numerical simulations were performed for laminar fluid flow in a porous tube with variable wall suction. The flow throughout the free flow region is considered to be fully developed. At the

permeable wall, the slip velocity is taken to be zero and the suction velocity is expressed by the Darcy's law. The simulations are carried out for a large range of Reynolds axial and filtration numbers with and without porous wall suctions. The simulated results are compared with available experimental results and found to be in close agreement. Theoretical validation of the results is based on quantitative evolutions of factors such as the overall mass balance. However, the assumption of the developed flow condition in these coupled flow regimes is inappropriate and problematic in general cases. Similar efforts have been reported in literature by Dufrêche *et al.* (2002) and Oxarango *et al.* (2004) who attempted to model the combined Navier-Stokes/Darcy equations by finite volume method and boundary element methods respectively.

4.6 Closure

The selection criteria for the finite element as a technique for numerical analysis of the current problem have been justified. Choice of approximating functions for the spatial discretisation and time-stepping schemes for the temporal discretization of governing equations have been discussed. Some of the previously reported work on combined flow simulation using finite element method has been listed in the context of the present situation.

5.   Development of Computational Scheme

The finite element method selected for the numerical analysis of governing equations is based on approximating procedure whose solutions desire the characteristics of stability, accuracy and convergence. The uniqueness and appropriateness of the solution relies on the approximations and the nature of the imposed boundary and initial conditions. The central theme behind finite element formulation is reduction of partial differential equations to a set of algebraic equations to be solved simultaneously by rigorous matrix manipulations. In the ongoing discussion, working equations of two finite element schemes have been derived distinguished by the type of interpolating approximations adopted for the primitive variables. The solution procedure for the assembled set of discretised algebraic equations has been explained. Finally, the idea behind the nodal replacement technique for imposing the Darcy equation as the free/porous interface condition in the finite element formulation has been elaborated.

5.1   U-V-P scheme

In few of the previous approaches related to solution of incompressible flow equations, the continuity equation is eliminated by using specialised shape functions. The pressure field is then determined from a Poisson equations containing the instantaneous velocity (Zienkiewicz *et al.*, 1965). Unfortunately, neither the pressure nor its gradient on the domain boundaries can be known until the velocity field is determined. To ameliorate this situation, Taylor and Hood (1973) attempted the direct coupling of all the equations associated with the incompressible flow problems. The direct coupling approach involves coupling of all the finite element equations into a single matrix. Though the bandwidth of final matrix is exceptionally large, the method is extremely simple to apply. This technique is also termed as the U-V-P scheme with reference to velocity-pressure formulation in which both the velocity and pressure in the governing incompressible flow equations are regarded as the primitive variables. To satisfy the LBB criteria to achieve spatial stability in solutions, two different UVP schemes are proposed distinguished by the order of interpolation functions for the primitive variables.

5.1.1 Perturbed continuity scheme

The perturbed continuity scheme allows the equal order interpolation functions for velocity and pressure by adding a temporal derivative of pressure in the equation of continuity which takes the form quite different from equation **(3.2)** as,

$$\frac{1}{\rho c^2}\frac{\partial p}{\partial t}+\frac{\partial u_x}{\partial x}+\frac{\partial u_y}{\partial y}=0 \qquad\qquad (5.1)$$

where, c is the speed of sound in the fluid medium. The inclusion of the term $\dfrac{1}{\rho c^2}$

signifies the fluid to be slightly compressible (Zienkiewicz and Wu, 1991). Thermodynamically, the system assumes to have constant entropy and the details behind this assumption can be referred from the work of Zienkiewicz *et al.* (1999). However, the inclusion of the parameter c in equation **(5.1)** resembles only the mathematical simplification and it doesn't affect the physical phenomena underlying the incompressible fluid flows. To comply with this perturbed form of continuity equation, it becomes inevitable to incorporate temporal derivatives of velocity components in equations of the conservation of momentum in free as well as porous flow regimes as,

Stokes equations (free flow regime):

$$\rho\frac{\partial u_x}{\partial t}=-\frac{\partial p}{\partial x}+\frac{\partial}{\partial x}\left(2\eta\frac{\partial u_x}{\partial x}\right)+\frac{\partial}{\partial y}\left[\eta\left(\frac{\partial u_x}{\partial y}+\frac{\partial u_y}{\partial x}\right)\right]=0 \qquad (5.2)$$

$$\rho\frac{\partial u_y}{\partial t}=-\frac{\partial p}{\partial y}+\frac{\partial}{\partial y}\left(2\eta\frac{\partial u_y}{\partial y}\right)+\frac{\partial}{\partial x}\left[\eta\left(\frac{\partial u_y}{\partial x}+\frac{\partial u_x}{\partial y}\right)\right]=0 \qquad (5.3)$$

Darcy equation (porous flow regime):

$$\rho\frac{\partial u_x}{\partial t}=-\frac{\partial p}{\partial x}-\frac{\eta}{K_x}\cdot u_x \qquad\qquad (5.4)$$

$$\rho\frac{\partial u_y}{\partial t}=-\frac{\partial p}{\partial y}-\frac{\eta}{K_y}\cdot u_y \qquad\qquad (5.5)$$

Due to the time-dependency included in the governing equations, the use of robust time-stepping schemes is mandatory even for obtaining the steady state solutions. As discussed in the previous chapter, two different time-stepping schemes namely, the first order Euler alias the implicit-θ method and second order Taylor-Galerkin method have been examined for their accuracy, stability and computational economy in simple domain geometries which will then be extended to calculate the coupled flow hydrodynamics in pleated cartridge domain.

5.1.1.1   Temporal discretisation by implicit-θ method

The field variables are normalized and renamed as,

$$\begin{cases} U = u_x, V = u_y \\ P = \dfrac{p}{\rho} \end{cases} \tag{5.6}$$

The normalised form of the equation of continuity becomes,

$$\frac{\partial P}{\partial t} = -c^2 \left(\frac{\partial U}{\partial x} + \frac{\partial V}{\partial y} \right) \tag{5.7}$$

With the equal order interpolation function for all the field unknowns, take the Galerkin weighted residual integral of equation (5.7),

$$\boxed{\iint_{\Omega_e} N_i \left(\frac{\partial P}{\partial t} \right) dx dy = \iint_{\Omega_e} -c^2 N_i \left(\frac{\partial U}{\partial x} \right) dx dy + \iint_{\Omega_e} -c^2 N_i \left(\frac{\partial V}{\partial x} \right) dx dy} \tag{5.8}$$

With the spatial discretisation of field unknowns in the elemental domain is carried out as,

$$\begin{cases} U = \displaystyle\sum_{j=1}^{np} N_j U_j = [\mathbf{N}]\{\dot{U}\} \\[2mm] V = \displaystyle\sum_{j=1}^{np} N_j V_j = [\mathbf{N}]\{\dot{V}\} \\[2mm] P = \displaystyle\sum_{j=1}^{np} N_j P_j = [\mathbf{N}]\{\dot{P}\} \end{cases} \tag{5.9}$$

Where, $\{\dot{U}\}$, $\{\dot{V}\}$ and $\{\dot{P}\}$ are the matrix vectors of nodal values of velocity components and normalised pressure respectively and np are the number of nodes

associated with single element for variables approximations. Substituting equation (5.9) into equation (5.8),

$$\left[\iint_{\Omega_e} N_i N_j \, dxdy \right] \frac{\partial \{\dot{P}\}}{\partial t} = \left[\iint_{\Omega_e} -c^2 N_i \frac{\partial N_j}{\partial x} dxdy \right] \{\dot{U}\} + \left[\iint_{\Omega_e} -c^2 N_i \frac{\partial N_j}{\partial y} dxdy \right] \{\dot{V}\} \qquad (5.10)$$

The temporal discretisation of the primitive variables is carried out by simple difference formula as,

$$\begin{cases} \dfrac{\partial \{U\}}{\partial t} = \dfrac{\{\dot{U}\}_{n+1} - \{\dot{U}\}_n}{\Delta t} \\[2mm] \dfrac{\partial \{\dot{V}\}}{\partial t} = \dfrac{\{\dot{V}\}_{n+1} - \{\dot{V}\}_n}{\Delta t} \\[2mm] \dfrac{\partial \{\dot{P}\}}{\partial t} = \dfrac{\{\dot{P}\}_{n+1} - \{\dot{P}\}_n}{\Delta t} \end{cases} \qquad (5.11)$$

where, Δt is the time difference between two successive time levels. At any time level $n + \theta \Delta t$ between time levels n and $n+1$, the field variables can be interpolated as,

$$\begin{cases} \{\dot{U}\} = \theta \{\dot{U}\}_{n+1} + (1 - \theta)\{\dot{U}\}_n \\[2mm] \{\dot{V}\} = \theta \{\dot{V}\}_{n+1} + (1 - \theta)\{\dot{V}\}_n \\[2mm] \{\dot{P}\} = \theta \{\dot{P}\}_{n+1} + (1 - \theta)\{\dot{P}\}_n \end{cases} \qquad (5.12)$$

Substituting equation (5.11) and (5.12) into equation (5.10) followed by algebraic manipulation, final discretised working form of equation of continuity is obtained.

5.1.1.1.1   Free flow regime

Inserting the normalised and renamed forms of the variables, the equation of motion in free flow regimes assumes the form as,

$$\frac{\partial U}{\partial t} = -\frac{\partial P}{\partial x} + \frac{2\eta}{\rho} \frac{\partial}{\partial x}\left(\frac{\partial U}{\partial x} \right) + \frac{\eta}{\rho} \frac{\partial}{\partial y}\left(\frac{\partial U}{\partial y} + \frac{\partial V}{\partial x} \right) \qquad (5.13)$$

$$\frac{\partial V}{\partial t} = -\frac{\partial P}{\partial y} + \frac{2\eta}{\rho} \frac{\partial}{\partial y}\left(\frac{\partial U}{\partial y} \right) + \frac{\eta}{\rho} \frac{\partial}{\partial x}\left(\frac{\partial U}{\partial y} + \frac{\partial V}{\partial x} \right) \qquad (5.14)$$

With the equal order interpolation function for all the field unknowns, take the Galerkin weighted residual integral of Equation (5.13),

$$\iint_{\Omega_e} N_i \frac{\partial U}{\partial t} dxdy = \iint_{\Omega_e} N_i \left(\frac{-\partial P}{\partial x} \right) dxdy + \iint_{\Omega_e} \frac{N_i}{\rho} \frac{\partial}{\partial x} \left(2\eta \frac{\partial U}{\partial x} \right) dxdy$$

$$+ \iint_{\Omega_e} \frac{N_i}{\rho} \frac{\partial}{\partial y} \left[\eta \left(\frac{\partial U}{\partial y} + \frac{\partial V}{\partial x} \right) \right] dxdy \qquad (5.\ 15)$$

Applying the Green's theorem to reduce the order of differentials on the R.H.S.,

$$\iint_{\Omega_e} N_i \left(\frac{\partial P}{\partial x} \right) dxdy = \int_{\Gamma_e} N_i (P)^e \eta_x d\Gamma + \iint_{\Omega_e} P \frac{\partial N_i}{\partial x} dxdy \qquad (5.\ 16)$$

$$\iint_{\Omega_e} N_i \frac{\partial}{\partial x} \left(2\eta \frac{\partial U}{\partial x} \right) dxdy = \int_{\Gamma_e} N_i \left(2\eta \frac{\partial U}{\partial x} \right)^e n_x d\Gamma - \iint_{\Omega_e} 2\eta \frac{\partial N_i}{\partial x} \frac{\partial U}{\partial x} dxdy \qquad (5.\ 17)$$

$$\iint_{\Omega_e} N_i \frac{\partial}{\partial y} \left[\eta \left(\frac{\partial U}{\partial y} + \frac{\partial V}{\partial x} \right) \right] dxdy = \int_{\Gamma_e} N_i \left[\eta \left(\frac{\partial U}{\partial y} + \frac{\partial V}{\partial x} \right) \right]^e n_y d\Gamma$$

$$- \iint_{\Omega_e} \frac{\partial N_i}{\partial y} \left[\eta \left(\frac{\partial U}{\partial y} + \frac{\partial V}{\partial x} \right) \right] dxdy \qquad (5.\ 18)$$

Substituting equations **(5.16)**, **(5.17)**, and **(5.18)** in equations **(5.15)**, spatial discretised form of equation **(5.13)** is obtained as,

$$\iint_{\Omega_e} N_i \frac{\partial U}{\partial t} dxdy = \iint_{\Omega_e} P \frac{\partial N_i}{\partial x} dxdy - \iint_{\Omega_e} \frac{2\eta}{\rho} \frac{\partial N_i}{\partial x} \frac{\partial U}{\partial x} dxdy$$

$$- \iint_{\Omega_e} \frac{\partial N_i}{\partial y} \left[\frac{\eta}{\rho} \left(\frac{\partial U}{\partial y} + \frac{\partial V}{\partial x} \right) \right] dxdy - \int_{\Gamma_e} N_i (P)^e n_x d\Gamma + \int_{\Gamma_e} \frac{N_i}{\rho} \left(2\eta \frac{\partial U}{\partial x} \right)^e n_x d\Gamma \qquad (5.\ 19)$$

$$+ \int_{\Gamma_e} \frac{N_i}{\rho} \left[\eta \left(\frac{\partial U}{\partial y} + \frac{\partial V}{\partial x} \right) \right]^e n_y d\Gamma$$

Substituting equation **(5.9)** into equation **(5.19)**,

$$\left[\iint_{\Omega_e} N_i N_j \, dxdy\right] \frac{\partial \{U\}}{\partial t} = \left[\iint_{\Omega_e} N_j \frac{\partial N_i}{\partial x} \, dxdy\right] \{\dot{P}\} -$$

$$\left[\iint_{\Omega_e} \frac{2\eta}{\rho} \frac{\partial N_i}{\partial x} \frac{\partial N_j}{\partial x} \, dxdy + \iint_{\Omega_e} \frac{\eta}{\rho} \frac{\partial N_i}{\partial y} \frac{\partial N_j}{\partial y} \, dxdy\right] \{U\} - \left[\iint_{\Omega_e} \frac{\eta}{\rho} \frac{\partial N_i}{\partial y} \frac{\partial N_j}{\partial x} \, dxdy\right] \{V\}$$

(5. 20)

$$- \int_{\Gamma_e} N_i (P)^e n_x d\Gamma + \int_{\Gamma_e} \frac{N_i}{\rho} \left(2\eta \frac{\partial U}{\partial x}\right)^e n_x \, d\Gamma$$

$$+ \int_{\Gamma_e} \frac{N_i}{\rho} \left[\eta \left(\frac{\partial U}{\partial y} + \frac{\partial V}{\partial x}\right)\right]^e n_y \, d\Gamma$$

Substituting equation (5.11) and (5.12) into equation (5.20) followed by algebraic manipulation, final discretised working equations for x as well as y-component of equation of motion are obtained.

The final set of working equations for the incompressible free flow dynamics can be expressed in matrix form as,

$$\begin{bmatrix} S_{ij}^{11} & S_{ij}^{12} & S_{ij}^{13} \\ S_{ij}^{21} & S_{ij}^{22} & S_{ij}^{23} \\ S_{ij}^{31} & S_{ij}^{32} & S_{ij}^{33} \end{bmatrix} \begin{Bmatrix} U_j \\ V_j \\ P_j \end{Bmatrix}^{n+1} = \begin{bmatrix} R_{ij}^{11} & R_{ij}^{12} & R_{ij}^{13} \\ R_{ij}^{21} & R_{ij}^{22} & R_{ij}^{23} \\ R_{ij}^{31} & R_{ij}^{32} & R_{ij}^{33} \end{bmatrix} \begin{Bmatrix} U_j \\ V_j \\ P_j \end{Bmatrix}^{n} + \begin{Bmatrix} B_j^I \\ B_j^I \\ B_j^I \end{Bmatrix}^{n} + \begin{Bmatrix} C_j^I \\ C_j^I \\ C_j^I \end{Bmatrix}^{n+1}$$

(5. 21)

where,

$$S_{ij}^{11} = \iint_{\Omega_e} \left[N_i N_j + \theta \Delta t \frac{\eta}{\rho} \left(2 \frac{\partial N_i}{\partial x} \frac{\partial N_j}{\partial x} \, dxdy + \frac{\partial N_i}{\partial y} \frac{\partial N_j}{\partial y}\right)\right] dxdy$$

(5. 22)

$$S_{ij}^{12} = \iint_{\Omega_e} \theta \Delta t \left[\frac{\eta}{\rho} \frac{\partial N_i}{\partial y} \frac{\partial N_j}{\partial x}\right] dxdy$$

(5. 23)

$$S_{ij}^{13} = \iint_{\Omega_e} -\theta \Delta t \left[N_j \frac{\partial N_i}{\partial x}\right] dxdy$$

(5. 24)

$$S_{ij}^{21} = \iint_{\Omega_e} \theta \Delta t \frac{\eta}{\rho} \left[\frac{\partial N_i}{\partial x} \frac{\partial N_j}{\partial y}\right] dxdy$$

(5. 25)

$$S_{ij}^{22} = \iint_{\Omega_e} \left[N_i N_j + \theta \Delta t \frac{\eta}{\rho} \left(2 \frac{\partial N_i}{\partial y} \frac{\partial N_j}{\partial y} + \frac{\partial N_i}{\partial x} \frac{\partial N_j}{\partial x}\right)\right] dxdy$$

(5. 26)

$$S_{ij}^{23} = \iint_{\Omega_e} -\theta \Delta t \left[N_j \frac{\partial N_i}{\partial y}\right] dxdy$$

(5. 27)

Error! Objects cannot be created from editing field codes.
(5. 28)

$$S_{ij}^{32} = \iint_{\Omega_e} -\theta \Delta t \left[N_i \frac{\partial N_j}{\partial y} \right] dx dy \tag{5.29}$$

$$S_{ij}^{33} = \iint_{\Omega_e} \left[\frac{1}{c^2} N_i N_j \right] dx dy \tag{5.30}$$

$$R_{ij}^{11} = \iint_{\Omega_e} \left[N_i N_j - (1-\theta)\Delta t \frac{\eta}{\rho} \left(2 \frac{\partial N_i}{\partial x} \frac{\partial N_j}{\partial x} + \frac{\partial N_i}{\partial y} \frac{\partial N_j}{\partial y} \right) \right] dx dy \tag{5.31}$$

$$R_{ij}^{12} = \iint_{\Omega_e} -(1-\theta)\Delta t \frac{\eta}{\rho} \left[\frac{\partial N_i}{\partial y} \frac{\partial N_j}{\partial x} \right] dx dy \tag{5.32}$$

$$R_{ij}^{13} = \iint_{\Omega_e} -(1-\theta)\Delta t \left[N_j \frac{\partial N_i}{\partial x} \right] dx dy \tag{5.33}$$

$$R_{ij}^{21} = \iint_{\Omega_e} -(1-\theta)\Delta t \frac{\eta}{\rho} \left[\frac{\partial N_i}{\partial x} \frac{\partial N_j}{\partial y} \right] dx dy \tag{5.34}$$

$$R_{ij}^{22} = \iint_{\Omega_e} \left[N_i N_j - (1-\theta)\Delta t \frac{\eta}{\rho} \left(2 \frac{\partial N_i}{\partial y} \frac{\partial N_j}{\partial y} + \frac{\partial N_i}{\partial x} \frac{\partial N_j}{\partial x} \right) \right] dx dy \tag{5.35}$$

$$R_{ij}^{23} = \iint_{\Omega_e} (1-\theta)\Delta t \left[N_j \frac{\partial N_i}{\partial y} \right] dx dy \tag{5.36}$$

$$R_{ij}^{31} = \iint_{\Omega_e} (1-\theta)\Delta t \left[N_i \frac{\partial N_j}{\partial x} \right] dx dy \tag{5.37}$$

$$R_{ij}^{32} = \iint_{\Omega_e} (1-\theta)\Delta t \left[N_i \frac{\partial N_j}{\partial y} \right] dx dy \tag{5.38}$$

$$R_{ij}^{33} = \iint_{\Omega_e} \left[\frac{1}{c^2} N_i N_j \right] dx dy \tag{5.39}$$

$$C_j^1 = \int_{\Gamma_e} \frac{\theta \Delta t}{\rho} \left[\left(2\eta \frac{\partial U^e}{\partial x} - P^e \right) n_x + \eta \left(\frac{\partial U^e}{\partial y} + \frac{\partial V^e}{\partial x} \right) n_y \right]^{n+1} d\Gamma \tag{5.40}$$

$$C_j^2 = \int_{\Gamma_e} \frac{\theta \Delta t}{\rho} \left[\eta \left(\frac{\partial U^e}{\partial y} + \frac{\partial V^e}{\partial x} \right) n_x + \left(2\eta \frac{\partial V^e}{\partial y} - P^e \right) n_y \right]^{n+1} d\Gamma \tag{5.41}$$

$$C_j^3 = 0 \tag{5.42}$$

$$B_j^1 = \int_{\Gamma_e} (1-\theta) \frac{\Delta t}{\rho} \left[\left(2\eta \frac{\partial U^e}{\partial x} - P^e \right) n_x + \eta \left(\frac{\partial U^e}{\partial y} + \frac{\partial V^e}{\partial x} \right) n_y \right]^n d\Gamma \tag{5.43}$$

$$B_j^2 = \int_{\Gamma_e} (1-\theta)\frac{\Delta t}{\rho}\left[\eta\left(\frac{\partial U^e}{\partial y}+\frac{\partial V^e}{\partial x}\right)n_x + \left(2\eta\frac{\partial V^e}{\partial y}-P^e\right)n_y\right]^n \, d\Gamma \qquad (5.\,44)$$

$$B_j^3 = 0 \qquad\qquad (5.\,45)$$

5.1.1.1.2   Porous flow regime

With the normalised form of variables as described in equation (5.6), the components of Darcy equation (5.4) and (5.5) become,

$$\frac{\partial U}{\partial t} = -\frac{\eta}{\rho K_x}\cdot U - \frac{\partial P}{\partial x} \qquad\qquad (5.\,46)$$

$$\frac{\partial V}{\partial y} = -\frac{\eta}{\rho K_y}\cdot V - \frac{\partial P}{\partial y} \qquad\qquad (5.\,47)$$

Taking the weighted residual integral of the x-component of the Darcy Equation (5.46),

$$\iint_{\Omega_e} N_i \frac{\partial U}{\partial t}\,dxdy = \iint_{\Omega_e} N_i\left(-\frac{\partial P}{\partial x}\right)dxdy + \iint_{\Omega_e} N_i\left(-\frac{\eta}{\rho K_x}\cdot U\right)dxdy \qquad (5.\,48)$$

Applying Green's theorem to the pressure differential on the R.H.S. of Equation (5.48),

$$\boxed{\iint_{\Omega_e} N_i \frac{\partial U}{\partial t}\,dxdy = \iint_{\Omega_e} P\left(\frac{\partial N_i}{\partial x}\right)dxdy + \iint_{\Omega_e} N_i\left(-\frac{\eta}{\rho K_x}\cdot U\right)dxdy - \int_{\Gamma_e} N_i P^e n_x \, d\Gamma} \qquad (5.\,49)$$

Substituting equation (5.9) into equation (5.49),

$$\left[\iint_{\Omega_e} N_i N_j\,dxdy\right]\left\{\frac{\partial \dot P}{\partial t}\right\} = \left[\iint_{\Omega_e} N_j \frac{\partial N_i}{\partial x}\,dxdy\right]\{\dot P\} + \left[\iint_{\Omega_e} -\frac{\eta}{\rho K_x}N_i N_j\,dxdy\right]\{\dot U\}$$
$$- \int_{\Gamma_e} N_i P^e n_x \, d\Gamma \qquad (5.\,50)$$

Substituting the temporal interpolation formulae of equations (5.11) and (5.12), the final temporal and final discretised form of Darcy equation is developed. Similar to the Stokes equation, the discretised Darcy equations for porous flow dynamics are expressed in matrix form as,

$$\begin{bmatrix} D_{ij}^{11} & D_{ij}^{12} & D_{ij}^{13} \\ D_{ij}^{21} & D_{ij}^{22} & D_{ij}^{23} \\ D_{ij}^{31} & D_{ij}^{32} & D_{ij}^{33} \end{bmatrix} \begin{Bmatrix} U_j \\ V_j \\ P_j \end{Bmatrix}^{n+1} = \begin{bmatrix} T_{ij}^{11} & T_{ij}^{12} & T_{ij}^{13} \\ T_{ij}^{21} & T_{ij}^{22} & T_{ij}^{23} \\ T_{ij}^{31} & T_{ij}^{32} & T_{ij}^{33} \end{bmatrix} \begin{Bmatrix} U_j \\ V_j \\ P_j \end{Bmatrix}^{n} + \begin{Bmatrix} E_j^I \\ E_j^I \\ E_j^I \end{Bmatrix}^{n+1} + \begin{Bmatrix} F_j^I \\ F_j^I \\ F_j^I \end{Bmatrix}^{n} \tag{5.51}$$

where,

$$D_{ij}^{11} = \iint\limits_{\Omega_e} \left[N_i N_j + \frac{\theta \Delta t}{\rho} \left(\frac{\eta}{K_x} \cdot N_i N_j \right) \right] dxdy \tag{5.52}$$

$$D_{ij}^{12} = 0 \tag{5.53}$$

$$D_{ij}^{13} = \iint\limits_{\Omega_e} \left[-\theta \Delta t \, N_j \frac{\partial N_i}{\partial x} \right] dxdy \tag{5.54}$$

$$D_{ij}^{21} = 0 \tag{5.55}$$

$$D_{ij}^{22} = \iint\limits_{\Omega_e} \left[N_i N_j + \frac{\theta \Delta t}{\rho} \left(\frac{\eta}{K_y} \cdot N_i N_j \right) \right] dxdy \tag{5.56}$$

$$D_{ij}^{23} = \iint\limits_{\Omega_e} \left[-\theta \Delta t \, N_j \frac{\partial N_i}{\partial y} \right] dxdy \tag{5.57}$$

$$T_{ij}^{11} = \iint\limits_{\Omega_e} \left[N_i N_j - (1-\theta)\frac{\Delta t}{\rho} \left(\frac{\eta}{K_x} \cdot N_i N_j \right) \right] dxdy \tag{5.58}$$

$$T_{ij}^{12} = 0 \tag{5.59}$$

$$T_{ij}^{13} = \iint\limits_{\Omega_e} \left[(1-\theta)\Delta t \, N_j \frac{\partial N_i}{\partial x} \right] dxdy \tag{5.60}$$

$$T_{ij}^{21} = 0 \tag{5.61}$$

$$T_{ij}^{22} = \iint\limits_{\Omega_e} \left[N_i N_j - (1-\theta)\frac{\Delta t}{\rho} \left(\frac{\eta}{K_y} \cdot N_i N_j \right) \right] dxdy \tag{5.62}$$

$$T_{ij}^{23} = \iint\limits_{\Omega_e} \left[(1-\theta)\Delta t \, N_j \frac{\partial N_i}{\partial y} \right] dxdy \tag{5.63}$$

The components in the third row of both the stiffness matrices **[D]** and **[T]** correspond to the terms related to the continuity equations as mentioned in equations **(5.28)-(5.30)** and equations **(5.37)-(5.39)**.

The components of the load vectors **[E]** and **[F]** are represented as,

$$E_j^1 = \int_{\Gamma_e} -\theta \Delta t \, N_i (P)^e \, n_x \, d\Gamma_e \qquad (5.64)$$

$$E_j^2 = \int_{\Gamma_e} -\theta \Delta t \, N_i (P)^e \, n_y \, d\Gamma \qquad (5.65)$$

$$E_j^3 = 0 \qquad (5.66)$$

$$F_j^1 = \int_{\Gamma_e} -(1-\theta)\Delta t \, N_i (P)^e \, n_x \, d\Gamma \qquad (5.67)$$

$$F_j^2 = \int_{\Gamma_e} -(1-\theta)\Delta t \, N_i (P)^e \, n_y \, d\Gamma \qquad (5.68)$$

$$F_j^3 = 0 \qquad (5.69)$$

The solution of constitutive equations is obtained independently.

5.1.1.2   Temporal discretisation by Taylor-Galerkin method

The described θ-time stepping scheme may result into spurious oscillation into results in some simple problems since it is only first degree accurate. To enhance the stability of solutions, a higher order time stepping schemes such as second-ordered Taylor-Galerkin scheme have been testified for a wide range of problems. The Taylor-Galerkin method relies on the approximation of temporal derivatives by Taylor-series expansion.

The Taylor-series expansion of the field unknowns at a time level equal to $n+\theta\Delta t$ for $0 \leq \theta \leq 1$,

$$\begin{cases} \dfrac{\Delta U}{\Delta t} = \dfrac{U|_{n+1} - U|_n}{\Delta t} = \dfrac{\partial U}{\partial t}\bigg|_{n+\theta\Delta t} + \dfrac{1}{2}\theta\Delta t \dfrac{\partial^2 U}{\partial t^2}\bigg|_{n+\theta\Delta t} \\[2ex] \dfrac{\Delta V}{\Delta t} = \dfrac{V|_{n+1} - V|_n}{\Delta t} = \dfrac{\partial V}{\partial t}\bigg|_{n+\theta\Delta t} + \dfrac{1}{2}\theta\Delta t \dfrac{\partial^2 V}{\partial t^2}\bigg|_{n+\theta\Delta t} \\[2ex] \dfrac{\Delta P}{\Delta t} = \dfrac{P|_{n+1} - P|_n}{\Delta t} = \dfrac{\partial P}{\partial t}\bigg|_{n+\theta\Delta t} + \dfrac{1}{2}\theta\Delta t \dfrac{\partial^2 P}{\partial t^2}\bigg|_{n+\theta\Delta t} \end{cases} \qquad (5.70)$$

5.1.1.2.1   Free flow regime

The first order temporal derivatives of field variables are obtained from the governing equations and the second-order differentials are obtained by the successive differentials of these first-order derivatives as,

$$
\begin{aligned}
\frac{\partial^2 P}{\partial t^2}\bigg|_{n+\theta\Delta t} &= \frac{\partial}{\partial t}\left(\frac{\partial P}{\partial t}\right)\bigg|_{n+\theta\Delta t} = \frac{\partial}{\partial t}\left[-c^2\left(\frac{\partial U}{\partial x}+\frac{\partial V}{\partial y}\right)\right]\bigg|_{n+\theta\Delta t} \\[2mm]
&= -c2\left[\frac{\partial}{\partial x}\left(\frac{\partial U}{\partial t}\right)+\frac{\partial}{\partial y}\left(\frac{\partial V}{\partial t}\right)\right]\bigg|_{n+\theta\Delta t} \\[2mm]
&= c^2\frac{\partial}{\partial x}\left\{\frac{\partial P}{\partial x}-\left[\frac{\partial}{\partial x}\left(2\eta\frac{\partial U}{\partial x}\right)+\frac{\partial}{\partial y}\left(\eta\frac{\partial U}{\partial y}+\eta\frac{\partial V}{\partial x}\right)\right]\right\}\bigg|_{\eta+\theta\Delta t} \\[2mm]
&+ c^2\frac{\partial}{\partial y}\left\{\frac{\partial P}{\partial y}-\left[\frac{\partial}{\partial y}\left(2\eta\frac{\partial U}{\partial y}\right)+\frac{\partial}{\partial x}\left(\eta\frac{\partial U}{\partial y}+\eta\frac{\partial V}{\partial x}\right)\right]\right\}\bigg|_{\eta+\theta\Delta t}
\end{aligned}
\tag{5.71}
$$

Similarly,

$$
\begin{aligned}
\frac{\partial^2 U}{\partial t^2}\bigg|_{n+\theta\Delta t} &= \frac{\partial}{\partial t}\left(\frac{\partial U}{\partial t}\right)\bigg|_{n+\theta\Delta t} \\[2mm]
&= -\frac{\partial}{\partial t}\left(\frac{\partial P}{\partial x}\right)\bigg|_{n+\theta\Delta t} + \frac{\partial}{\partial t}\left\{\frac{\partial}{\partial x}\left(2\eta\frac{\partial U}{\partial x}\right)+\frac{\partial}{\partial y}\left[\eta\left(\frac{\partial U}{\partial y}+\frac{\partial V}{\partial x}\right)\right]\right\}\bigg|_{n+\theta\Delta t} \\[2mm]
&= -\frac{\partial}{\partial x}\left(\frac{\partial P}{\partial t}\right)\bigg|_{n+\theta\Delta t} + \frac{\partial}{\partial t}\left\{\frac{\partial}{\partial x}\left(2\eta\frac{\partial U}{\partial x}\right)+\frac{\partial}{\partial y}\left[\eta\left(\frac{\partial U}{\partial y}+\frac{\partial V}{\partial x}\right)\right]\right\}\bigg|_{n+\theta\Delta t} \\[2mm]
&= c^2\frac{\partial}{\partial x}\left(\frac{\partial U}{\partial x}+\frac{\partial V}{\partial y}\right)\bigg|_{n+\theta\Delta t} + \frac{\partial}{\partial t}\left\{\frac{\partial}{\partial x}\left(2\eta\frac{\partial U}{\partial x}\right)+\frac{\partial}{\partial y}\left[\eta\left(\frac{\partial U}{\partial y}+\frac{\partial V}{\partial x}\right)\right]\right\}\bigg|_{n+\theta\Delta t}
\end{aligned}
\tag{5.72}
$$

The third order differentials of velocity in equations (5.71) and (5.72) arising from discretisation of viscous stress components are omitted to avoid numerical complicacy.

After substituting the first-order and second-order derivatives of velocity and pressure in equation (5.70), final forms of the working equations are obtained by spatial discretisations. Within two time intervals the variables at any point are approximated by θ-interpolation method as given in equation (5.12). The final working equations of the scheme can be represented as,

$$
\begin{bmatrix} M_{ij}^{11} & M_{ij}^{12} & M_{ij}^{13} \\ M_{ij}^{21} & M_{ij}^{22} & M_{ij}^{23} \\ M_{ij}^{31} & M_{ij}^{32} & M_{ij}^{33} \end{bmatrix} \begin{Bmatrix} U_j \\ V_j \\ P_j \end{Bmatrix}^{n+1} = \begin{bmatrix} S_{ij}^{11} & S_{ij}^{12} & S_{ij}^{13} \\ S_{ij}^{21} & S_{ij}^{22} & S_{ij}^{23} \\ S_{ij}^{31} & S_{ij}^{32} & S_{ij}^{33} \end{bmatrix} \begin{Bmatrix} U_j \\ V_j \\ P_j \end{Bmatrix}^{n} + \begin{Bmatrix} C_j^1 \\ C_j^2 \\ C_j^3 \end{Bmatrix}^{n} + \begin{Bmatrix} B_j^1 \\ B_j^2 \\ B_j^3 \end{Bmatrix}^{n+\theta\Delta t} \tag{5.73}
$$

where,

$$
M_{ij}^{11} = \iint\limits_{\Omega_e} \left[N_i N_j + \theta\Delta t \frac{\eta}{\rho} \left(2\frac{\partial N_i}{\partial x}\frac{\partial N_j}{\partial x} + \frac{\partial N_i}{\partial y}\frac{\partial N_j}{\partial y} \right) + \frac{1}{2}\theta(\Delta t)^2 c^2 \frac{\partial N_i}{\partial x}\frac{\partial N_j}{\partial x} \right] dxdy \tag{5.74}
$$

$$
M_{ij}^{12} = \iint\limits_{\Omega_e} \left[\frac{\eta}{\rho}\theta\Delta t \frac{\partial N_i}{\partial y}\frac{\partial N_j}{\partial x} + \frac{1}{2}\theta(\Delta t)^2 c^2 \frac{\partial N_i}{\partial x}\frac{\partial N_j}{\partial y} \right] dxdy \tag{5.75}
$$

$$
M_{ij}^{13} = \iint\limits_{\Omega_e} -\theta\Delta t \frac{\partial N_i}{\partial x} N_j \; dxdy \tag{5.76}
$$

$$
M_{ij}^{21} = \iint\limits_{\Omega_e} \left[\frac{\eta}{\rho}\theta\Delta t \frac{\partial N_i}{\partial x}\frac{\partial N_j}{\partial y} + \frac{1}{2}\theta(\Delta t)^2 c^2 \frac{\partial N_i}{\partial y}\frac{\partial N_j}{\partial x} \right] dxdy \tag{5.77}
$$

$$
M_{ij}^{22} = \iint\limits_{\Omega_e} \left[N_i N_j + \theta\Delta t \frac{\eta}{\rho} \left(2\frac{\partial N_i}{\partial y}\frac{\partial N_j}{\partial y} + \frac{\partial N_i}{\partial x}\frac{\partial N_j}{\partial x} \right) + \frac{1}{2}\theta(\Delta t)^2 c^2 \frac{\partial N_i}{\partial y}\frac{\partial N_j}{\partial y} \right] dxdy \tag{5.78}
$$

$$
M_{ij}^{23} = \iint\limits_{\Omega_e} -\theta\Delta t \frac{\partial N_i}{\partial y} N_j \; dxdy \tag{5.79}
$$

$$
M_{ij}^{31} = \iint\limits_{\Omega_e} -\theta\Delta t N_i \frac{\partial N_j}{\partial x} \; dxdy \tag{5.80}
$$

$$
M_{ij}^{32} = \iint\limits_{\Omega_e} -\theta\Delta t N_i \frac{\partial N_j}{\partial y} \; dxdy \tag{5.81}
$$

$$
M_{ij}^{33} = \iint\limits_{\Omega_e} \left[-\frac{1}{c^2} N_i N_j + \frac{1}{2}\theta(\Delta t)^2 c^2 \left(\frac{\partial N_i}{\partial x}\frac{\partial N_j}{\partial x} + \frac{\partial N_i}{\partial y}\frac{\partial N_j}{\partial y} \right) \right] dxdy \tag{5.82}
$$

$$
S_{ij}^{11} = \iint\limits_{\Omega_e} \begin{bmatrix} N_i N_j - (1-\theta)\Delta t \frac{\eta}{\rho} \left(2\frac{\partial N_i}{\partial x}\frac{\partial N_j}{\partial x} + \frac{\partial N_i}{\partial y}\frac{\partial N_j}{\partial y} \right) \\ -\frac{1}{2}(1-\theta)(\Delta t)^2 c^2 \frac{\partial N_i}{\partial x}\frac{\partial N_j}{\partial x} \end{bmatrix} dxdy \tag{5.83}
$$

$$
S_{ij}^{12} = \iint\limits_{\Omega_e} -\left[\frac{\eta}{\rho}(1-\theta)\Delta t \frac{\partial N_i}{\partial y}\frac{\partial N_j}{\partial x} + \frac{1}{2}(1-\theta)(\Delta t)^2 c^2 \frac{\partial N_i}{\partial x}\frac{\partial N_j}{\partial y} \right] dxdy \tag{5.84}
$$

$$
S_{ij}^{13} = \iint\limits_{\Omega_e} -\theta\Delta t \frac{\partial N_i}{\partial x} N_j \; dxdy \tag{5.85}
$$

$$S_{ij}^{21} = \iint\limits_{\Omega_e} -\left[\frac{\eta}{\rho}(1-\theta)\Delta t \frac{\partial N_i}{\partial x}\frac{\partial N_j}{\partial y} + \frac{1}{2}(1-\theta)(\Delta t)^2 c^2 \frac{\partial N_i}{\partial y}\frac{\partial N_j}{\partial x} \right] dxdy \qquad (5.86)$$

$$S_{ij}^{22} = \iint\limits_{\Omega_e} \left[\begin{array}{c} N_i N_j - (1-\theta)\Delta t \frac{\eta}{\rho}\left(2\frac{\partial N_i}{\partial y}\frac{\partial N_j}{\partial y} + \frac{\partial N_i}{\partial x}\frac{\partial N_j}{\partial x} \right) \\ -\frac{1}{2}(1-\theta)(\Delta t)^2 c^2 \frac{\partial N_i}{\partial y}\frac{\partial N_j}{\partial y} \end{array} \right] dxdy \qquad (5.87)$$

$$S_{ij}^{23} = \iint\limits_{\Omega_e} (1-\theta)\Delta t \frac{\partial N_i}{\partial y} N_j \ dxdy \qquad (5.88)$$

Error! Objects cannot be created from editing field codes.
$$(5.89)$$

$$S_{ij}^{32} = \iint\limits_{\Omega_e} (1-\theta)\Delta t N_i \frac{\partial N_j}{\partial y} \ dxdy \qquad (5.90)$$

$$S_{ij}^{33} = \iint\limits_{\Omega_e} \left[-\frac{1}{c^2} N_i N_j - \frac{1}{2}(1-\theta)(\Delta t)^2 c^2 \left(\frac{\partial N_i}{\partial x}\frac{\partial N_j}{\partial x} + \frac{\partial N_i}{\partial y}\frac{\partial N_j}{\partial y} \right) \right] dxdy \qquad (5.91)$$

$$C_j^1 = \int\limits_{\Gamma_e} N_i \left[\frac{1}{2}(1-\theta)(\Delta t)^2 c^2 \frac{\partial U^e}{\partial x} + \frac{1}{2}(1-\theta)(\Delta t)^2 c^2 \frac{\partial V^e}{\partial y} - (1-\theta)\Delta t P^e \right] n_x \ d\Gamma$$

$$+ \int\limits_{\Gamma_e} (1-\theta)\Delta t N_i \frac{\eta}{\rho}\left[2\frac{\partial U^e}{\partial x} n_x + \left(\frac{\partial U^e}{\partial y} + \frac{\partial V^e}{\partial x} \right) n_y \right] d\Gamma \qquad (5.92)$$

$$C_j^2 = \int\limits_{\Gamma_e} N_i \left[\frac{1}{2}(1-\theta)(\Delta t)^2 c^2 \frac{\partial U^e}{\partial x} + \frac{1}{2}(1-\theta)(\Delta t)^2 c^2 \frac{\partial V^e}{\partial y} - (1-\theta)\Delta t P^e \right] n_y \ d\Gamma$$

$$+ \int\limits_{\Gamma_e} (1-\theta)\Delta t N_i \frac{\eta}{\rho}\left[2\frac{\partial U^e}{\partial x} n_x + \left(\frac{\partial U^e}{\partial y} + \frac{\partial V^e}{\partial x} \right) n_y \right] d\Gamma \qquad (5.93)$$

$$C_j^3 = \int\limits_{\Gamma_e} \frac{1}{2}(1-\theta)(\Delta t)^2 N_i \left(\frac{\partial P^e}{\partial x} n_x + \frac{\partial P^e}{\partial y} n_y \right) d\Gamma \qquad (5.94)$$

$$B_j^1 = \int\limits_{\Gamma_e} N_i \left[\frac{1}{2}\theta(\Delta t)^2 c^2 \frac{\partial U^e}{\partial x} + \frac{1}{2}\theta(\Delta t)^2 c^2 \frac{\partial V^e}{\partial y} - \theta\Delta t P^e \right] n_x \ d\Gamma$$

$$+ \int\limits_{\Gamma_e} \theta\Delta t N_i \frac{\eta}{\rho}\left[2\frac{\partial U^e}{\partial x} n_x + \left(\frac{\partial U^e}{\partial y} + \frac{\partial V^e}{\partial x} \right) n_y \right] d\Gamma \qquad (5.95)$$

$$B_j^2 = \int\limits_{\Gamma_e} N_i \left[\frac{1}{2}\theta(\Delta t)^2 c^2 \frac{\partial U^e}{\partial x} + \frac{1}{2}\theta(\Delta t)^2 c^2 \frac{\partial V^e}{\partial y} - \theta\Delta t P^e \right] n_y \, d\Gamma$$

$$+ \int\limits_{\Gamma_e} \theta\,\Delta t\, N_i \frac{\eta}{\rho} \left[2\frac{\partial V^e}{\partial y} n_y + \left(\frac{\partial U^e}{\partial y} + \frac{\partial V^e}{\partial x} \right) n_x \right] d\Gamma \qquad \text{(5. 96)}$$

$$B_j^3 = \int\limits_{\Gamma_e} -\frac{1}{2}\theta(\Delta t)^2 N_i \left(\frac{\partial P^e}{\partial x} n_x + \frac{\partial P^e}{\partial y} n_y \right) d\Gamma \qquad \text{(5. 97)}$$

5.1.1.2.2   Porous flow regime

The first order temporal derivatives of field variables are obtained from the governing equations and the second-order differentials are obtained by the successive differentials of these first-order derivatives as,

$$\left.\frac{\partial^2 P}{\partial t^2}\right|_{n+\theta\Delta t} = \left.\frac{\partial}{\partial t}\left(\frac{\partial P}{\partial t} \right)\right|_{n+\theta\Delta t}$$

$$= -c^2 \left.\frac{\partial}{\partial t}\left(\frac{\partial U}{\partial x} + \frac{\partial V}{\partial y} \right)\right|_{n+\theta\Delta t} = -c^2 \left.\frac{\partial}{\partial x}\left(\frac{\partial U}{\partial t} \right)\right|_{n+\theta\Delta t} - c^2 \left.\frac{\partial}{\partial y}\left(\frac{\partial V}{\partial t} \right)\right|_{n+\theta\Delta t} \qquad \text{(5. 98)}$$

$$= c^2 \left.\left(\frac{\eta}{K_x\rho} \cdot \frac{\partial U}{\partial x} + \frac{\eta}{K_y\rho} \cdot \frac{\partial V}{\partial y} + \frac{\partial^2 P}{\partial x^2} + \frac{\partial^2 P}{\partial y^2} \right)\right|_{n+\theta\Delta t}$$

Similarly,

$$\left.\frac{\partial^2 U}{\partial t^2}\right|_{n+\theta\Delta t} = \left.\frac{\partial}{\partial t}\left(\frac{\partial U}{\partial t} \right)\right|_{n+\theta\Delta t} = -\left.\frac{\partial}{\partial t}\left(\frac{\eta}{K_x\rho}U + \frac{\partial P}{\partial x} \right)\right|_{n+\theta\Delta t} \qquad \text{(5. 99)}$$

$$= \left.\left[\frac{\eta^2}{K_x^2\rho^2} \cdot U + \frac{\eta}{K_x\rho} \cdot \frac{\partial P}{\partial x} + c^2\left(\frac{\partial U}{\partial x} + \frac{\partial V}{\partial y} \right) \right]\right|_{n+\theta\Delta t}$$

And

$$\left.\frac{\partial^2 V}{\partial t^2}\right|_{n+\theta\Delta t} = \left.\frac{\partial}{\partial t}\left(\frac{\partial V}{\partial t} \right)\right|_{n+\theta\Delta t} = -\left.\frac{\partial}{\partial t}\left(\frac{\eta}{K_x\rho}U + \frac{\partial P}{\partial x} \right)\right|_{n+\theta\Delta t} \qquad \text{(5. 100)}$$

$$= \left.\left[\frac{\eta^2}{K_x^2\rho^2} \cdot U + \frac{\eta}{K_x\rho} \cdot \frac{\partial P}{\partial x} + c^2\left(\frac{\partial U}{\partial x} + \frac{\partial V}{\partial y} \right) \right]\right|_{n+\theta\Delta t}$$

After substituting the first-order and second-order derivatives of velocity and pressure in equation (5.70), final form of the working equations are obtained by spatial discretisations. Within two time intervals the variables at any point are

approximated by θ-interpolation method as given in equation **(5.12)**. The final working equations of the scheme can be represented as,

$$\begin{bmatrix} M_{ij}^{11} & M_{ij}^{12} & M_{ij}^{13} \\ M_{ij}^{21} & M_{ij}^{22} & M_{ij}^{23} \\ M_{ij}^{31} & M_{ij}^{32} & M_{ij}^{33} \end{bmatrix} \begin{Bmatrix} U_j \\ V_j \\ P_j \end{Bmatrix}^{n+1} = \begin{bmatrix} S_{ij}^{11} & S_{ij}^{12} & S_{ij}^{13} \\ S_{ij}^{21} & S_{ij}^{22} & S_{ij}^{23} \\ S_{ij}^{31} & S_{ij}^{32} & S_{ij}^{33} \end{bmatrix} \begin{Bmatrix} U_j \\ V_j \\ P_j \end{Bmatrix}^{n} + \begin{Bmatrix} C_j^1 \\ C_j^2 \\ C_j^3 \end{Bmatrix}^{n} + \begin{Bmatrix} B_j^1 \\ B_j^2 \\ B_j^3 \end{Bmatrix}^{n+\theta\Delta t} \tag{5.101}$$

Where,

$$M_{ij}^{11} = \iint_{\Omega_e} \left\{ N_i N_j + \theta\Delta t \left[\frac{\eta}{K_x \rho} N_i N_j + \frac{1}{2}\Delta t \left(c^2 \frac{\partial N_j}{\partial x} \frac{\partial N_i}{\partial x} - \frac{\eta^2}{K_x^2 \rho^2} N_i N_j \right) \right] \right\} dx\,dy \tag{5.102}$$

$$M_{ij}^{12} = \iint_{\Omega_e} \frac{1}{2}\theta(\Delta t)^2 c^2 \frac{\partial N_i}{\partial x} \frac{\partial N_j}{\partial y} dx\,dy \tag{5.103}$$

$$M_{ij}^{13} = \iint_{\Omega_e} N_i \theta\Delta t \left[1 - \frac{1}{2}\Delta t \frac{\eta}{K_x \rho} \right] \frac{\partial N_j}{\partial x} dx\,dy \tag{5.104}$$

$$M_{ij}^{21} = \iint_{\Omega_e} \frac{1}{2}\theta(\Delta t)^2 c^2 \frac{\partial N_i}{\partial y} \frac{\partial N_j}{\partial x} dx\,dy \tag{5.105}$$

$$M_{ij}^{22} = \iint_{\Omega_e} \left\{ N_i N_j + \theta\Delta t \left[\frac{\eta}{K_y \rho} N_i N_j + \frac{1}{2}\Delta t \left(c^2 \frac{\partial N_j}{\partial y} \frac{\partial N_i}{\partial y} - \frac{\eta^2}{K_y^2 \rho^2} N_i N_j \right) \right] \right\} dx\,dy \tag{5.106}$$

$$M_{ij}^{23} = \iint_{\Omega_e} N_i \theta\Delta t \left[1 - \frac{1}{2}\Delta t \frac{\eta}{K_y \rho} \right] \frac{\partial N_j}{\partial y} dx\,dy \tag{5.107}$$

$$M_{ij}^{31} = \iint_{\Omega_e} N_i \theta\Delta t\, c^2 \left(1 - \frac{1}{2}\Delta t \frac{\eta}{K_x \rho} \right) \frac{\partial N_j}{\partial x} dx\,dy \tag{5.108}$$

$$M_{ij}^{32} = \iint_{\Omega_e} N_i \theta\Delta t\, c^2 \left(1 - \frac{1}{2}\Delta t \frac{\eta}{K_y \rho} \right) \frac{\partial N_j}{\partial y} dx\,dy \tag{5.109}$$

$$M_{ij}^{33} = \iint_{\Omega_e} \left\{ N_i N_j + \frac{1}{2}\theta(\Delta t)^2 \left(\frac{\partial N_i}{\partial x} \frac{\partial N_j}{\partial x} + \frac{\partial N_i}{\partial y} \frac{\partial N_j}{\partial y} \right) \right\} dx\,dy \tag{5.110}$$

$$D_{ij}^{11} = \iint_{\Omega_e} \left\{ N_i N_j - (1-\theta)\Delta t \left[\frac{\eta}{K_x \rho} N_i N_j + \frac{1}{2}\Delta t \left(c^2 \frac{\partial N_j}{\partial x} \frac{\partial N_i}{\partial x} - \frac{\eta^2}{K_x^2 \rho^2} N_i N_j \right) \right] \right\} dx\,dy \tag{5.111}$$

$$D_{ij}^{12} = \iint_{\Omega_e} -\frac{1}{2}(1-\theta)(\Delta t)^2 c^2 \frac{\partial N_i}{\partial x}\frac{\partial N_j}{\partial y}\, dx\, dy \qquad (5.\,112)$$

$$D_{ij}^{13} = \iint_{\Omega_e} -N_i(1-\theta)\Delta t\left[1-\frac{1}{2}\Delta t\frac{\eta}{K_x\rho}\right]\frac{\partial N_j}{\partial x}\, dx\, dy \qquad (5.\,113)$$

$$D_{ij}^{21} = \iint_{\Omega_e} -\frac{1}{2}(1-\theta)(\Delta t)^2 c^2 \frac{\partial N_i}{\partial y}\frac{\partial N_j}{\partial x}\, dx\, dy \qquad (5.\,114)$$

$$D_{ij}^{22} = \iint_{\Omega_e}\left\{N_i N_j - (1-\theta)\Delta t\left[\begin{array}{l}\dfrac{\eta}{K_y\rho}N_i N_j \\[2mm] +\dfrac{1}{2}\Delta t\left(c^2\dfrac{\partial N_j}{\partial y}\dfrac{\partial N_i}{\partial y} - \dfrac{\eta^2}{K_y^{\,2}\rho^2}N_i N_j\right)\end{array}\right]\right\}dx\, dy \qquad (5.\,115)$$

$$D_{ij}^{23} = \iint_{\Omega_e} -N_i(1-\theta)\Delta t\left[1-\frac{1}{2}\Delta t\frac{\eta}{Ky\rho}\right]\frac{\partial N_j}{\partial y}\, dx\, dy \qquad (5.\,116)$$

$$D_{ij}^{31} = \iint_{\Omega_e} -N_i(1-\theta)\Delta t\, c^2\left(1-\frac{1}{2}\Delta t\frac{\eta}{K_y\rho}\right)\frac{\partial N_j}{\partial y}\, dx\, dy \qquad (5.\,117)$$

$$D_{ij}^{32} = \iint_{\Omega_e} -N_i(1-\theta)\Delta t\, c^2\left(1-\frac{1}{2}\Delta t\frac{\eta}{K_y\rho}\right)\frac{\partial N_j}{\partial y}\, dx\, dy \qquad (5.\,118)$$

$$D_{ij}^{33} = \iint_{\Omega_e}\left\{N_i N_j - \frac{1}{2}(1-\theta)(\Delta t)^2\left(\frac{\partial N_i}{\partial x}\frac{\partial N_j}{\partial x} + \frac{\partial N_i}{\partial y}\frac{\partial N_j}{\partial y}\right)\right\}dx\, dy \qquad (5.\,119)$$

$$E_j^1 = \int_{\Gamma_e}\frac{1}{2}(1-\theta)(\Delta t)^2 c^2 N_i\left(\frac{\partial U^e}{\partial x} + \frac{\partial V^e}{\partial y}\right)n_x\, d\Gamma \qquad (5.\,120)$$

$$E_j^2 = \int_{\Gamma_e}\frac{1}{2}(1-\theta)(\Delta t)^2 c^2 N_i\left(\frac{\partial U^e}{\partial x} + \frac{\partial V^e}{\partial y}\right)n_y\, d\Gamma \qquad (5.\,121)$$

$$E_j^3 = \int_{\Gamma_e}\frac{1}{2}(1-\theta)(\Delta t)^2 c^2\left[N_i\left(\frac{\partial U^e}{\partial x}n_x + \frac{\partial V^e}{\partial y}n_y\right)\right]d\Gamma \qquad (5.\,122)$$

$$F_j^1 = \int_{\Gamma_e}\frac{1}{2}\theta(\Delta t)^2 c^2 N_i\left(\frac{\partial U^e}{\partial x} + \frac{\partial V^e}{\partial y}\right)n_x\, d\Gamma \qquad (5.\,123)$$

$$F_j^2 = \int_{\Gamma_e}\frac{1}{2}\theta(\Delta t)^2 c^2 N_i\left(\frac{\partial U^e}{\partial x} + \frac{\partial V^e}{\partial y}\right)n_y\, d\Gamma \qquad (5.\,124)$$

$$F_j^3 = \int_{\Gamma_e}\frac{1}{2}\theta(\Delta t)^2 c^2\left[N_i\left(\frac{\partial U^e}{\partial x}n_x + \frac{\partial V^e}{\partial y}n_y\right)\right]d\Gamma \qquad (5.\,125)$$

As the foundation of perturbed continuity scheme is solely lies on use of transient form of the governing equations, the steady state solutions are only obtainable by use of smallest time step values converting the system in pseudo unsteady state.

5.1.2   Taylor-Hood scheme: Cartesian coordinate system

The Taylor-Hood scheme is based on the mixed form of interpolation functions. Taylor-Hood elements are the lowest member of the bubble element family in which velocity is approximated by second order bi-quadratic interpolations whereas the pressure is approximated by first order bilinear interpolation.

5.1.2.1   Free flow regime

In Taylor-Hood scheme, the governing equations take their steady state original form as explained in chapter 3. For better understanding of the ongoing derivations, these equations are reproduced here as,

$$-\frac{\partial p}{\partial x}+\frac{\partial}{\partial x}\left(2\eta\frac{\partial u_x}{\partial x}\right)+\frac{\partial}{\partial y}\left[\eta\left(\frac{\partial u_x}{\partial y}+\frac{\partial u_y}{\partial x}\right)\right]=0 \qquad (5.126)$$

$$-\frac{\partial p}{\partial y}+\frac{\partial}{\partial y}\left(2\eta\frac{\partial u_y}{\partial y}\right)+\frac{\partial}{\partial x}\left[\eta\left(\frac{\partial u_y}{\partial x}+\frac{\partial u_x}{\partial y}\right)\right]=0 \qquad (5.127)$$

and;

$$\frac{\partial u_x}{\partial x}+\frac{\partial u_y}{\partial y}=0 \qquad (5.128)$$

The primitive field variables u_x, u_y and p are approximated over elemental domain as,

$$\begin{cases} u_x \approx \dot{u}_x = \sum_{i=1}^{n} N_{v_i}\dot{u}_{x_i} \\[2ex] u_y \approx \dot{u}_y = \sum_{i=1}^{n} N_{v_i}\dot{u}_{y_i} \\[2ex] p \approx \dot{p} = \sum_{i=1}^{m} N_{p_i}\dot{p} \end{cases} \qquad (5.129)$$

where, n and m are the number of nodes for interpolation of velocity ($m < n$) and pressures respectively and N_v and N_p are their respective shape or interpolation functions.

The Galerkin weighted residual statement for the system of Stokes equation can be described as,

$$\iint_{\Omega_e} N_{v_i} \left[\begin{array}{l} \left(-\dfrac{\partial \sum\limits_{l=1}^{m} N_{p_l} \dot{p}_l}{\partial x} + \dfrac{\partial}{\partial x}\left(2\eta \dfrac{\partial \sum\limits_{j=1}^{n} N_{v_j} \dot{u}_{x_j}}{\partial x} \right) \right. \\ \\ \left. + \dfrac{\partial}{\partial y}\left[\eta \left(\dfrac{\partial \sum\limits_{j=1}^{n} N_{v_j} \dot{u}_{x_j}}{\partial y} + \dfrac{\partial \sum\limits_{j=1}^{n} N_{v_j} \dot{u}_{y_j}}{\partial x} \right) \right] \right) \end{array} \right] dxdy = 0 \qquad (5.130)$$

$$\iint_{\Omega_e} N_{v_i} \left[\begin{array}{l} \left(-\dfrac{\partial \sum\limits_{l=1}^{m} N_{p_l} \dot{p}_l}{\partial y} + \dfrac{\partial}{\partial y}\left(2\eta \dfrac{\partial \sum\limits_{j=1}^{n} N_{v_j} \dot{u}_{y_j}}{\partial y} \right) \right. \\ \\ \left. + \dfrac{\partial}{\partial x}\left[\eta \left(\dfrac{\partial \sum\limits_{j=1}^{n} N_{v_j} \dot{u}_{x_j}}{\partial y} + \dfrac{\partial \sum\limits_{j=1}^{n} N_{v_j} \dot{u}_{y_j}}{\partial x} \right) \right] \right) \end{array} \right] dxdy = 0 \qquad (5.131)$$

$$\iint_{\Omega_e} - N_{p_i} \left(\dfrac{\partial \sum\limits_{j=1}^{n} N_{v_j} \dot{u}_{x_j}}{\partial x} + \dfrac{\partial \sum\limits_{j=1}^{n} N_{v_j} \dot{u}_{y_j}}{\partial y} \right) dxdy = 0 \qquad (5.132)$$

The signs of the terms in the parent continuity equations are inverted to maintain symmetry in the final stiffness matrix of the equations. The second order velocity differentials and first order pressure differential terms are weakened by the means of Green's theorem to comply the inter-elemental continuity of C^0-continuous elements. The assembled system of working equations are conventionally expressed in matrix form as,

$$\begin{bmatrix} S_{ij}^{11} & S_{ij}^{12} & S_{ij}^{13} \\ S_{ij}^{21} & S_{ij}^{22} & S_{ij}^{23} \\ S_{il}^{31} & S_{il}^{32} & S_{il}^{33} \end{bmatrix} \begin{Bmatrix} u_x^j \\ u_y^j \\ p^l \end{Bmatrix} = \begin{Bmatrix} F_j^1 \\ F_j^2 \\ F_l^3 \end{Bmatrix} \qquad (5.133)$$

where,

$$S_{ij}^{11} = \iint\limits_{\Omega_e} \left(2\eta \frac{\partial N_{v_i}}{\partial x} \frac{\partial N_{v_j}}{\partial x} + n \frac{\partial N_{v_i}}{\partial y} \frac{\partial N_{v_j}}{\partial y} \right) dxdy \qquad (5.134)$$

$$S_{ij}^{12} = \iint\limits_{\Omega_e} \left(n \frac{\partial N_{v_i}}{\partial y} \frac{\partial N_{v_j}}{\partial x} \right) dxdy \qquad (5.135)$$

$$S_{ij}^{13} = \iint\limits_{\Omega_e} \left(-N_{p_j} \frac{\partial N_{v_i}}{\partial x} \right) dxdy \qquad (5.136)$$

$$S_{ij}^{21} = \iint\limits_{\Omega_e} \left(n \frac{\partial N_{v_i}}{\partial x} \frac{\partial N_{v_j}}{\partial y} \right) dxdy \qquad (5.137)$$

$$S_{ij}^{22} = \iint\limits_{\Omega_e} \left(2\eta \frac{\partial N_{v_i}}{\partial y} \frac{\partial N_{v_j}}{\partial y} + n \frac{\partial N_{v_i}}{\partial x} \frac{\partial N_{v_j}}{\partial x} \right) dxdy \qquad (5.138)$$

$$S_{ij}^{23} = \iint\limits_{\Omega_e} \left(-N_{pl} \frac{\partial N_{v_i}}{\partial y} \right) dxdy \qquad (5.139)$$

$$S_{il}^{31} = \iint\limits_{\Omega_e} \left(-N_{pl} \frac{\partial N_{v_j}}{\partial x} \right) dxdy \qquad (5.140)$$

$$S_{il}^{32} = \iint\limits_{\Omega_e} \left(-N_{pl} \frac{\partial N_{v_j}}{\partial y} \right) dxdy \qquad (5.141)$$

$$S_{il}^{33} = 0 \qquad (5.142)$$

$$F_j^1 = \int\limits_{\Gamma_e} N_{v_i} \left[\left(p^e - 2\eta \frac{\partial u_x^e}{\partial x} \right) n_x - \eta \left(\frac{\partial u_x^e}{\partial y} + \frac{\partial u_y^e}{\partial x} \right) n_y \right] d\Gamma \qquad (5.143)$$

$$F_j^2 = \int\limits_{\Gamma_e} N_{v_i} \left[\left(p^e - 2\eta \frac{\partial u_y^e}{\partial y} \right) n_y - \eta \left(\frac{\partial u_x^e}{\partial y} + \frac{\partial u_y^e}{\partial x} \right) n_x \right] d\Gamma \qquad (5.144)$$

$$F_l^3 = 0 \qquad (5.145)$$

5.1.2.2   Porous Flow regime

The Darcy equation can be resolved in its Cartesian components as,

$$\frac{\partial p}{\partial x} + \frac{\eta}{K_x} \cdot u_x = 0$$

(5. 146)

$$\frac{\partial p}{\partial y} + \frac{\eta}{K_y} \cdot u_y = 0$$

(5. 147)

Using the mixed form of the interpolation functions shown in equation (5.129), the Galerkin weighted residual statements of the porous flow equations are written as,

$$\iint_{\Omega_e} N_{v_i} \left[\frac{\partial \sum\limits_{l=1}^{m} N_{p_l} \dot{p}_l}{\partial x} + \frac{\eta}{K_x} \cdot \sum\limits_{j=1}^{n} N_{v_j} \dot{u}_{x_j} \right] dxdy = 0$$

(5. 148)

$$\iint_{\Omega_e} N_{v_i} \left[\frac{\partial \sum\limits_{l=1}^{m} N_{p_l} \dot{p}_l}{\partial y} + \frac{\eta}{K_y} \cdot \sum\limits_{j=1}^{n} N_{v_j} \dot{u}_{y_j} \right] dxdy = 0$$

(5. 149)

$$\iint_{\Omega_e} N_{p_l} \left[\frac{\partial \sum\limits_{i=1}^{n} N_{v_j} \dot{u}_{x_j}}{\partial x} + \frac{\partial \sum\limits_{i=1}^{n} N_{v_j} \dot{u}_{y_j}}{\partial y} \right] dxdy = 0$$

(5. 150)

The first order pressure differential terms are reduced by using the Gauss theorem to satisfy the inter-elemental continuity requirement. The final assembly of discretised working equations is expressed in matrix form as,

$$\begin{bmatrix} D_{ij}^{11} & D_{ij}^{12} & D_{ij}^{13} \\ D_{ij}^{21} & D_{ij}^{22} & D_{ij}^{23} \\ D_{il}^{31} & D_{il}^{32} & D_{il}^{33} \end{bmatrix} \begin{Bmatrix} u_x^j \\ u_y^j \\ p^l \end{Bmatrix} = \begin{Bmatrix} F_j^1 \\ F_j^2 \\ F_l^3 \end{Bmatrix}$$

(5. 151)

where,

$$D_{ij}^{11} = \iint_{\Omega_e} \frac{\eta}{K_x} N_{v_i} N_{v_j} \, dxdy$$

(5. 152)

$$D_{ij}^{12} = 0$$

(5. 153)

$$D_{ij}^{13} = \iint_{\Omega_e} - N_{p_l} \frac{\partial N_{v_i}}{\partial x} \, dxdy$$

(5. 154)

$$D_{ij}^{21} = 0 \tag{5.155}$$

$$D_{ij}^{22} = \iint_{\Omega_e} \frac{\eta}{K_y} N_{v_i} N_{v_j} \ dxdy \tag{5.156}$$

$$D_{ij}^{23} = \iint_{\Omega_e} - N_{p_l} \frac{\partial N_{v_i}}{\partial y} \ dxdy \tag{5.157}$$

$$D_{ij}^{31} = \iint_{\Omega_e} \left(N_{p_l} \frac{\partial N_{v_j}}{\partial x} \right) dxdy \tag{5.158}$$

$$D_{ij}^{32} = \iint_{\Omega_e} \left(N_{p_l} \frac{\partial N_{v_j}}{\partial y} \right) dxdy \tag{5.159}$$

$$D_{ij}^{33} = 0 \tag{5.160}$$

$$F_j^1 = \int_{\Gamma_e} N_{v_i} (-p)^e n_x \ d\Gamma \tag{5.161}$$

$$F_j^2 = \int_{\Gamma_e} N_{v_i} (-p)^e n_y \ d\Gamma \tag{5.162}$$

$$F_l^3 = 0 \tag{5.163}$$

5.1.3 Taylor-Hood scheme: Axisymmetric coordinate system

5.1.3.1 Free flow regime

In case of steady incompressible flow, the equation for conservation of momentum in free flow regime i.e. equations (4.27) explained in Chapter 4, take the form as,

$$-\frac{\partial p}{\partial r} + \frac{1}{r}\frac{\partial}{\partial r}\left(r \cdot 2\eta \frac{\partial u_r}{\partial r} \right) - \frac{2\eta}{r}\frac{u_r}{r} + \frac{\partial}{\partial r}\left[\eta\left(\frac{\partial u_z}{\partial r} + \frac{\partial u_r}{\partial z} \right) \right] = 0 \tag{5.164}$$

$$-\frac{\partial p}{\partial z} + \frac{\partial}{\partial z}\left(2\eta \frac{\partial u_z}{\partial z} \right) + \frac{1}{r}\frac{\partial}{\partial r}\left[r\left(\frac{\partial u_z}{\partial r} + \frac{\partial u_r}{\partial z} \right) \right] = 0 \tag{5.165}$$

and the equation of continuity becomes,

$$\frac{\partial u_r}{\partial r} + \frac{u_r}{r} + \frac{\partial u_z}{\partial z} = 0 \tag{5.166}$$

The primitive variables u_r, u_z and p are approximated over elemental domain as,

$$
\begin{cases}
u_r \approx \dot{u}_r = \sum_{i=1}^{n} N_{v_i} \dot{u}_{r_i} \\[2mm]
u_z \approx \dot{u}_z = \sum_{i=1}^{n} N_{v_i} \dot{u}_{z_i} \\[2mm]
p \approx \dot{p} = \sum_{i=1}^{m} N_{p_l} \dot{p}_l
\end{cases}
\tag{5.167}
$$

Taking the weighted residual of these equations and integrating them over the elemental domain,

$$
\iint_{\Omega_e} N_{v_i} \left\{
\begin{array}{l}
-\dfrac{\partial \sum_{l=1}^{m} N_{p_l} \dot{p}_l}{\partial r} + \dfrac{1}{r}\dfrac{\partial}{\partial r}\left(\dfrac{1}{r} \cdot 2\eta \dfrac{\partial \sum_{j=1}^{n} N_{v_j} \dot{u}_{r_j}}{\partial r} \right) \\[4mm]
-\dfrac{2\eta}{r} \dfrac{\sum_{j=1}^{n} N_{v_j} \dot{u}_{r_j}}{r} + \dfrac{\partial}{\partial z}\left[\eta\left(\dfrac{\partial \sum_{j=1}^{n} N_{v_j} \dot{u}_{r_j}}{\partial z} + \dfrac{\partial \sum_{j=1}^{n} N_{v_j} \dot{u}_{z_j}}{\partial r} \right) \right]
\end{array}
\right\} r\, dr\, dz = 0
$$

(5.168)

$$
\iint_{\Omega_e} N_{v_i} \left\{
\begin{array}{l}
-\dfrac{\partial \sum_{l=1}^{m} N_{p_l} \dot{p}_l}{\partial z} + \dfrac{\partial}{\partial z}\left(2\eta \dfrac{\partial \sum_{j=1}^{n} N_{v_j} \dot{u}_{z_j}}{\partial z} \right) \\[4mm]
+\dfrac{1}{r}\dfrac{\partial}{\partial r}\left[\eta\left(\dfrac{\partial \sum_{j=1}^{n} N_{v_j} \dot{u}_{z_j}}{\partial r} + \dfrac{\partial \sum_{j=1}^{n} N_{v_j} \dot{u}_{r_j}}{\partial z} \right) \right]
\end{array}
\right\} r\, dr\, dz = 0
\tag{5.169}
$$

$$
\iint_{\Omega_e} -N_{p_l}\left(\dfrac{\partial \sum_{j=1}^{n} N_{v_j} \dot{u}_{r_j}}{\partial r} + \dfrac{\sum_{j=1}^{n} N_{v_j} \dot{u}_{z_j}}{\partial z} \right) r\, dr\, dz = 0
\tag{5.170}
$$

Applying the Green's theorem, the second order velocity derivatives and first order pressure derivative terms are reduced to the lower order. Followed by algebraic manipulations, the final set of equations are obtained as,

$$
\begin{bmatrix}
AS_{ij}^{11} & AS_{ij}^{12} & AS_{ij}^{13} \\
AS_{ij}^{21} & AS_{ij}^{22} & AS_{ij}^{23} \\
AS_{il}^{31} & AS_{il}^{32} & AS_{ll}^{33}
\end{bmatrix}
\begin{Bmatrix}
u_r^j \\
u_z^j \\
p^l
\end{Bmatrix}
=
\begin{Bmatrix}
F_j^1 \\
F_j^2 \\
F_l^3
\end{Bmatrix}
\tag{5.171}
$$

where,

$$AS_{ij}^{11} = \iint\limits_{\Omega_e} \left(2\eta \frac{\partial N_{v_i}}{\partial r}\frac{\partial N_{v_j}}{\partial r} + \frac{2\eta}{r^2} N_{v_i} N_{v_j} + \eta \frac{\partial N_{v_i}}{\partial z}\frac{\partial N_{v_j}}{\partial z} \right) r dr\, dz \tag{5.172}$$

$$AS_{ij}^{12} = \iint\limits_{\Omega_e} \left(\eta \frac{\partial N_{v_i}}{\partial z}\frac{\partial N_{v_j}}{\partial r} \right) r dr\, dz \tag{5.173}$$

$$AS_{ij}^{13} = \iint\limits_{\Omega_e} \left(-N_{p_l} \frac{\partial N_{v_i}}{\partial r} \right) r dr\, dz \tag{5.174}$$

$$AS_{ij}^{21} = \iint\limits_{\Omega_e} \left(\eta \frac{\partial N_{v_i}}{\partial r}\frac{\partial N_{v_j}}{\partial z} \right) r dr\, dz \tag{5.175}$$

$$AS_{ij}^{22} = \iint\limits_{\Omega_e} \left(\eta \frac{\partial N_{v_i}}{\partial r}\frac{\partial N_{v_j}}{\partial r} + 2\eta \frac{\partial N_{v_i}}{\partial z}\frac{\partial N_{v_j}}{\partial z} \right) r dr\, dz \tag{5.176}$$

$$AS_{ij}^{23} = \iint\limits_{\Omega_e} \left(-N_{p_l} \frac{\partial N_{v_i}}{\partial z} \right) r dr\, dz \tag{5.177}$$

$$AS_{il}^{31} = \iint\limits_{\Omega_e} -N_{p_l} \left(\frac{\partial N_{v_j}}{\partial r} + \frac{N_{v_j}}{r} \right) r dr\, dz \tag{5.178}$$

$$AS_{il}^{32} = \iint\limits_{\Omega_e} -N_{p_l} \left(\frac{\partial N_{v_j}}{\partial r} \right) r dr\, dz \tag{5.179}$$

$$AS_{il}^{33} = 0 \tag{5.180}$$

$$F_j^1 = \int\limits_{\Gamma_e} N_{v_i} \left[\left(-p^e + 2\eta \frac{\partial u_r^e}{\partial r} \right) n_r + \frac{\eta}{r}\left(\frac{\partial u_r^e}{\partial z} + \frac{1}{r}\frac{\partial u_z^e}{\partial r} \right) n_z \right] d\Gamma \tag{5.181}$$

$$F_j^2 = \int\limits_{\Gamma_e} N_{v_i} \left[\eta\left(\frac{\partial u_r^e}{\partial z} + \frac{\partial u_z^e}{\partial r} \right) n_r + \left(-p^e + 2\eta \frac{\partial u_r^e}{\partial z} \right) n_z \right] d\Gamma \tag{5.182}$$

$$F_l^3 = 0 \tag{5.183}$$

5.1.3.2   Porous Flow Regime

In case of steady incompressible flow through porous media, the equation for conservation of momentum given by the Darcy's law i.e. equations (4.28) explained in Chapter 4 take the form as,

$$\frac{\partial p}{\partial r} + \frac{\eta}{K_r} \cdot u_r = 0 \tag{5.184}$$

$$\frac{\partial p}{\partial z} + \frac{\eta}{K_z} \cdot u_z = 0 \tag{5.185}$$

The equation of continuity for conservation of mass is already given by Equation (5.163). Approximating the solution variables u_r, u_z and p by the mixed interpolation functions expressed in equation (5.164) and taking the Galerkin weighted residual over the element,

$$\iint_{\Omega_e} N_{v_i} \left(\frac{\partial \sum_{l=1}^{m} N_{p_l} \dot{p}_l}{\partial r} + \frac{\eta}{K_r} \cdot \sum_{j=1}^{n} N_{v_j} \dot{u}_{r_j} \right) r\, dr\, dz = 0 \tag{5.186}$$

$$\iint_{\Omega_e} N_{v_i} \left(\frac{\partial \sum_{l=1}^{m} N_{p_l} \dot{p}_l}{\partial z} + \frac{\eta}{K_z} \cdot \sum_{j=1}^{n} N_{v_j} \dot{u}_{z_j} \right) r\, dr\, dz = 0 \tag{5.187}$$

$$\iint_{\Omega_e} -N_{p_l} \left(\frac{\partial \sum_{j=1}^{n} N_{v_j} \dot{u}_{r_j}}{\partial r} + \frac{\sum_{j=1}^{n} N_{v_j} \dot{u}_{z_j}}{\partial z} \right) r\, dr\, dz = 0 \tag{5.188}$$

Applying the Green's theorem, the first order pressure derivative term is reduced to the lower order. Followed by algebraic manipulations, the final set of equations are obtained as,

$$\begin{bmatrix} AD_{ij}^{11} & AD_{ij}^{12} & AD_{ij}^{13} \\ AD_{ij}^{21} & AD_{ij}^{22} & AD_{ij}^{23} \\ AD_{il}^{31} & AD_{il}^{32} & AD_{il}^{33} \end{bmatrix} \begin{Bmatrix} u_r^j \\ u_z^j \\ p^l \end{Bmatrix} = \begin{Bmatrix} F_j^1 \\ F_j^2 \\ F_l^3 \end{Bmatrix} \tag{5.189}$$

Where,

$$AD_{ij}^{11} = \iint_{\Omega_e} \frac{\eta}{K_r} \cdot N_{v_i} N_{v_j}\, r\, dr\, dz \tag{5.190}$$

$$AD_{ij}^{12} = 0 \tag{5.191}$$

$$AD_{ij}^{13} = \iint\limits_{\Omega_e} -N_{pl} \frac{\partial N_{v_i}}{\partial r} \, r \, dr \, dz \tag{5.192}$$

$$AD_{ij}^{21} = 0 \tag{5.193}$$

$$AD_{ij}^{22} = \iint\limits_{\Omega_e} \frac{\eta}{K_z} \cdot N_{v_i} N_{v_j} \, r \, dr \, dz \tag{5.194}$$

$$AD_{ij}^{23} = \iint\limits_{\Omega_e} -N_{pl} \frac{\partial N_{v_i}}{\partial z} \, r \, dr \, dz \tag{5.195}$$

The elements in the third row of the stiffness matrix [**AD**] correspond to the terms of the continuity equation and are already mentioned in equations (5.175)-(5.177). The components of the load vector {**F**} are,

$$F_j^1 = \int\limits_{\Gamma_e} -N_{v_i} p^e \, n_r \, d\Gamma \tag{5.196}$$

$$F_j^2 = \int\limits_{\Gamma_e} -N_{v_i} p^e \, n_z \, d\Gamma \tag{5.197}$$

$$F_j^3 = 0 \tag{5.198}$$

5.2   Numerical linking of free/porous regimes

To couple the two different flow regimes, the Darcy equation is imposed effectively as the boundary condition for the Stokes equation at the free/porous interface. This imposition will circumvent the difficulty of matching the flux terms (i.e. line integrals) arising in both the domains. In the stiffness matrix of the free flow elements present on the free/porous interface, the Stokes terms corresponding to the interfacial nodes are replaced by the appropriate form of the discretised Darcy components and vice-versa at the porous/free interface. This procedure has been illustrated in **Figure 5.1.**
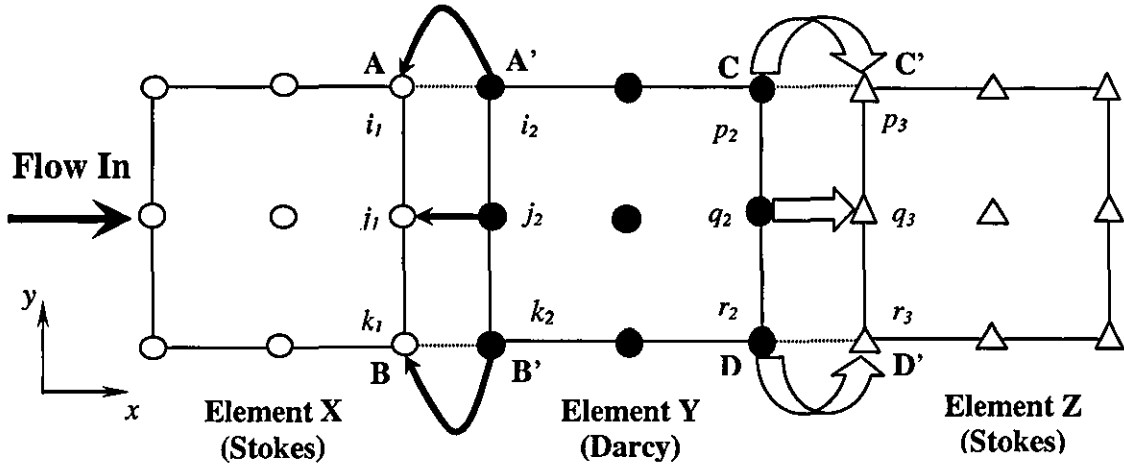
Figure 5. 1: Schematic representation of linking of Stokes and Darcy Regime in dead-end filtration

Figure 5. 1 shows three different elements X, Y and Z connected in series. Element X is in Stokes flow region connected to element Y in Darcy region. Element Y is further connected to element Z in Stokes flow region on the right hand side. This system is a typical representation of coupled free-porous-free flow system, which is the actual flow phenomenon in pleated cartridge filters operated in dead-end filtration mode. The boundary AB of element X coincides with the boundary A'B' of element Y at the interface. Similarly, the boundary CD of the element Y coincides with boundary C'D' of element Z at the interface.

i_1, j_1, k_1 are the nodes of Stokes flow element X on the interface AB-A'B' whereas i_2, j_2 and k_2 are the nodes of the Darcy element Y on the same interface. The stiffness matrices of elements X and Z will be of the form expressed by the Stokes matrix **[S]** in equation **(5.133)**. The stiffness matrix of the Darcy element Y will be similar to matrix **[D]** of equation **(5.151)**. In the assembly of stiffness matrices, the terms of nodes i_1, j_1, and k_1 in the stiffness matrix of Stokes element X are replaced by the terms of corresponding nodes i_2, j_2 and k_2 from the stiffness matrix of the neighbouring element Y which is in Darcy region.

Similarly, on the interface CD-C'D' between the Darcy element Y and the Stokes element Z, the terms of nodes p_2, q_2 and r_2 in the stiffness matrix of element Y are replaced by the term of corresponding nodes p_3, q_3 and r_3 from the stiffness matrix of element Z. Therefore, instead of specifying any artificial boundary condition on the interface, this is the direct linking of two distinct flow

regimes which proves to be physical, since the Darcy equation is valid on the porous interface (Nassehi *et al.*, 2004).

The identical procedure could be applied for coupling the free and porous flow regimes found in cross-flow filtration except the fact that the relative positions of Stokes and Darcy elements change as shown in **Figure 5. 2**.
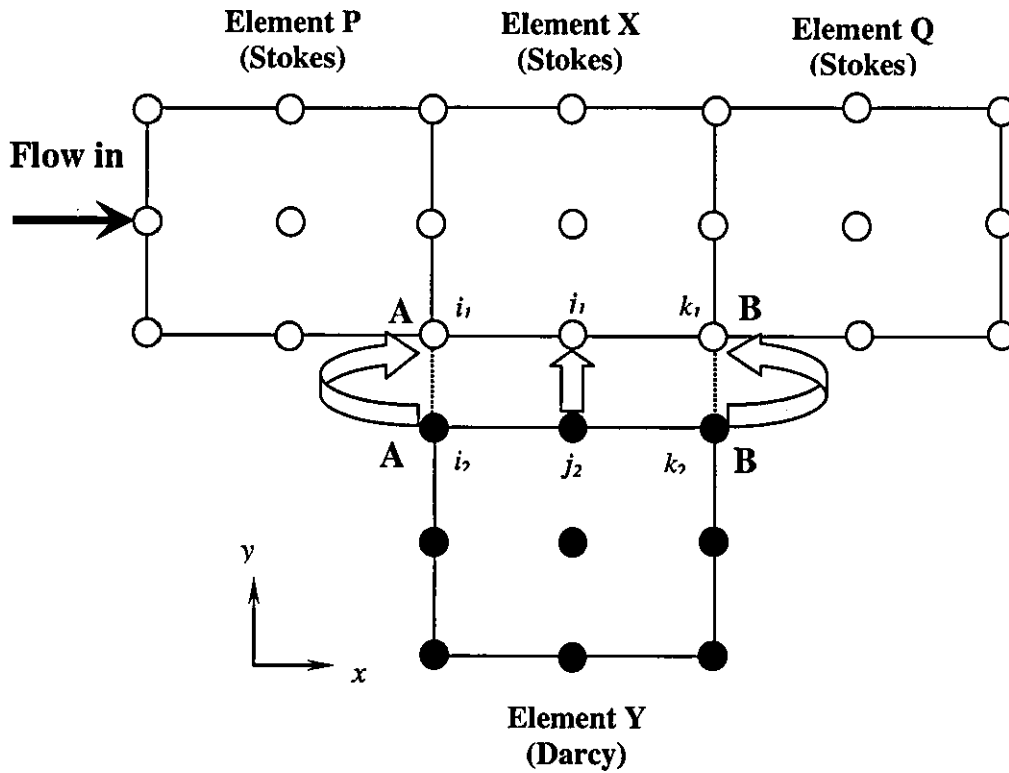
Figure 5. 2: Schematic representation of linking of Stokes and Darcy regimes in cross-flow filtration

5.3   Accuracy, stability and convergence

In finite element solution of incompressible flow problems, three distinct types of errors generally occur. The domain discretisation error arises when the curved or irregular boundaries of the solution domain are approximated by straight sided finite element. In the current study, these errors are alleviated using the isoparametric elements. The quadrature errors or round-off errors come into pictures during the numerical computations mainly because of limitations on computers precision. The errors introduced because of the approximation of dependent variables over the elemental domain are inherent to any problem. The accuracy and convergence of the solution is decided by the type of differential equation and the level of approximation done by proper selection of finite elements. The element by element satisfaction of inf-sup condition is a necessary and sufficient criterion for the stable and accurate solution of combined free/porous flow problem. This condition is based on the definition of distance between the exact and finite element approximate solution and is defined as,

$$d(u, V_h) = \inf_{u_h \in V_h} \|u - u_h\| = \|u - \tilde{u}_h\| \qquad (5.199)$$

Therefore, it is requisite to find condition on V_h so that,

$$\|u - u_h\| = \leq c \, d(u, V_h) \qquad (5.200)$$

Where, h is a characteristic length of finite element and c is a constant independent of h.

The error estimates in the solution like that in equations (5.199) and (5.200) are very useful since it gives an idea of how the finite element solution approaches the exact true solution. The accuracy of the finite element approximation can be enhanced either by reducing the size of elements, in turn by increasing the number of elements or by increasing the degree of approximation. Convergence of the finite element solution is checked by successive mesh refinements. Convergence with increase in degree of the approximation of the polynomial is termed as p-version of mesh refinement. In the present work, the level of convergence is attempted to improve just by increasing the number of elements with same degree of approximation which is termed as h-version of mesh refinement.

The global assembly of working equations is expressed in matrix form as,

$$[S(\{X\})]\{X\} = \{F(\{X\})\}$$
(5. 201)

Where, $\{X\}$ is the variable vector, $[S(\{X\})]$ and $\{F(\{X\})\}$ are the stiffness matrix and load vector respectively. Unlike the structural mechanics, the stiffness matrices in fluid dynamics problem are asymmetric and the working equations are non-linear which could be solved by an iterative technique such as the picard method or Newton-Raphson method. To avoid complications arising due the calculation of derivatives in the Newton-Raphson method, picard iteration method provides a more suitable alternative. In this method, equation (5.201) can be rewritten as,

$$[S(\{X\}^i)]\{X\}^{i+1} = \{F(\{X\}^i)\}$$
(5. 202)

Where, i is the iteration number. The non-linear terms in the stiffness matrix and the load vector are computed at each iteration using the values of $\{X\}$ from the previous iteration. This procedure is repeated until the convergence is obtained which is calculated by ratio of Euclidean norm between successive iterations to the norm of solutions (Lapidus and Pindar, 1982) as,

$$\sqrt{\frac{\sum\limits_{j=1}^{N}\left|X_j^{i+1} - X_j^i\right|^2}{\sum\limits_{j=1}^{N}\left|X_j^{i+1}\right|^2}} \le \varepsilon$$
(5. 203)

Where, N is the total number of degrees of freedom and ε is the pre-selected convergence tolerance value.

The linearised equations associated with the picard iteration method are solved by elimination methods such as band solvers (Conte and deBoor, 1980), Profile solvers (Bathe, 1982) and frontal solvers (Irons, 1970). In the present work, the frontal solver routine modified by Hood (1976) to handle the unsymmetrical matrices, have been deployed. The technique performs the assembly and elimination process simultaneously and in addition reduces the size and memory requirements suitable particularly from pc workstations or notebook computers.

In finite element analysis of incompressible flow problems, the stability signifies the measure of boundness of approximate solution with both space and time. The spatial stability requirement i.e. LBB stability criterion is fulfilled by proper selection of approximating functions as discussed earlier. The stability of approximation solution is mainly decided by the level of temporal approximation

and the selection of time step. A numerical scheme is said to be conditionally stable if it is stable only when certain restrictions on the time step are satisfied. In case of θ time stepping methods, factors such as non-linearity of physical parameters and order of spatial approximation influences the selection of θ and time step Δt. The stability associated with finite difference temporal approximation can be possibly ameliorated by higher order time-stepping scheme such as Taylor-Galerkin methods (Donea, 1984) or predictor-corrector time-splitting method (Townsend and Webster, 1987) as discussed in the previous chapter. Taking into consideration the scope of the numerical analysis in the present study, the stability criterion are not considered in detail.

5.4   Development of solution algorithm

The prime objective behind the present study is development of robust, reliable and cost-effective design and analysis tool for high performance pleated cartridge aeronautical filters. The essential units of this software tool are represented in **Figure** 5. 3 as,
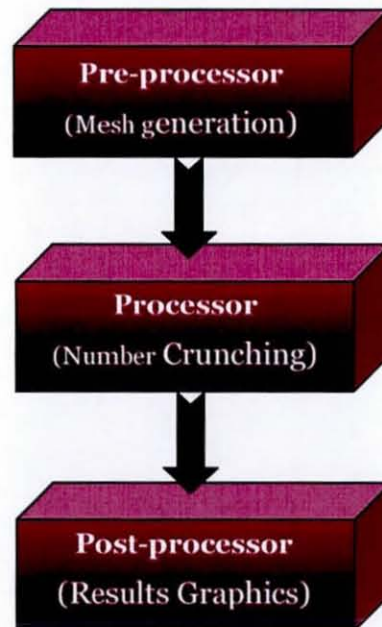
Figure 5. 3: The modules of the finite element analysis package

All these basic units are operated individually and information from one unit to the other is supplied manually. The pre-processing and post-processing tasks are achieved using commercially available computer applications and the major concentration is delivered to the generation of processor unit.

The pre-processing involves the domain discretisation by finite elements. In the present study, the finite element mesh generation is carried out in commercial software **COSMOS GEOSTAR**® developed by the Structural Research and Analysis Group. The file generated from COSMOS contains all the relevant geometrical details about the points, curves, surfaces, elements and nodes along with the nodal connectivity. The processor unit solves the discretised form of governing equations by finite element technique. Two different generic computer codes have been developed and scripted in the **Compaq Digital Visual FORTRAN** 6.6 programming environment suitable for compiling and executing in the Windows 2000 Professional operating system.

Aircraft **C**artridge **F**ilter **A**nalysis **M**odelling **P**rogram (**ACFAMP**) is a Finite Element Based (FEM) computer code designed to simulate the hydrodynamics and design parameters for pleated filter cartridge fabrication.
Coupled Flow **Dynamics** (**CFDYNAMICS**) is also a FEM based computational procedure for simulating combined free/porous flow dynamics for a specialized geometry of high performance pleated cartridge aeronautical filters. The details about development and modular structuring of **ACFAMP** have been described in detail in future chapter related to experimental and numerical evaluations of operating characteristic of pleated cartridge filters and can be referred from the Appendix.

In numerical computations within **CFDYNAMICS**, the finite element working equations pertaining to the free flow Stokes equations and porous flow Darcy equations are solved simultaneously for all the field variables i.e. the velocity components and hydrostatic pressure field. In case of Generalised Newtonian fluid flow, the power law equation for the viscosity calculation has been solved independent of the flow equations. For each iteration, the viscosity value is updated using the new value of the calculated velocity. The use of updated value of viscosity of each solution stage as pre-estimate for the next step makes the solutions to reach towards the stage of convergence quite fast. The inflow and

outflow of the information data through the blackbox of **CFDYNAMICS** can be understood in simpler way from **Figure 5. 4**.
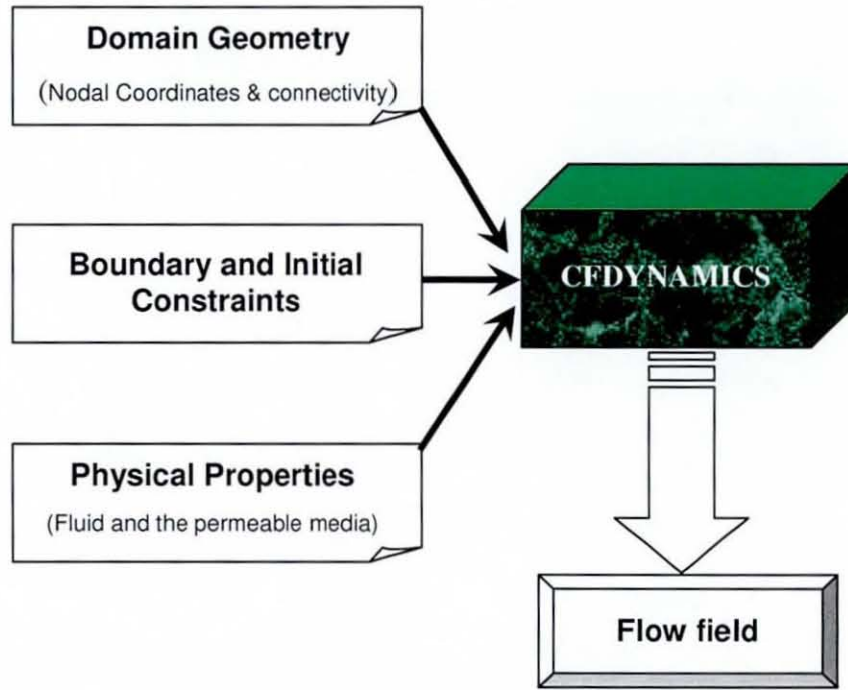
Figure 5. 4: Data processing through the processor unit CFDYNAMICS

The detailed scripting of the program **CFDYNAMICS** is provided within the appendix section for reference purposes. The subroutines embedded with the main body of the program are explained with their functionality. These subroutines are portrayed in form of flowcharts showcasing the basic steps involved in their execution and their way of interactions with other subroutines. The important variables associated with **CFDYNAMICS** are listed in chronological order which may be useful to understand their significance in order to perform any further modifications in the main program.

The solution algorithm behind the processing unit **CFDYNAMICS** is summarised in a conventional way of flowchart as shown in **Figure 5. 5**,

```
                        ┌──────────────────┐
                        │      START        │
                        └──────────────────┘
                                 │
                                 ▼
                        ┌──────────────────┐
                        │ DISCRETIZE THE DOMAIN │
                        └──────────────────┘
                                 │
  ┌───────────┐                  ▼
  │ VELOCITY  │──┐      ┌──────────────────┐
  └───────────┘  ├─────►│ INITIAL CONDITIONS READ │
  ┌───────────┐  │      └──────────────────┘
  │ PRESSURE  │──┘               │
  └───────────┘                  ▼
                        ┌──────────────────┐
                        │ BOUNDARY CONSTRAINTS │
                        │  ARE SPECIFIED    │
                        └──────────────────┘
                                 │
                                 ▼
                        ┌──────────────────┐
                        │ TIME VARIABLES ARE │
                        │   INCREMENTED     │
                        └──────────────────┘
                                 │
                                 ▼                 ┌──────────────────┐
                              ╱────────╲           │   UPDATE THE     │
                 Yes        ╱  PRESET    ╲         │  RHEOLOGICAL     │
        ◄──────────────────   TIME         │       │  PARAMETERS      │
                            ╲ REACHED ?   ╱         └──────────────────┘
                              ╲────────╱                    ▲
                                 │ No
                                 ▼
                        ┌──────────────────┐
                        │ SOLVE THE COUPLED │
                        │ FREE/POROUS FLOW  │
                        │ EQUATIONS FOR     │
                        │ VELOCITY AND PRESSURE │
                        └──────────────────┘
                                 │
                                 ▼
                              ╱────────╲       No
                            ╱    HAS     ╲──────────────►
                            CONVERGENCE
                            ╲ REACHED ? ╱
                              ╲────────╱
                                 │ Yes
                                 ▼
                           ╱──────────╲
                           │ PRINT THE │
                           │  OUTPUT   │
                           ╱──────────╱
                                 │
                                 ▼
                        ┌──────────────────┐
                        │      STOP         │
                        └──────────────────┘
```
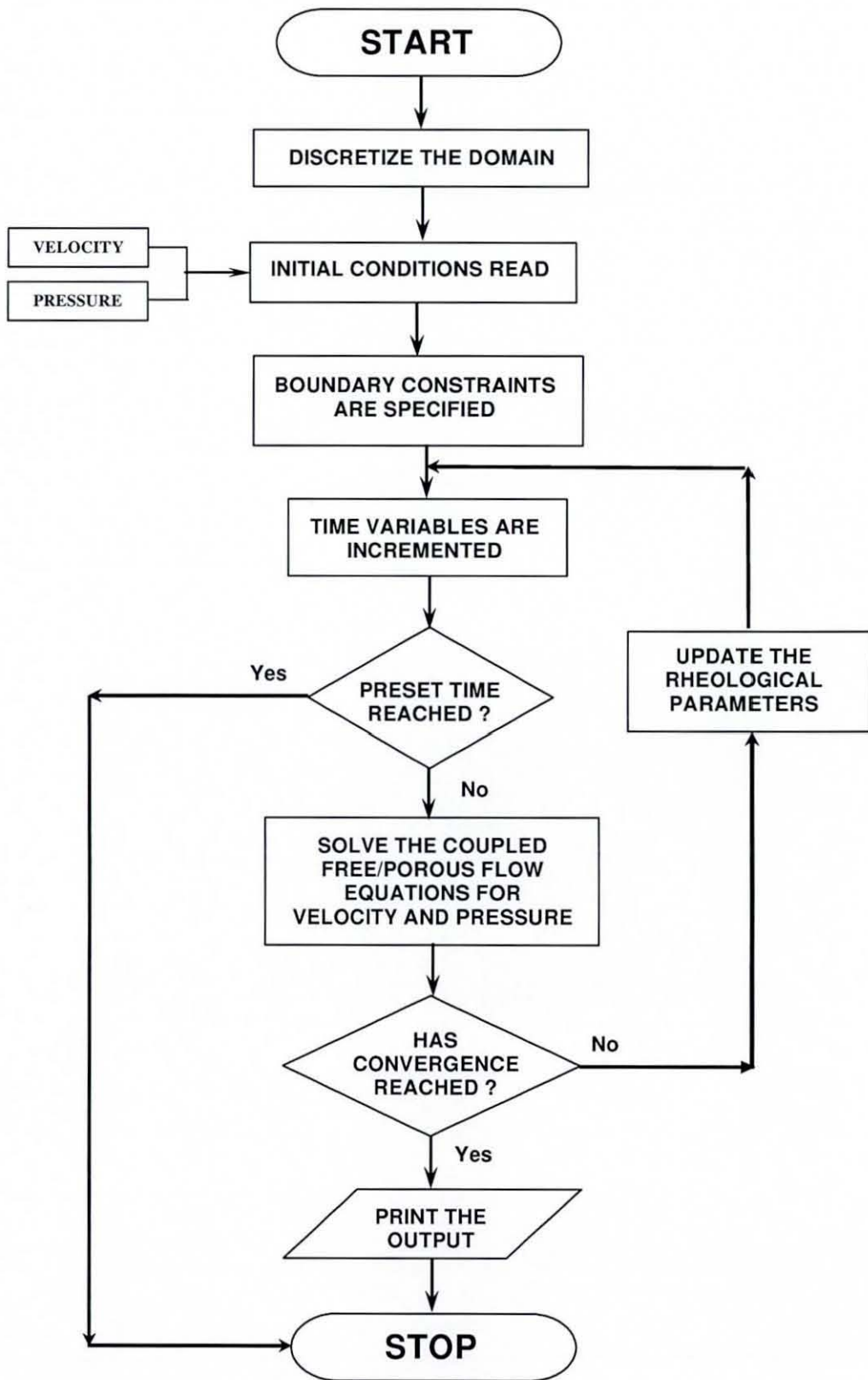
Figure 5. 5: Solution algorithm of the processor unit CFDYNAMICS

6   Computational Results and Discussions

Based on the two computational schemes, namely the perturbed continuity scheme and the Taylor-Hood scheme, computer codes have been developed in the Fortran 90 programming environment to compute fluid dynamics in coupled free/porous regimes pertaining to pleated cartridge aeronautical filters. The same compiler has been used to execute the subsidiary auxiliary programs for generating input data files. The mesh output exported by the pre-processor **Geostar**® is converted in a form readable by the main code StokesDarcyUVP.for of **CFDYNAMICS** using a finite element utility transfer (FEUT) program compiled and executed using the same compiler. All the results have been generated and post-processed on a Desktop workstation having Intel Pentium-4 processor with 1.4 GHz processing speed and 512 MB DDR RAM. The development of model is carried out in stages. Accordingly, results are initially presented for individual free flow dynamics and porous flow dynamics in domains with different geometrical characteristics using both the perturbed continuity and Taylor-Hood schemes. Thereafter, the developed algorithm has been testified to compute fluid dynamics in a variety of different free/porous coupled domains with varying geometrical features. In some specific cases, the simulated performances have been accompanied by available experimental data and theoretical analyses. In the context of simulated results, both the numerical schemes have been debated for their possible advantages and drawbacks in dealing with coupled flow hydrodynamics.

6.1   Geometrical and physical characteristics of domains

As the algorithm is developed aiming towards providing the user with maximum geometric flexibility, the complexity in the domain geometrical features have been increased in stepwise manner. Solutions to the governing equations have also been obtained for different types of boundary conditions depending on the geometry of the domain. Results have been generated for a wide range of permeation characteristics of porous media. The fluid flow behaviour in the coupled flow regimes have been observed for an incompressible fluid with different rheological properties. As the hydraulic fluids employed in aircraft

machine system are highly viscous generalised Newtonian fluids, the validity of the numerical algorithm has been examined for different power law indices.

In all the simulations, the porous medium is homogeneous and have isotropic permeability within the range of 10^{-6} m^2 to 10^{-12} m^2. The power law indices for the generalised Newtonian incompressible fluid are varied between 0.85 and 1.15 representing shear-thinning and shear thickening behaviours, respectively. The consistency coefficient in the power law equation or the viscosity of the fluid at zero shear rate is maintained at 80 Pas in most of the cases. For an isothermal situation, density of the incompressible fluid is taken to be 970 kg m^{-3}. The boundary constraints imposed artificially or arising from the underlying physics have been explained pictorially with each domain considered in the present study.

6.2   Graphical interpretation of the simulated results

The results generated by the computer code StokesDarcyUVP.for of **CFDYNAMICS** are in format of mere numbers designating the values of individual primitive variables. Development of the flow field for a particular set of boundary and initial constraints can be better visualized as a spatial variation over the domain geometry in form of coloured pictorial views.

6.2.1   Representation of velocity field

The individual velocity components can be plotted separately in the form of vector plots. The vectors correspond to the magnitude of the variable and also indicate its direction of orientation. The sign conventions for representing their directions, associated with their magnitude are assumed as shown in **Figure 6. 1**.
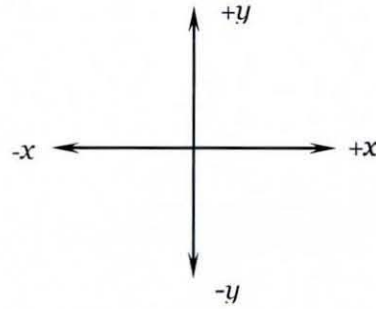
Figure 6. 1: Sign conventions for direction of velocity components

The vectors can be plotted in unicolour format in which the vector length changes in a definite proportion with the magnitude of velocity. Alternatively, the vectors may be coloured arrows of uniform lengths with each individual colour representing a particular value of magnitude of velocity. In the present study, developed flow field has been represented by vectors using commercial post-processing tools such as Tecplot® Verson 8.0 or Surfer®. Generally, the resultant vector of individual components of velocity is represented by the coloured vectors and is calculated as,

$$u = \sqrt{u_x^2 + u_y^2} \quad or \quad u = \sqrt{u_r^2 + u_z^2} \tag{6. 1}$$

A sample of colour scale used in Tecplot® post-processor is shown in **Figure 6. 2**.
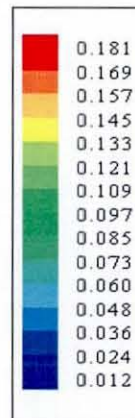
Figure 6. 2: A sample velocity vector colour scale

The scale shows rise in the resultant velocity values representing bands of colours ranging from blue to red. All the numerical figures on scale are in SI unit of m s^{-1}.

6.2.2   Representation of pressure field

The development of hydrostatic pressure field is represented by line contours or flooded coloured contours. In flooded contours, the values in the interior of each elemental domain are calculated by interpolating its corresponding nodal values. In the ongoing discussion, the coloured flooded contours are plotted in Geostar® and the black and white line contours are plotted in Surfer Version 8.0 if required. A representative colour scale usually associated with flooded contours of Geostar® is shown in **Figure 6. 3**.
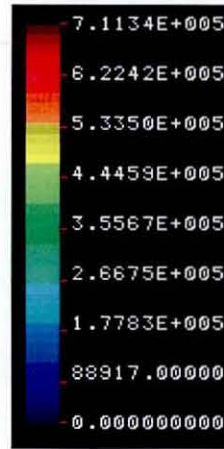
Figure 6. 3:A sample pressure contour colour scale

All the numerical figures on scale are in the SI units of Pa unless otherwise stated. In certain cases, the scale can be expanded or contracted to cover the all range of values.

6.3   UVP scheme with perturbed continuity method

The perturbed continuity scheme has been testified for free and porous flow dynamics in the initial steps of model development and later extended to analyse coupled flow dynamics. The results are calculated for simple geometries and the scheme has been further examined for a set of complex and irregular shaped geometries. Since the perturbed continuity formulation is based on the use of

transient form of the governing equations, a range of time step values and time-stepping parameter θ have been selected to achieve stable and accurate solutions.

6.3.1   Hydrodynamics in the free flow regime

6.3.1.1   Free flow in rectangular channel

As the simplest case, flow through an open rectangular channel is considered as a case governed by the Stokes equations. The domain measures 0.015 m in length in x-direction (i.e. $L = 0.015$ m) and 0.005 m in width in y-direction (i.e. $2b = 0.005$). The finite element computational mesh of the domain contains 9801 number of nodal points corresponding to 2400 number of elements. The boundary constraints imposed on the domain walls are shown in **Figure 6. 4.**
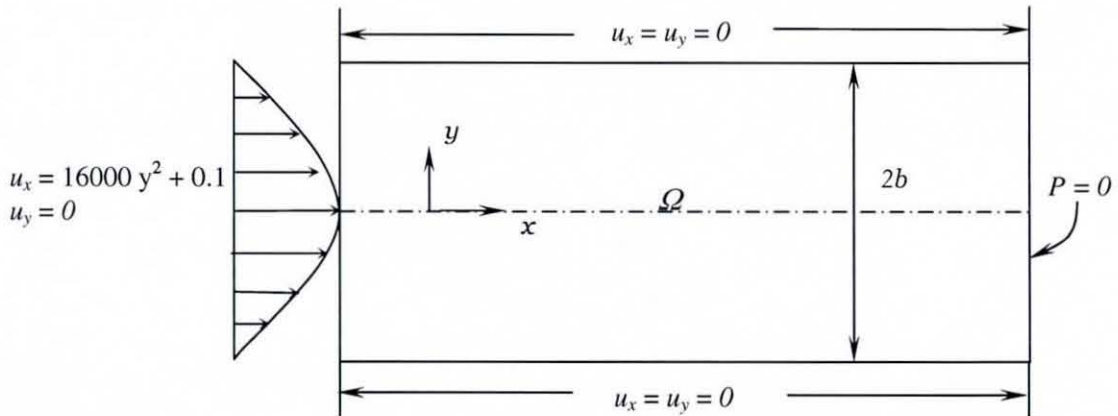
Figure 6. 4: Boundary conditions imposed on rectangular free flow channel

Parabolic flow of a purely Newtonian fluid having density of 970 kg m^{-3} and viscosity of 80 Pa s, is imposed at the inlet of the reactor to avoid any entrance effects. To measure the pressure drop across the domain, a datum of zero pressure is maintained at the exit. For the numerical computations, the time step of 10^{-9} s is used to approximate the temporal variations of variables between two successive time levels, time-stepping parameter of 0.75 is found to be quite reasonable.

Responding to the boundary and initial constraints, the developed flow field takes the form as shown in **Figure 6. 5.**
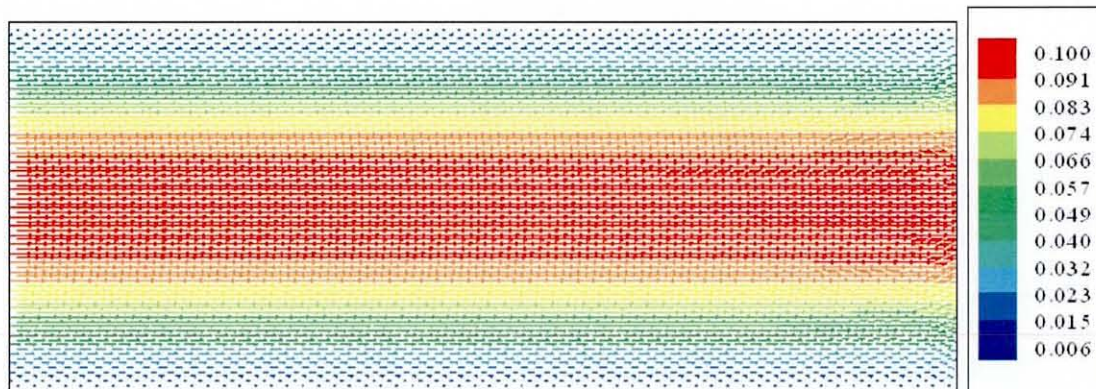
Figure 6. 5: Flow field developed over free flow rectangular channel

The velocity profile is plotted at a steady state obtained after the 5th time step. The profile matches agreeably with the profiles described by many authors for simple rectangular channel flow such as Bird *et al.* (1999). The corresponding pressure field developed in the channel is expressed by coloured flooded contours in **Figure 6. 6.**
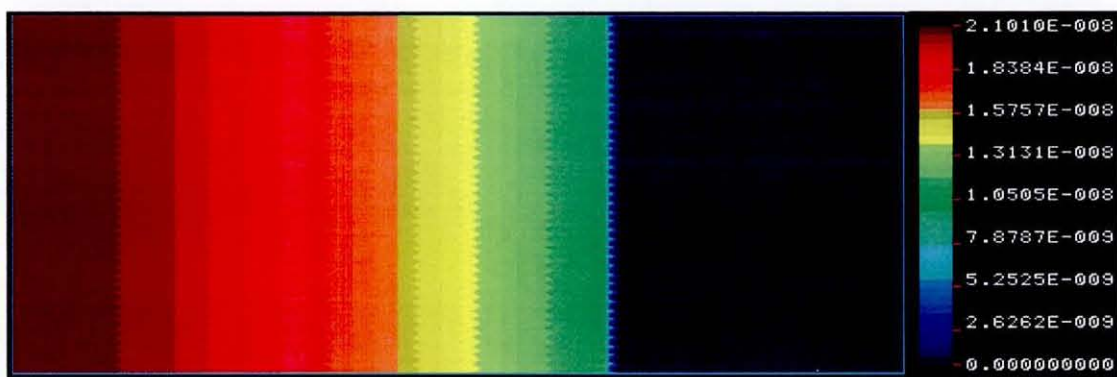
Figure 6. 6: Pressure distribution over rectangular free flow channel

As the zero pressure datum is applied at the exit, a successive drop in pressure value is observed in the direction of flow with the value of pressure gradient measured as 2.11×10^{-8} Pa.

6.3.1.1.1   Theoretical validation of simulated results for free flow dynamics

The incompressible flow in the rectangular channel depicted in **Figure 6. 4** is a simplified case of one dimensional flow in a two dimensional solution domain. In this situation, the momentum conservation can be represented by the x-component of equation of motion as,

$$-\frac{\partial p}{\partial x}+\frac{\partial}{\partial x}\left(2\eta\frac{\partial u_x}{\partial x}\right)+\frac{\partial}{\partial y}\left[\eta\left(\frac{\partial u_x}{\partial y}+\frac{\partial u_y}{\partial x}\right)\right]=0 \qquad (6.\,2)$$

As the flow in the channel has reached the fully-developed steady state status, any change in velocity components in the flow direction is assumed to be negligible.

$$\frac{\partial u_x}{\partial x}\approx 0;\frac{\partial u_y}{\partial x}\approx 0 \quad and \quad \frac{\partial u_x}{\partial y}\approx\frac{du_x}{dy} \qquad (6.\,3)$$

Therefore,

$$\frac{\partial p}{\partial x}=\frac{d}{dy}\left(\eta\frac{du_x}{dy}\right) \qquad (6.\,4)$$

For a fully developed flow of purely Newtonian Fluid,

$$\frac{\partial p}{\partial x}=\frac{\Delta p}{\Delta x}=\eta\frac{d}{dy}\left(\frac{du_x}{dy}\right) \qquad (6.\,5)$$

Integrating both sides,

$$\frac{du_x}{dy}=\frac{1}{\eta}\left(\frac{\Delta p}{\Delta x}\right)\cdot y+C_1 \qquad (6.\,6)$$

With repeated integration,

$$u_x=\frac{1}{2\eta}\left(\frac{\Delta p}{\Delta x}\right)\cdot y^2+C_1\cdot y+C_2 \qquad (6.\,7)$$

B.C.:

$$At\ y=\pm L\quad u_x=0 \qquad (6.\,8)$$

Substituting the boundary condition of equation **(6.8)**, after algebraic manipulation of equation **(6.7)**,

$$
\begin{cases}
C_1 = 0 \\
u_x = \dfrac{1}{2\eta}\left(\dfrac{\Delta p}{\Delta x}\right) \cdot y^2 + C_2
\end{cases}
$$

(6. 9)

B.C.:

$$At \ y = 0 \quad u_x = u_{x_{max}}$$

(6. 10)

Substituting the boundary condition of equation **(6.10)** into equation **(6.9)**,

$$C_2 = u_{x_{max}}$$

(6. 11)

$$
\boxed{u_x - u_{x_{max}} = \dfrac{1}{2\eta}\left(\dfrac{\Delta p}{\Delta x}\right) \cdot y^2}
$$

(6. 12)

The simulations are carried out for fluid of viscosity of 80 Pa s and density of 970 kg m^{-3}. We take two sampling points P1 and P2 in the elemental domain to measure the pressure drop. The coordinates of P1 are ($L/2$, $+b/2$) and those of P2 are (L, $+b/2$). The velocity value at these two points u_x is 0.075 m s^{-1} and the maximum value of velocity, u_{xmax} found at the plane $y = 0$ is 0.1 m s^{-1}. The distance between points P1 and P2 is L/2, i.e. 0.0075 m. Substituting this figures in equation **(6.12)**, the pressure differential measured between these two points is calculated as 1.92×10^4 Pa. However, the corresponding simulated value of pressure drop is found to be 1.44×10^{-8} Pa.

For a creeping free flow of an incompressible fluid, the total stress imposed on the fluid is carried by the fluid itself during the course of flow. Pressure forms an integral form of this Cauchy's total stress and the only way to measure a pressure drop is to apply pressure datum at a point in the solution domain and calibrate the value of resultant simulated pressure drop with its corresponding analytical value. Therefore, the calibration parameter for this situation is found to be 1.33×10^{12}. Further simulations are carried out for a range of viscosity values and the simulated pressure gradients across the two points P1 and P2 are corrected by the calibration parameter. The details of these numerical analyses are summarised in **Table 6. 1**.

Table 6. 1: Comparison of simulated and analytical pressure gradients

No.	Viscosity (Pa s)	Simulated pressure drop (Pa)	Simulated pressure drop with calibration (Pa)	Analytical Pressure drop (Pa)
1.	80	1.44×10^{-8}	1.92×10^{4}	1.92×10^{4}
2.	160	2.88×10^{-8}	3.84×10^{4}	3.84×10^{4}
3.	240	4.32×10^{-8}	5.76×10^{4}	5.76×10^{4}
4.	320	5.76×10^{-8}	7.68×10^{4}	7.68×10^{4}

From **Table 6. 1**, it can be concluded that by multiplying the originally simulated values of pressure drops by the calibration parameter, the new values are in closest vicinity of their corresponding analytical solutions.

6.3.1.2   Hydrodynamics in a free flow split duct

As the flow regime considered in earlier case is some sort of a pseudo 2-dimensional flow, it is essential to examine applicability of the developed solution scheme for an actual 2-dimensional free flow system. In this direction, the UVP perturbed continuity scheme based on isoparametric Lagrange elements is further extended to free flow through a split duct domain as shown in **Figure 6. 7**.
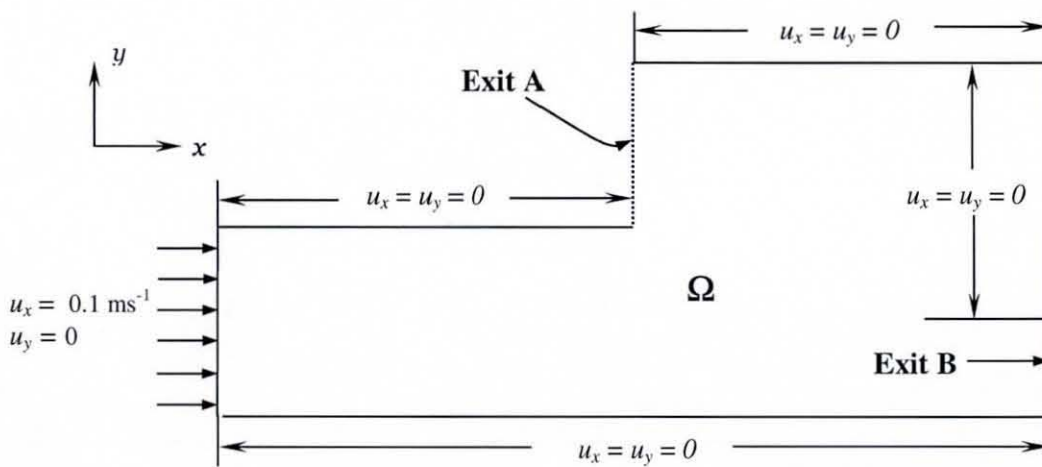
Figure 6. 7: Boundary conditions on free flow split duct

Plug flow Dirichlet boundary conditions are imposed at the inlet of the domain and the exit boundaries A and B are kept stress free by applying no boundary constraints. The fluid is a purely Newtonian fluid of viscosity 80 Pa s and density of 970 kg m^{-3}. The flow field in the domain is simulated using the time step value of 0.1 s and the time-stepping parameter in the Taylor-Galerkin formulation is chosen to be 0.75. The velocity of sound in fluid is maintained at 1150 m s^{-1}. Using these boundary constraints and numerical data, the simulated flow field over the domain is represented in **Figure 6. 8**.
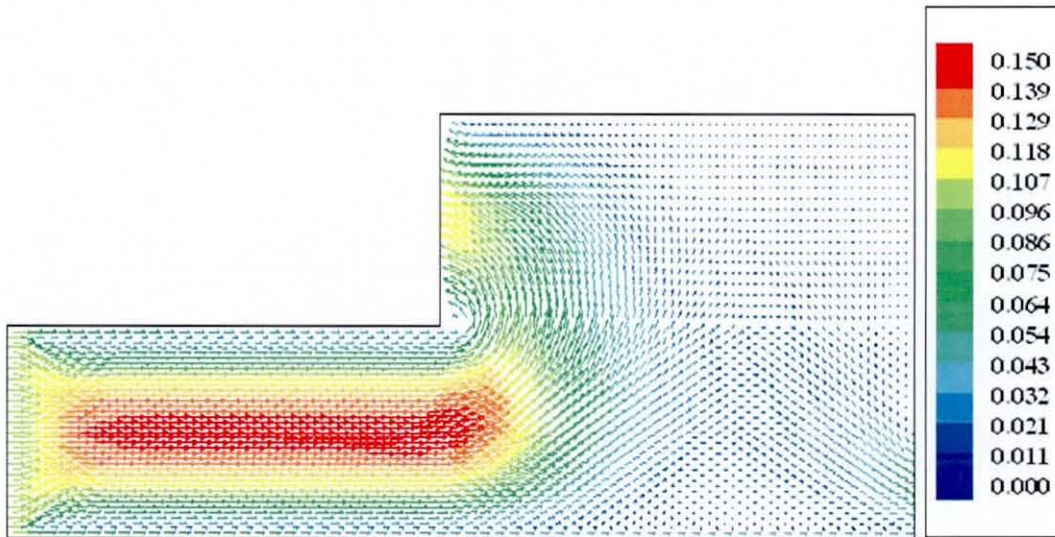
Figure 6. 8: Flow field developed over free flow split rectangular duct

The velocity vectors are plotted for profile obtained at steady state reached after 4 time steps. The vector plot shows a developed plug flow profile with major amount of fluid leaving as a backflow from exit A. The discrepancy between inlet and outlet masses is calculated to be 0.1% proving the preservation of continuity of mass. The pressure distribution over the entire computational domain is shown in **Figure 6. 9**.

Figure 6. 9: Pressure field distribution over free flow split duct domain

As a result of the stress-free boundary conditions, the numerical algorithm generates pressure profile truly justified by the underlying physical concepts and therefore the pressure drop across the domain is extremely small and almost negligible. Simulations are also carried out using the commercial Finite Element software **FEMLAB** using the same boundary and initial conditions. The developed flow field is expressed in the form of unicolour vector plot in **Figure 6. 10**.

Figure 6. 10: Flow field over the split duct domain simulated by FEMLAB

The profile generated by **FEMLAB** in exactly resembles the simulated one detailed in **Figure 6. 8**. The average value of cell Reynolds number is found to be 2 × 10^{-4}. The corresponding pressure profile over the solution domain is plotted in **Figure 6. 11**.

Figure 6. 11: Pressure profile in split duct domain simulated by FEMLAB

From the 3-D contours a gradual decline in pressure values is observed along the domain since the pressure values are already calibrated.

6.3.1.3   Hydrodynamics in free flow converging-diverging duct

To provide an additional evidence for the versatility of the algorithm for the solution of the free flow dynamics, a converging-diverging duct is considered as a domain under consideration. To analyse the incorporation of power law equation for viscosity in fluid dynamics calculation, the fluid is considered to be a generalised Newtonian fluid with power law index of 0.85. The boundary conditions imposed on the domain are picturised in **Figure 6. 12**.
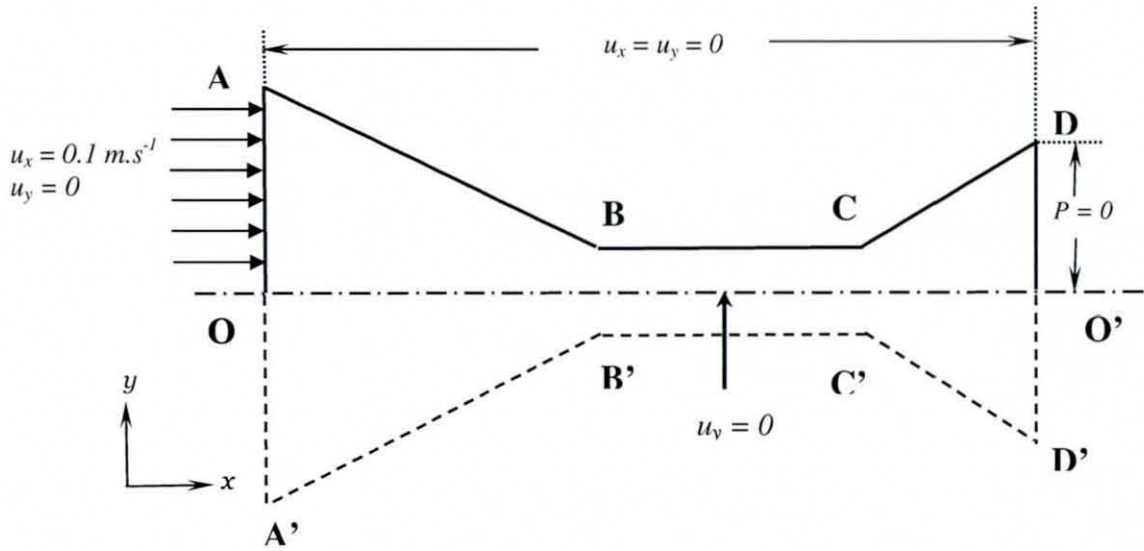
Figure 6. 12: Boundary conditions on free flow converging-diverging duct

The domain is symmetrical along the axis OO' parallel to the x-axis in 2-dimensional Cartesian coordinate system. The fluid is forced into the domain in plug flow and the exit is kept at zero datum. A symmetrical boundary condition is imposed at the axis of symmetry OO'. Responding to these boundary impositions, the developed flow field for this shear thinning fluid flow would appear as shown in **Figure 6. 13** obtained after attaining steady state in 7 iterations.
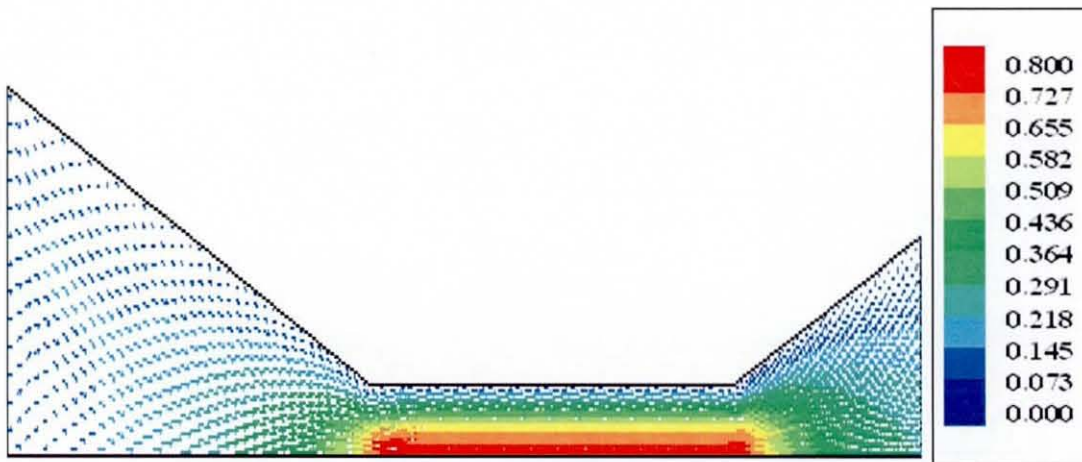
Figure 6. 13: Flow behaviour in free flow converging-diverging section

The flow attains fully developed state in the straight pipe section before entering the diverging cone where the flow expands to the full scale. The imposition of symmetrical boundary condition seems to be compliable with the mathematical analysis and is well justified by the generated flow profile in **Figure 6. 13**. The accompanied pressure field distribution over the domain has been exhibited by coloured contours in **Figure 6. 14**.
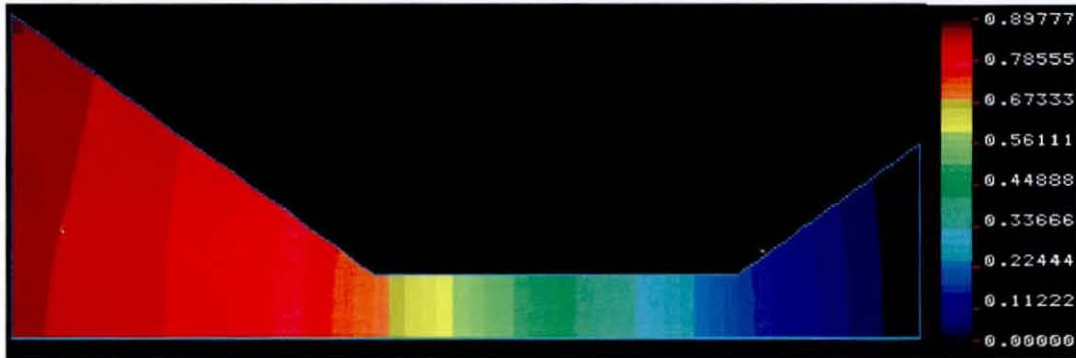
Figure 6. 14: Simulated pressure field in converging-divergence duct

As the pressure variation is restricted by the datum at the exit, gradual decline in the pressure values are found in the flow direction though the fluid is not losing any of its stress physically. The hydrostatic pressure drop over the domain amounts to be around 0.9 Pa. Similar to the previous case of split duct domain, the validity of results have been verified by computing the discrepancy between and outlet flows which comes up to around -0.4% within quite satisfactory limit.

The problem is again attempted to solve using commercial finite element simulation tool **FEMLAB** using triangular elements with P2/P1 mixed interpolation functions. The resultant flow field is expressed by unicolour vectors in **Figure 6. 15**.
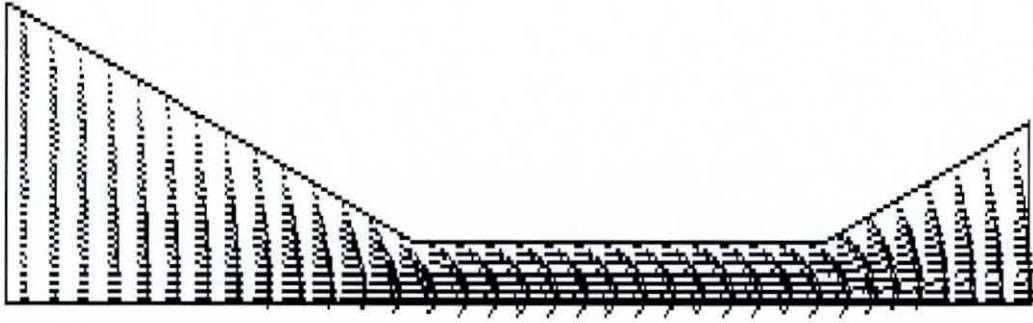
Figure 6. 15: Fluid flow behaviour in converging-diverging duct generated by FEMLAB

The vector length is in definite proportion with the magnitude of resultant velocity. The flow starts to gain the fully developed status before entering the horizontal channel section and retains similar even after expanding in the diverging duct. The profile shows good agreement with the simulated field shown in **Figure 6. 13.** The small deviations between these two simulated profiles can be accounted to the perturbed mass continuity equation, the details of which will be explained subsequently. The pre-calibrated hydrostatic pressure field resulted from the numerical analysis in **FEMLAB** is shown in the form of 3-D surface colour plot in **Figure 6. 16.**
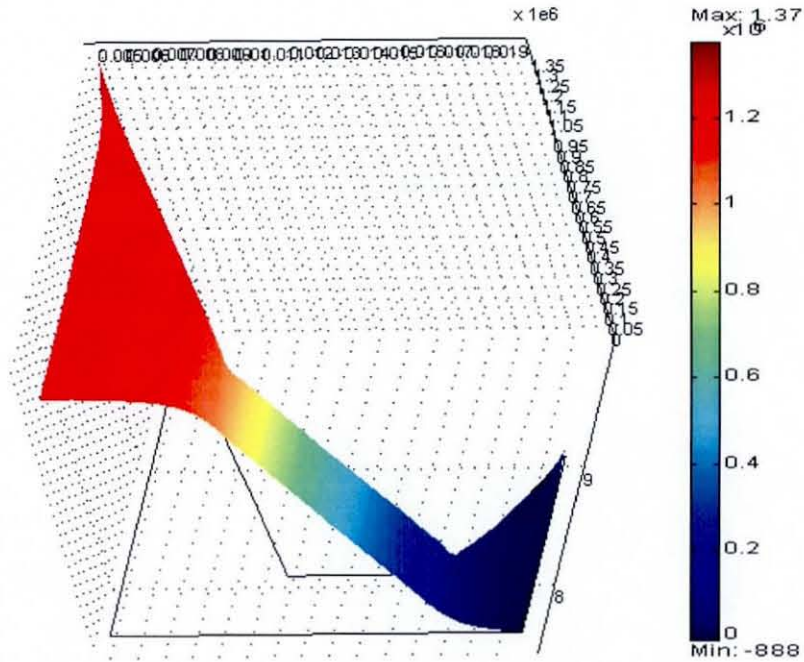
Figure 6. 16: 3-D surface contours of pressure in converging-diverging duct generated by FEMLAB

The overall pressure drop across the domain measures around 1.4×10^6 Pa.

6.3.2   Hydrodynamics of porous flow regime

6.3.2.1   Flow in rectangular porous domain

In the simplest case, an incompressible fluid flow is analysed in a rectangular porous matrix. The solution domain measures 0.015 m in length in flow direction and 0.005 m in width. The boundary conditions prescribed on the boundaries of the solution domain have been explained with the help of **Figure 6. 17**.
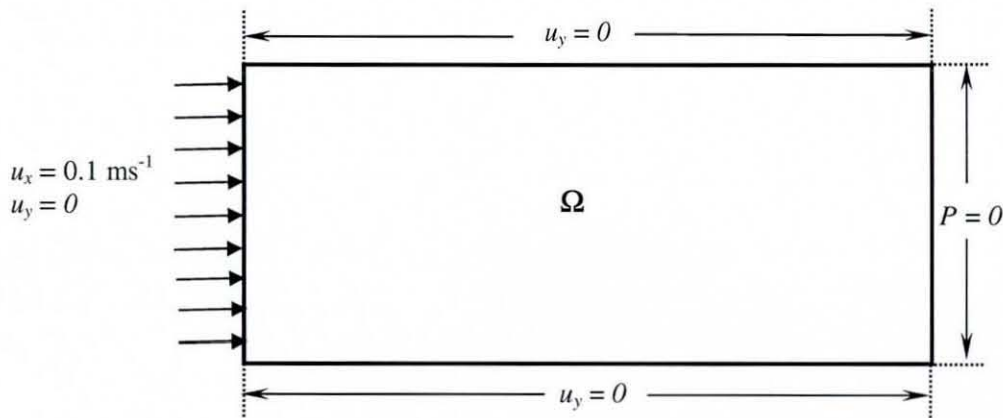
Figure 6. 17: Boundary conditions prescribed on rectangular porous matrix

The fluid is a purely Newtonian fluid with density of 970 kg m^{-3} and consistency coefficient of 80 Pa s. The porous medium is homogeneous and the isotropic permeability of the solid matrix is 10^{-12} m^2. With these prescribed boundary conditions, the flow field simulated by the porous flow routine of **CFDYNAMICS** takes the form as depicted in **Figure 6. 18**.

Figure 6. 18: Fluid dynamical behaviour in rectangular porous matrix

The time-step value of 20 s is found to be sufficient for achieving stability in the transient results. The velocity of sound in the fluid has been assumed to be 1150 m s^{-1}. The fluid velocity throughout the porous matrix is found to be in plug flow as theoretically predicted. The corresponding nodal pressures accompanied with the velocity values have been shown in **Figure 6. 19**.
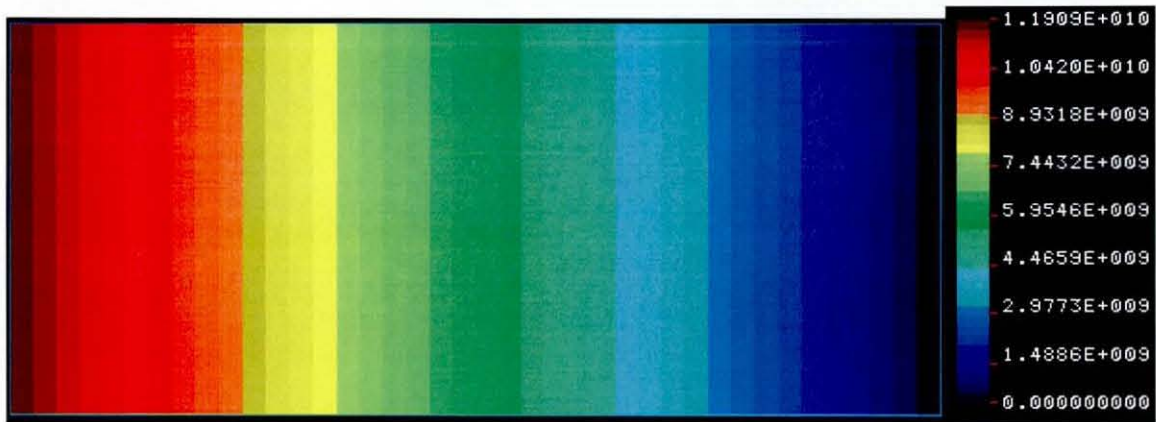
Figure 6. 19: Simulated pressure variations in the rectangular porous regime

As the fluid seeps through the low permeability porous matrix, the viscous stress associated with the bulk fluid gets transferred to the solid porous matrix. Therefore, a gradual decline in pressure is expected along the flow direction driving the flow, which has been proven by the numerical analysis represented by **Figure 6. 19**. The overall pressure differential across the bulk of the matrix is calculated to be 1.19×10^{10} Pa.

The porous medium considered in this case and hereafter is taken to be a Fibre Glass medium having a definite thickness and has been supported upstream and downstream by a metal wire mesh to maintain its structural integrity. The mesh aperture or mean pore size of the Fibre Glass medium is around 2.7 μm. The pore Reynolds number can be calculated as,

$$Re_p = \frac{u d_p \rho}{\eta}$$

(6. 13)

Where,

u is the fluid velocity normal to the surface of medium = 0.1 ms^{-1}

d_p is the diameter of pore = 2.7 μm

ρ is the fluid density = 970 kg m^{-3}

η is the viscosity of the fluid = 80 Pa s

Inserting these values in equation (6. 13), the value of pore Reynolds number comes around to be 3.27×10^{-6} which readily affirms the applicability of the Darcy's law for the problems considered in this study (Nield and Bejan, 1992). The Darcy's

law shows deviation resulting into non-linear drag when the pore Reynolds number Re_p is increased in the range of 1 to 10. In such cases, the Darcy's law needs modification to account for this non-linear drag and the Darcy-Forchheimer equation comes into picture (Joseph *et al.*, 1982). The transition from Darcy regime to Forchheimer regime can be decided by the modified Reynolds number Re_K (Ward, 1964), calculated as,

$$Re_K = \frac{u\sqrt{K}\rho}{\eta} \qquad\qquad (6.14)$$

Where, K is the permeability of the isotropic porous medium $= 10^{-12}$ m^2.

Inserting the numerical values of the physical entities, the value of the modified Forchheimer Reynolds number Re_K, comes to be around 3.27×10^{-6} which also signifies that there is no transition from linear Darcy's law to any non-linearity in drag, according to Ward (1964). The term $\sqrt{K}$ is termed as a length scale for the porous structure. Since in the present study, the bulk porous medium is considered as a continuum instead of a single pore, the modified Reynolds number Re_K is more appropriate than the pore Reynolds number to examine the applicability and validity of the Darcy's laws in the problems considered in the present study.

The corresponding simulated velocity profile generated by **FEMLAB** is shown in unicolour vectors in **Figure 6. 20**.
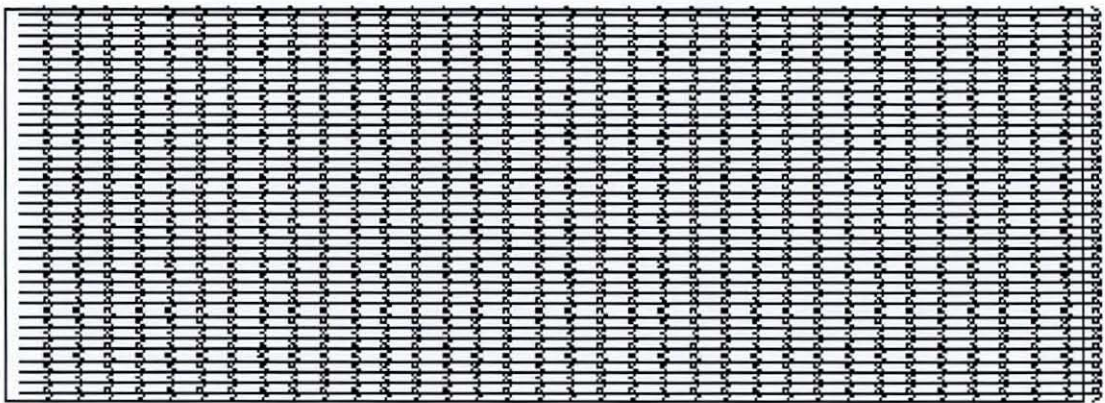
Figure 6. 20: Flow field in rectangular porous domain simulated by FEMLAB

The flow is uniform throughout the domain with the velocities in plug flow pattern identical to those plotted in **Figure 6. 18.**
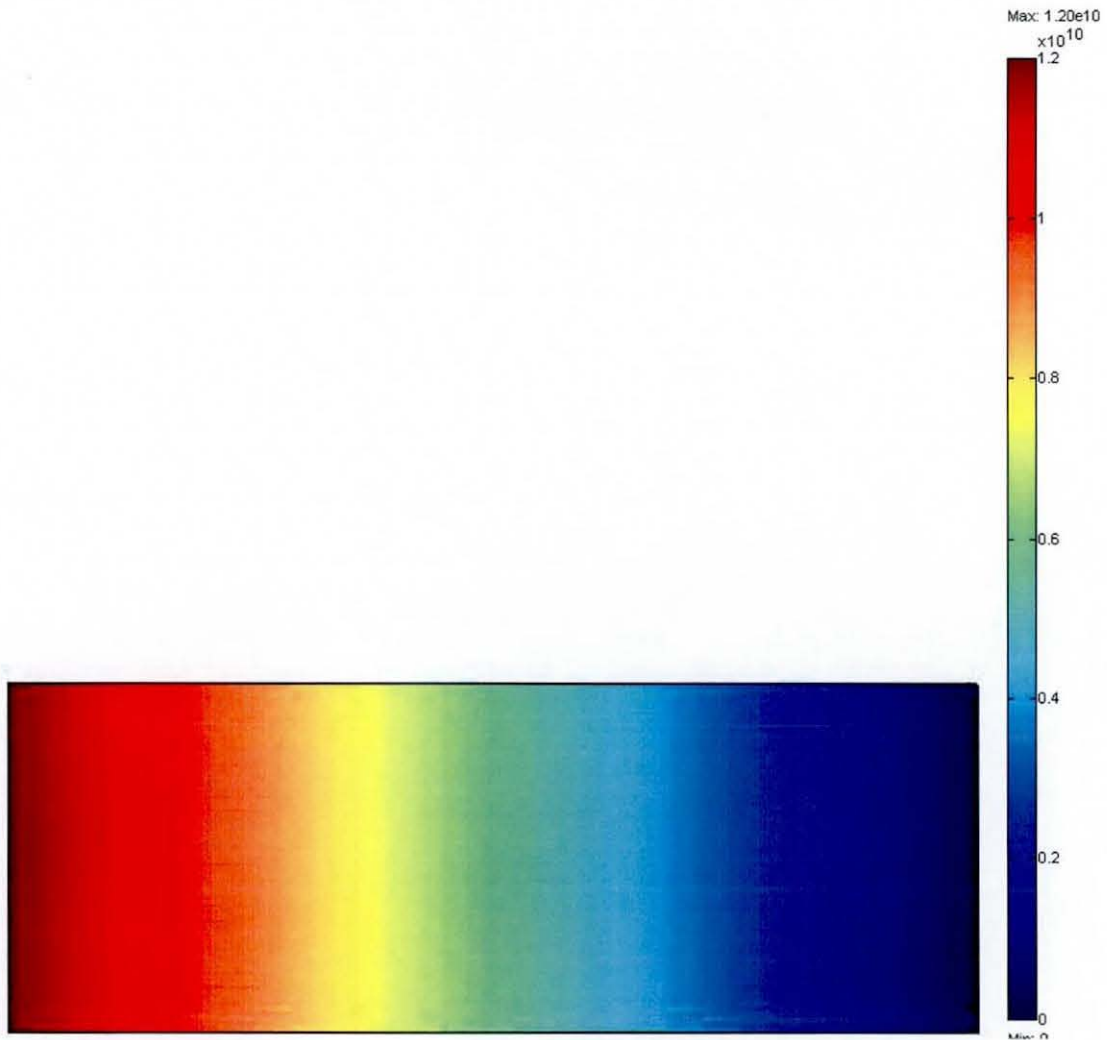
Figure 6. 21: Pressure variations in rectangular porous domain generated by FEMLAB

The flooded contours generated by using the finite element Darcy subroutine of **FEMLAB** shows gradual losses in pressure in the flow direction. The pressure drop computed across the domain is 1.2×10^{10} Pa which closely matches with the value calculated earlier using the simulation algorithm **CFDYNAMICS.**

6.3.2.2   Flow in concentric circular porous domain

To check the suitability and flexibility of the developed algorithm to cope with curved geometries, a concentric circular porous region is taken as a solution domain under consideration. This represents the prototype of cylindrical membrane used in tubular microfiltration equipment. The boundary conditions imposed on the periphery of the domain are shown in **Figure 6. 22**.
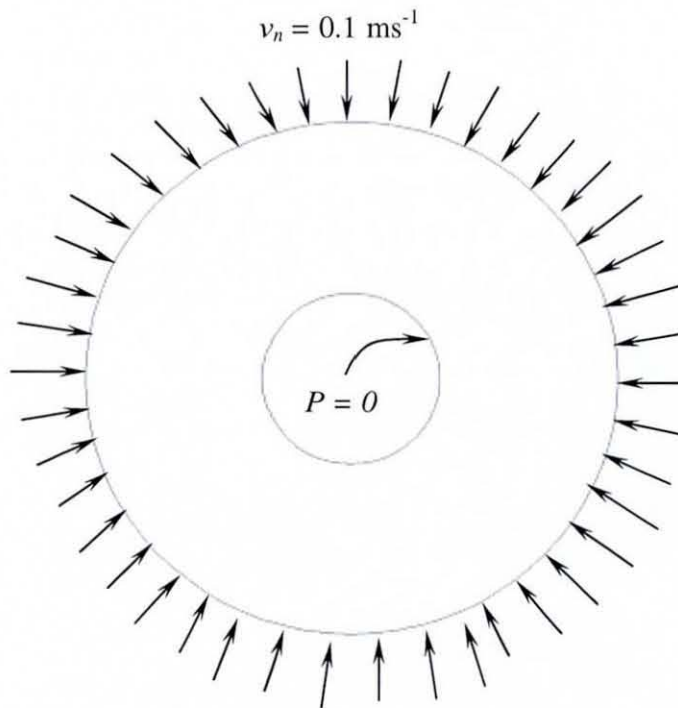
Figure 6. 22: Boundary conditions on the concentric circular porous domain

The external diameter of the membrane is 0.038 m with thickness of 0.032 m. The flow enters in the direction normal to the outer periphery and the pressure is restricted to zero value at the exit. The resultant flow field generated by using the porous flow subroutine in **CFDYNAMICS** is shown in **Figure 6. 23**.
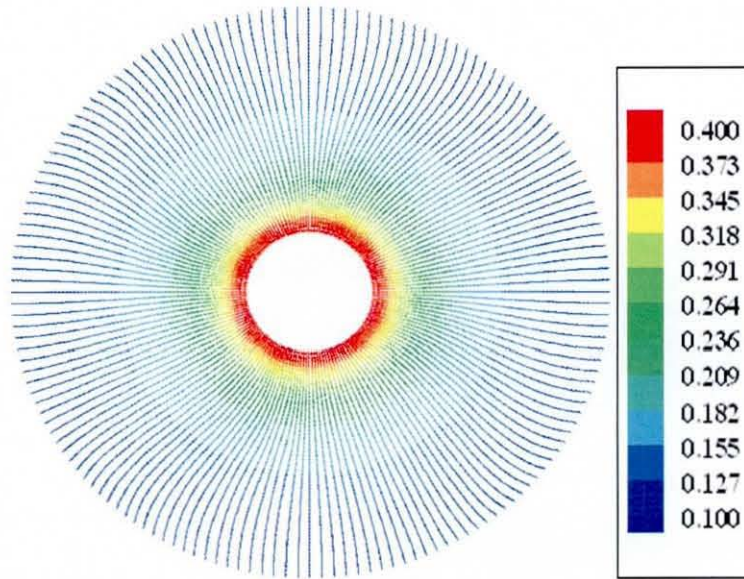
Figure 6. 23: Velocity vectors over concentric circular porous domain

The velocity values are increasing from outer periphery of the membrane surface towards the exit due to reduction in cross-sectional area for the flow. The validity of the results has been testified by computing mass balance of the material over the solution domain which comes around 0.2% confirming the continuity of mass. The steady state value of pressure is obtained from the solution of continuity equation and is represented in **Figure 6. 24**.
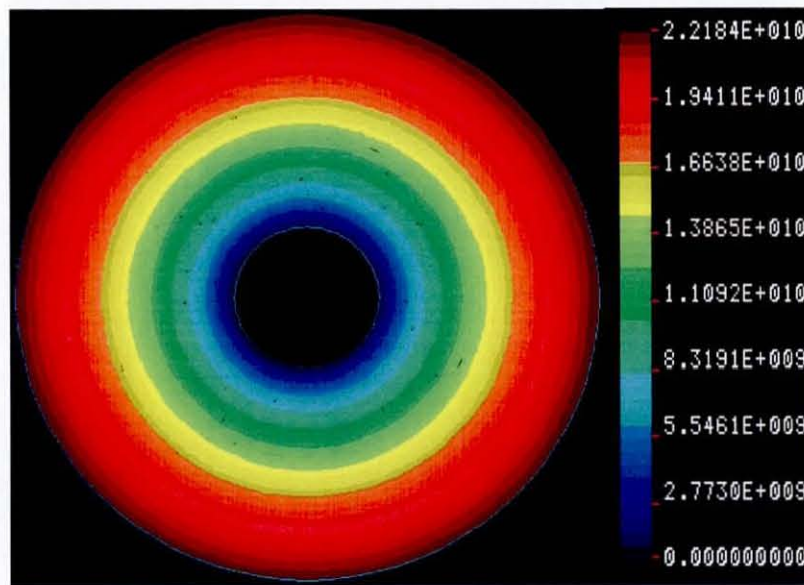
Figure 6. 24: Pressure variations over concentric circular porous domain

The pressure values are changing in each elemental level in radial direction with flow. The simulated pressure drop developed across the solution domain is calculated to be 2.2×10^{10} Pa.

6.3.3   Hydrodynamics of coupled free/porous regime

6.3.3.1   Fluid dynamics of rectangular free/porous coupled regime in dead-end filtration

Fluid dynamics of coupled free/porous regime represented by the Stokes and the Darcy equations has been analysed for a rectangular domain which resembles a simple dead-end filter, as shown in **Figure 6. 25**.
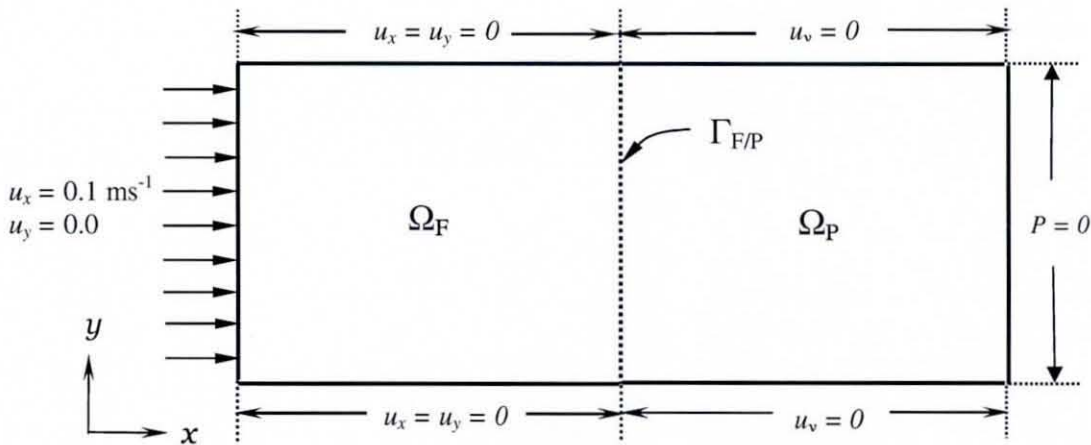
Figure 6. 25: Boundary conditions on the rectangular coupled free/porous regime

Ω_F and Ω_P represent free and porous domains respectively with $\Gamma_{F/P}$ signifying the porous barrier separating them. Both the domains extend to the length of 0.0075 m each with 0.015 m in height and a finite width in direction perpendicular to the plane of paper. The porous region is homogeneous in all the coordinate directions having isotropic permeability value of 10^{-12} m^2. The filtering liquid is a purely Newtonian incompressible fluid with constant viscosity of 80 Pa s

and specific gravity of 0.97. The solution domain is tessellated with 2400 C⁰-continuous finite elements consisting of 9801 number of nodal points. The ratio of number of elements in the Stokes region to that in the Darcy region is 2:1.

The fluid enters the free flow region in plug flow and the porous domain is confined by zero pressure datum at the exit of the domain. No slip velocity conditions are imposed on the impermeable boundaries of the free flow regime and the flow normal to the porous boundaries is restricted by applying perfect slip condition. At the free/porous interface $\Gamma_{F/P}$, Darcy equation is substituted as an exit boundary condition for the free flow region Ω_F. With all these boundary and inlet conditions, the simulated fluid dynamics in the couple flow regime, obtained at stationary level of reference takes the form as shown by the velocity vectors in **Figure 6. 26.**
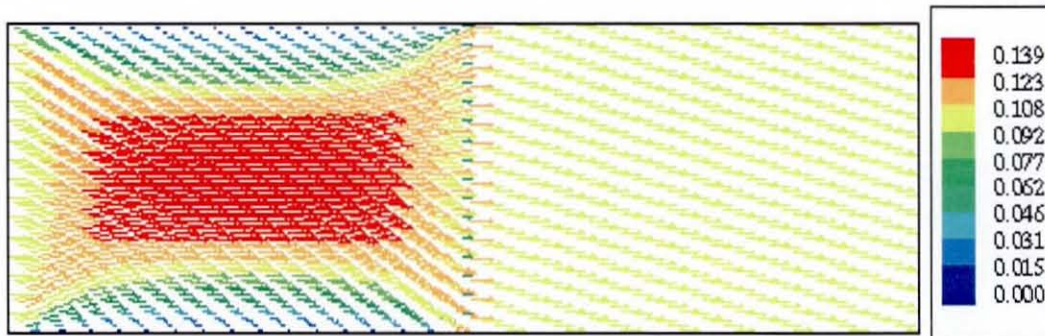
Figure 6. 26: Developed flow field in rectangular free/porous domains coupled in dead-end fashion

Various combinations of time-step values, Δt and speed of sound in the fluid, c are tried in the equation of continuity to achieve temporal stability in the numerical solutions. A range of time-stepping parameters are tested for accurate temporal approximations obtained from previous time steps values. Finally, stable and accurate solutions are achieved for time step of 10^{-12} s and the value of speed of sound of 5×10^9 m s^{-1}. The time stepping values have been kept greater than 0.9.

In the free flow regime, the length of channel is found to be sufficient for the fluid to obtain the fully developed parabolic state. At the free/porous barrier, the fluid faces strong hindrance due to sudden contraction in flow area offered by the low permeability interface. The fluid forces itself through the very fine pores

with high velocity and remains in plug flow throughout the bulk of the porous region. The pressure field developed at each nodal point of the discretised domain have been approximated over the individual elemental domains as shown in flooded contours of **Figure 6. 27**.
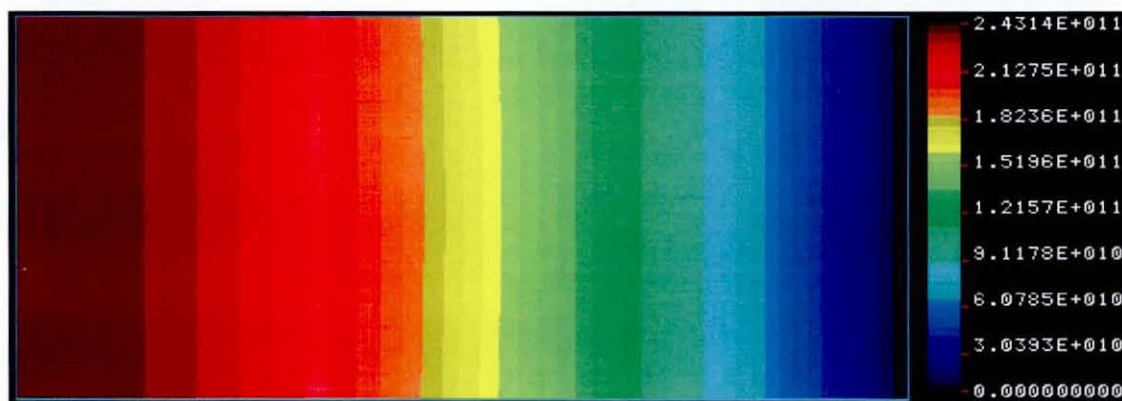
Figure 6. 27: Pressure contours for rectangular dead-end filter domain with permeability 10^{-12} m² for a purely Newtonian fluid flow

Steep pressure gradients are observed in each elemental layer in the porous flow regime as, the fluid recovers from its viscous stress while penetrating through the solid pores. However, somewhat unexpected pressure variations are also visible in the free flow regime as a result of the perturbed continuity equation to calculate the pressure in the system of governing equations, the details of which will be given in the subsequent discussions. The overall pressure drop developed over the domain is 2.43×10^{11} Pa of which around 75% pressure differential is developed only across the porous region.

6.3.3.1.1   Theoretical validation of coupled flow computational model

A set of numerical experiments is carried out for a flow of a purely Newtonian fluid with power law index of 1.0. The hydrodynamics has been simulated for the flow through the same rectangular coupled free/porous duct considered in the previous case. The permeability of the porous section is varied from 10^{-8} to 10^{-12} m² which lies within the applicable range of the Darcy's law, in

the order of magnitude of 10. The simulated pressure drop values developed across the porous medium are plotted against the corresponding permeability values and the relationship can be well explained in the graph in **Figure 6. 28**. Any change in permeability, resulted in a change of the same magnitude in pressure which shows the success of nodal replacement scheme in linking the Stokes and Darcy regimes. Since the magnitudes of permeability and pressure drop vary by the same order of magnitude of 10, the results are plotted on logarithmic scale for better visualisation.
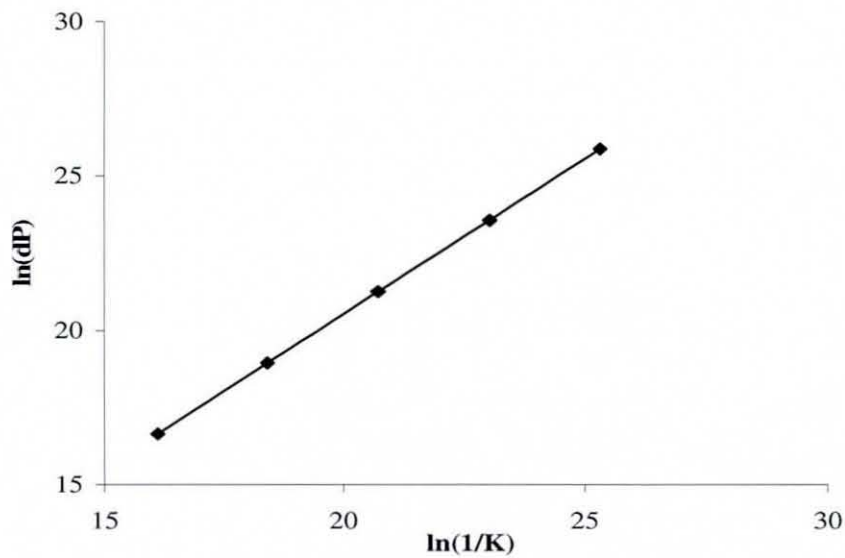
Figure 6. 28: Pressure drop vs. permeability relationship in the porous section of rectangular dead-end filter domain

The velocity fields in all these cases are observed to be the same. The continuity of the field variables is found to be maintained across the interfacial boundary in all the cases. In all the three different cases considered here, the discrepancy between inlet and outlet masses is around 0.12 % confirming the continuity of the mass.

6.3.3.1.2   Experimental validation of coupled flow computational model

The developed code has been validated against experimental data. The experiments were carried out using a standard multi-pass filtration rig designed according to ISO 16889 (1999) [*ISO/FDIS 16889, 1999. Hydraulic fluid power filters – Multi-pass method for evaluating filtration performance of a filter element*]. The experiments followed the ISO recommendations except for that a flat sheet sample of the medium, located in a filter holder, was used in place of a filter element so that the compression characteristics of the medium could be evaluated and the experiments were all permeation tests (rather than filtration), so no test dust was added to the fluids.

Briefly, a fluid of density 880 kg m^{-3} was permeated at a constant rate through a flat permeable medium and the pressure drop across the medium was measured. The test was repeated at a number of different flow rates so that a relationship between flow rate and pressure loss was developed. The permeable Fibre Glass medium used had an original thickness of 0.59 mm, and the flat sheet samples had a cross-sectional area of 28.3 cm^2. The mesh aperture or the mean pore size in the filter medium was 2.7 μm and the dry permeability of the medium was measured to be 1.97×10^{-12} m^2. The temperature during the experiment was kept constant at around 45^0 C. The test fluid was a Newtonian fluid with a constant viscosity throughout the operation. Precise details of the procedures are set out in ISO 16889 (1999).

A finite element mesh with 250 elements and 2121 nodes was generated based on the dimensions of the porous domain. The finite element mesh was extended to include a free flow feed region with the same area and a thickness 1/10 that of the permeable medium. Finite element simulations were carried out for various flow rates and **Table 6. 2** shows the experimental and simulation data.

Table 6. 2: Experimental and Simulation Data

No.	Flow Rate (m³ s⁻¹)	T °C	Viscosity of fluid (Pa s)	Experimental Pressure Drop across Permeable Medium (Pa)	Simulated Pressure Drop across Permeable Medium (Pa)
1.	7.5×10^{-6}	42.5	0.0593	47960	46961
2.	1.1×10^{-5}	44.0	0.0554	66945	60950
3.	1.5×10^{-5}	45.5	0.0519	89926	89926
4.	1.9×10^{-5}	45.0	0.0531	110909	112907
5.	2.3×10^{-5}	45.0	0.0531	126896	138886

Figure 6. 29 shows a comparison of simulated and experimental pressure drops for various flow rates.
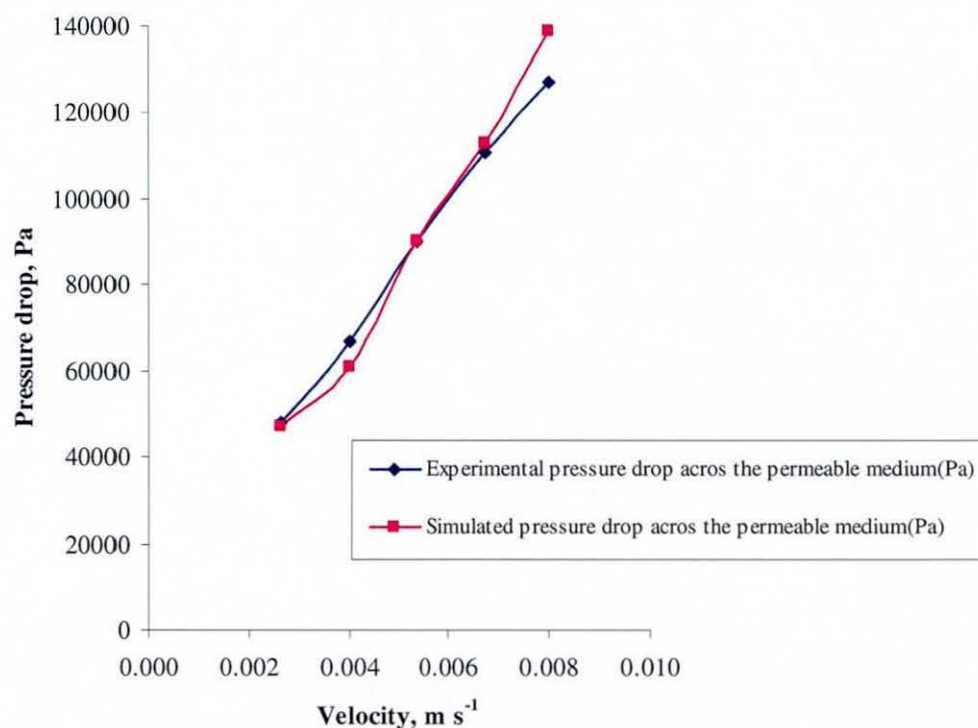
Figure 6. 29: Comparison of experimental and simulated data

As seen from the **Figure 6. 29**, the simulated pressure drop values compare favourably with the corresponding experimental pressure drop values. The maximum pressure drop is in the porous region which amounts to around 94 % of total pressure drop developed across the overall domain. The distribution of pressure in free and porous flow domains is observed to be consistent with the change in flow rates and is shown in **Table 6. 3**.

Table 6. 3: Distribution of pressures in flow regimes

	Flow rate (lit/min)	Free flow region %ΔP	Porous flow region %ΔP
1.	0.45	5.80	94.20
2.	0.68	5.87	94.13
3.	0.91	5.87	94.13
4.	1.14	5.88	94.12
5.	1.36	5.92	94.08

6.3.3.2   Fluid dynamics of quarter circular coupled free/porous regimes

A concentric quarter circular region is taken as a domain under consideration. The geometrical characteristics of the domain can be explained with the help of **Figure 6. 30**. The thickness of the free and porous flow regions is 0.008 m each and the radius of the entire domain is 0.024 m. Line of symmetry boundary conditions have been imposed on the vertical and horizontal edges of the domain. An inlet velocity of 0.1 m s^{-1} is applied at the inlet i.e. on the periphery of the free flow region whilst a pressure datum of zero has been imposed at the porous domain exit. The applied boundary conditions on the periphery of the domain are explained in **Figure 6. 30**.
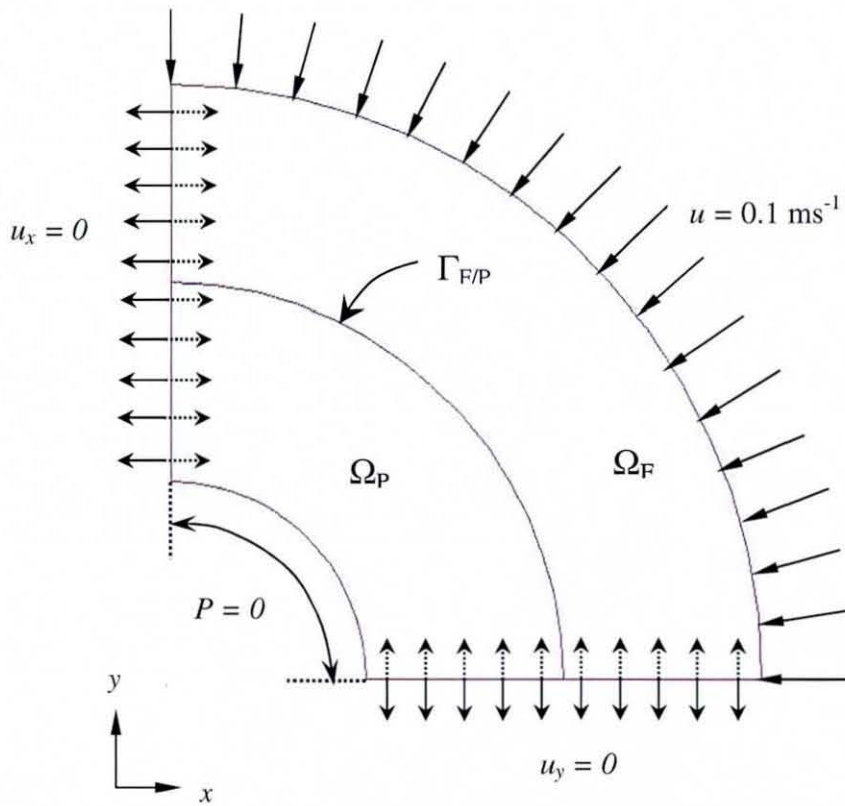
Figure 6. 30: Boundary constraints on concentric quarter circular free/porous coupled regime

The finite element mesh of the domain comprises of 4141 nodes corresponding to 1800 elements. The ratio of elements in the Stokes region to that in the Darcy region is 8:1. The mesh is relatively coarse in the free flow region as shown in **Figure 6. 31**. However, near to the Stokes/Darcy interface, the mesh is densely refined in the free flow zone since the variation in the field variables is expected to be significant.
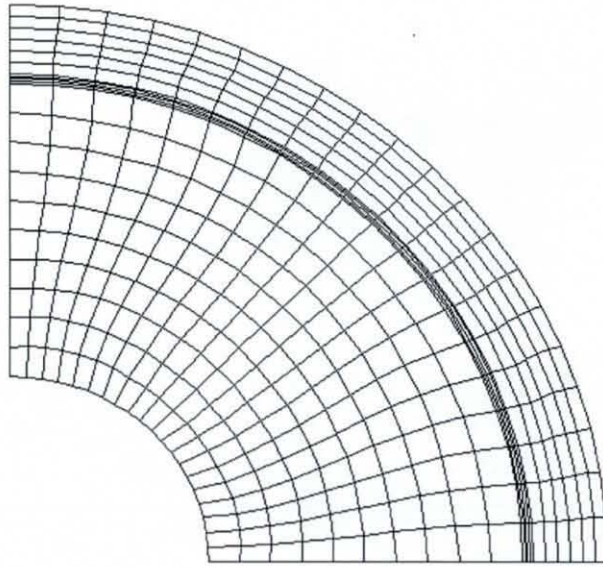
Figure 6. 31: Computational mesh of concentric quarter circular coupled free/porous regime

The permeability of the porous region considered in both the longitudinal and transverse directions is taken as 10^{-12} m^2. It was observed that stable solutions are obtained at steady state using time step of 10^{-11} s and speed of sound of 5×10^9 m s^{-1} with the value of time stepping parameter, θ used in the simulations being 0.75. **Figure 6. 32** represents the developed pressure field over this concentric circular quarter domain for a shear thickening fluid having the power law index of 1.15 with the pressure values indicated in the unit of Pascal (Pa). The total pressure drop in each case is made up of the pressure drops in the free and porous flow regions and the pressures at the inlet and the interface are 1.80×10^{10} Pa and 9.93×10^9 Pa, respectively.

	1.60E+010
	1.50E+010
	1.40E+010
	1.30E+010
	1.20E+010
	1.10E+010
	1.00E+010
	9.00E+009
	8.00E+009
	7.00E+009
	6.00E+009
	5.00E+009
	4.00E+009
	3.00E+009
	2.00E+009
	1.00E+009
	0.00E+000
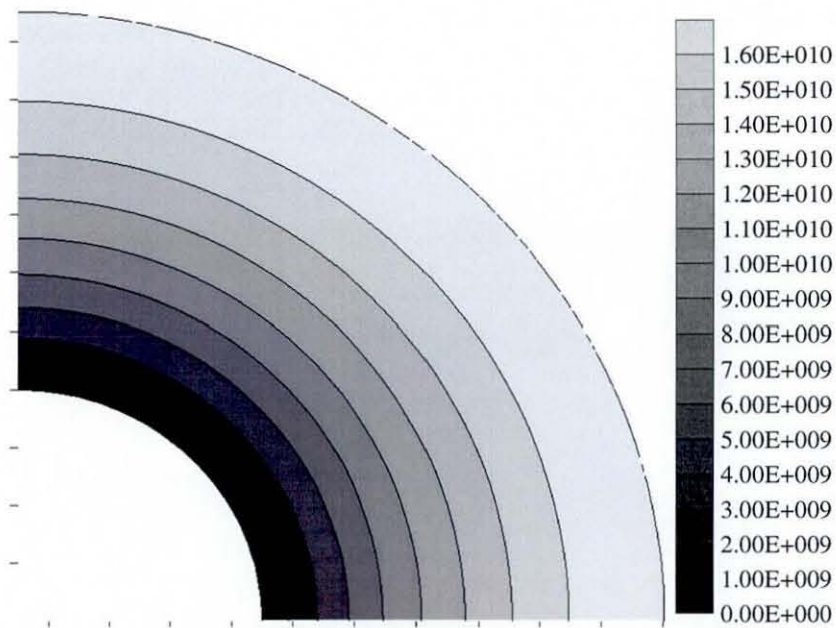
Figure 6. 32: Pressure contours in the concentric quarter circular coupled free/porous regime for a shear-thickening generalised Newtonian fluid flow

Figure 6. 32 shows expected decrease in pressure as the fluid permeates from the free flow into the porous flow regime. The pressure values in the free flow region are not exhibiting significant fluctuations but, as the fluid crosses the free/porous barrier, the pressure values gradually decline in direction of flow since in the low permeability porous region, pressure differential is the only driving force for the movement of the fluid.

The simulated flow field developed over the domain can be well explained with the help of velocity vectors as shown in **Figure 6. 33**. The flow enters the free flow domain radially and at the exit of the porous flow regime, the velocity values are the highest due to the lowest cross-sectional area for the flow. The model results indicate only 0.18% discrepancy between the inlet and outlet flows signifying the preservation of the mass.
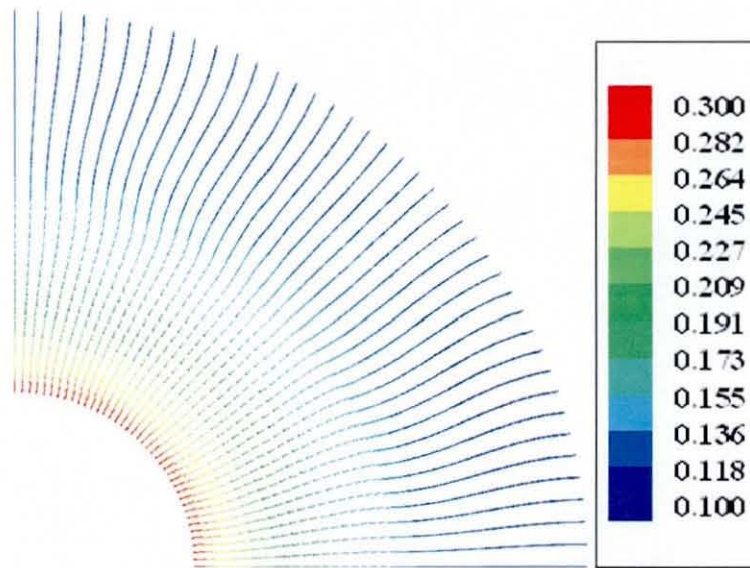
Figure 6. 33: Simulated flow field over concentric quarter circular coupled free/porous domain for shear-thickening generalised Newtonian fluid flow

In the similar way, simulations are carried out for two fluids with identical physical properties but varying rheological characteristics. The first fluid is purely Newtonian fluid whereas the other is a shear-thinning generalised Newtonian fluid with power law index 0.85 having the viscosity value at zero-shear of 80 Pas.

It has been deduced from the three cases considered here, that the fluid flow phenomenon is identical in every case in nature and order of magnitude of the developed pressures. The pressure variations are symmetric in all the cases. The maximum pressure drop is observed in the Darcy region which is inevitable due to the maximum resistance to flow by the porous matrix. The amount of pressure drop developed in the individual regions depends mainly on the rheology of fluid. The percentages of the pressure drops associated with free flow and porous flow regions have been listed in **Table 6. 4**.

Table 6. 4: Pressure drop variation with power law index

Fluid	Power law index	Stokes Region %ΔP	Darcy Region %ΔP
Shear Thinning	0.85	22.7 %	77.3 %
Newtonian	1.00	26.9 %	73.1%
Shear Thickening	1.15	37.7 %	63.3 %

6.3.3.3   Computational fluid dynamics in coupled free/porous rectangular domain with slant interface

In the third case, the influence of the nature of the interface on the fluid dynamics of coupled free/porous regimes have been analysed for temporal stability and accuracy. The rectangular free flow channel confined by the porous matrix identical to that shown in **Figure 6. 25** is considered as the domain under analysis. However, the free/porous interface is inclined at an angle of 5^0 as shown in **Figure 6. 34**.
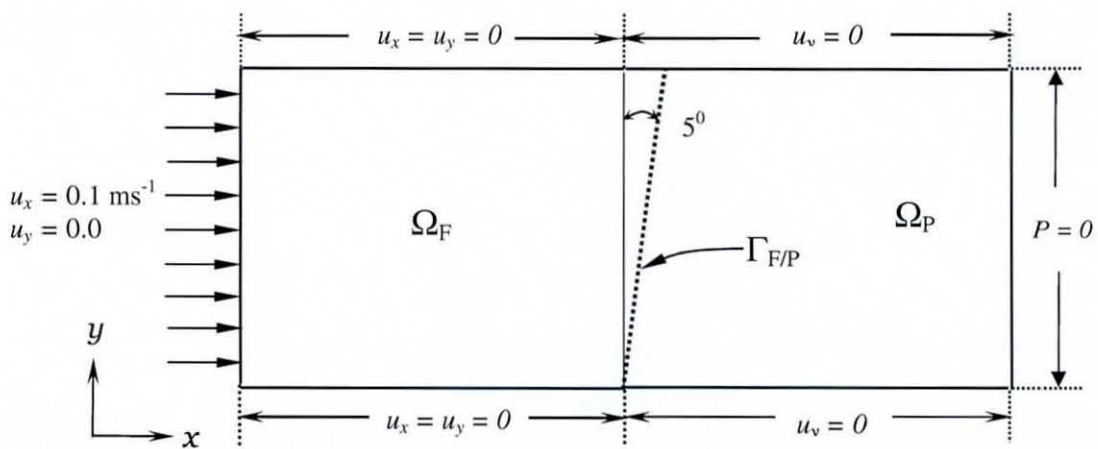
Figure 6. 34: Boundary conditions on the rectangular coupled free/porous regime with slant interface

The finite element mesh of the domain comprises of 9801 number of nodes corresponding to 2400 elements. The ratio of elements in the Stokes region to that in the Darcy region is 2:1. The boundary constraints enforced on the domain are identical to those imposed on domain in **Figure 6. 25**.

Simulations are carried out for attaining steady state profiles with various combinations of time-step values, time-step parameters and velocity of sound in fluid. It was observed that stable and convergent steady state solutions are obtained for a time-step value of 10^{-12} s which simply implies that the problem is pseudo unsteady state. After various permutations and combinations, the appropriate value of speed of sound in fluid comes to be around 4×10^9 m s^{-1} accompanied by the time-stepping parameter θ of 0.95. The stable solutions

obtained after 7 time steps are presented in the form of normal velocity vectors in **Figure** 6. 35.
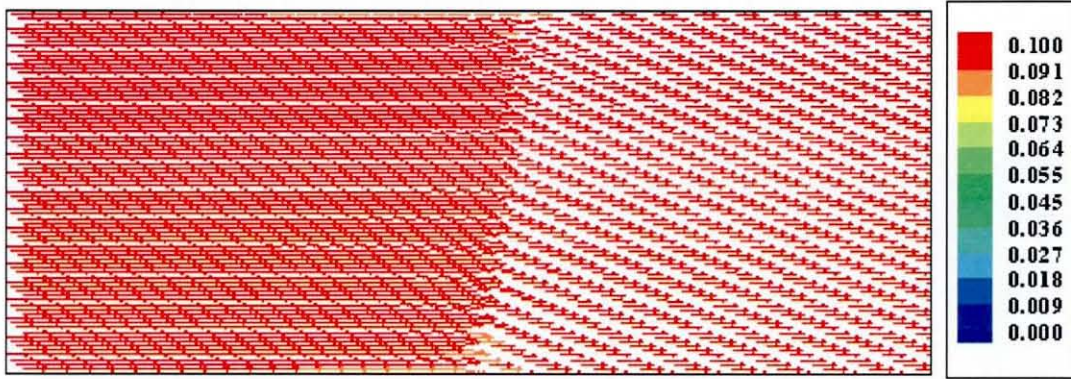
Figure 6. 35: Fluid flow behaviour in coupled free/porous regimes with slant interface

The velocity vectors are indicating plug flow profile throughout the solution domain. In free-flow regime, the flow doesn't seem to have the sufficient length to get developed unlike the profile shown in **Figure** 6. 26. The fluid is observed to be having maximum hindrance at the free-porous barrier caused by sudden contraction in flow area. In porous region, the flow regains its plug flow characteristics as expected. The hydrostatic pressure field computed by the solution of perturbed mass continuity equation is plotted in **Figure** 6. 36.
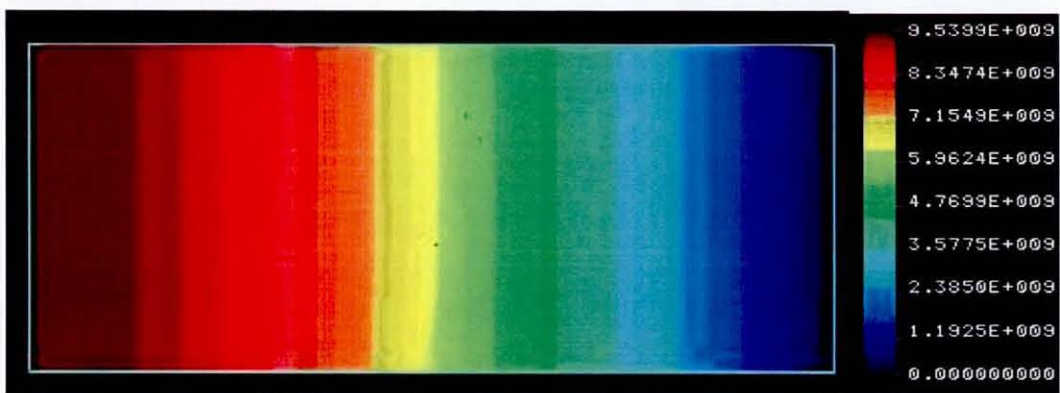
Figure 6. 36: Hydrostatic pressure field in coupled free/porous regime with slant interface

The total pressure drop developed over the domain is calculated to be 9.54×10^6 kPa. The maximum pressure drop is found in the porous region and contributes to around 63% of the total pressure drop. The variations in the pressure values in each elemental layer of free flow region in the flow direction are quite unusual and unexpected. Though the spatial stability in the solutions of free and porous flow equations is attempted to achieve using perturbed form of the continuity equation, in conjunction with equal order interpolation functions, it appears to satisfy the LBB condition sufficiently but not necessarily.

A number of numerical experiments are performed by changing the permeability of porous matrix in each individual case by the order of magnitude of 10 ranging from 10^{-8} m² to 10^{-14} m². The spatially and temporally stable solutions to the governing equations of coupled free/porous flow dynamics are only obtained if proper values of speed of sound and time-step values are chosen as listed in **Table 6. 5.**

Table 6. 5: Stability parameters for coupled flow dynamics with slant interface

No.	Permeability m²	Time step, Δt s	Speed of sound, c_s M s^{-1}
1.	10^{-8}	10^{-8}	4×10^5
2.	10^{-9}	10^{-9}	4×10^6
3.	10^{-10}	10^{-10}	4×10^7
4.	10^{-11}	10^{-11}	4×10^8
5.	10^{-12}	10^{-12}	4×10^9
6.	10^{-13}	10^{-13}	4×10^{10}
7.	10^{-14}	10^{-14}	4×10^{11}

As the permeation characteristics of the porous medium changes, the fluid receives greater resistance for penetration through the bulk of the matrix resulting into increasing pressure differentials. For each value of permeability parameter, the flow field is found to be intact. As the calculation of pressure is accounted by the continuity equation consisting of the term $\dfrac{1}{\rho c^2}\dfrac{\partial p}{\partial t}$, the linked system of

parameters c and Δt, plays an important role in achieving stable and accurate solutions in time domain which is evident from **Table 6. 5.**

One important thing to note that, though the geometrical characteristics, the mesh density and the distribution of elements in the two rectangular domains shown in **Figure 6. 25** and **Figure 6. 34** are exactly the same except the nature of free/porous interface, the value of c used in these two cases are somewhat different. It implies that though the parameter c is not having any direct significance to the underlying physics of coupled flow phenomena, its value significantly affects the simulated fluid dynamics as the mesh parameter h changes. The detailed discussions related to this point are omitted and left for any further investigations in this direction.

6.3.4   Hydrodynamics of coupled free/porous/free flow regime

6.3.4.1   Computational fluid dynamics of rectangular coupled free/porous/free regime

A second free flow region is connected to the coupled domain of **Figure 6. 25** in dead-end mode, in a view of examining the versatility of the numerical linking scheme of **Figure 5.1.** The modified version of the rectangular coupled free/porous domain with prescribed boundary conditions is shown in **Figure 6. 37.**
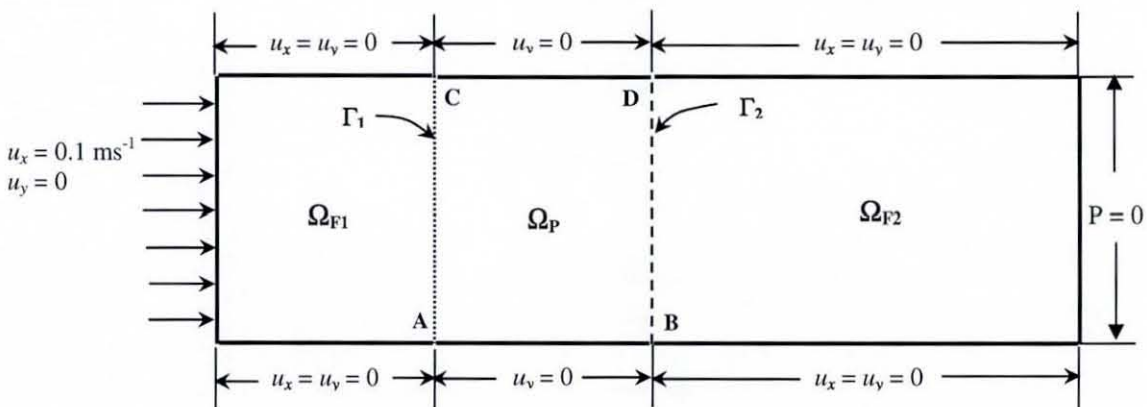
Figure 6. 37: Boundary conditions on rectangular coupled free/porous/free flow domain

Ω_P is an isotropic homogeneous porous medium of permeability 10^{-12} m² sandwiched between two free flow channels Ω_{F1} and Ω_{F2}. The length of the entire domain is 0.0225 m. The first Stokes region is 0.0075 m long; whilst the second stokes region is 0.01125 m long. The Darcy region measures 0.00375 m in length.

A purely Newtonian fluid is allowed to enter the free flow channel Ω_{F1} in plug flow and the exit is fixed with zero pressure to measure a definite value of hydrostatic pressure drop across the overall domain. The incompressible fluid has a density of 970 kg m⁻³ and viscosity at zero shear of 80 Pa s. For the prescribed boundary conditions, stabilised flow field is obtained after 9 time steps of 10^{-12} s and speed of sound, c of 5×10^9 m s⁻¹. The time-stepping parameter in both second-order Taylor-Galerkin method for the Stokes equations and implicit θ method for the Darcy equation is kept greater than 0.9. The stationary flow of fluid has been described by vector arrow plots in **Figure 6. 38.**
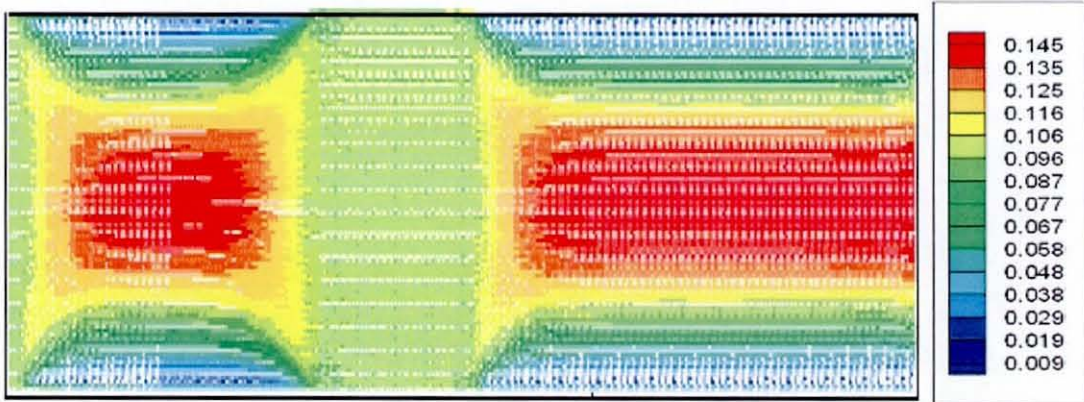
**Figure 6. 38: Steady state flow pattern in rectangular coupled
free/porous/free solution domain**

The fluid readily attains fully developed parabolic flow profile after entering the first free flow region. The rate of change of momentum of the fluid alters after it receives an obstruction by the fine porous barrier Γ_1 and throughout the bulk of the matrix, the fluid remains in plug flow. As the fluid overcomes the second porous/free barrier Γ_2, the fluid receives greater open channel length to retain its fully developed status. The solutions have been validated by performing overall mass balance over the domain which showed a meagre discrepancy of 1.2%.

However, it has been observed that the boundary conditions applied at the interfacial boundary points such as A, B, C and D shown in **Figure 6. 37** play an important role in simulating the fluid flow in the present case. The simulated hydrostatic pressure field of the Cauchy's stress tensor is resolved over the entire computational domain in form of contours in **Figure 6. 39**.
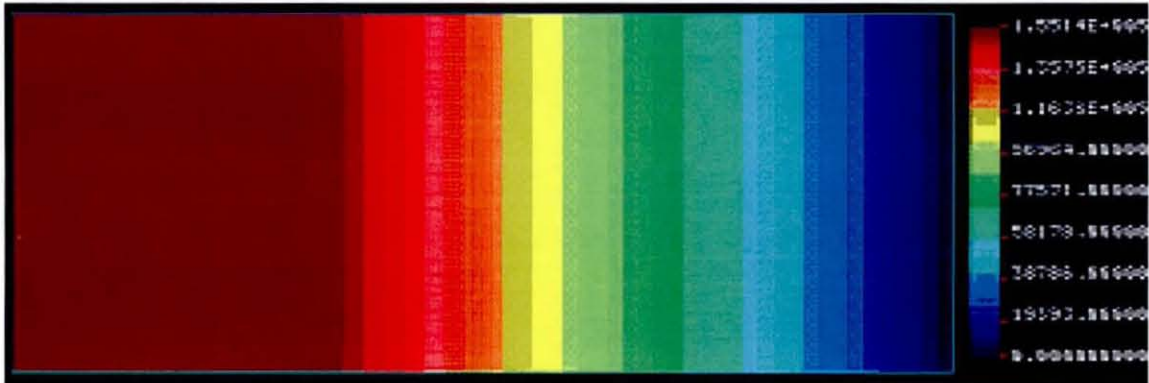
Figure 6. 39: Hydrostatic pressure variations in rectangular combined free/porous/fee coupled domain

In the first free flow channel, the stress associated with the incompressible purely Newtonian fluid is observed to be remaining intact. As the fluid succeeds in crossing the first free/porous barrier Γ_1, it starts losing the viscous stress to the solid porous matrix and as a result, the pressure declines gradually until it again faces the similar situation of overcoming the second porous/free barrier. In the second free flow region, the fluid is expected to retain almost of its total stress throughout the channel. Despite this fact, variations in pressure values are found in the direction of flow.

As a matter of fact, the solution to the pressure field is to the greater extent relies on the proper selection of the mathematical parameters c, Δt and θ. However, the *ad hoc* selection of all the three parameters is not trivial. In most of the cases, temporal instability in results incurs in conjunction with the spatial instability due to improper selection of these parameters. In the present situation, a range of different combinations of c, Δt and θ have been tried and the pressure profile depicted in **Figure 6. 39** has not been improved any further.

As an alternative, mesh refinement has been opted for, to improve the stability in the pressure distribution. The accuracy of every finite element solution relies to certain extent on selection of appropriate meshes. To have an idea about the optimum mesh density generating converged solutions, successive h-version of mesh refinements are carried out in the second free flow channel. The mesh is first refined in the flow direction to duplicate the total number of elements that were present in the parent mesh. No improvements have been found in pressure profile compared to those obtained before the mesh refinement. When the mesh is successively refined to triplicate the number of elements, the same performance is repeated confirming that the solutions obtained with the original mesh were already converged. However, a significant rise in computational time is reported which for the densest mesh is several hours.

6.3.4.2   Computational fluid dynamics in coupled free/porous free/rectangular domain with slant interface

To quantify the effects of nature of free/porous interface on combined flow dynamics, a domain similar to that shown in **Figure 6. 37** is considered except that the first free/porous flow interface is inclined to 5^0 to x-coordinate direction as shown in **Figure 6. 40**.
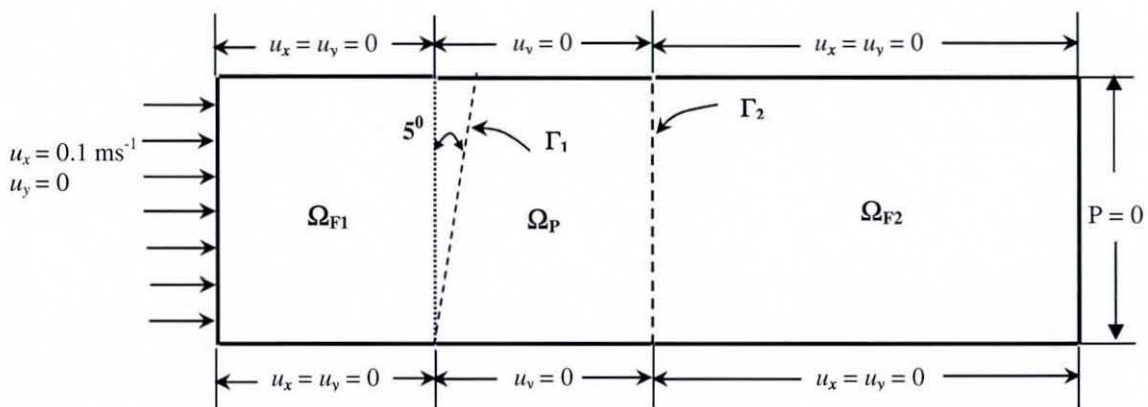
Figure 6. 40: Boundary conditions on rectangular coupled free/porous/free flow domain with slant interface

The boundary constraints imposed on the domain exactly replicated those prescribed on the periphery of domain in **Figure 6. 37**. For obtaining oscillations-free stationary solutions as in the previous case, the values of Δt and θ are kept constant at 10^{-12} s and 0.95 respectively and the value of speed of sound, c is modified to 4×10^9 m s^{-1}. With all these boundary values and numerical data, the simulated flow field over the domain is expressed as in **Figure 6. 41**.
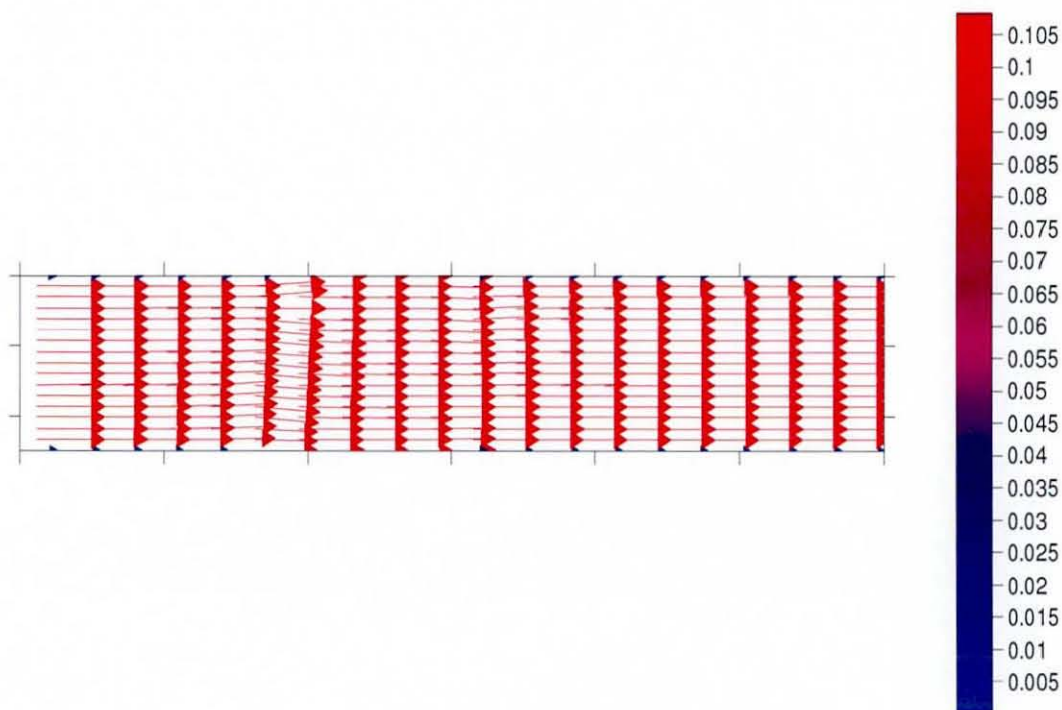
Figure 6. 41: Simulated flow field over rectangular coupled free/porous/free domain with slant interface

The flow throughout the computational domain is in plug flow which is in contradiction to the profile shown in **Figure 6. 38**. The nature of free/porous barrier has greatly influenced the flow field within the solution domain. The velocity values at the interfacial boundary points A, B, C and D in **Figure 6. 40** are comparatively higher than any point in the domain and are greatly affected by the nature of boundary constraints applied. The mass continuity in the flow is found to be preserved satisfactorily with just 0.3% positive discrepancy. However, the numerical solutions pertaining to the pressure variations don't seem to be compliant with the physical fundamentals of the overall process. The inadequacy

of the perturbed continuity scheme for the present problem has been clearly understood from the nature of pressure field distribution over the domain in **Figure** 6. 42.
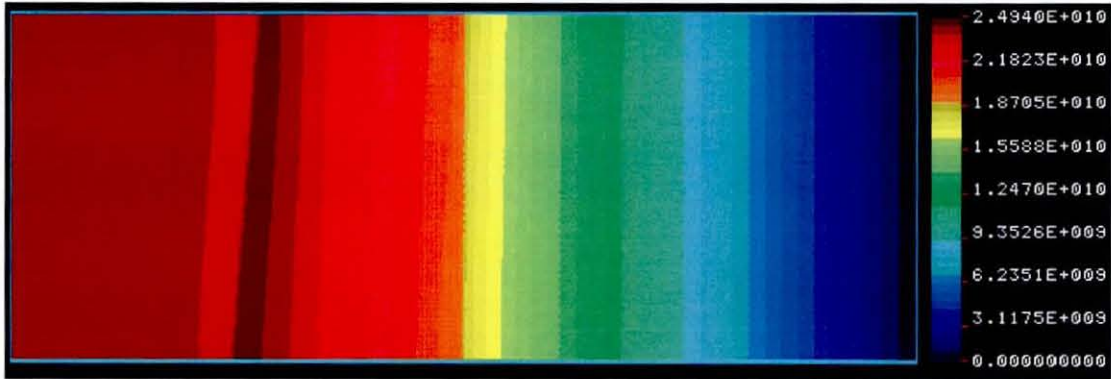
Figure 6. 42: Hydrostatic pressure field in rectangular coupled free/porous/free domain with slant interface

The pressure variations in the first free flow region Ω_{F1} are not significant till the fluid approaches the free/porous barrier Γ_1. In the bulk of the porous matrix, pressure gradients are observed in the flow direction. However, the pressure field in the second free flow channel also experiences gradients very similar to that in **Figure** 6. 39. This kind of spatial instability has not been resolved by various combinations of c, Δt and θ. In addition, successive h-version of mesh refinements could not improve the results to the greater extent.

6.3.4.3   Computational fluid dynamics in coupled free/porous/free quarter circular domain

In the third case, the solution domain is concentric quarter circular region which resembles a symmetric part of tubular membrane dead-end ultrafiltration or microfiltration module. The fluid enters the filtration module through the outer metal hollow casing and gets distributed uniformly over the periphery and penetrates through concentric circular porous medium having a definite thickness. The clean filtered fluid leaves the module through the inner hollow perforated

core. The boundary conditions chosen to simulate fluid dynamics in the domain have been presented in **Figure 6. 43.**
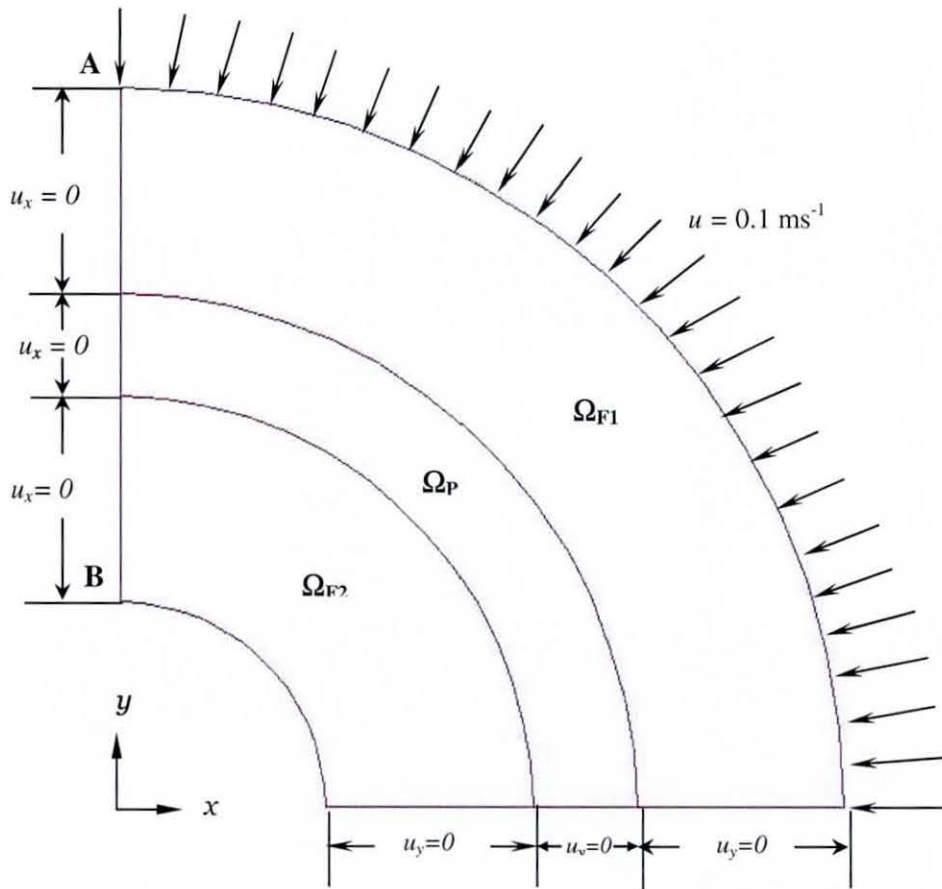
Figure 6. 43: Boundary conditions on concentric quarter circular coupled free/porous/free flow domain

The thickness of first Stokes region is 0.003 m whilst the second Stokes region measures 0.0126 m in thickness. The thickness of the Darcy region is 0.0004 m. The computational mesh with optimum mesh density consists of 4700 elements accompanied by 19311 numbers of nodal points. The distribution of elements in the Stokes and Darcy regimes is in the proportion of 54:1. As the variations in all the field variables are presumed to be significant near the interfaces, mesh is densely refined in those regions as visible from **Figure 6. 44.**
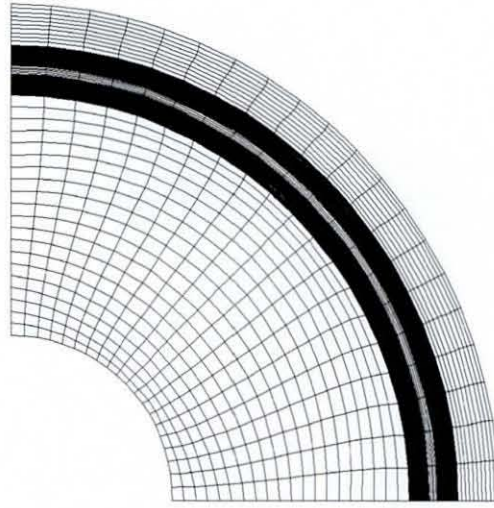
**Figure 6. 44: Computational mesh for concentric quarter circular
free/porous/free coupled flow domain**

The fluid being filtered is an incompressible homogeneous dilatent fluid.
The density of the fluid is 970 kg m^{-3} and the values of consistency coefficient and
power law index are 80 Pa s and 1.15, respectively. To imply the symmetry across
the boundaries AB and BC, the outflow normal to these boundaries is restricted.
The mean flow path of fluid through this microfiltration module can be visualised
from the normal velocity vectors in **Figure 6. 45**.
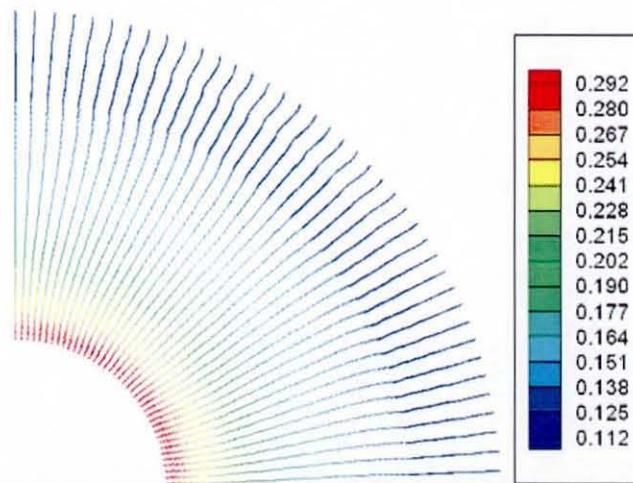
**Figure 6. 45: Steady state velocity profile in concentric quarter circular
coupled free/porous/free domain**

A stable velocity profile is obtained for the time-step value, Δt of 10^{-11} s and speed of sound c of 5×10^9 m s^{-1}. The value of time-stepping parameter θ in second order Taylor-Galerkin formulation for the Stokes equation and implicit-θ formulation of Darcy equation is kept at 0.75. The velocity increases from inlet to outlet as the fluid receives less available cross-sectional area for the flow. As observed from **Figure 6. 45**, the magnitude of velocity at the exit cross-section is almost thrice that of the inlet fluid. The mass balance calculations show a negative discrepancy of 0.3% revealing the mass conservation. The hydrostatic pressure field computed by **CFDYNAMICS** is plotted in **Figure 6. 46**.
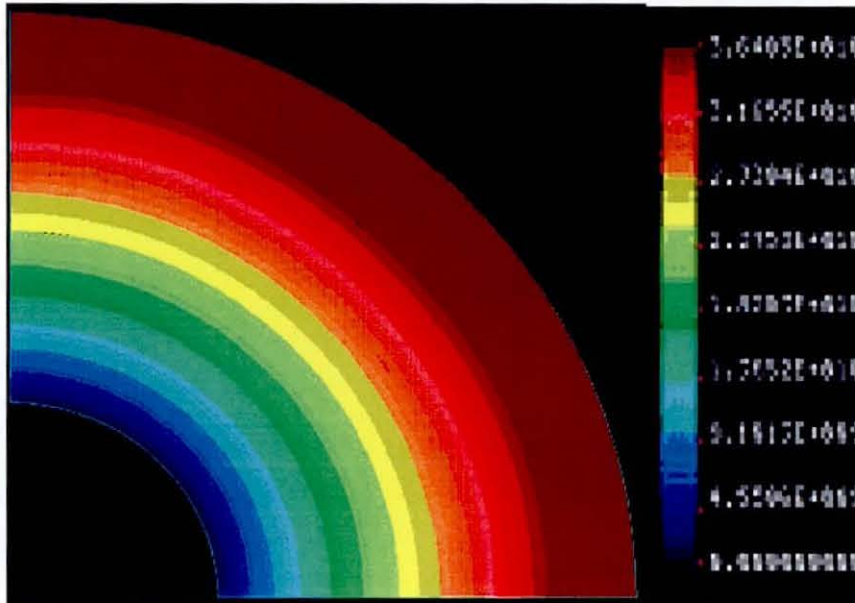
Figure 6. 46: Hydrostatic pressure field in concentric quarter circular coupled free/porous/free flow domain

The pressure in the outer hollow metal casing is almost invariant. As the fluid succeeds in crossing the first free/porous barrier, the pressure gradually decreases during the course of flow throughout the porous matrix. In the inner hollow metal core, the flow is expected to retain its stress, however significant pressure gradients are observed similar to the previous case shown in **Figure 6. 42**. The simulated pressure distribution is observed to be insensitive for different temporal approximations by selecting different values of parameters c, Δt and θ. In the second free-flow region Ω_{F2}, the extent of spatial approximation has been tried

to improve by mesh refinement which signified no further improvement in results, however deteriorated the computational economy.

6.3.4.4   Computational fluid dynamics of concentric circular coupled free/porous/free flow domain

From the previous cases, it can be inferred that the numerical algorithm based on the perturbed continuity equation with equal order velocity-pressure interpolations exhibited its shortcoming in calculating the accurate pressure field when dealt with irregular geometries of flow domain. To provide more supportive evidence to the above conclusion, a flow situation is considered in an extended version of flow domain considered previously in **Figure 6. 43**.
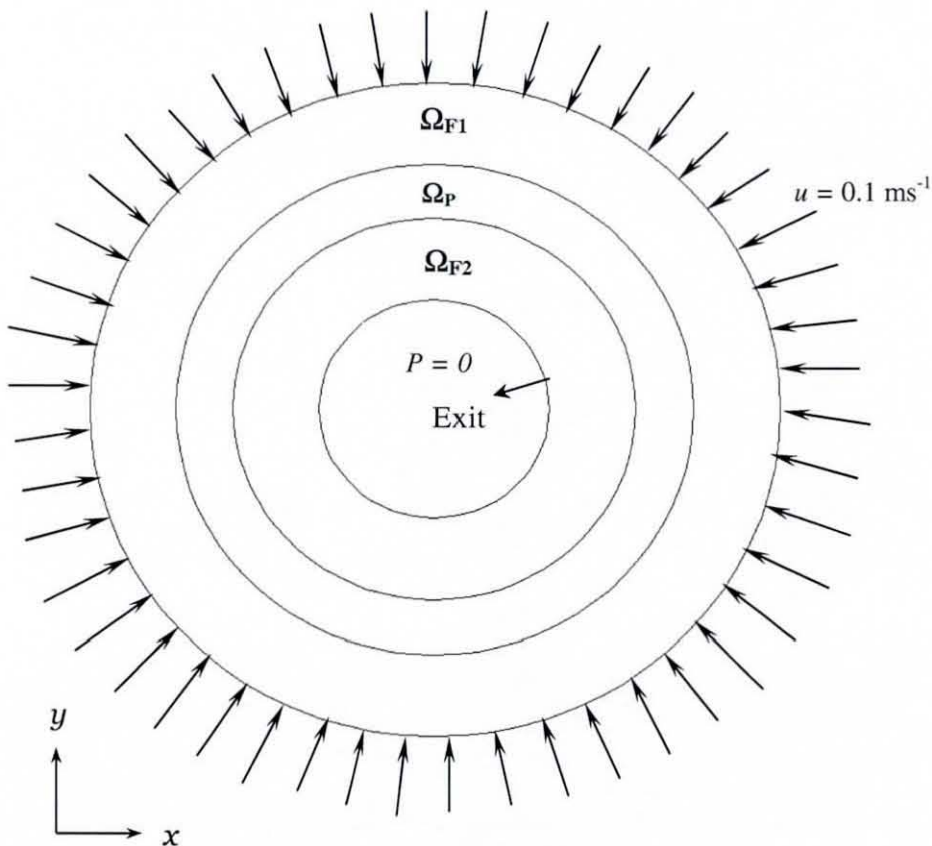
Figure 6. 47: Boundary conditions on concentric circular combined free/porous/free flow domain

With centre of the overall flow domain at the origin of coordinate axes, the external radii of the regions Ω_{F1}, Ω_P and Ω_{F2} are 0.020 m, 0.012 m and 0.008 m, respectively in **Figure 6. 47**. The total number of nodal points in the computational mesh counts to be 9760 corresponding to 2400 number of 9-noded C^0-continuous isoparametric elements. The number of elements associated with porous region Ω_P are 480 and equal number of elements are distributed in both the free flow regions.

Normal velocity boundary conditions are imposed uniformly at the inlet of the domain. The fluid in the present case, possesses the same physical and rheological properties as that considered in the quarter domain analysis. The flow field simulated using the values of c, Δt and θ of 10^7 m s^{-1}, 10^{-12} s and 0.99 respectively is presented in **Figure 6. 48**.
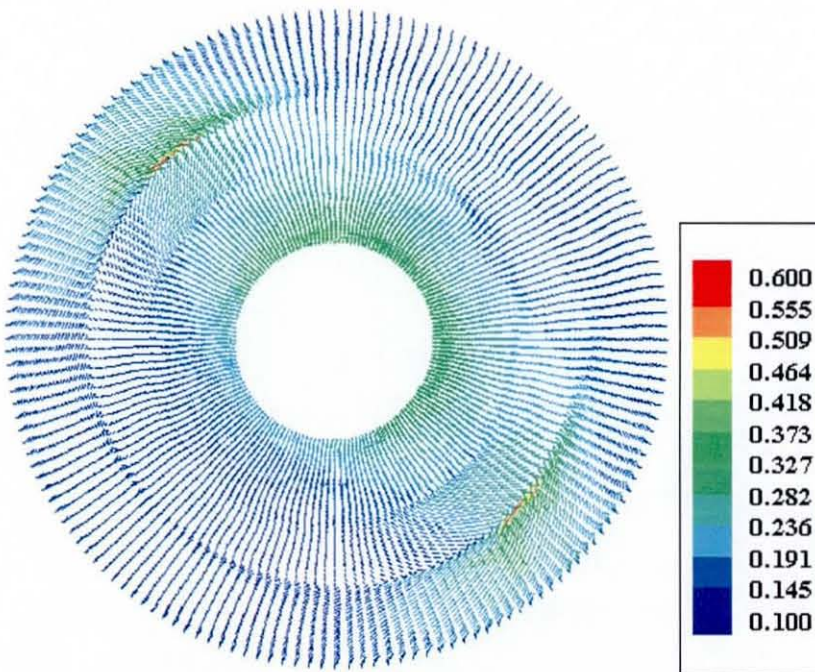
Figure 6. 48: Simulated velocity profile in concentric circular coupled free/porous/free flow domain

The flow profile is completely unsymmetrical showing inaccuracy and spatial instability in the results. The mass continuity is found to be violated over the entire computational domain exhibiting the theoretical inconsistency of the

results. At the first free/porous interface, extremely high velocity values are observed signifying the inability of the numerical scheme in linking the Stokes and Darcy equations on such curved interfaces. The pressure field also shows spurious deteriorations over the entire computational domain as shown in **Figure 6. 49.**
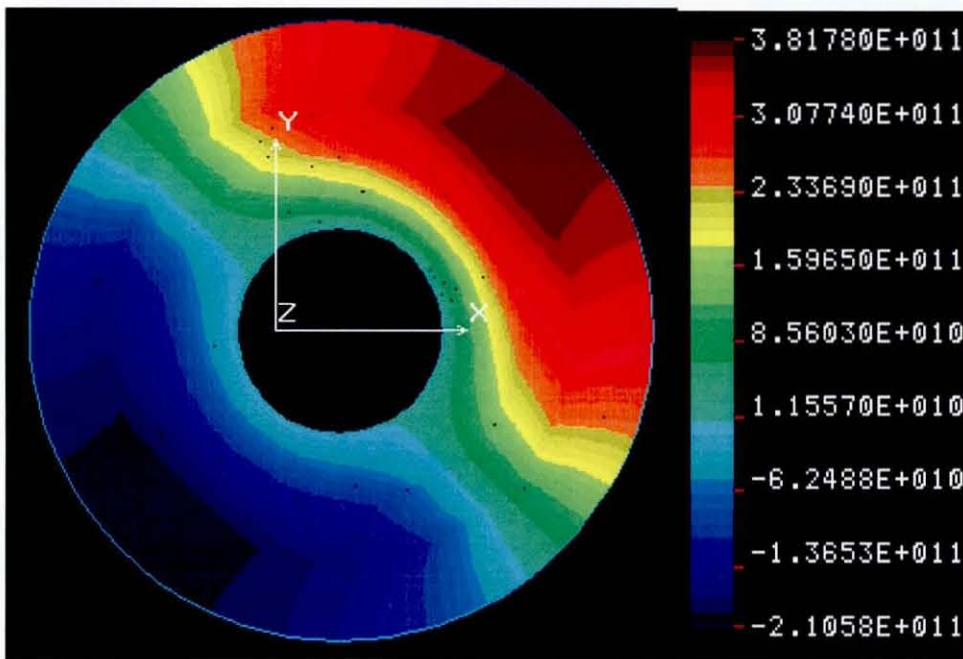
Figure 6. 49: Simulated pressure variations in concentric circular coupled free/porous/free flow domain

Similar to the flow profile, the variation of simulated pressures in this symmetrical domain in response to the symmetrical inlet velocity boundary condition, is totally unsymmetrical which is completely unjustified on the grounds of physics and mathematical analyses of the finite element scheme involved in the computations. To achieve the temporal as well as spatial stability, smoothing is carried out using various combinations of stability parameters associated with perturbed continuity scheme which fails to circumvent the oscillations.

As a routine alternative, mesh refinement is performed in each of the flow regions successively which proved to be ineffective in ameliorating the quality of the numerical solution. On the contrary, with the refined mesh, the computational time requited for a single iteration is now measured in several hours.

6.3.4.5   Computational fluid dynamics of rectangular coupled free/porous/free flow regime with curved interfaces

If the flow regimes in the pleated cartridge filter domain are considered, the free/porous interfaces are curved due to highly complex geometrical structure of pleat. With no aim of being directly involved in such a complicated situation at this moment, we consider a domain with curved interface as shown in **Figure 6. 50**.
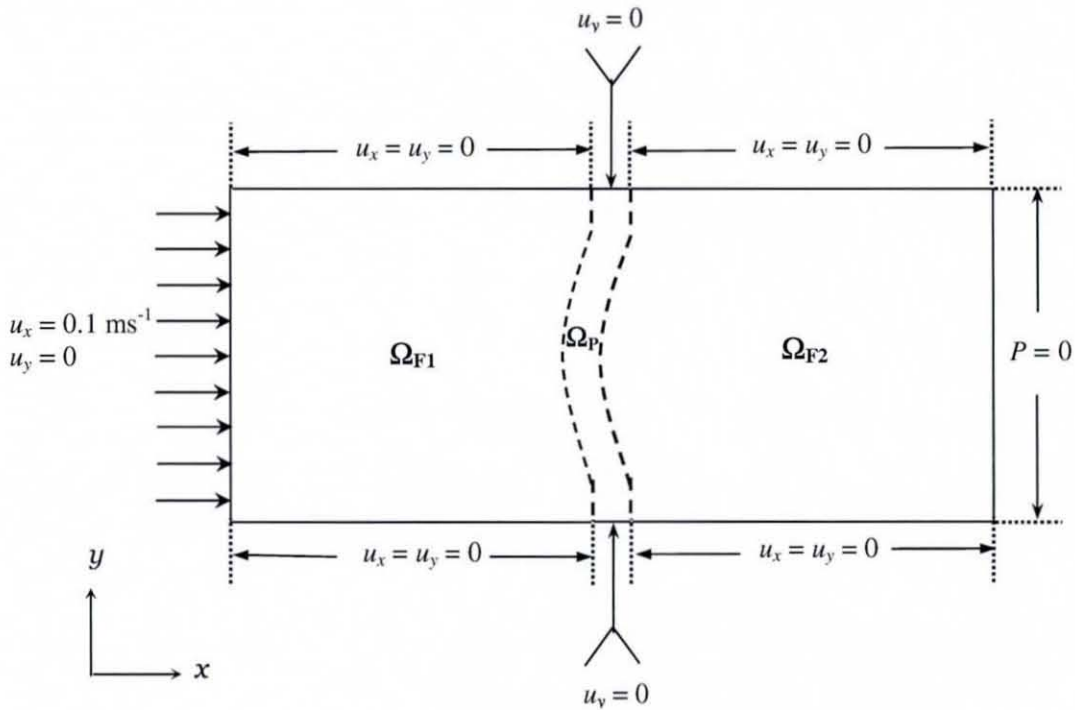
Figure 6. 50: Boundary conditions on the rectangular coupled free/porous/free flow domain with curved interface

The complete rectangular domain Ω has been divided into two free flow channels Ω_{F1} and Ω_{F2} by a porous medium having curvilinear geometry. The length of each of the free flow regions are 0.07 m while the thickness of the porous medium is 0.003 m. The flow domain Ω measures 0.035 m in width a definite breadth in the perpendicular direction. The computational domain is tessellated into a finite element mesh containing 5658 number of elements with 22971 number of associated nodes. The distribution of elements in the Stokes and the Darcy regime is in the proportion of 40:1.

The fluid is a purely Newtonian material with density of 970 kg m^{-3} and viscosity of 80 Pa s. The isotropic permeability of the homogeneous porous medium is 10^{-12} m^2. Responding to the boundary conditions mentioned in **Figure 6. 50**, the fluid finds its path through the combined domain as shown in **Figure 6. 51**.
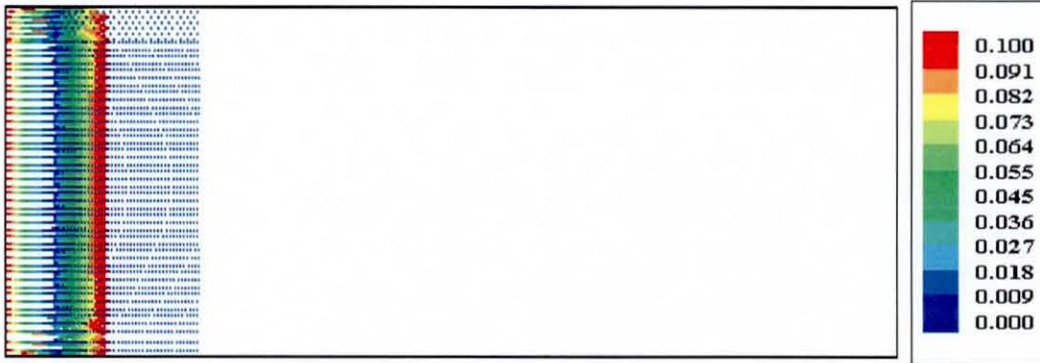
Figure 6. 51: Fluid flow in rectangular coupled free/porous/free domain with curved interface

The fluid entering the domain is observed to be being lost after covering a short distance from the entrance. The flow is not capable of reaching the free/porous barrier. The same behaviour has been reflected in the pressure variations over every nodal point of the domain as shown in **Figure 6. 52**.
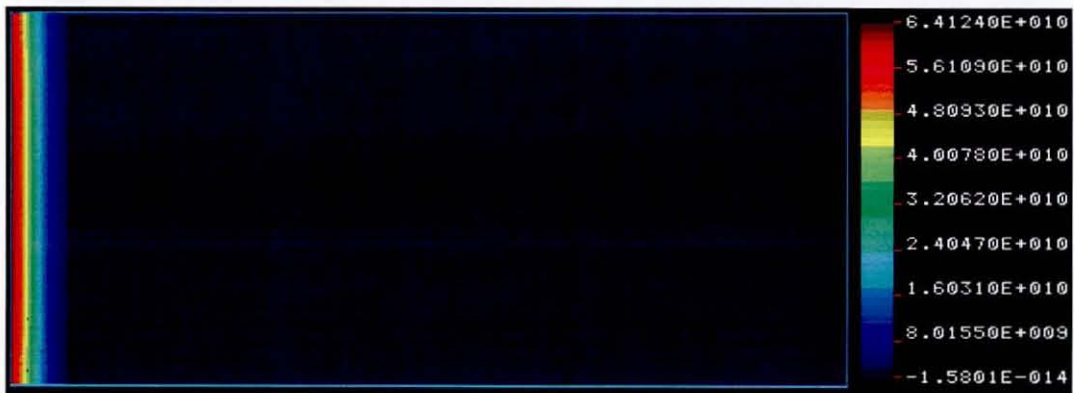
Figure 6. 52: Hydrostatic pressure variations in rectangular coupled free/porous/free flow domain with curved interfaces

Highly steep pressure gradients are observed in the region nearest to the entrance of the domain. The magnitudes of the hydrostatic pressures vary considerable within a range of order of magnitudes of 10^{10} to 10^{-14} Pa in this region. The computed results are found to be completely insensitive to the numerical parameters c, Δt and θ. In addition, the mesh refinement is found to be unsuccessful and economically unfeasible in minimising these detrimental effects on velocity and pressure variations.

6.3.5 Critical assessment of perturbed continuity method

In the incompressible flow simulations by the finite element method, choice of approximating spaces for velocity and pressure is a crucial point to be addressed. As the velocities are divergence free, the absence of pressure term in the equation of continuity, restricts the selection of these approximating spaces. To achieve stability in the solutions of incompressible flow equations, it is a necessary and sufficient condition that the order of interpolation functions for pressure should always be lower than that of velocity interpolations, as explained with the essence of mathematics by LBB stability criterion.

The perturbed continuity method as first put forward by Zienkiewicz and Wu (1991), facilitates the use of equal order interpolation functions for velocity and pressure, however necessitates the addition of a temporal differential term such as $\dfrac{1}{\rho c^2}\dfrac{\partial p}{\partial t}$ in the equation of continuity. The inclusion of this term signifies the fluid to be slightly compressible and the incompressibility can only be asymptotically approached by selecting proper values of the speed of sound c and time-step values Δt in temporal discretisations. In addition, this pseudo-compressible term forces the addition of temporal derivatives of velocity in the equations of motion. Though the perturbed continuity scheme pacifies to some extent the LBB spatial stability restriction, it creates severe concern about temporal stability due to the incorporation of time-differential terms.

The results presented using the perturbed continuity approach shows stable, accurate and converged solutions for simple geometrical flow domains. The stability and accuracy of the steady state solutions are found to be highly sensitive

towards the values of numerical parameters c and Δt. Since the underlying physics of the incompressible flow problems have been compromised for numerical simplicity, he computational results generated by finite element approximations are in someway erroneous. Normally, the accuracy of the approximations improves by successive mesh refinements. However, in case of the numerical analysis using perturbed continuity method, the approximating error gets cumulatively added per each elemental domain and finally on the scale of the overall solution domain, this error shows a large magnitude. In almost all of the problems considered, the global mass continuity calculated over the entire computational domain is found to be conserved. Despite this fact, the continuity is violated for solutions considered over each individual elemental domain. Therefore, the pressure distribution obtained from the individual Stokes and Darcy equations shows unusual gradients in the flow direction.

In the coupled flow simulations, the solutions obtained using the perturbed continuity scheme shows a critical parametric sensitivity for the selection of c and Δt. The selection of these parameters is highly dependent of mesh parameter, mesh density and geometrical characteristics of the solution domain and can be carried out only by ad hoc trial and error.

"The perturbed continuity method can generate stable and accurate solutions for coupled flow dynamics in simple domain geometries and fails to cope with complex and irregular solution domains."

It was interesting point to note that though the parameter c has no direct linkage to the incompressible flow phenomena, its selection makes a remarkable influence on stability and accuracy of solutions. The temporal discretisations of Stokes and the Darcy equations have been carried out by second order Taylor-Galerkin and first order implicit-θ method respectively. Unfortunately, the temporal approximations were found to be inadequate for the coupled flow simulations. Though the time-step values Δt used in the simulations are extremely small, a small variation in them can prove to be detrimental, generating spurious oscillations. The conclusion was that this scheme perhaps could only generate stable and accurate solutions in complex geometries if more sophisticated time-stepping schemes such as predictor-corrector time-stepping methods (Townsend and Webster, 1987) or adaptive time stepping methods (Donea and Huerta, 2003) have been implemented. A detailed mathematical analysis of this ambiguous

situation is highly requisite however, omitted here taking into consideration the scope of the present work.

6.4 UVP scheme with Taylor-Hood method

In the context of LBB stability criterion, finite element numerical formulations have been derived based on mixed order approximating spaces for velocity and pressure. The velocities are discretised by bi-quadratic interpolation functions while pressure is approximated by bilinear interpolation functions. Quadrilateral finite elements with Q2/Q1 interpolation functions are the lowest members of the bubble element family. Numerical solutions have been generated for hydrodynamics in free and porous regimes, individually. The same algorithm is then implemented to simulate coupled free and porous flow dynamics in a variety of solution domains.

6.4.1 Hydrodynamics of free flow regime

6.4.1.1   Flow through a rectangular duct

As the simplest case, an incompressible flow through a two-dimensional rectangular duct is considered as a problem under consideration. The domain measures 0.015 m in length in the flow direction and 0.005 m in the longitudinal direction. The domain with its imposed boundary conditions has been plotted in **Figure 6. 53.**
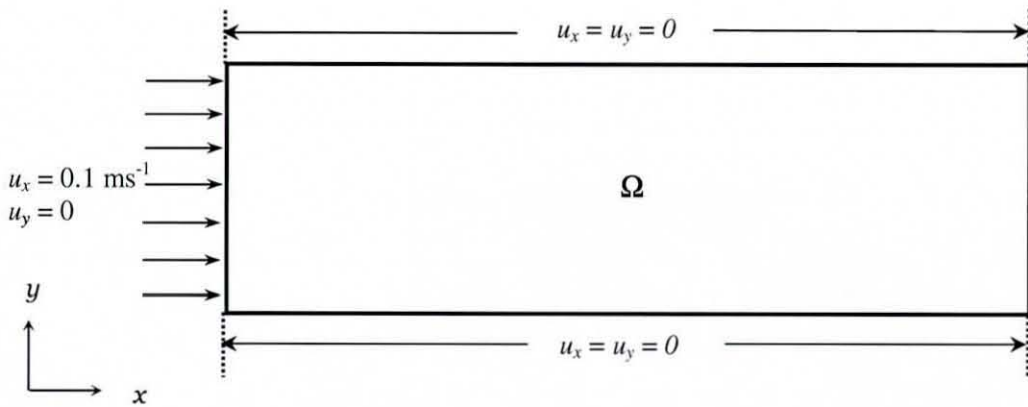
Figure 6. 53: Boundary conditions on rectangular free flow duct

A purely Newtonian fluid enters the channel in plug flow and the exit of the domain is kept stress-free. In the finite element approximations using mixed order interpolation functions, the imposition of pressure boundary condition is not generally requisite. The fluid has a consistency coefficient of 80 Pa s and power law index of 1.0. The steady state simulated flow path for this incompressible flow of fluid having density of 970 kg m^{-3} is shown in **Figure 6. 54**.
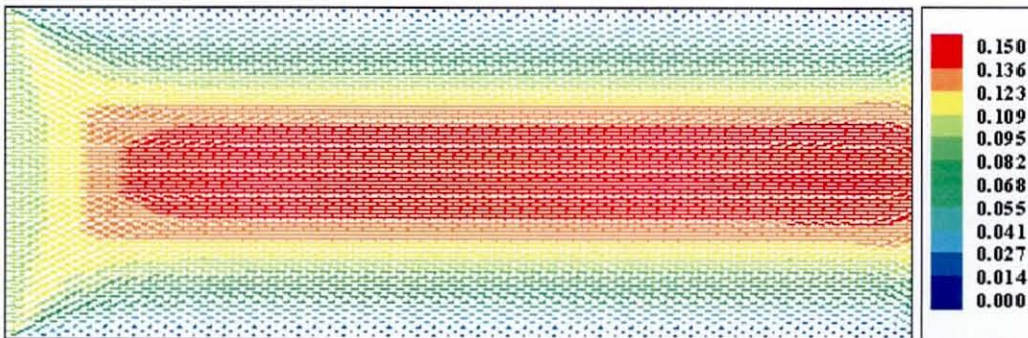
Figure 6. 54: Velocity profile in free flow channel using Taylor-Hood scheme

The flow is observed to be fully developed throughout the length of the channel with maximum velocity observed at the centreline to be 0.15 m s^{-1}. The corresponding pressure variations in the channel are shown in **Figure 6. 55**.
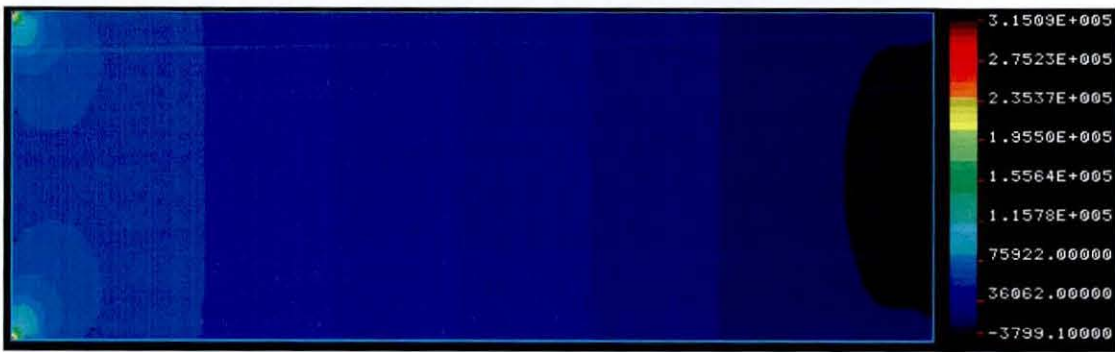
Figure 6. 55: Simulated pressure distribution in rectangular free flow duct

The variation in pressure values over the channel length is not very significant. However, the entrance effects are significantly visible resulting from the application of boundary conditions at the corner points. The simulated results can be validated for consistency using commercial CFD software **FEMLAB** using the identical mixed order P2/P1 interpolation functions with triangular finite elements. For the same imposed boundary conditions and material properties, the velocity profile generated using **FEMLAB** is shown in **Figure 6. 56**.
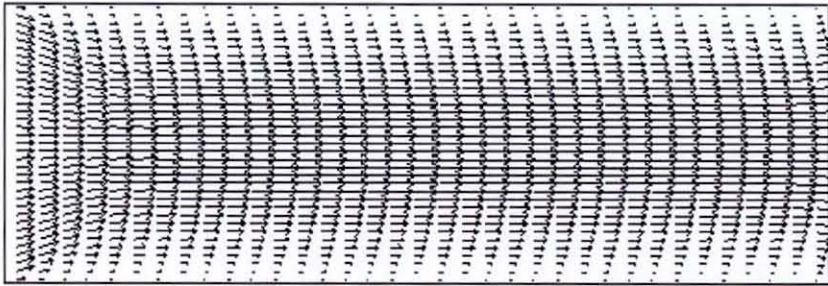
Figure 6. 56: Simulated flow field in rectangular free flow duct generated using FEMLAB

The vector lengths are in proportion with the magnitude of velocity values. The profile is the exact resemblance of the profile generated by the numerical solution algorithm **CFDYNAMICS**. The maximum value of velocity at the centreline of channel is found to be 0.152 m s^{-1}. The maximum value of cell

Reynolds number is 4.65×10^{-4}. The corresponding hydrostatic pressure field calculated by **FEMLAB** is shown in **Figure 6. 57**.
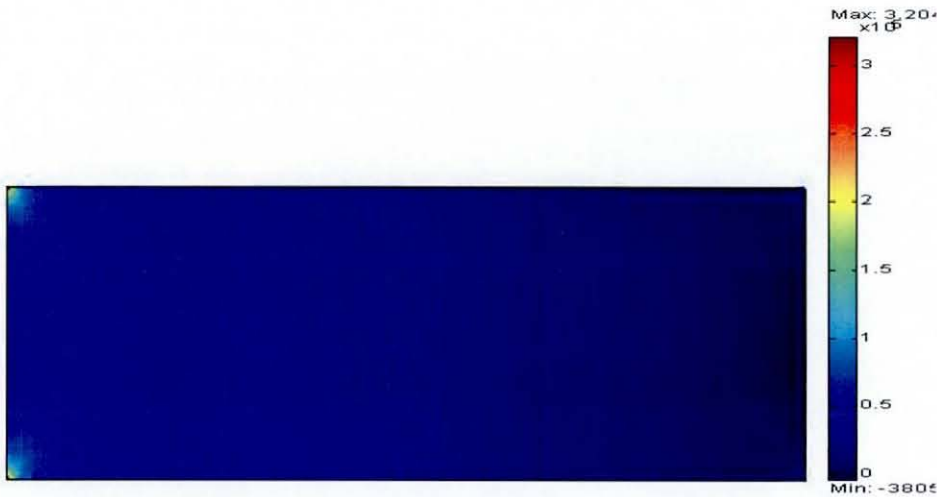
Figure 6. 57: Pressure variations in free flow duct computed using FEMLAB

There are high pressure contours found near the entrance point corners resulting from singularity at those nodal points. The pressure profile exactly replicated that of the simulated profile shown in **Figure 6. 55** in nature and magnitude of pressure, as visible in the colour scale.

6.4.1.2   Flow through a microreactor containing catalyst cylinder

In the second case, a microreactor channel is considered as a flow domain containing a centrally located catalytically active cylinder. The hydrodynamics and heat transfer analysis within this microreactor channel has been already explained in the work of Waghode *et al.* (2005). The details of the microreactor assembly with the required boundary conditions can be understood from **Figure 6. 58**.
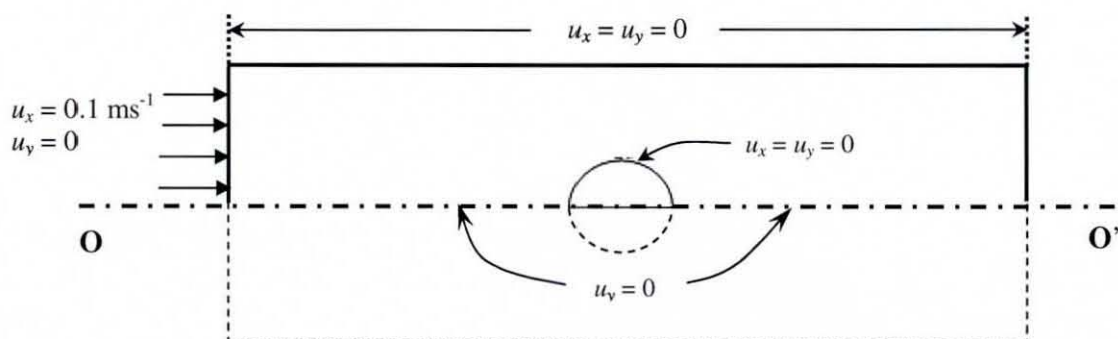
Figure 6. 58: Boundary conditions on symmetrical domain of channel microreactor with centrally located catalytically active cylinder

The channel microreactor is supposed to be used for decomposition of ammonia for the production of hydrogen for Proton Exchange Membrane (PEM) fuel cell application. The channel measures 0.295 m in length and 0.02 m in width in longitudinal direction. The reaction takes place on the surface of catalytically active cylinder impregnated with monolayer Ni catalyst which is located centrally in the channel The cylinder measures 0.01 m in diameter and 0.01 m in width in the perpendicular z-direction.

Since the decomposition of ammonia is carried out at low pressure, assumption that the homogeneous gaseous mixture is incompressible is quite reasonable. The density of the inlet fluid containing ideal gases is 0.77 kg m^{-3} and viscosity of 1.28×10^{-5} Pa s at the reaction temperature of 873 K.

The reacting gas ammonia and the inert carrier argon enter the reactor in equimolar proportion with a velocity of 0.1 m s^{-1}. No-slip wall boundary conditions are prescribed on the surface of catalytically active cylinder. The exit section of the reactor is restrained by applying the neutral boundary condition. Taking into consideration the symmetry of the domain along the x-coordinate axis, line of symmetry boundary conditions are imposed on the axis of symmetry OO'. The flow profile simulated by the Stokes equation solver subroutine of **CFDYNAMICS** is shown in **Figure 6. 59.**
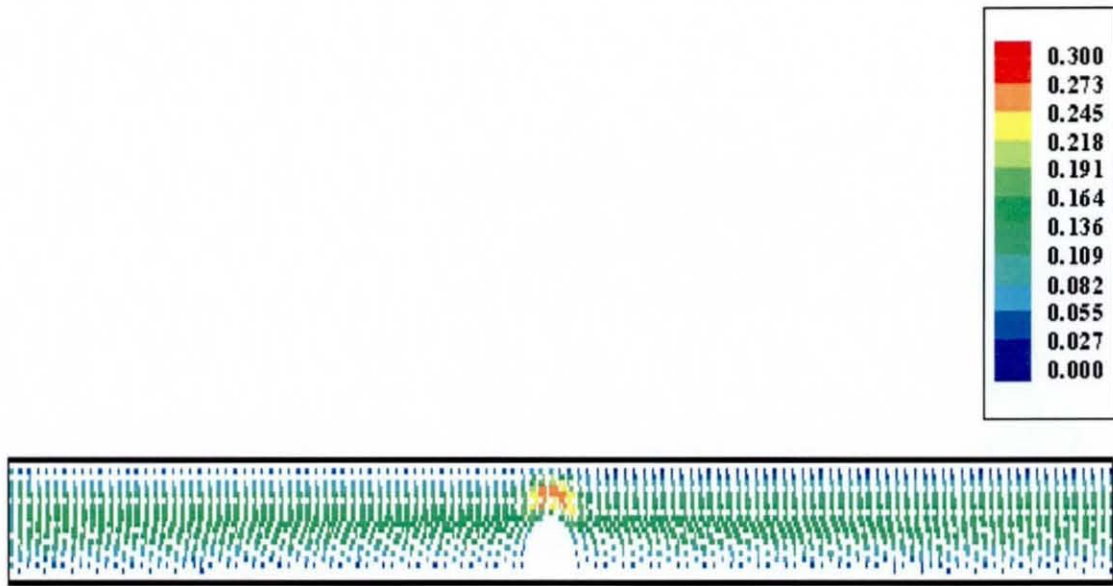
Figure 6. 59: Simulated flow field in microreactor with centrally located catalytically active cylinder

The flow throughout the domain is observed to be fully developed which is evident from the parabolic velocity profile. The velocity values in the narrow gap between the cylinder and the domain walls are maximum due the channelling effect. The resulting pressure field distribution over the domain is shown in **Figure 6. 60**. All the pressure values are in Pa, gradually decreasing in the direction of flow The channelling near the catalytic cylinder, observed from the velocity profile, is also reflected in the pressure contours.
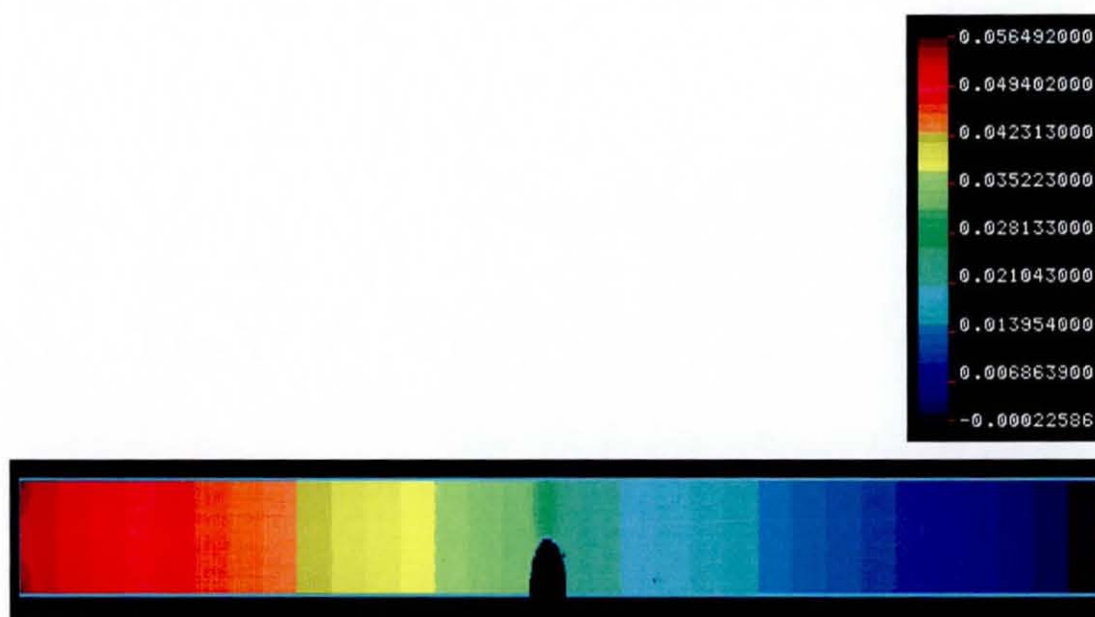
Figure 6. 60: Variations in pressure values in microreactor with centrally located catalytically active cylinder

In the surroundings of the catalytic cylinder, a narrow orifice like channel is formed confined by the microreactor wall. Due to the interconversion of pressure energy into kinetic energy and vice-versa in vicinity of this catalyst section, the pressure values in the overall domain are observed to be changing and the hydrostatic pressure drop is calculated to be 0.055 Pa.

With the aim of checking the accuracy and validity of the computational algorithm, the results are compared against the simulated results generated by **FEMLAB** using the mixed order of interpolation functions. The simulated flow field, post-processed in **FEMLAB** in the form of unicoloured vectors is shown in **Figure 6. 61**.

Figure 6. 61: Pressure field simulated by FEMLAB in microreactor with catalytically active catalyst cylinder

The profile shows fully developed flow throughout the length of the reactor. The channelling effect shown in **Figure 6. 59** is found to be replicated in **Figure 6. 61**. The application of symmetric boundary conditions is proven to appropriate and well implemented. The validity of the Stokes flow solution algorithm based on Taylor-Hood elements is further confirmed by the pressure distribution obtained using **FEMLAB** which is presented in **Figure 6. 62** below.
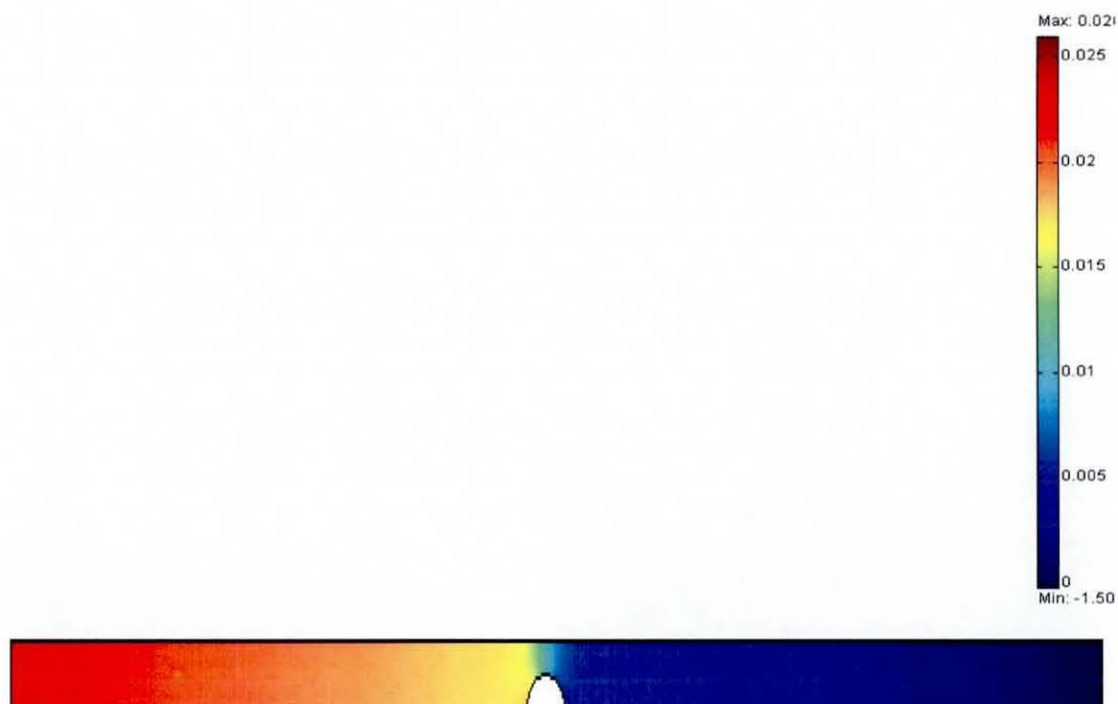
Figure 6. 62: Pressure distribution in microreactor with centrally located catalytically active cylinder generated using FEMLAB

6.4.2 Hydrodynamics of porous flow regime

6.4.2.1 Flow through a rectangular porous matrix

To examine the performance and validity of the Darcy solver of **CFDYNAMICS** to compute the porous flow dynamics using weighted residual finite element technique with unequal order interpolations, a 2-dimensional simple rectangular porous matrix is considered as a test flow domain. The domain measures 0.015 m of flow length with 0.005 m in width and has a definite thickness in the z-direction. The necessary physical boundary conditions associated with the Darcy equation and those requisite by the numerical technique are shown in **Figure 6. 63**.
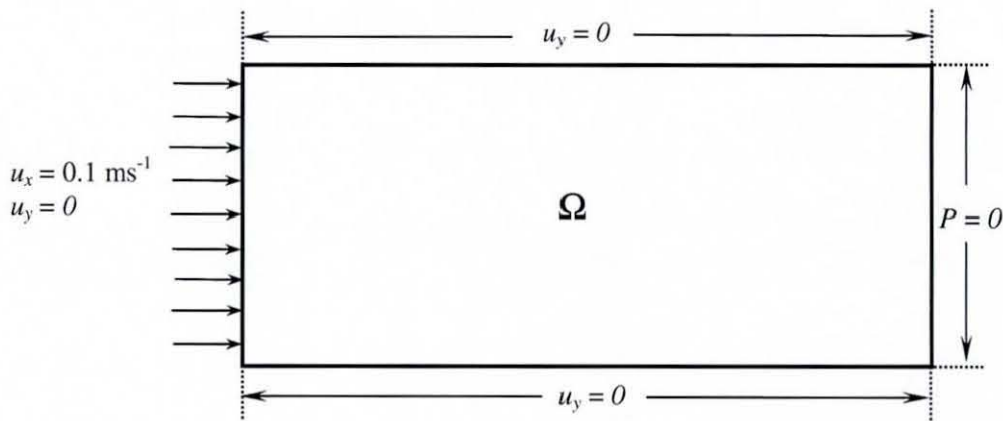
Figure 6. 63: Boundary conditions imposed on the rectangular porous matrix domain

The fluid is a purely Newtonian incompressible medium with density of 970 kg m^{-3} and constant viscosity of 80 Pa s. As the flow through the bulk of the porous matrix is driven by the pressure differential, the exit of the domain is confined by applying a zero pressure datum to measure the hydrostatic pressure drop. The simulated hydrodynamics in the bulk of the porous matrix is shown in **Figure 6. 64**.
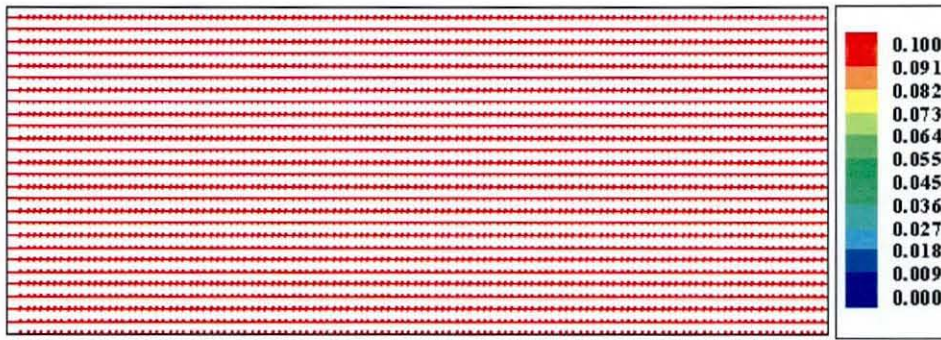
Figure 6. 64: Simulated flow field over rectangular porous matrix

The flow throughout the solution domain is found to be uniform in plug flow. From the flow domain configuration and applied boundary conditions, the problem could be considered as a one-dimensional flow situation. The y-component of the Darcy equation can be neglected and the x-component takes the form as,

Error! Objects cannot be created from editing field codes.
(6. 15)

Where,

Δp is the pressure differential and Δx is the length of the flow path whose maximum value is the thickness of the porous medium. Inserting the values of parameters in equation **(6.15)**, the pressure drop developed across the porous matrix is calculated to be 1.2×10^{10} Pa. On the other hand, the simulated pressure variations obtained at the nodal points are shown in **Figure 6. 65**.
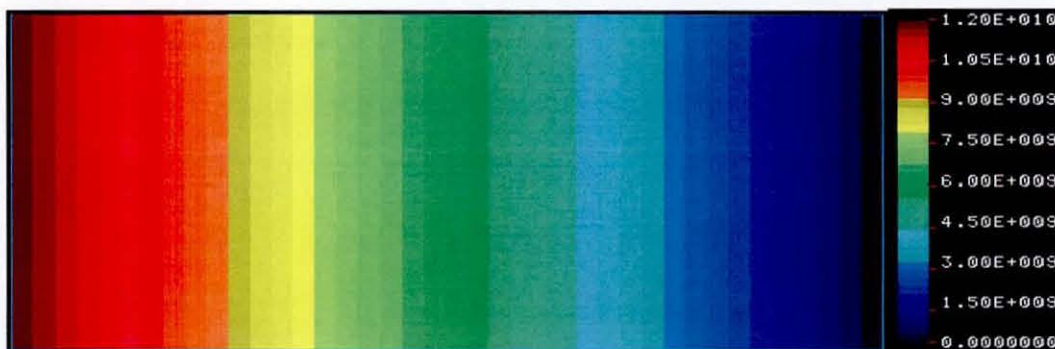
Figure 6. 65: Simulated pressure field in porous rectangular matrix

As the fluid finds its path through the bulk porous medium, the pressure values decline gradually. The viscous stress associated with the fluid gets dissipated to the solid matrix due to the boundary layer separation caused by the fine pores of micron size. The simulated pressure differential developed across the medium is found to be 1.2×10^{10} Pa which is perfectly equal to its analytical value calculated from the Darcy equation.

6.4.2.2　　Flow through a composite porous media

A composite porous matrix composed of two different porous materials having distinct permeation characteristics is considered as a test flow domain for the Darcy equation solver. The T-shaped composite porous matrix is described in **Figure 6. 66** with its adjunct boundary conditions.
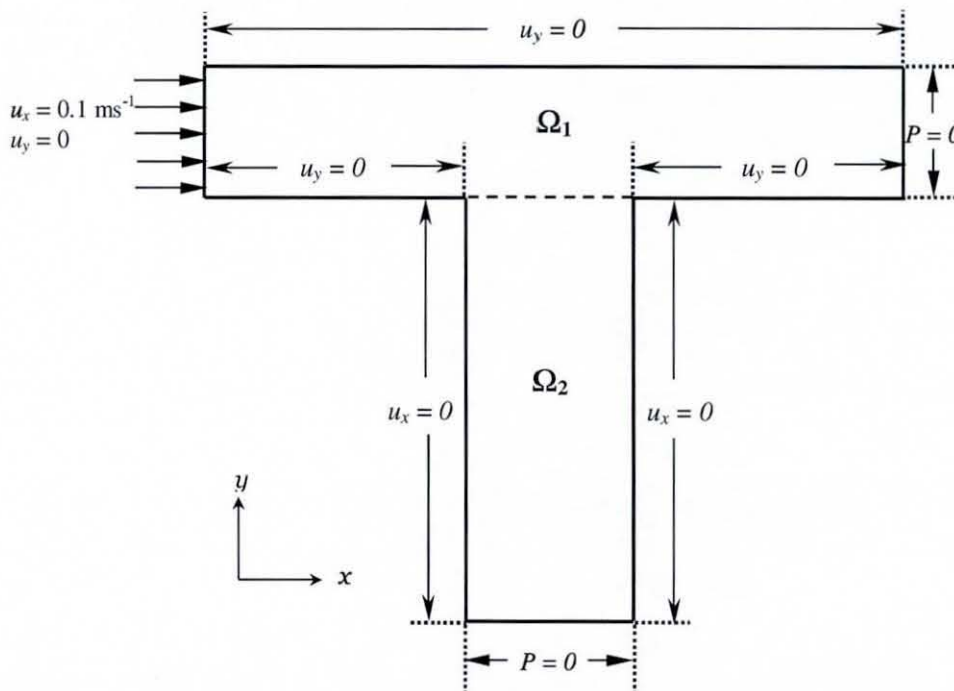
Figure 6. 66: Boundary conditions imposed on heterogeneous porous domain

In **Figure 6. 66**, Ω_1 and Ω_2 are two homogeneous permeable media connected in cross-flow situation. The length of the porous domain Ω_1 is 0.015 m and width is 0.005 m whereas the second domain Ω_2 measures 0.005 m in length and 0.015 m in height. The isotropic permeability of Ω_1 is 10^{-12} m^2 and that of Ω_2 is 10^{-8} m^2. At the interface separating these two porous matrices, the permeability is taken as 10^{-8} m^2. There are two exits for the solution domain with imposed pressure datum of zero. A purely Newtonian fluid with density of 970 kg m^{-3} and constant viscosity value of 80 Pa s enters the porous domain Ω_1 with a plug flow velocity of 0.1 m s^{-1}. The flow field simulated using the Darcy solver of **CFDYNAMICS** is represented by vectors in **Figure 6. 67**.
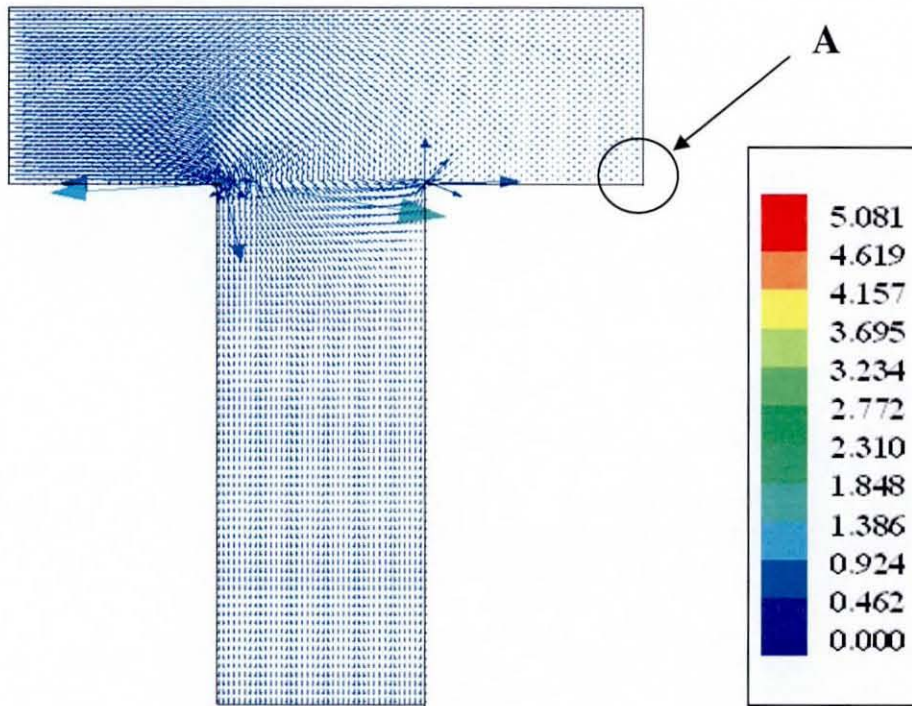
Figure 6. 67: Simulated flow field in composite porous media

As the permeability of porous matrix Ω_2 is comparatively higher than that of Ω_1, a significant amount of fluid crosses the porous-porous interface barrier to find the shortest way towards exit through Ω_2. A negligible amount of fluid is successful is seeping through the porous media Ω_1 and as a results a dead zone is

observed near the right bottom corner of the region Ω_1 as shown by circle A in **Figure 6. 67.** The corner points at the porous-porous interface are found to be highly sensitive to the imposed boundary conditions. A singularity situation signified by the distorted high velocity vectors is observed at these sharp corner points. The pressure field resulted from the porous flow phenomenon, is shown in flooded contours of **Figure 6. 68.**
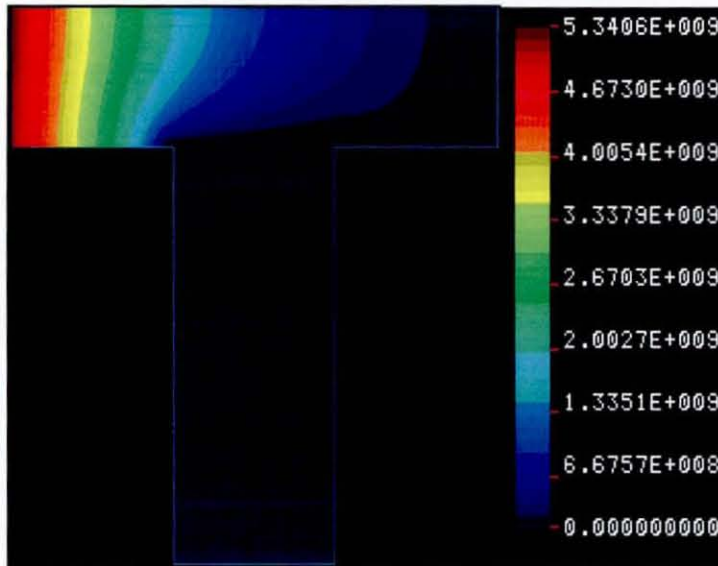
Figure 6. 68: Simulated pressure variations in heterogeneous porous structure

A gradual pressure gradient is observed in the porous domain Ω_1 till the fluid reaches the porous-porous interface. Most of the fluid readily penetrates through the porous domain Ω_2 having greater permeation properties and no further reduction in hydrostatic pressure are requisite to maintain the flow.

6.4.3 Hydrodynamics of coupled free/porous flow regime

In the next step of the model development, the Stokes equations and Darcy equations are linked at the free/porous interface using the nodal replacement scheme explained in Chapter 5. Though the results are obtained for steady state

situations, iterative procedure is adopted for generalised Newtonian flow simulations modelled by the power law equation. In the discussions hereafter, the computed results have been presented for various domain geometries in increasing order of their geometric complexities. A selected version of the simulated data has been already published in journals and conference proceedings and received wide acclaim.

6.4.3.1   Flow through a rectangular coupled flow/porous regime

As a preliminary step in testing the developed computational scheme for combined Stokes/Darcy flow simulations, the most simplified rectangular coupled domain is considered as a flow regime under consideration as presented in **Figure 6. 69**.
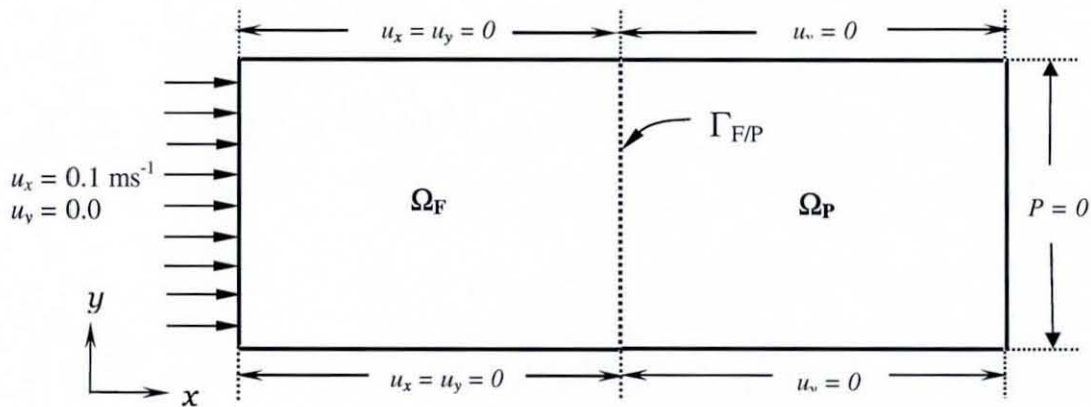
Figure 6. 69: Boundary constraints imposed on rectangular coupled free/porous flow domain

As stated earlier, at the free/porous interface $\Gamma_{F/P}$, Darcy equation is valid and this validity is further extended to the homogeneous porous matrix having isotropic permeation property of 10^{-12} m^2. A purely Newtonian incompressible fluid enters the flow domain with Dirichlet velocity inlet conditions. The path of fluid throughout the solution domain is simulated on a computational finite element mesh containing 2400 elements and 9801 nodal points. With a presumption of change in flow patterns in the part of domain beyond free/porous barrier, the mesh is more refined in the porous region. Path of the fluid calculated

at each nodal point in the computational mesh is visualised by vectors indicating the magnitude and direction of velocity in **Figure 6. 70.**
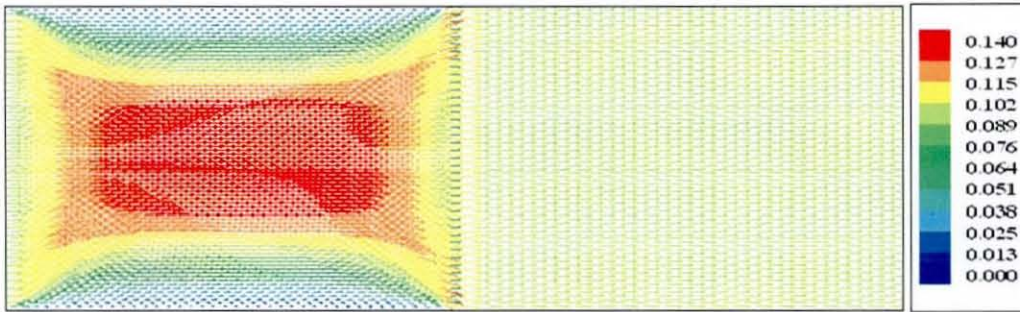
Figure 6. 70: Simulated flow path throughout the solution domain of rectangular coupled free/porous regime

At the free/porous interface, the flow path is distracted due to sudden hindrance caused by very fine porous structure which impedes the fluid motion in the bulk of the matrix and causes change in the momentum. As the viscous stress associated with the fluid in the free flow regime is absent in the porous structure, the flow throughout the matrix remains in plug flow to affirm the conservation of momentum. This behaviour decides the variations in the pressure forces throughout the solution domain as seen from **Figure 6. 71.**
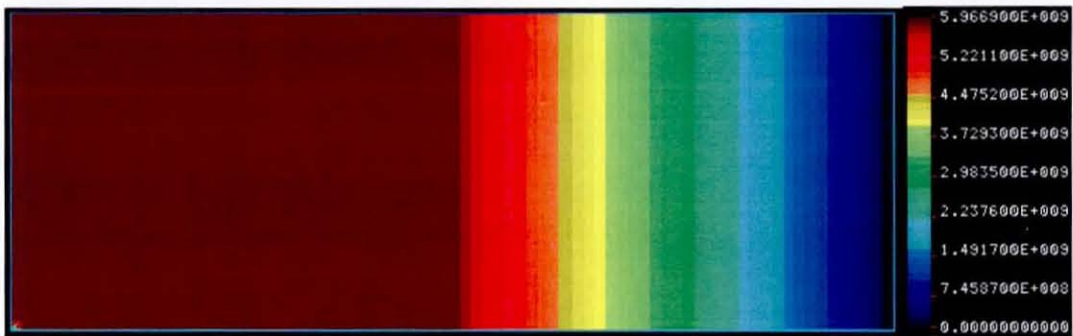
Figure 6. 71: Simulated pressure variations in the rectangular coupled free/porous regime

The hydrostatic pressure in the free flow region of the solution domain is almost invarient which characterises the incompressible creeping flow. The pressure in the porous regime declines per elemental layer in the direction of flow.

In the steady-state Darcy equation, the pressure gradient and velocity are interchangeable terms. To get an idea about the developed pressure drop in response to velocity inlet boundary condition, the pressure value at the exit should be restricted to bind the variations in pressure values over the domain. As a result, clear steep pressure gradients are observed in the porous domain which is evident from **Figure 6. 71**. The total pressure drop across the solution domain is calculated to be around 6 MPa.

The computational results have been examined for validity on the theoretical basis by computing mass balance over the entire solution domain which shows a negative discrepancy of 0.2%. In certain cases, the discrepancy limit can be further reduced by successive mesh refinements.

6.4.3.1   Flow through a rectangular coupled free/porous domain with slant interface

From the excerpts of the literature review, it could be concluded that the interfacial phenomena of combined free/porous regimes still receive serious attention from physicists and engineers. The geometrical and physical properties of the free/porous interface influence the hydrodynamics of the combined free/porous flow to a greater extent. In this direction, the rectangular domain described in section 6.4.2.1 is considered with the exception that the interface is slanted at the angle of 5^0 with the flow direction as shown in **Figure 6. 72**.
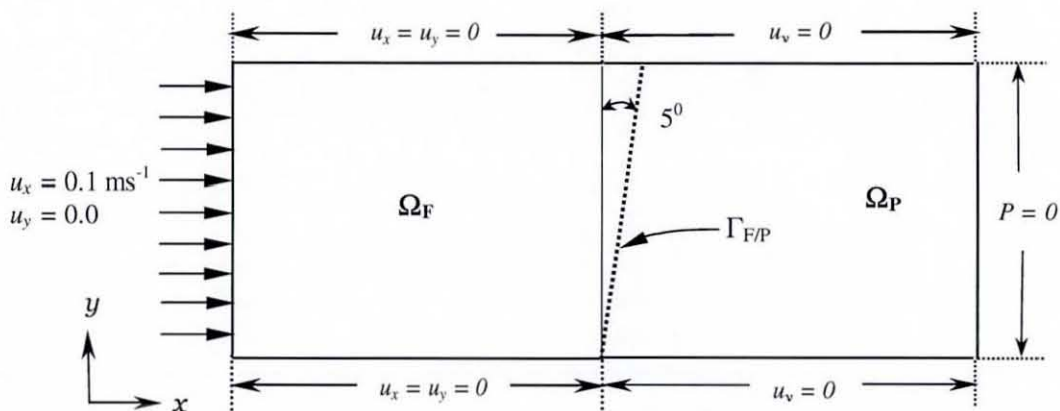
Figure 6. 72: Boundary conditions on rectangular combined free/porous regime with slanted interface

Physical properties of the fluid and material properties of the porous medium are identical to that considered in section 6.4.2.1. With the prescribed boundary conditions, the hydrodynamics is simulated for the computational mesh consisting of 2400 elements and 9801 nodes. The effect of the nature of the interface on the flow pattern can be visualised from **Figure 6. 73**.
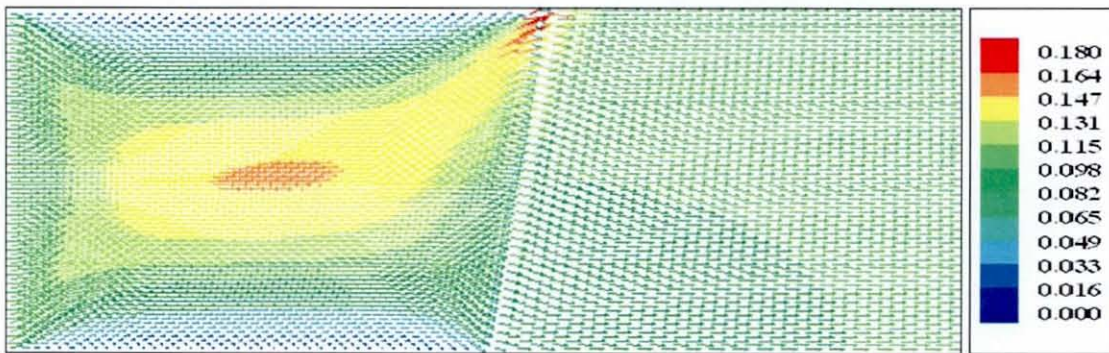
Figure 6. 73: Simulated flow patterns in combined free/porous rectangular regime having inclined interface

As presumed, the flow in the free flow regime has attained the fully developed parabolic status well before colliding with the rigid porous barrier. As the interface possesses a porous structure having the mean aperture of about 2.7 microns, a small amount of fluid is successful in overcoming the barrier directly. Maximum amount of fluid has chosen to slide along the interface and finally encounters the dead-end situation formed by the solid domain walls. A tail of developed flow follows the inclination of interface where the highest velocity of 0.18 ms^{-1} is observed. However, the stressed situation associated with the fluid in the free flow regime is relaxed when it penetrates through the porous matrix.

The pressure variations observed over each nodal point of the computational mesh are plotted over the entire solution domain in **Figure 6. 74**.
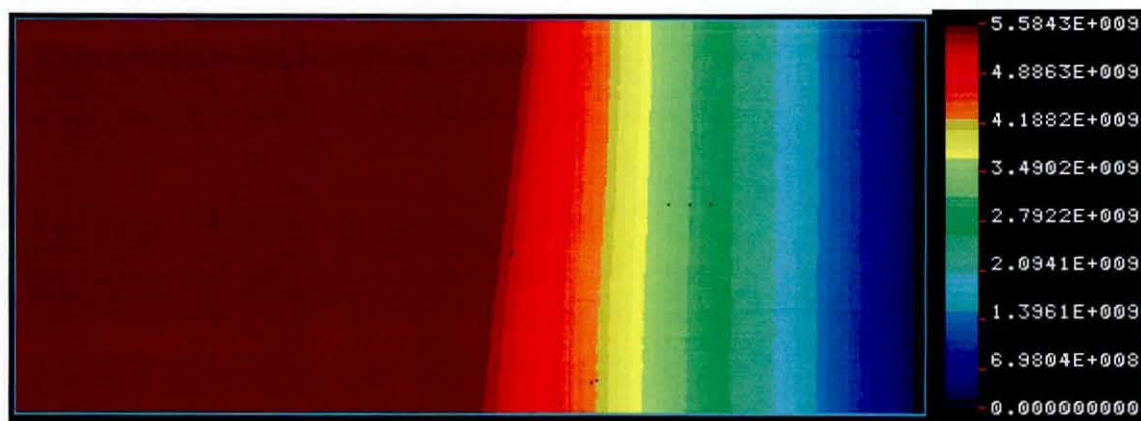
Figure 6. 74: Simulated hydrostatic pressure variations in rectangular coupled free/porous regime with inclined interface

The pattern for variations in pressure resembles the profile observed in rectangular flow domain with straight interface shown in **Figure 6. 71**. The total hydrostatic pressure potential difference developed over the solution domain is around 5.6 MPa.

6.4.3.2   Incompressible flow through concentric circular combined free/porous regime

To access flexibility of the developed coupled flow computational model using the Taylor-Hood scheme towards the complex solution domains encountered in practical field problems, a concentric circular free/porous region is taken into consideration as shown in **Figure 6. 75**.
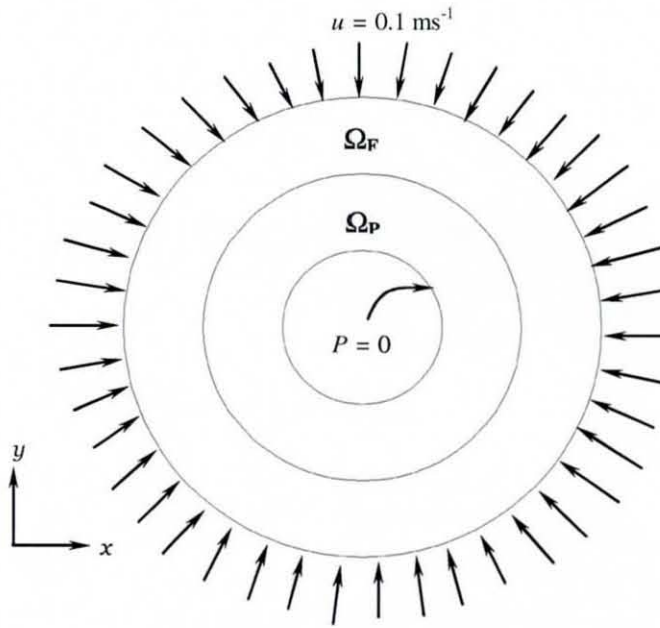
Figure 6. 75: Geometrical features of concentric circular combined free/porous regime with the specified boundary constraints

The thickness of the free and porous flow regions is 0.008 m each and the radius of the entire domain is 0.024 m. The computational mesh generated using **COSMOS** for this concentric circular domain is plotted in **Figure 6. 76** in order to have an idea about intensity of mesh refinements in individual regions.
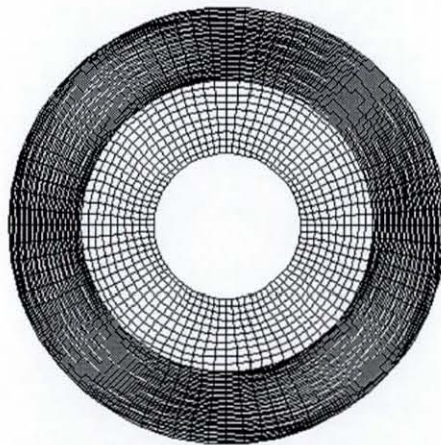
Figure 6. 76: Computational finite element mesh of concentric circular Stokes/Darcy flow regime

Total number of nodal points counts to be 16160 corresponding to 4000 numbers of finite elements. Overall, this mesh is highly refined in the free flow region just as a precautionary measure, taking into consideration the sensitivity of the previously generated results on the similar geometry using the perturbed continuity scheme towards, the mesh density.

An incompressible homogeneous fluid flows in the radial direction towards the centre of the circular core with a normal velocity of 0.1 m s^{-1}. The generalised Newtonian fluid obeys power law model for viscosity variations and the coefficients η_0 and n in the power law model are taken as 80 Pas and 1.15. The simulated flow path adopted by this shear-thickening fluid is traced in the form of velocity vectors in **Figure 6. 77**.
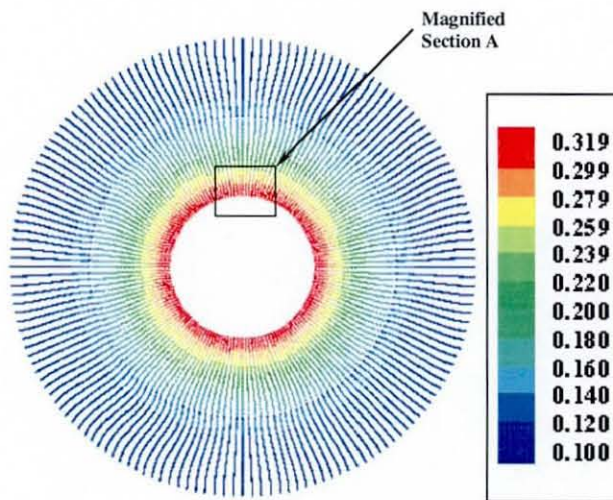
Figure 6. 77: Simulated fluid dynamics over concentric circular series connected free/porous flow regimes

The velocity vectors are directed towards the centre of the domain from inlet to exit. At the exit of porous region i.e. at outlet boundary of the domain, the velocity values are maximum due to lowest cross-sectional area available for the flow. Some parts of the domain from **Figure 6. 77** are magnified in **Figure 6. 78** to have a better idea about the fluid flow behaviour. The model results show only 0.12% discrepancy between the inlet and total outlet flow at the exit, confirming the preserved continuity of the mass.
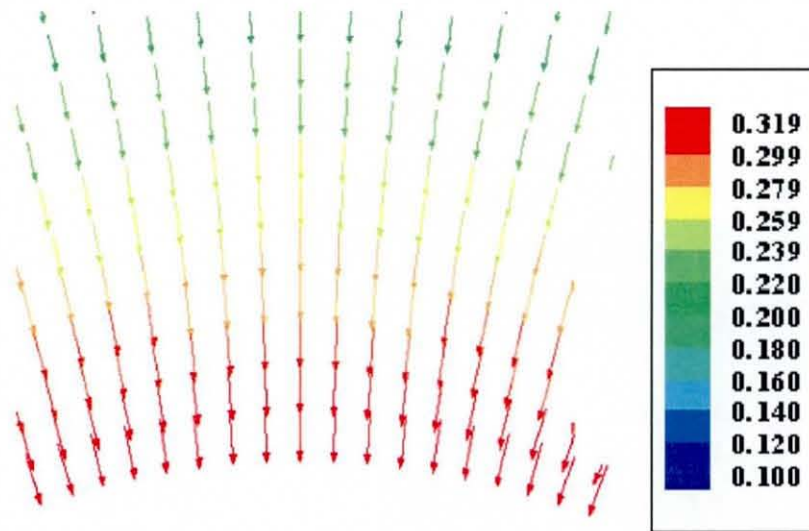
Figure 6. 78: Magnified view of section A in Figure 6. 77

The predicted pressure developed over the entire computational domain is shown in **Figure 6. 79** in the form of multicolour flooding contour plot with a colour scale to compare their relative values.
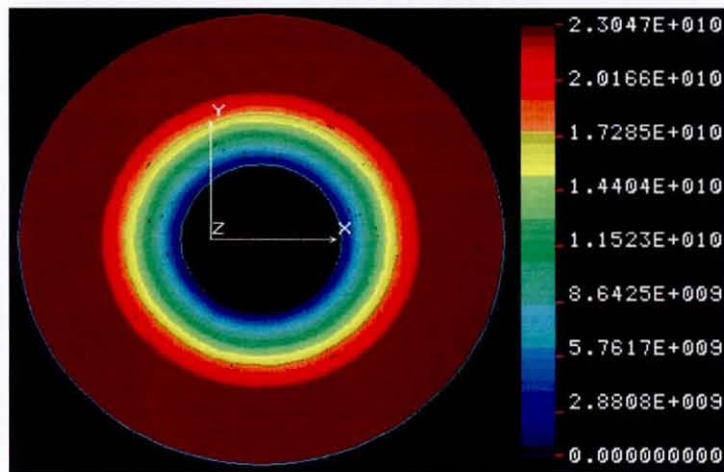
Figure 6. 79: Predicted pressure variations over concentric circular coupled Stokes/Darcy flow regimes

The overall pressure drop is calculated to be 2.3×10^7 kPa. The pressure drop values in the free flow regions are almost negligible. The gradual pressure variations are observed in the porous matrix accounting more than 99% of the total pressure drop. The simulated pressure contours can be well justified

considering the predicted velocity vectors over the domain as shown in **Figure 6. 77.**

6.4.3.3   Hydrodynamics of coupled free/porous regime in cross-flow filtration

Cross-flow filtration is a highly efficient separation process finding its applications in a variety of industrial sectors such as downstream processing, chemical processing, food engineering, pharmaceuticals and medicine. As explained briefly in Chapter 2, fundamentally cross-flow filtration involves flow of suspension tangential to the filtering surface. An integral part of cross-flow filtration process is the fluid flow phenomenon that needs serious attention to appraise the particulate mass transport mechanisms.

In dead-end filtration process, the fluid mass of fluid entering the free flow region is directly transported to the porous region and hence the continuity of mass can be readily preserved. However, it is bit difficult in having a prior estimate of the distribution of fluid mass in free and porous regions in cross-flow filtration process. Though the computational model (**CFDYNAMICS**) has been developed with the aim of analysing hydrodynamics of coupled free/porous regimes in pleated cartridge filters, operated generally in dead-end mode, it would be immensely interesting to explore its applicability and performance for cross-flow filtration systems. In this subsection, we consider two identical cross-flow filtration modules having identical geometrical features with the only discrimination in the nature of interface separating free and porous flow regimes.

6.4.3.3.1   Flow in cross-flow filtration domain having linear free/porous interface

The free flow sub-domain is connected in parallel to the porous flow domain along a horizontal stationary rigid porous interface. During the initial period of filtration, the cross flow provides initial shear to drive away the particles away from the surface and avoids blockage of interface pores. The deformation of interface caused by the cross-flow shear is beyond the scope of the fluid flow analysis presented here. The complete assembly of the cross-flow filtration module

is schematically expressed in **Figure 6. 80** along with the necessary boundary constraints.
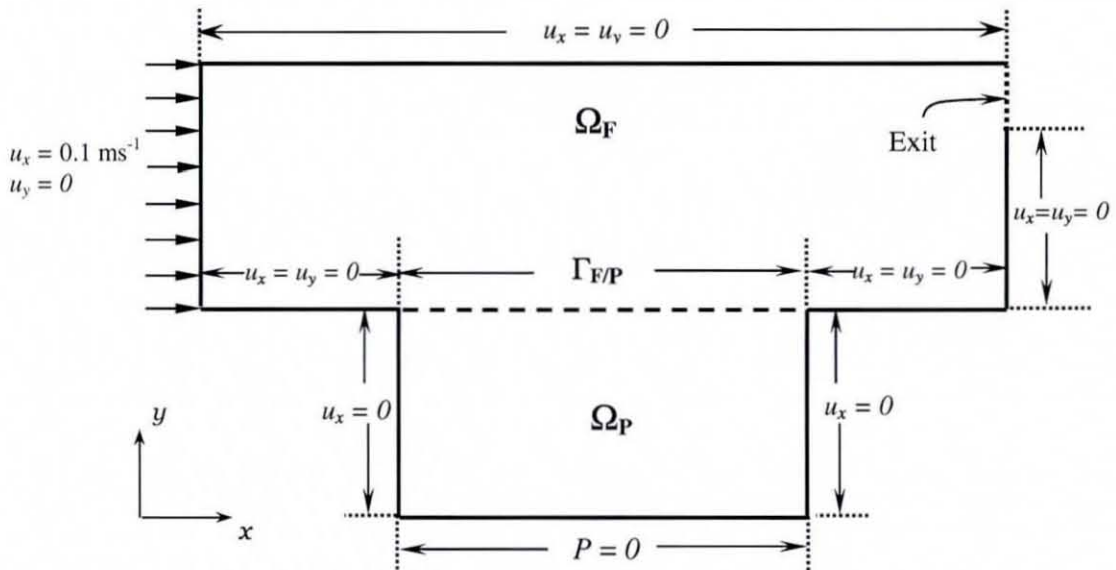
Figure 6. 80: Boundary conditions on rectangular cross-flow filtration domain with flat free/porous interface

The individual flow domains are rectangular in shape. The length of the free flow domain measures to be 0.015 m with 0.005 m of width. The length of the porous region is 0.0075 m with 0.0025 m of width. The overall domain extends to the width of 0.005 m in z-direction. To encourage the maximum flow through the porous region, the width of the exit is kept small compared to that of the inlet and measures to be 0.00125 m.

The fluid to be filtered is an incompressible homogenous liquid having specific gravity of 0.97. The rheological behaviour of the fluid is assumed to be constant throughout the course of filtration and the constant viscosity of fluid is 80 Pa s. For the computational purposes, the domain has been tessellated into finite element mesh consisting of 2000 isoparametric Taylor-Hood elements with 8221 number of associated nodal points. The fluid dynamical behaviour in this coupled flow system has been analysed for varying permeability values of porous media in the range of 10^{-6} m^2 to 10^{-12} m^2. Within the bounds of the imposed boundary

conditions, the simulated flow behaviour in the coupled domain having permeability of 10^{-6} m² is shown in **Figure 6. 81.**
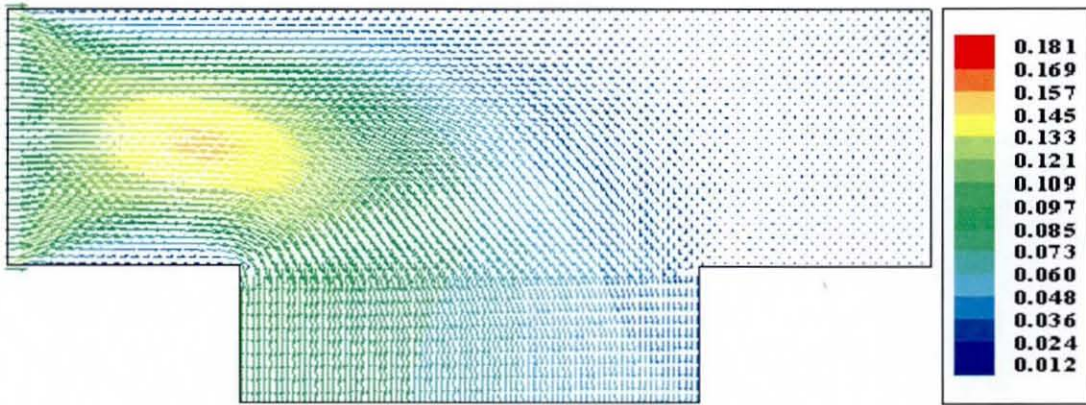
Figure 6. 81: Developed flow field in the rectangular cross-flow filtration domain with flat interface and permeability of porous medium 10^{-6} m²

As the permeability of the porous medium is comparatively high, most of the fluid entering the domain seeps across the free/porous interface to the bulk of the porous medium. A small amount finds its way through the exit of the rectangular free flow channel and as a result a dead-zone is observed in the bottom right corner in the free flow channel Ω_F. The flow tends to attain a developed parabolic state before entering the porous matrix. At every point in the porous regime, the flow is in plug flow condition.

The developed pressure field over the entire computational domain is presented in the form of coloured contours in **Figure 6. 82.**

Figure 6. 82: Predicted pressure variations over the rectangular cross-flow filtration domain with a flat free/porous interface having permeability of 10^{-6} m²

The pressure values in the free flow channel are relatively unchanged before the fluid reaches the free/porous barrier. As the fluid penetrates across the interface, a pressure gradient is observed getting developed in the bulk porous matrix in the direction of flow. In the porous matrix, a somewhat gradual decrease in pressure values is observed as the fluid seeps through the pores. Neutral boundary conditions or stress free conditions have been prescribed at the narrow exit of the free flow region which resulted a localised low pressure region. At the sharp end points at the free/porous interface, an ambiguous singularity situation occurs signified by the high pressure swirls.

In the second case, the computations have been performed changing the permeability of the porous media to 10^{-12} m². The simulated hydrodynamics for this extreme situation could be justified with the help of **Figure 6. 83.**
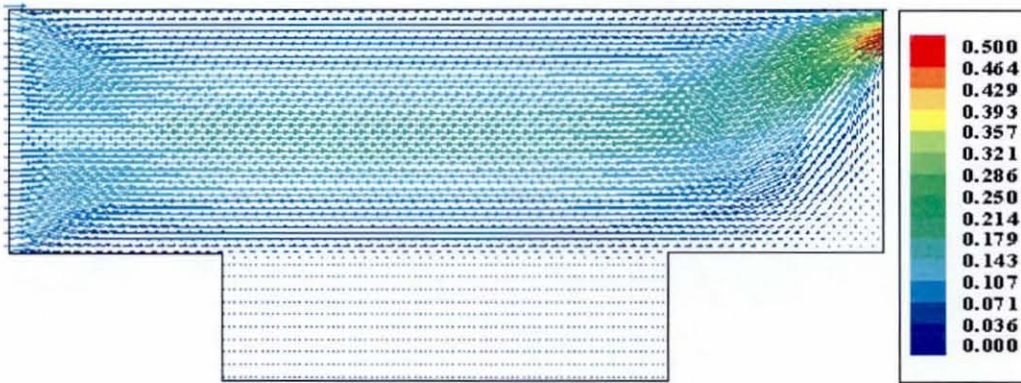
Figure 6. 83: Simulated flow field in the cross-flow filtration domain with a flat free/porous interface having permeability of 10^{-12} m²

Though, the inlet fluid is in uniform plug flow condition, it shows the tendency to attain a fully developed parabolic profile in the free flow region. Since the permeability of the interface is very low, a very small amount of fluid is observed to be successful in penetrating across the free/porous interface. Bulk of the fluid is striving hard to push itself through the narrow exit in the free flow channel and a localised high velocity field is observed in that region. The amount of fluid flowing through the porous matrix can be found out by calculating the mass balance over the domain. It is found that only 1.5% of the inlet fluid is seeping through the porous barrier and the rest about 98.5 % is flowing across the free flow region.

The hydrostatic pressure force component of the Cauchy's total stress tensor is plotted in **Figure 6. 84**.
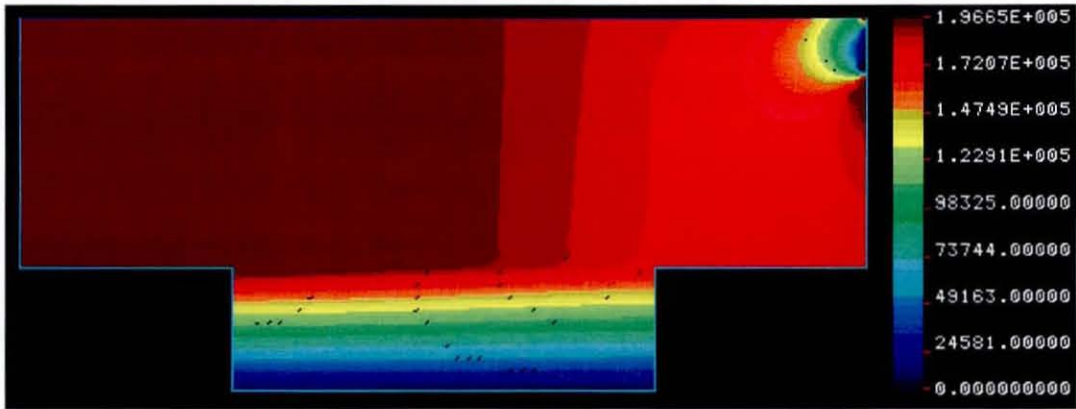
Figure 6. 84: Predicted pressure variations over the rectangular cross-flow filtration domain with a flat free/porous interface having permeability of 10^{-12} **m²**

Pressure in the free flow region is changing as the fluid seeps through the porous region. The pressure gradients found in the porous domain are considerably steeper than those shown in **Figure 6. 82**. However, unlike the previous case, the pressure values in the free flow channel are more or less constant throughout. Due to the stress-free boundary condition at the narrow exit, a localised low pressure field is observed there.

For all the simulations, the validity of the simulated results has been examined by the means of mass balance calculated over the entire computational domain. All the mass balance figures are listed in **Table 6. 6** against the corresponding permeability values. At the high permeability values, the discrepancy between the inlet and outlet masses increases in the negative direction. Under these circumstances, the validity of the Darcy equation for those high permeability values could be questionable. On the other hand, the discrepancy increases in positive direction for lower permeability values of the porous medium. Despite the fact that the Darcy equation is perfectly valid in these cases, the only reason for the discrepancy is the inadequacy of the mesh refinement necessary for the spatial approximation of the variables over the domain. However, extensive mesh refinement could desired to improve the situations causing serious impact on the computational economy.

Table 6. 6: Mass balance calculations for rectangular cross-flow filtration domain with flat free/porous interface

No.	Perm. m^2	Total Mass in (M_{in}) kg	Mass at Exit (E_{mass}) Kg	Mass of Permeate (P_{mass}) kg	Total Mass Out (M_{out}) = E_{mass} + P_{mass} Kg	% Error = Error! Objects cannot be created from editing field codes.
1.	1×10^{-6}	4.79×10^{-4}	5.64×10^{-6}	4.75×10^{-4}	4.81×10^{-4}	-0.38
2.	1×10^{-7}	4.79×10^{-4}	3.17×10^{-5}	4.48×10^{-4}	4.80×10^{-4}	-0.17
3.	1×10^{-8}	4.79×10^{-4}	1.93×10^{-4}	2.81×10^{-4}	4.74×10^{-4}	1.10
4.	1×10^{-9}	4.79×10^{-4}	4.05×10^{-4}	6.05×10^{-5}	4.65×10^{-4}	2.79
5.	1×10^{-10}	4.79×10^{-4}	4.56×10^{-4}	7.01×10^{-6}	4.64×10^{-4}	3.20
6.	1×10^{-11}	4.79×10^{-4}	4.63×10^{-4}	7.14×10^{-7}	4.63×10^{-4}	3.25
7.	1×10^{-12}	4.79×10^{-4}	4.63×10^{-4}	7.14×10^{-7}	4.63×10^{-4}	3.25

6.4.3.3.2   Flow in cross-flow filtration domain having curved free/porous interface

In realistic cross-flow filtration process, continuous particle deposition leads to build up of the filter cake on the interface. Some of the deposited particles are driven away from the surface by the shear produced by the cross-flow of fluid and after a sufficient length of time, the flat free/porous interface shown in **Figure 6. 80** turns into curved one as described in **Figure 6. 85**.
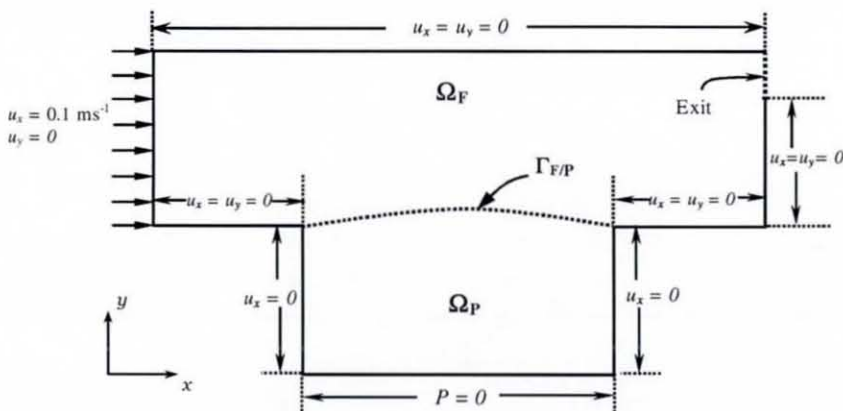
Figure 6. 85: Boundary conditions on rectangular cross-flow filtration domain with curved free/porous interface

The geometrical characteristics of the cross-flow filtration domain shown in are identical to that presented in **Figure 6. 80** except the fact that the interface is curved, convex to the free flow channel. Similar to the previous case, simulations have been performed for different permeability values ranging from 10^{-6} m^2 to 10^{-12} m^2, varied by the order of magnitude of 10. The simulated flow field in this cross-flow filtration domain, with the permeability of porous medium of 10^{-6} m^2 is plotted in **Figure 6. 86**.
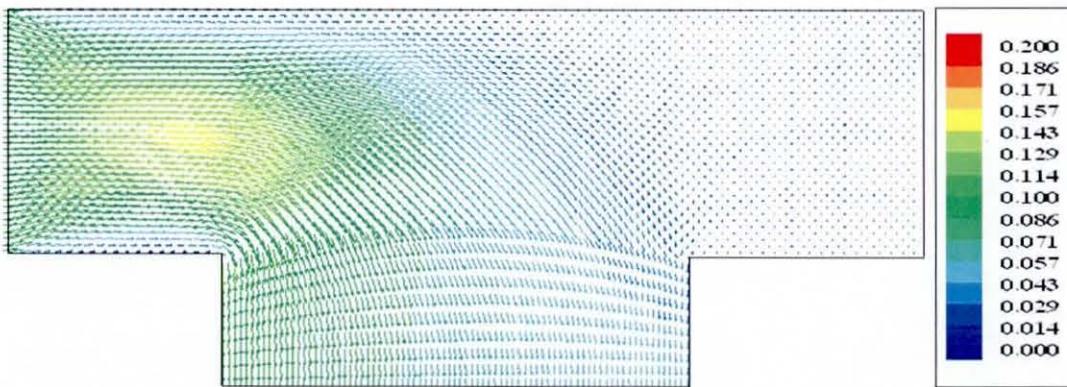
Figure 6. 86: Simulated flow field in rectangular cross-flow filtration domain with curved free/porous interface having permeability of 10^{-6} m^2

As seen from **Figure 6. 86**, due to the high permeability of the porous regime, the free/porous interface don't pose any severe obstruction for the fluid to enter the bulk of the porous medium and most of the fluid finds its way out through the porous matrix. A tiny amount of fluid is successful in approaching the narrow exit of the free flow channel. The curved shape of the free/porous interface has clearly reflected in the flow path taken by fluid to penetrate through the porous matrix.

The pressure field simulated over the entire computational domain can be analysed with the help of flooded contours of **Figure 6. 87**.
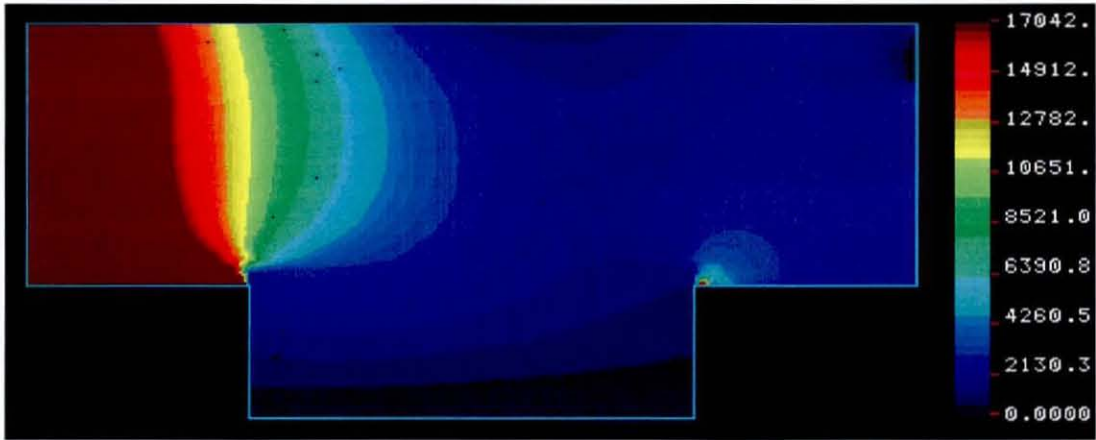
Figure 6. 87: Predicted pressure variations over the rectangular cross-flow filtration domain with curved free/porous interface having the permeability of 10⁻⁶ m²

The pressure drop values in the free flow channel are relatively small before the fluid reaches the free/porous barrier. As the fluid penetrates across the interface, a steep pressure gradient is observed in the free flow channel. In the porous matrix, a gradual decrease in pressure values is observed as the fluid seeps through the pores. A localised low pressure region is observed in the vicinity of the narrow exit of the free flow region. A small high pressure region is observed at the right hand side corner point on the free/porous interface designating it as a singular point in mathematical sense.

Similar to the case with the cross-flow filtration domain with flat interface, the permeability of the porous medium is lowered down to the value of 10^{-12} m² and the simulated flow field over the domain is represented in the form of velocity vectors in **Figure 6. 88**.
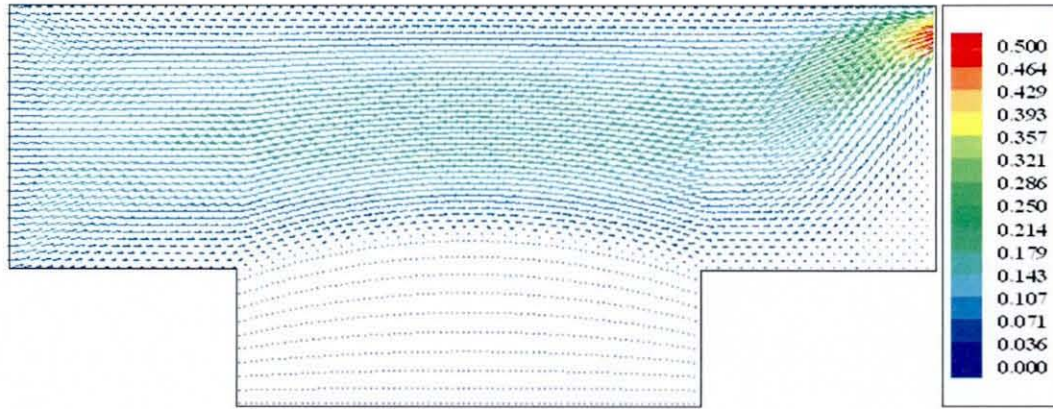
Figure 6. 88: Simulated flow field in the rectangular cross-flow filtration domain with curved free/porous interface having the permeability of 10^{-12} m^2

The flow field developed over this coupled domain with curved free/porous interface is similar to that observed in the domain with flat interface. As the permeability of the porous medium is relatively low, the free/porous interface presents a stringent barrier for the fluid to enter the bulk porous matrix. Therefore, a very small amount of the inlet fluid seeps through the porous medium and most of the fluid slides across along the curved interface and marches towards the narrow exit of the rectangular free flow channel. A high velocity region is observed in the vicinity of the exit since the fluid pushes itself at high flow rate. The mass balance is checked over the domain calculating the discrepancy between the inlet and outlet mass of the fluid, which is about 3%. The amount of fluid passing through the porous barrier is just 1.4% and most of the fluid finds its way through the exit of the free flow domain.

The hydrostatic pressure developed over the domain due to incompressible flow of a Newtonian fluid is shown in **Figure 6. 89.**
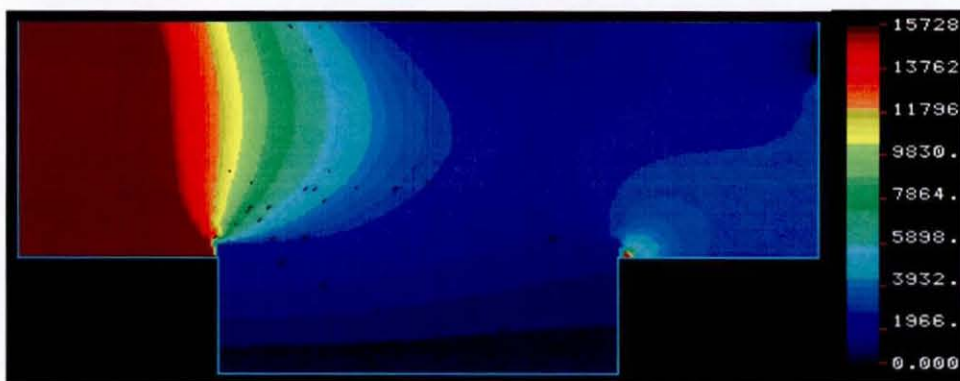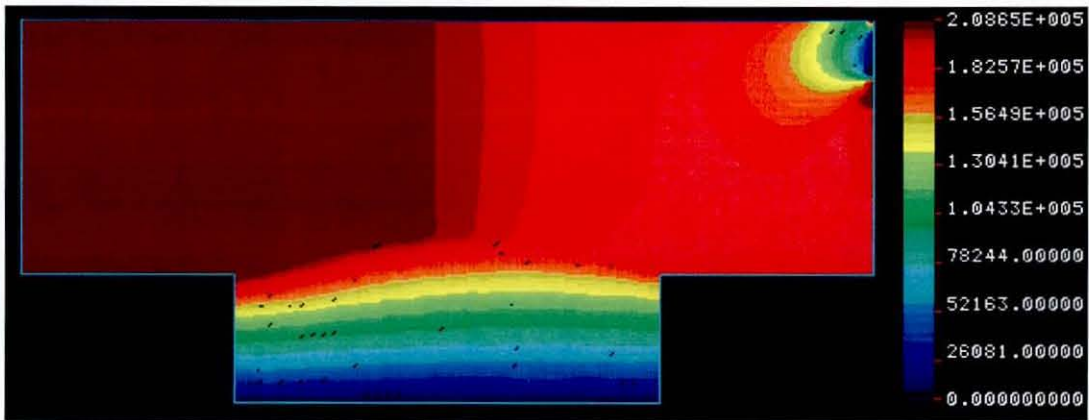
Figure 6. 89: Predicted pressure variations over the rectangular cross-flow filtration domain with curved free/porous interface having the permeability of 10^{-12} m²

Before the porous barrier, the pressure drop in the free flow region is almost negligible. As the fluid approaches the free/porous interface, the pressure in the free flow region decreases since some of the fluid is penetrating the porous medium. In the porous regime, the pressure gradually decreases and attains a null value at the exit of the permeate zone. A localised low-pressure vortex is observed at the exit of free flow region and most of the fluid is pushing itself through that narrow outlet.

Similar to the previous domain, the model is testified for validation by quantitative evaluations based on the overall mass balance calculations. The mass inflows and outflows figures for a range of permeability values are listed in **Table 6. 7**. In the present case, the discrepancy between inlet and outlet masses is found to be increasing as the porous medium becomes less permeable. The possible solution to minimize this discrepancy may be accomplished by refining the computational mesh.

Table 6. 7: Mass balance calculations for the rectangular domain with curved free/porous interface

No.	Permeability m^2	Total Mass in (M_{in}) kg	Mass at Exit (E_{mass}) kg	Mass of Permeate (P_{mass}) kg	Total Mass Out $(M_{out}) = E_{mass} + P_{mass}$ kg	% Error = Error! Objects cannot be created from editing field codes.
1.	1×10^{-6}	4.79×10^{-4}	4.87×10^{-6}	5.08×10^{-4}	5.13×10^{-4}	-7.13
2.	1×10^{-7}	4.79×10^{-4}	3.32×10^{-5}	4.77×10^{-4}	5.10×10^{-4}	-6.50
3.	1×10^{-8}	4.79×10^{-4}	2.06×10^{-4}	2.86×10^{-4}	4.92×10^{-4}	-2.76
4.	1×10^{-9}	4.79×10^{-4}	4.13×10^{-4}	5.79×10^{-5}	4.71×10^{-4}	1.71
5.	1×10^{-10}	4.79×10^{-4}	4.59×10^{-4}	6.58×10^{-6}	4.66×10^{-4}	2.71
6.	1×10^{-11}	4.79×10^{-4}	4.65×10^{-4}	6.68×10^{-7}	4.66×10^{-4}	2.83
7.	1×10^{-12}	4.79×10^{-4}	4.65×10^{-4}	6.67×10^{-8}	4.63×10^{-4}	2.84

6.4.3.4   Flow through a coupled cross-flow and dead-end filtration domain

The versatility of the developed computational scheme has been kept under severe criticism by applying to a complex filtration system in which two distinct porous regions are linked to a free flow region in both cross-flow and dead-end mode as depicted in **Figure 6. 90.**
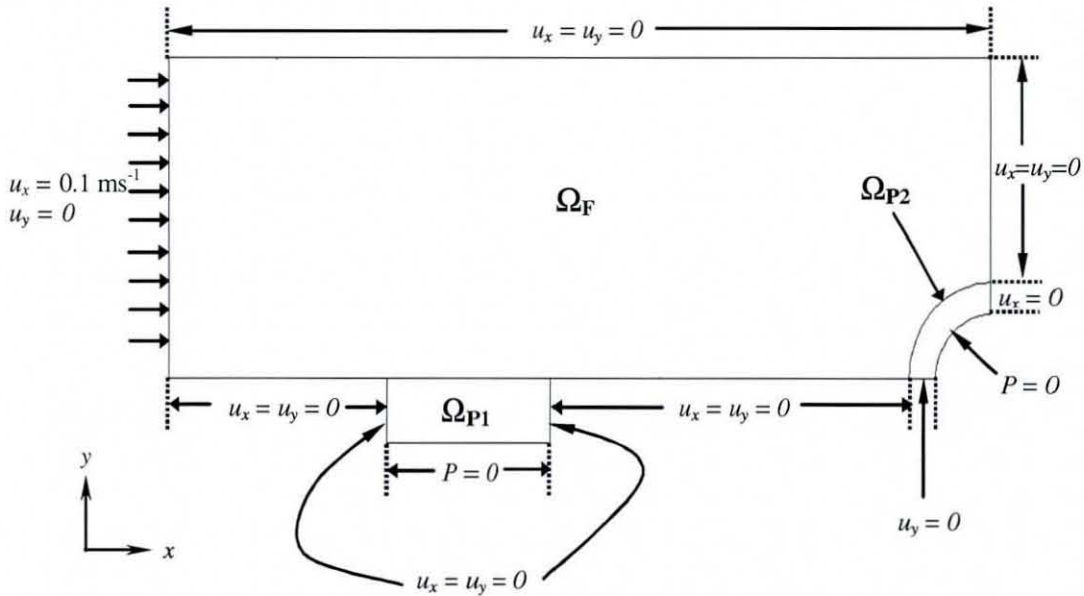
Figure 6. 90: Boundary conditions on combined cross-flow and dead-end filtration domain

The overall domain Ω is composed of a free flow region Ω_F and two porous flow regions designated as Ω_{P1} and Ω_{P2} having the permeability values of 10^{-12} m^2 and 10^{-10} m^2, respectively. The porous sub-domain Ω_{P1} is connected to the free flow regime Ω_F in cross-flow fashion and the porous matrix Ω_{P2} is attached in dead-end mode. The domain Ω measures 0.015m in length and 0.005m in width in the direction perpendicular to the flow. The thickness of the porous matrix Ω_{P1} is 0.003 m and the quarter circular porous regime Ω_{P2} measures 0.0005 m in thickness. The flow domain Ω is 0.001m in width perpendicular to the xy coordinate plane. The fluid is a generalised Newtonian power law type fluid having the value of power law index 1.15 and incompressible density of 970 kgm^{-3}.

The solution domain has been discretised into a finite element mesh containing 4500 number of elements and 18331 numbers of nodes. In context of the imposed boundary constraints, the resultant flow field developed over the domain is represented by the vectors in **Figure 6. 91**. As the fluid enters the flow domain, it gets diverted to the porous matrix Ω_{P1} which offers a stringent barrier

for the fluid to penetrate completely due to its very low permeability value. A small amount of the viscous fluid succeeds in penetrating through the porous solid and the bulk of it travels in the direction towards the exit.
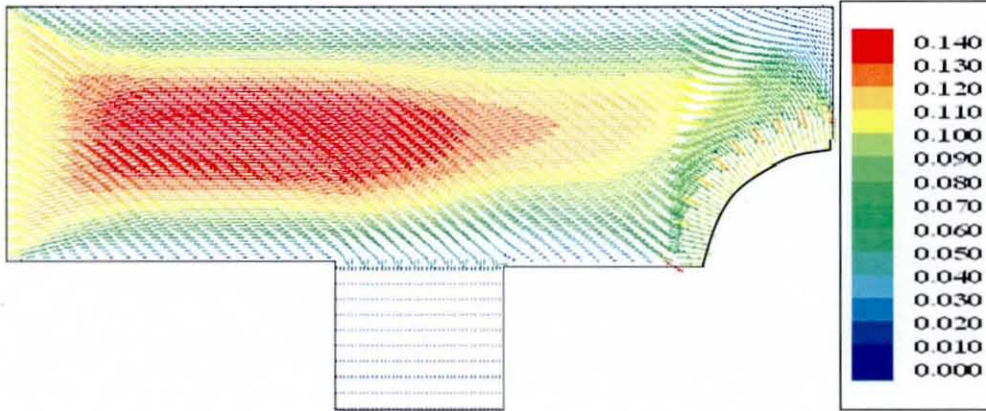
Figure 6. 91: Simulated flow field in combined cross-flow and dead-end filtration domain

Throughout the porous matrix Ω_{P1}, the flow is in plug flow condition and in the free flow channel, the fluid attains the fully developed parabolic profile. After bypassing the porous barrier led by Ω_{P1}, the total flow concentrates near the second porous matrix Ω_{P2}. As the permeability of Ω_{P2} is higher than that of the cross-flow porous sub-domain Ω_{P1}, the fluid pushes itself hard through the pores of Ω_{P2} and as a result high velocity values are observed at the exit. The hydrostatic pressure developed over the domain is shown by the flooded contours in **Figure 6. 92** with all the values in the units of Pascal (Pa).
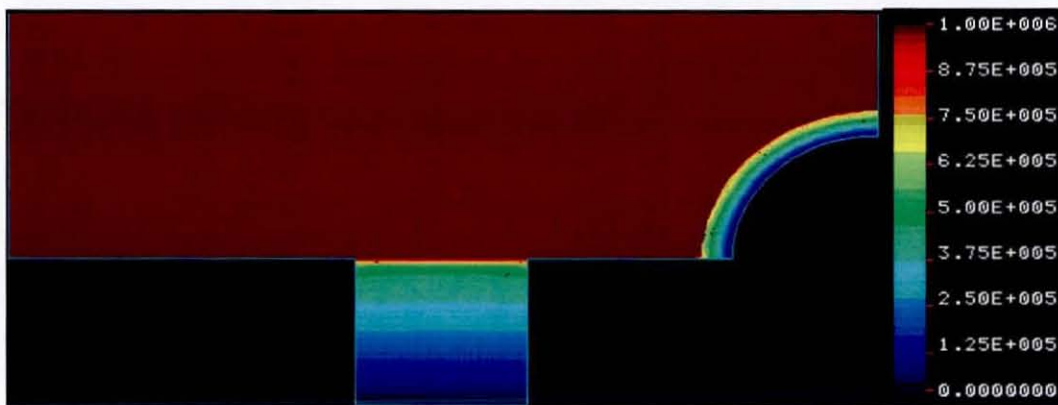
Figure 6. 92: Predicted pressure variations over the combined cross-flow and dead-end filtration domain

Referring to the completely developed flow field in the free flow region, the nearly constant hydrostatic pressure is completely justified. The permeability values of both the porous matrices Ω_{P1} and Ω_{P2} lie within the bounds of the domain of applicability of the Darcy's law and henceforth, gradual pressure variations are observed in the bulk of the matrices driving the flow of the dilatent fluid. The pressure drop across the cross-flow porous region Ω_{P1} is 1.0×10^8 Pa whereas the pressure drop developed across the dead-end porous matrix Ω_{P2} is 0.97×10^8 Pa. The amount of fluid penetrating through each of the porous regions is calculated by carrying out mass balance checks over the domain. It was observed that about 99% of the fluid passes through the dead-end sub-domain Ω_{P2} obviously due to its higher permeability than that of the cross-flow sub-domain Ω_{P1}. The discrepancy between the inlet and outlet masses of the fluid comes less than 1% which supports the successful linking of cross-flow and dead-end porous flow regimes to the viscous channel flow.

6.4.4   Hydrodynamics of coupled free/porous/free flow regimes

Up to this point in the discussion, we have described the simulated results pertaining to the free flow dynamics, porous flow dynamics and coupled free/porous flow dynamics in a variety of distinguished flow geometries, obtained using the finite element formulations based on Taylor-Hood elements. The free and porous flow regimes have been linked mathematically at the interface by employing the nodal replacement scheme. In the advanced stage of the computational model development, free-porous-free flow regimes have been linked in series or dead-end fashion to epitomise the flow regimes in the pleated cartridge filter assembly explained in Chapter 1. At nodal points present on the free/porous as well as porous/free separating barriers, the components of the Stokes equations are substituted by their corresponding Darcy components coming from the other side of the interface.

6.4.4.1 Flow through the rectangular coupled free/porous/free flow regime in dead-end filtration domain

As per the strategy adopted in the previous cases, the simplest case considered at the start is a two-dimensional rectangular dead-end filtration domain with straight free/porous and porous/free interfaces. The assembly of the flow sub-domains has been pictorially represented in **Figure 6. 93**.
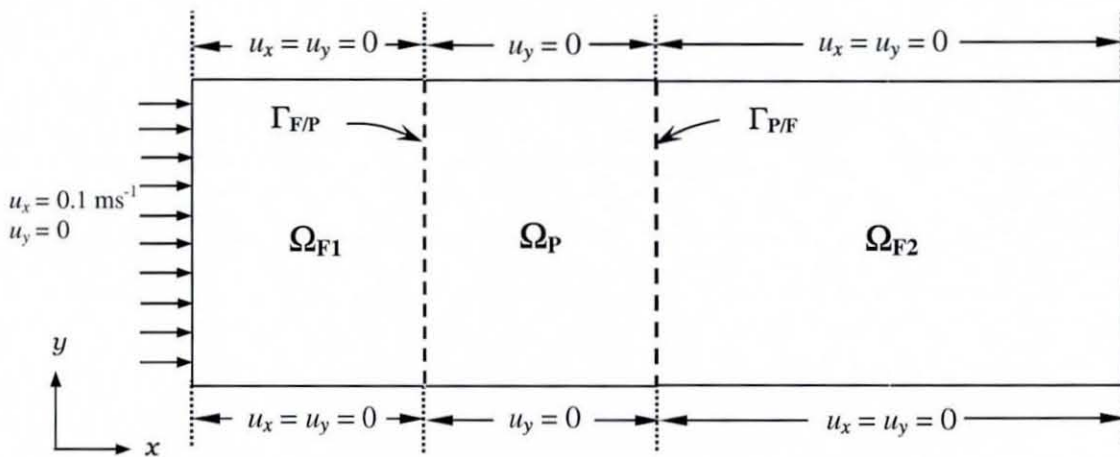
Figure 6. 93: Boundary conditions on the rectangular coupled free/porous/free flow domain

The porous sub-domain Ω_P is sandwiched between two free flow channel sections Ω_{F1} and Ω_{F2}. The width of the solution domain shown in **Figure 6. 93** is 0.005 m. The length of the first Stokes and the Darcy regions is 0.0075 m and the length of the second Stokes region is 0.015 m. The exit of the domain is maintained stress free by virtually imposing the neutral boundary condition. The computational mesh generated with the purpose of domain discretisation, consists of 5600 numbers of elements with 22761 numbers of adjoining nodal points. The total number of elements in the first free flow region is 1600 whereas that in the second flow region is 3200. Number of elements contributed by the porous flow region is merely 800.

The fluid to be cleaned through this dead-end-filtration module is considered to be an incompressible single phase fluid having a specific weight per unit volume of 970 kg. In rheological point of view, the fluid is a purely Newtonian

liquid having a constant viscosity value of 80 Pa s. The simulated flow field in this combined Stokes/Darcy/Stokes regime is plotted in the form of velocity vectors in **Figure 6. 94.**
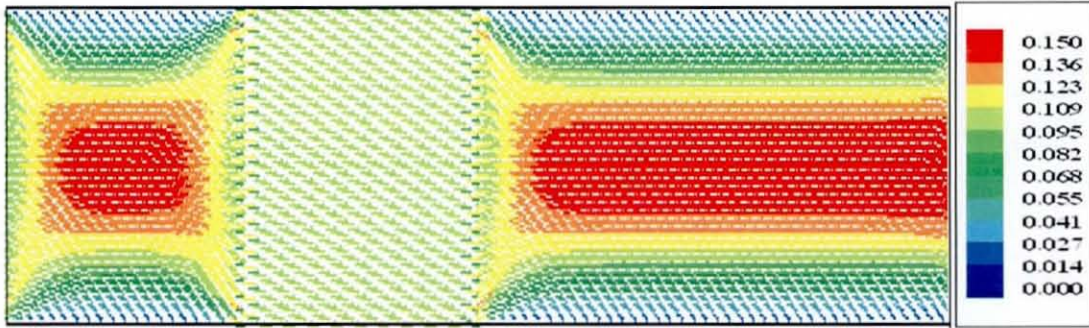
Figure 6. 94: Simulated flow field in rectangular coupled Stokes/Darcy/Stokes regime

As observed from **Figure 6. 94**, the velocity field in the first free flow region rapidly develops to assume a parabolic profile before the porous section. At the interface, the flow becomes disturbed due to the sudden obstruction and becomes a plug flow regime, as expected. In the second free flow regime, the flow resumes towards parabolic development and near the exit it is seen to be fully parabolic. The flow profile is exactly symmetric along axis parallel to the direction of flow. The continuity of field variables is examined by computing the mass balance of the fluid over the domain and the discrepancy between the inlet and outlet masses is computed to be only 0.12 %. However, this performance could be further enhanced, if needed, by repeated mesh refinements. For this sole purpose, h-type mesh refinement has been carried out. The mesh is refined with the total number of elements being 8400. In this case, the mass balance discrepancy is found out to be 0.10 %. For both these cases, The simulated pressure field distribution can be well understood from **Figure 6. 95.**
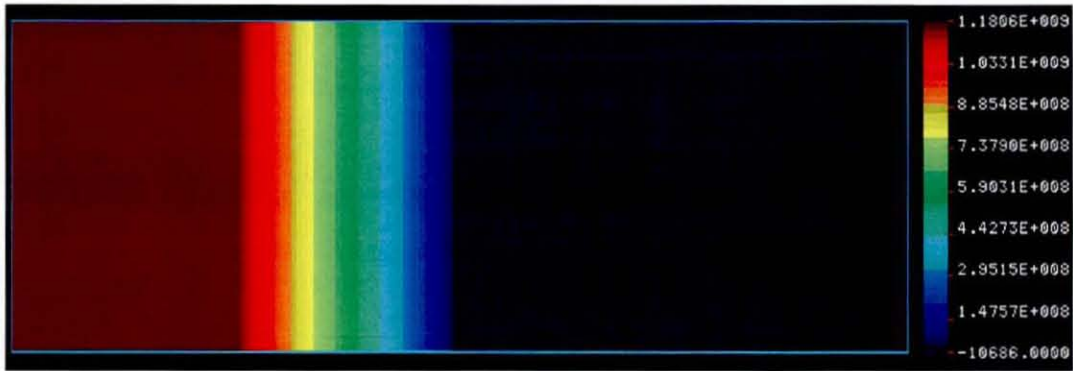
Figure 6. 95: Predicted pressure variations over the rectangular coupled Stokes/Darcy/Stokes regime

The total pressure drop over the domain is computed to be 1.1×10^6 kPa. The maximum contribution to the pressure drop value is by virtue of the flow through the porous medium. An expected rise in the pressure gradient is observed in the porous matrix along the flow direction as a result of low permeability. The pressure difference values over both the free flow regimes are comparatively very small. Both the predicted pressure drop and the velocity fields are as theoretically expected.

6.4.4.1.1   Theoretical validation of computational model for combined free/porous/free flow regime

To answer the question raised regarding the validity of the developed computational scheme when applied to the types of the series-connected alternate free/porous regimes similar to that drawn in **Figure 6. 93**, a series of numerical experiments have been performed. Simulations have been carried out by changing the permeability of the porous matrix Ω_P between 10^{-8} m^2 to 10^{-12} m^2 well within the range of validity of the Darcy's law. For each of these cases, the analytical solutions to the pressure drop developed across Ω_P have been found out using the x-component of the Darcy's law taking into consideration of the pseudo two-dimensionality of the problem. The simulated values and analytical values of the pressure drops have been compared from **Table 6. 8**.

**Table 6. 8: Comparison of simulated and analytical pressure drops at
different permeability values**

No.	Permeability m²	Pressure drop according to the Darcy's law Pa	Simulated Pressure drop Pa
1.	10^{-8}	6.00E+05	6.13E+05
2.	10^{-9}	6.00E+06	6.00E+06
3.	10^{-10}	6.00E+07	5.98E+07
4.	10^{-11}	6.00E+08	5.98E+08
5.	10^{-12}	6.00E+09	5.98E+09

In all the experiments, the operating parameters such as the flow velocity are kept unchanged. The analytical values of pressure drops tally closely with their simulated counterparts affirming the validity of the developed computational scheme. A graph of inverse of the permeability values against the pressure drop values is plotted in **Figure 6. 96.**
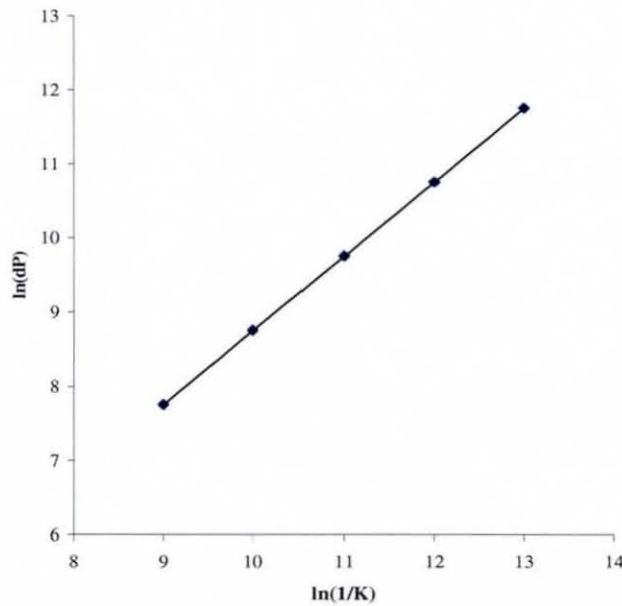
Figure 6. 96: Pressure drop versus permeability relationship in the porous medium

Since the magnitudes of the permeability and pressure drop varies by the order of the magnitude of 10, for better visualisation, the graph has been plotted

on the logarithmic scale. The plot shows a linear relationship between the permeability and the corresponding pressure drop value across the porous structure validating the applicability of the Darcy's law governing the flow through the porous media.

6.4.4.1.2   Validity of the numerical linking scheme for Stokes/Darcy regime

The linking of the Stokes and Darcy equations occurs in the elemental system of finite element working equations, particularly for those elements which are present on the either side of the free/porous interface. With an idea of cross-examining the nodal replacement scheme, numerical experimentations are carried out on the solution domain identical to that shown in **Figure 6. 93**. The only exception made is that the porous sub-domain Ω_P is shrunk to just one elemental length of the computational mesh of that domain. The parent computational mesh for the rectangular coupled Stokes/Darcy/Stokes domain is shown in **Figure 6. 97**.

Porous subdomain, Ω_P

(a)

Porous subdomain, Ω_P

Free flow region, Ω_{F1} Free flow region, Ω_{F2}

(b)
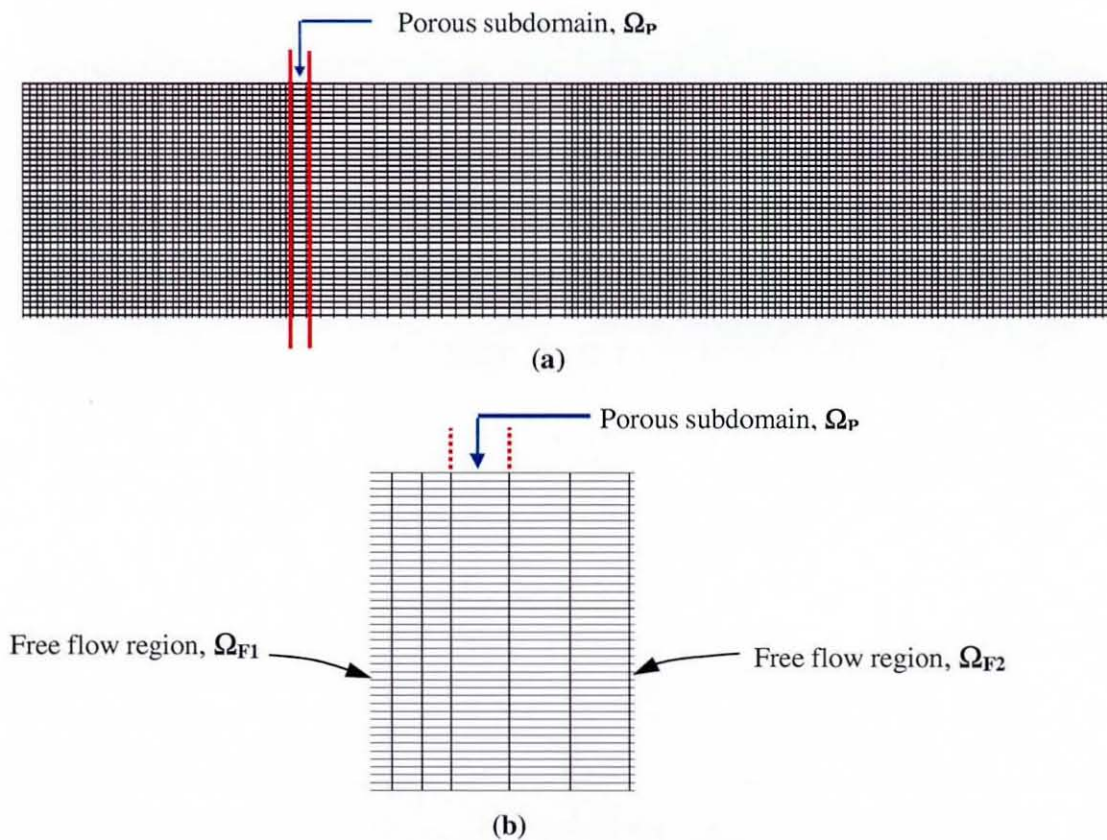
Figure 6. 97: (a) Modified version of the solution domain described in Figure 6. 93 and (b) it's magnified view

The types of the boundary conditions applied to this modified domain are exactly similar to those shown in **Figure** 6. 93. The fluid and the permeable medium possess the same physical properties as in the previous case. For the purely Newtonian incompressible fluid flow, the variations in pressures over the solution domain are plotted in **Figure** 6. 98(a) and the pressure distributions in the monoelemental layered porous matrix are magnified in **Figure** 6. 98(b).

(a)

(b)
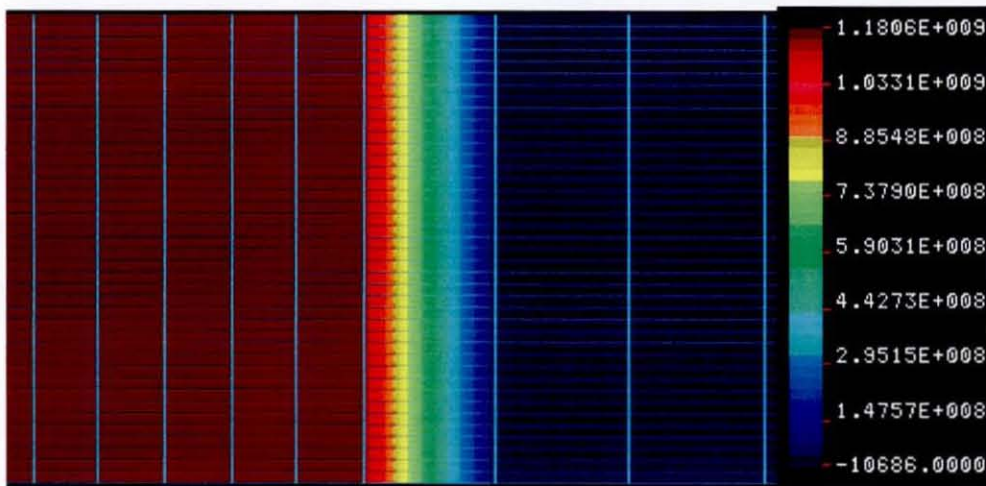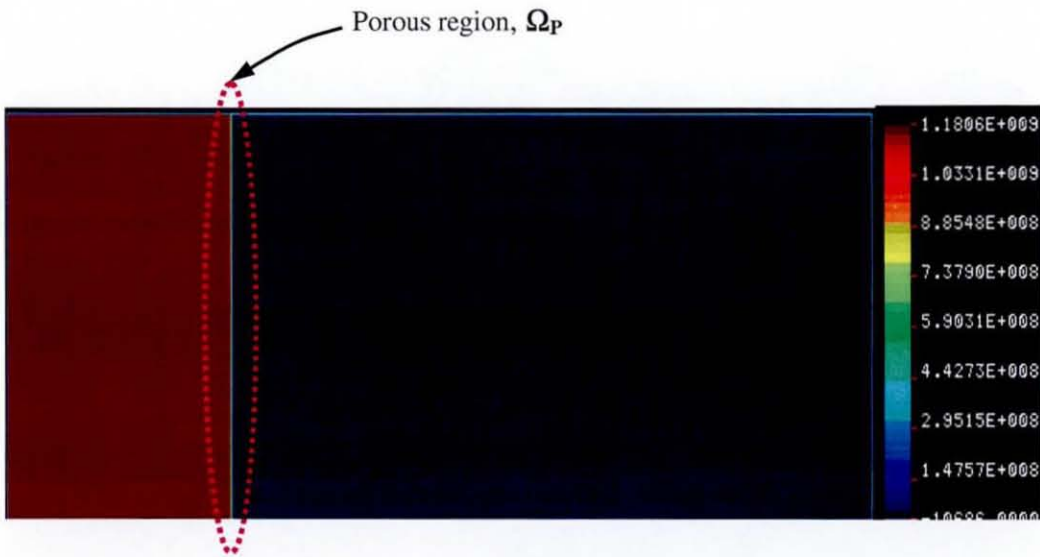
Figure 6. 98: (a) Predicted pressure variations in the modified coupled Stokes/Darcy/Stokes rectangular domain; (b) Magnified view of the pressure profile developed across the porous regime

Unlike the previously reported schemes mentioned in the literature concerning the coupling of Stokes and Darcy regimes, the nodal development scheme devised by the author doesn't encourage artificial enforcement of continuity of field variables; velocity and pressure across the free/porous interface. Rather, the linking scheme defines the correct boundaries for the applicability of the individual flow equations and couples them at the interface by replacement of one with the other without any compromise with the underlying physical phenomena.

As evident from **Figure 6. 98**(a) and (b), the flow perfectly obeys the Stokes equation in the free flow regime and as soon as it approaches the interface, it starts following the path described by the Darcy equation. Though, the porous regime is made of a elemental monolayer, a gradual variation in pressure is observed in this single element confirming the successful linking of the two distinct flow regimes at the interface and proves the validity of Darcy's law in the bulk of the porous matrix.

The lower order interpolation function for the pressure in the Taylor-Hood elements completely avoids the over-riching of the pressure approximation spaces unlike the case with perturbed continuity scheme based on equal order approximations. Therefore, the LBB condition is satisfied over each individual elemental domain of the computational mesh and the mass continuity is maintained locally over the elemental scale as well as globally over the entire domain without any possible occurrence of the approximation errors.

6.4.4.2   Flow through a rectangular coupled free/porous/free domain with slant interface

Following the typical chronology adopted in the representation of results before, simulations have been carried out by taking the rectangular domain shown in **Figure 6. 99** under consideration. The first free/porous interface is tilted to the axis parallel to the flow direction at an angle of 5^0.
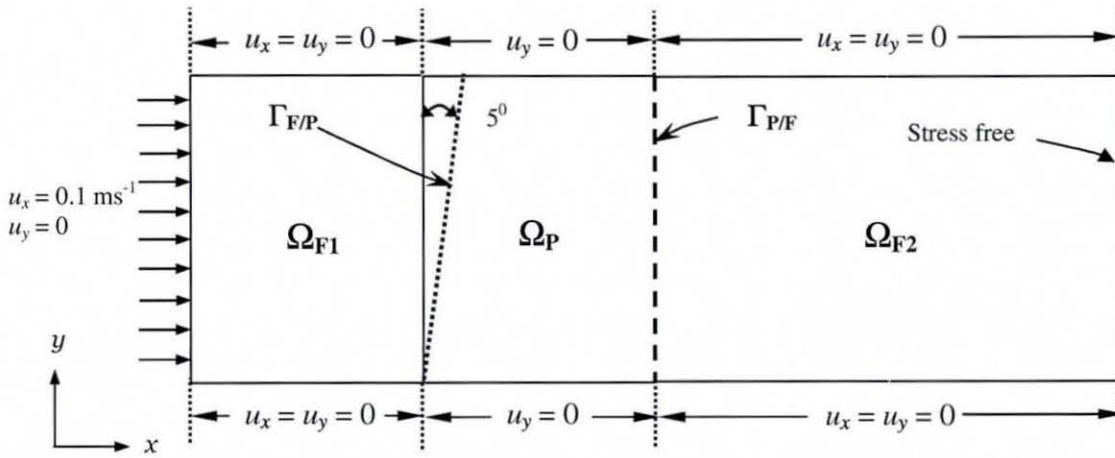
Figure 6. 99: Boundary conditions imposed on the rectangular coupled free/porous/free domain with slant interface

The boundary conditions enforced on the domain wall are exactly similar to those described in **Figure 6. 93**. The computational mesh obtained after the domain discretisation has the identical density as that used in the previous case.

The incompressible fluid to be cleaned through this filtration module is homogeneous material having density of 970 kg m^{-3}. The rheological behaviour of the fluid is described by the power law model in which the consistency coefficient is 80 Pa s and the power law index is 1.15. The simulated flow path taken by this shear-thickening fluid is plotted in **Figure 6. 100**.
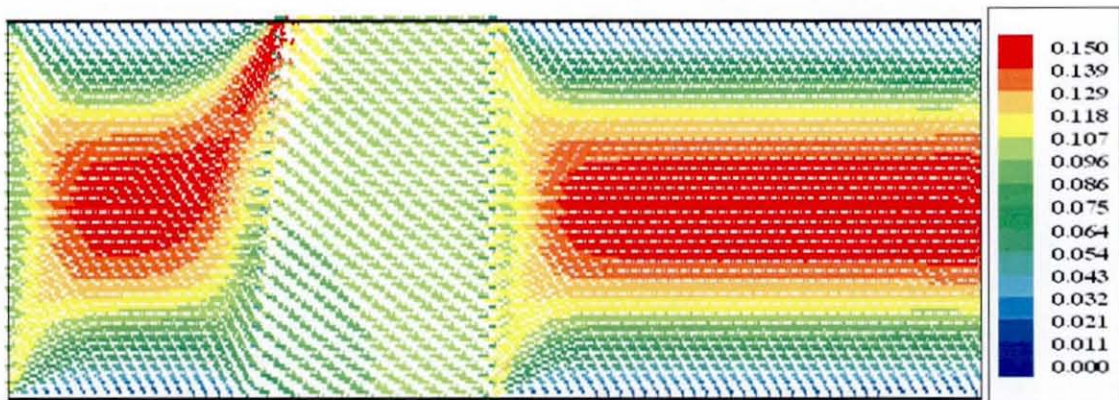
Figure 6. 100: Simulated flow field in the rectangular coupled free/porous/free domain with slant interface

The velocity profile is found to be fully developed parabolic in the free flow regions. At the interface of free and porous region the flow direction is seen to be distracted slightly due to sudden hindrance by the porous surface and portrays the nature of interface. The velocities in the bulk porous matrix are in plug flow. The pressure distribution in the overall domain is shown by contour plots as shown in **Figure 6. 101** below.
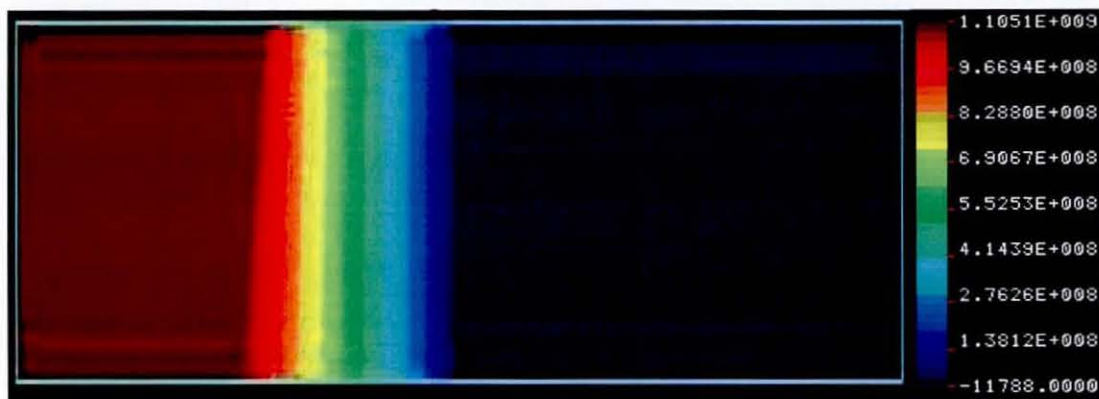
Figure 6. 101: Simulated pressure distribution in the rectangular coupled free/porous/free flow domain with slant interface

The total pressure drop developed over the domain is calculated to be 1.10×10^9 Pa. The maximum pressure drop is found in the porous region and contributes around 68% of the total pressure drop. The pressure drop values in both the free flow regions are almost constant in the direction of flow.

6.4.4.3   Flow through concentric circular coupled free/porous/free domain

The solution domain considered in the present case is a circular porous ring of a definite thickness sandwiched between two concentric open channels forming annular sections as shown in **Figure 6. 102**.
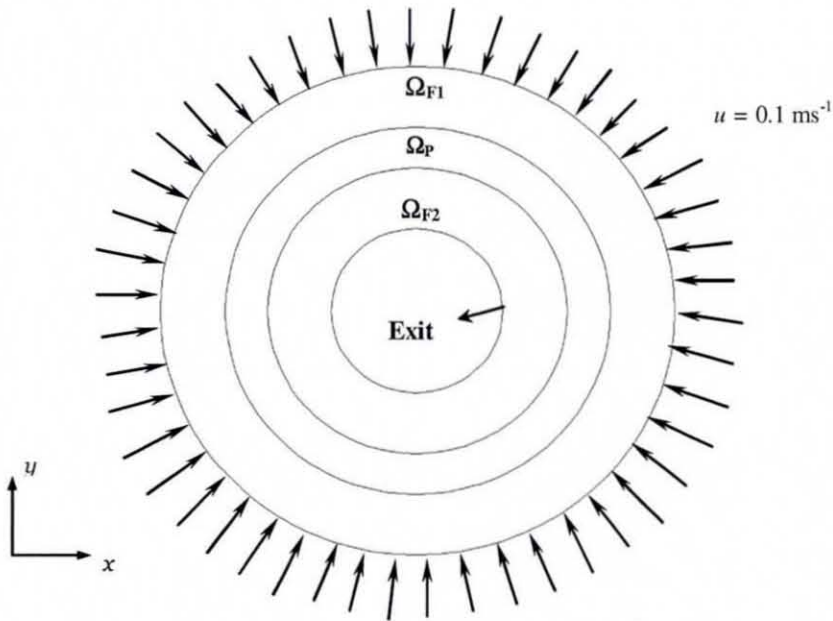
Figure 6. 102: Boundary conditions on concentric circular coupled Stokes/Darcy/Stokes flow regime

The radii of the zones corresponding to outer Stokes, Darcy and inner Stokes regions are 0.020 m, 0.012 m and 0.008 m, respectively. The total number of elements in the computational mesh counts to be 2400 corresponding to 9760 number of nodes. The number of elements contributed by the porous flow region is 480 with equal distribution of elements in both the free flow regions. The simulated flow path of an incompressible purely Newtonian fluid having density of 970 kg m^{-3} and zero shear rate viscosity of 80 Pa s is plotted in **Figure 6. 103**.
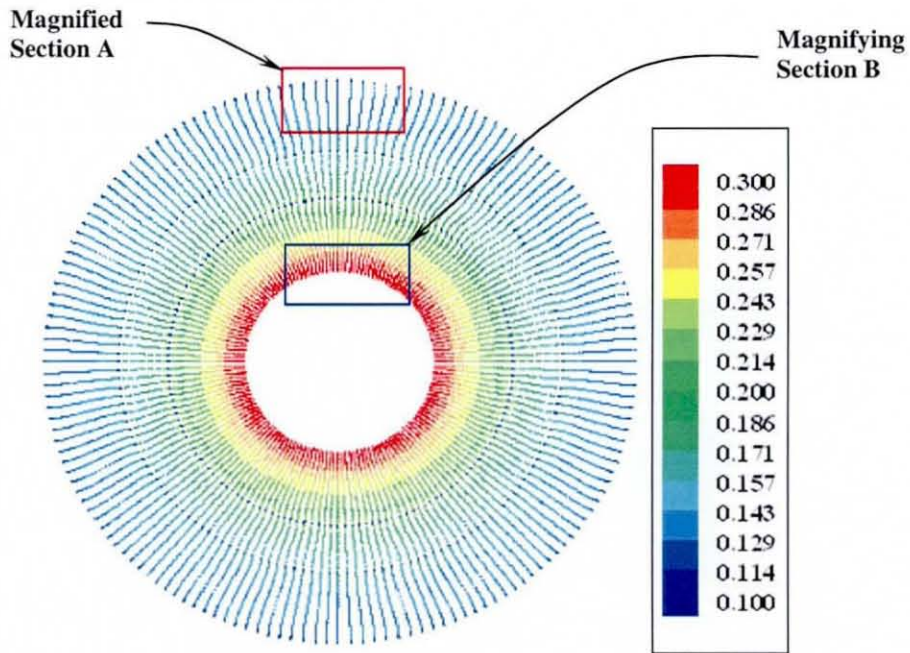
Figure 6. 103: Simulated flow field in the coupled concentric circular Stokes/Darcy/Stokes regime

The velocity vectors are directed towards the centre of the domain from inlet towards the exit. At the exit of inner free flow region, the velocity values are maximum due to the lowest cross-sectional area for the flow. Some sections of the domain from **Figure 6. 103** are magnified in **Figure 6. 104** to have a better idea about the fluid flow behaviour. The model results show only 0.14% discrepancy between the inlet and total outlet flow at the exit, confirming the preserved continuity of the mass.

(a)

(b)
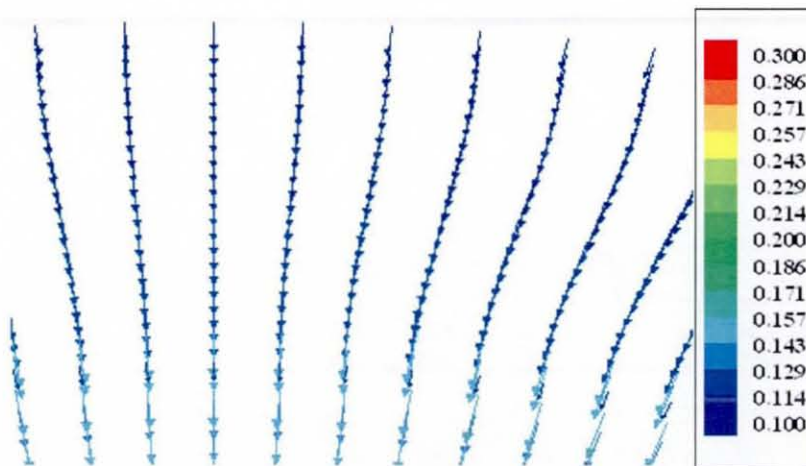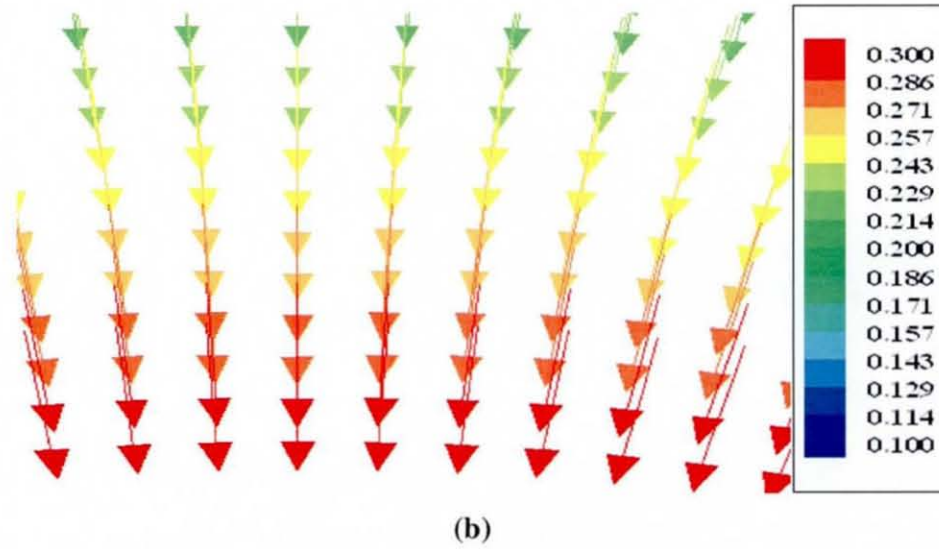
Figure 6. 104: (a) Magnified view of section A; (b) Magnified view of section B

The predicted pressure developed over the entire computational domain are shown in **Figure 6. 105** in the form of multicolour flooding contour plot with a colour scale to compare the relative values of their magnitudes.
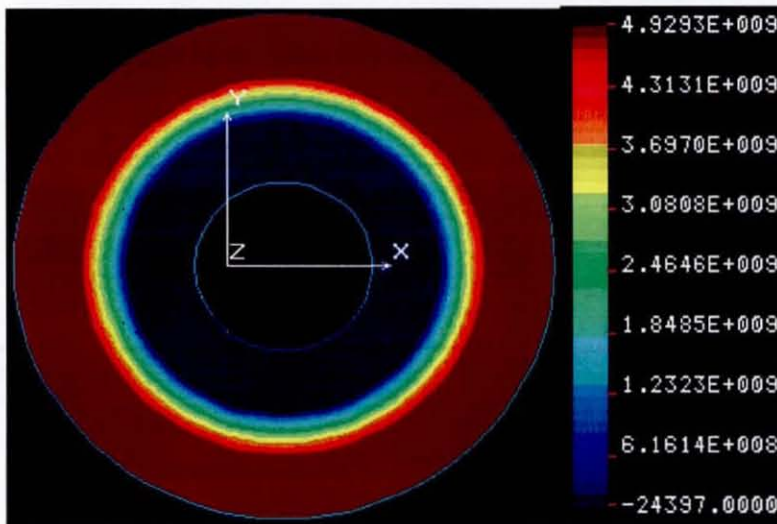
Figure 6. 105: Predicted pressure variations over coupled concentric circular Stokes/Darcy/Stokes flow domain

The overall pressure drop is calculated to be 4.9×10^6 kPa. The pressure values in both the free flow regions are nearly constant. The gradual pressure variation is observed in the porous matrix accounting 99% of the total pressure

drop. The simulated pressure contours can be well justified considering the predicted velocity vectors over the domain as shown in **Figure 6. 103.**

It is quite interesting to note that the fluid dynamical behaviour in this type of coupled flow regime has also been computed using the perturbed continuity scheme. However, the scheme based on equal order interpolations showed it inadequacy to approximate the field variables along the curved boundaries of the domain which is evident from the detrimental effects in pressure variations in **Figure 6. 49.** On the other hand, the Taylor-Hood scheme completely satisfies the spatial stability requirements related to the mass continuity on the elemental as well as global scale of reference which is proved successful in avoiding the so called "numerical locking" at the free/porous interface.

6.4.4.4   Flow through combined free/porous/free regime in a single pleat region of the pleated cartridge domain

Up to this point, the numerical scheme based on Taylor-Hood elements confirmed its versatility and robustness towards curvilinear geometries of the flow domains and free/porous interfaces. Aiming towards achieving the central objective of this multidisciplinary project, it's the right point to start understanding the flow phenomena in the pleated cartridge filter module. In this direction, the second step has been taken by considering the single pleat domain from the multipleated cartridge assembly, as shown in **Figure 6. 106.**
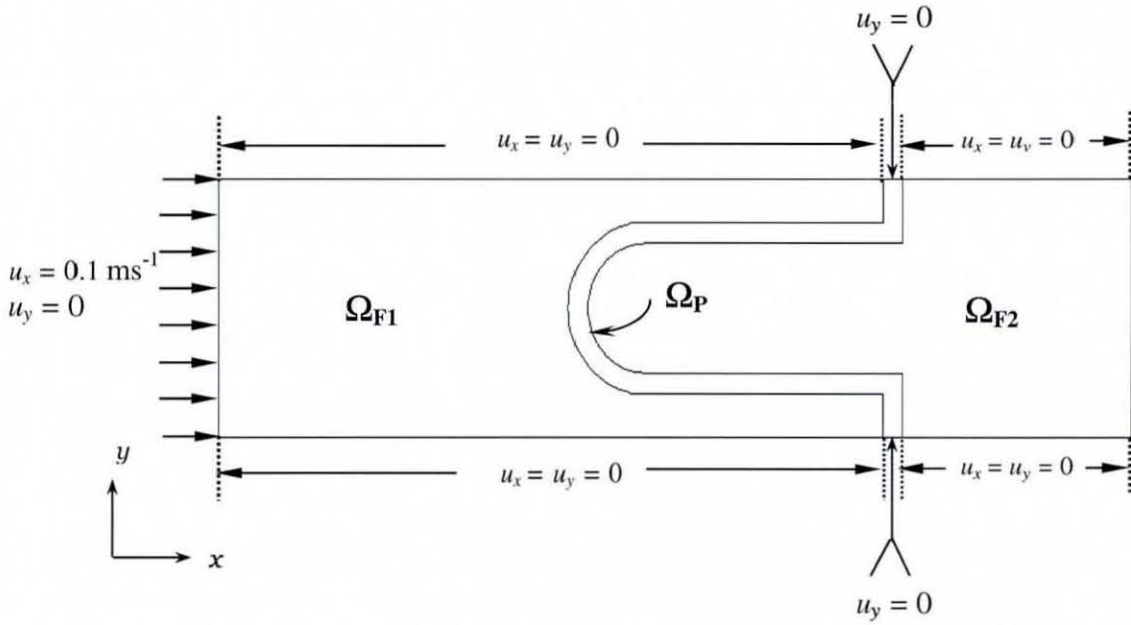
Figure 6. 106: Schematic representation of the single pleat cartridge domain

The Dirichlet type boundary conditions are specified on the boundaries confining the domain. No boundary condition is specified on exit boundary of the domain called as a stress-free boundary condition (Papanastasiou *et al.*, 1992) which actually imposes an effective neutral boundary condition.

The pleat is perfectly symmetrical along the flow direction parallel to x-axis and has a definite thickness of 0.59 mm which is very small compared to the dimensions of the overall domain measuring 0.005 m in width and 0.02 m in entire length. The computational mesh used in the simulations for this single pleat domain is shown in **Figure 6. 107**.
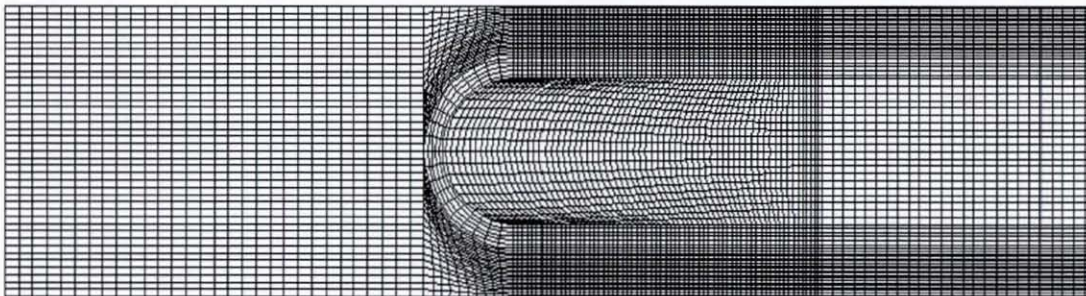
Figure 6. 107: Computational finite element mesh for the single pleated combined Stokes/Darcy/Stokes regime

The total number of elements in the computational mesh is 8272 and the accompanying number of nodes is 33463. The mesh is relatively coarse in both the free flow regions, Ω_{F1} and Ω_{F2}. However, near the curved boundaries of the porous region Ω_P, the mesh is refined in the free flow region. The mesh density is the highest in the narrow gap between the straight portion of the pleat and impermeable bounding walls of the free flow region.

The incompressible fluid has a density of 970 kg m^{-3} and exhibits a purely Newtonian rheological behaviour with a constant zero shear rate viscosity value of 80 Pa s. The trajectory of the fluid in three distinct regions of the solution domain is plotted in the form of velocity vectors in **Figure 6. 108**.
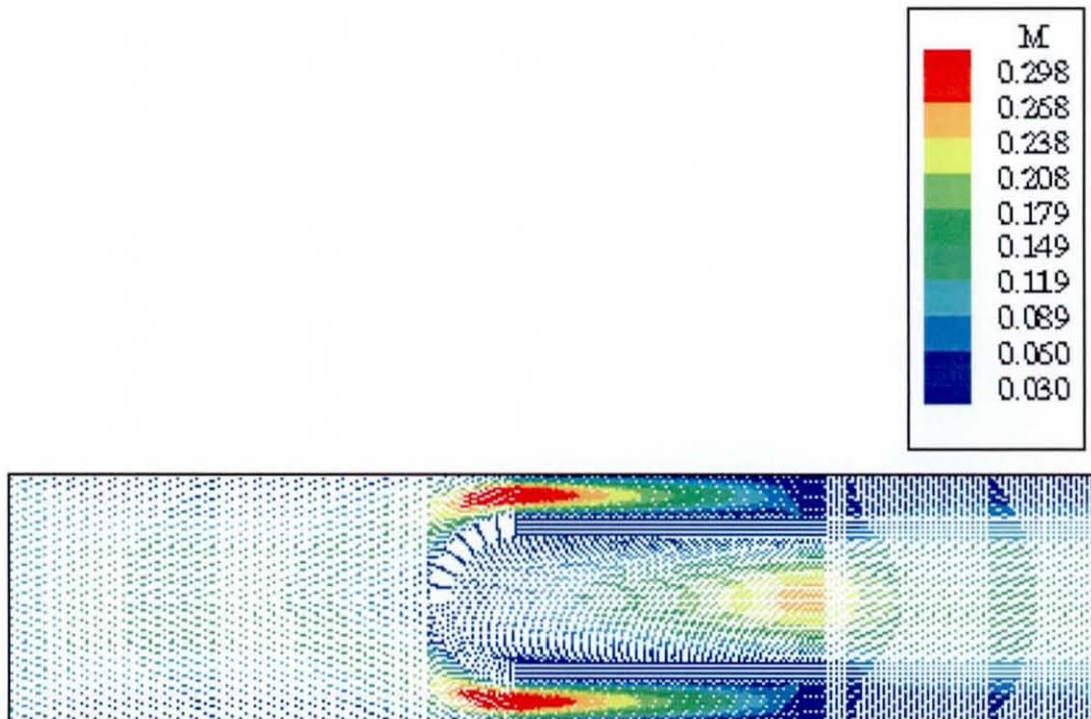
Figure 6. 108: Simulated fluid dynamical behaviour in a single pleat domain

Though the fluid enters the domain in plug flow, it shows some tendency towards getting fully developed in the free flow channel. When the fluid hits the curved exterior boundaries of the porous matrix, it experiences an obstruction to flow due the low permeability porous interface. A small amount of the colliding fluid seeps through the semi-circular portion of the porous domain and most of fluid slides along the curved boundaries finding its way towards the exit. The fluid

gets concentrated in the narrow channels confined by the impermeable walls of the domain and straight porous walls which, is evident from highly dense velocity vectors in these regions. Since these narrow channels are closed by the porous walls, the accumulated fluid strives hard to push itself through straight section of porous walls and intrudes into the second free flow region. The filtered fluid finds its direction towards the main exit as it attains the fully developed flow pattern in the second free flow region. The developed flow field strongly supports the pressure distribution obtained over the entire domain as shown in **Figure 6. 109**.
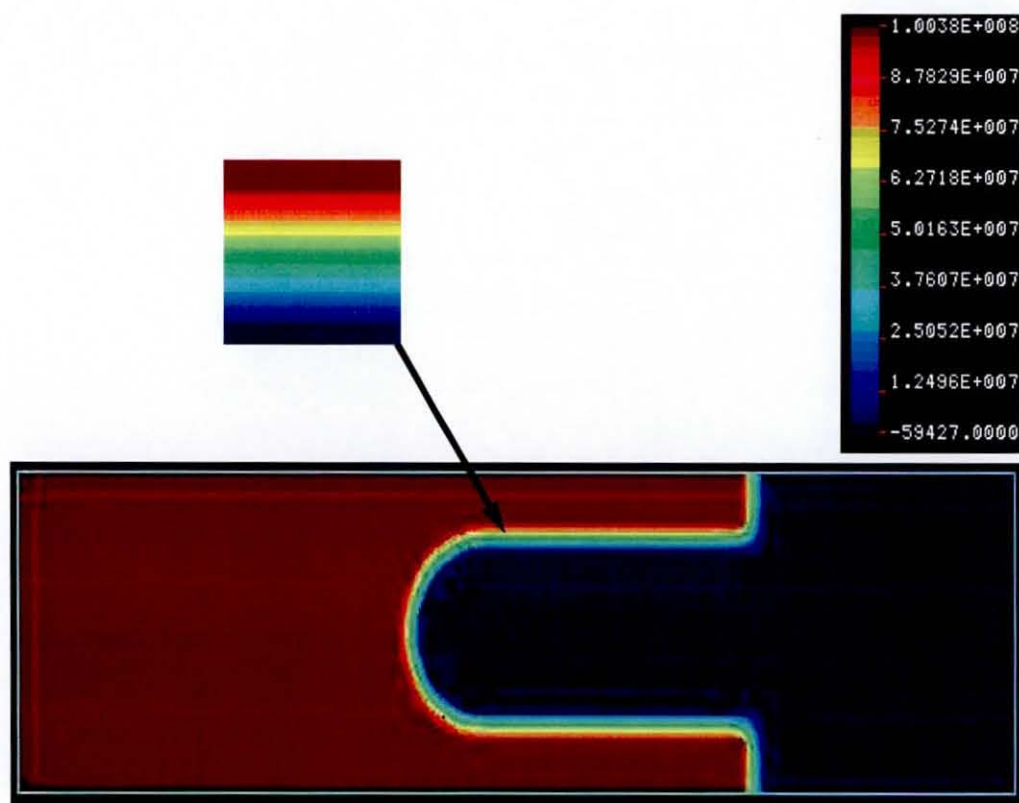
Figure 6. 109: Predicted pressure distribution in the single pleat domain

The simulated total pressure drop in the single pleat domain is 1.0×10^5 kPa. The pressure drop figure in both the free flow regions is obviously small and the sole contribution to the overall pressure drop value is by the porous matrix where a gradual variation in the pressure drop can be observed in the flow direction. The developed pressure field in a porous region is shown as an enlarged view at the top of **Figure 6. 109**.

6.4.4.5   Flow through the quarter circular pleated cartridge domain

The computational scheme based on the weighted residual finite element method using Taylor-Hood elements is found to be successful in accurately predicting the hydrodynamics in the single pleat domain. In the final stage of the model development, it has been decided to adopt the same methodology to scale up the hydrodynamics in the overall pleated cartridge filter assembly. Since, the single pleat represents the circular full-cartridge on larger scale of reference, the exactly similar fluid dynamical behaviour is presumed. Giving a due consideration to the symmetrical geometry of the full-cartridge structure along both the coordinate axes, it would be wise enough to select its repetitive section as a solution domain to save the computational time. Therefore, a quarter section of the circular cartridge assembly is selected which will also simplify the application of the line of symmetry boundary conditions. The quarter circular repetitive cartridge domain with its prescribed boundary conditions is shown in **Figure 6. 110.**
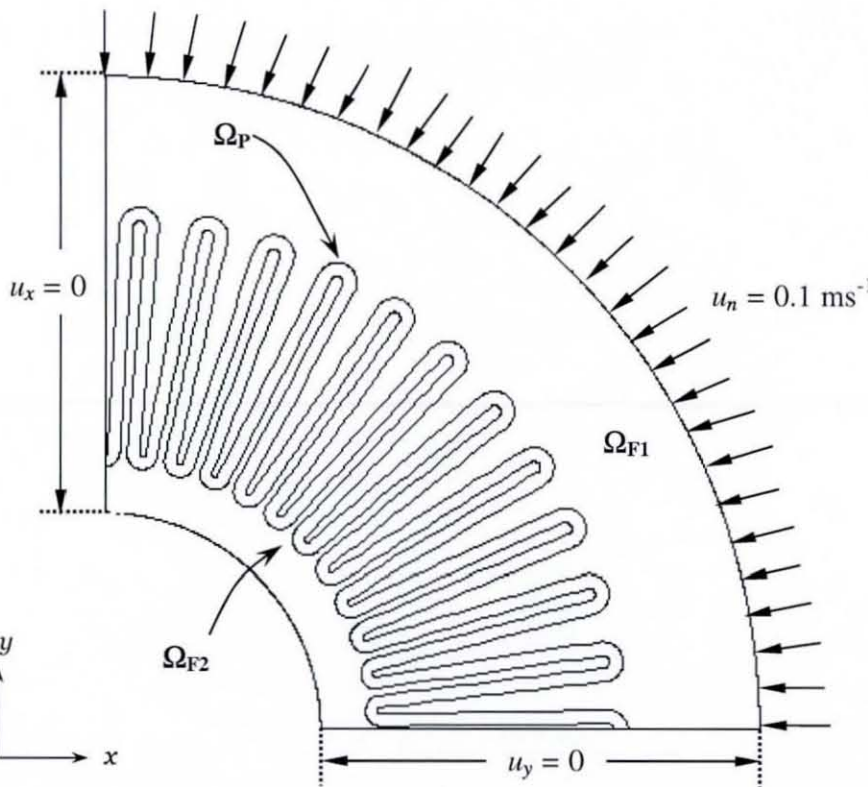
Figure 6. 110: Boundary conditions on pleated cartridge Stokes/Darcy/Stokes quarter domain

The first free flow zone Ω_{F1} near the inlet is composed of the outer metal casing holding the porous cartridge. The porous region Ω_P is made up of the porous pleated cartridge and the inner metal core carrying the clean fluid forms the second free flow region Ω_{F2}. The quarter circular repetitive unit is taken from an existing cartridge filter element whose geometrical characteristics are listed in **Table 6. 9.**

Table 6. 9: Geometrical characteristics of the cartridge filter element

No.	Property	Value
1.	Number of pleats (N)	46
2.	Height of pleat (H)	17 mm
3.	Thickness of pleat (TH)	0.8 mm
4.	Height of filter element (L)	127 mm
5.	Diameter of inner core (ID)	34 mm
6.	Filtration area (Af)	0.218 m^2
7.	Diameter of the outer metal casing (D$_0$)	85 mm

The computational mesh selected for the numerical analysis contains 9 noded C^0-continuous rectangular isoparametric elements. The mesh is contributed by 10350 numbers of elements with 41831 numbers of associated nodes. Overall, the mesh is highly dense as shown in **Figure 6. 111** with maximum mesh density in the vicinity of curved regions of the domain where the variations in the values of field variables are expected to be significant.
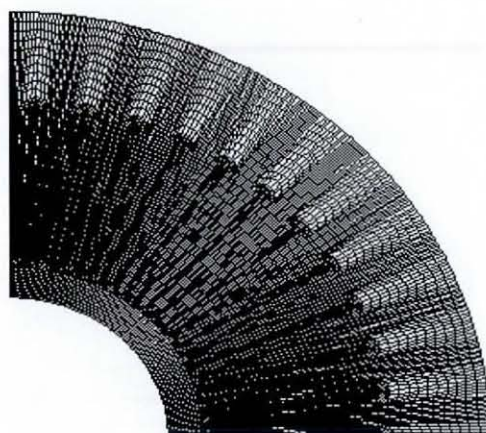
Figure 6. 111: Computational mesh for pleated cartridge Stokes/Darcy/Stokes quarter domain

Since the cartridge is operated in constant filtration throughput mode, velocity is imposed as the boundary condition at the inlet of the domain. Stress free boundary conditions are imposed at the outlet. Line of symmetry boundary conditions are imposed on the vertical and horizontal straight sides of the domain.

The fluid is a purely Newtonian material having a constant viscosity of 80 Pa s and density of 970 kg m^{-3}. The pleated porous material is homogenous in all the coordinate directions, having isotropic permeability of 10^{-12} m^2. The flow path taken by the fluid while passing through three different flow regimes of this quarter pleated domain in traced in **Figure 6. 112**.
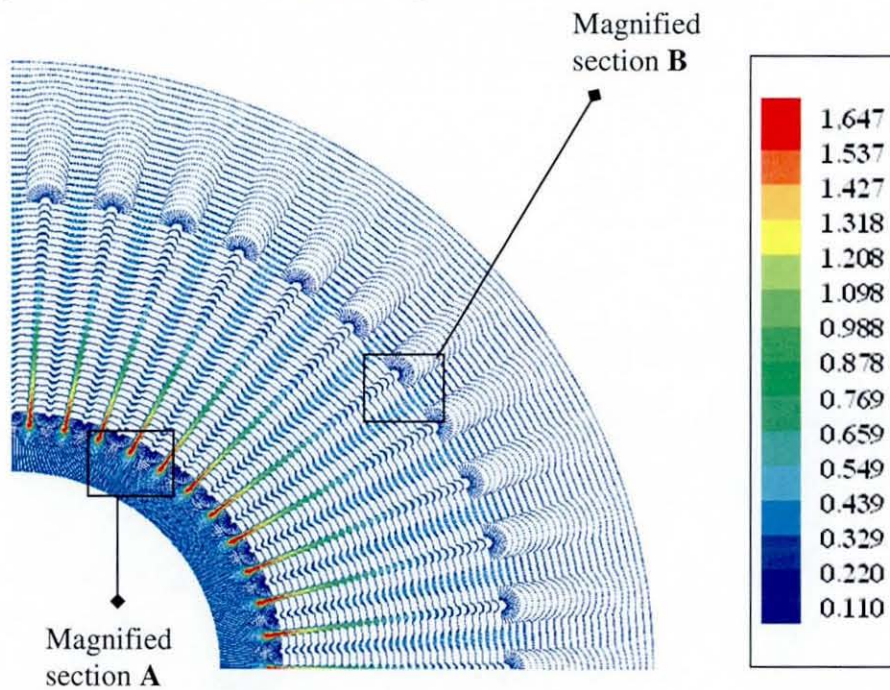
Figure 6. 112: Simulated flow field in pleated cartridge Stokes/Darcy/Stokes quarter domain

The open annular region between the inlet of the fluid and the pleated porous cartridge is too small in length for the flow to get developed. As the fluid approaches the porous matrix, it tries to push itself through the porous wall in the direction of applied driving force. Due to low permeable medium, a small amount of fluid is successful in crossing the barrier caused by the porous structure and the rest slides along the curved boundaries of the pleat. Most of the fluid gets diverted towards a narrow gap between two adjacent pleats. Since the pleat length is comparable to diameter of the cartridge, the narrow channel length is enough for

the flow to achieve fully developed profile. At the downstream end of the pleat gap channel, the fluid experiences an expansion effect in the second free flow channel. This scattering effect can be better visualised by magnifying particular sections of the velocity profile as shown in **Figure 6. 113**.

(a)

(b)
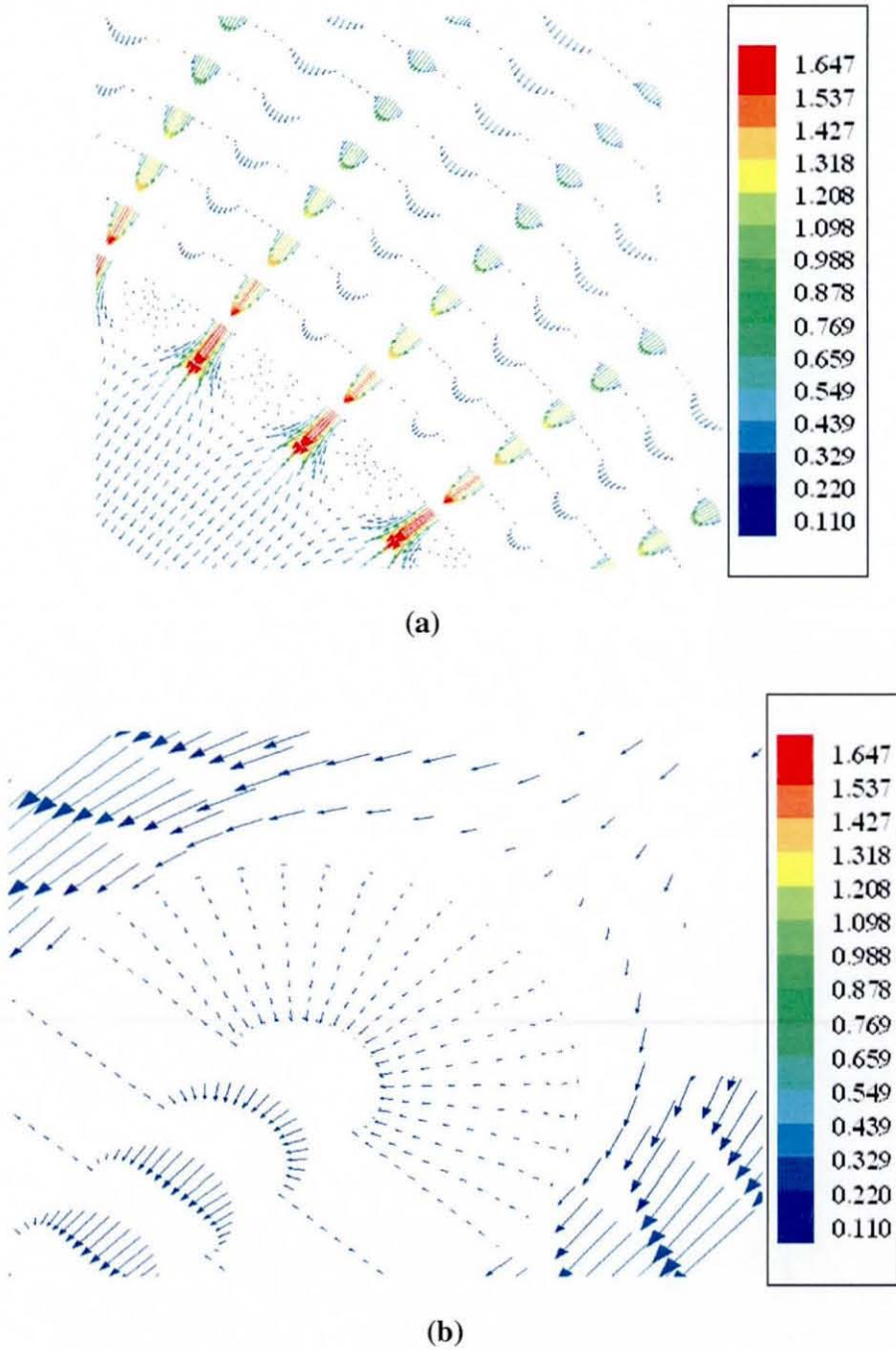
Figure 6. 113: (a) Magnified view of section A; (b) Magnified view of section B

The fluid seeps into the porous matrix from the top curved heads of the pleats and along the straight sections of the pleat in the direction almost normal to the permeable surface. The fluid filtered through the porous region enters the inner free flow core and attains a parabolic form till it reaches the bottom curved ends of the pleats. In the second free flow region, the fluid exhibits plug flow behaviour due to sudden expansion of flow. The continuity of mass is almost preserved and the discrepancy between inflow and outflow is only 0.22%.

The Reynolds number for the free flowing fluid is calculated in the first Stokes regime Ω_{F1} as,

$$R_e = \frac{u D_0 \rho}{\eta} \tag{6.16}$$

Where,

u is the inlet normal fluid velocity; D_0 is the diameter of the outer metal casing; ρ is the density of the incompressible fluid and η is the viscosity of the purely Newtonian fluid.

Since the inlet flow is in normal direction to the pleated structure,

$$D_o = D_{eq} \tag{6.17}$$

Where, D_{eq} is the equivalent diameter of the entry section and,

$$D_{eq} = 4 * r_H = 4 * \frac{A_F}{W_P} \tag{6.18}$$

Where, r_H is the hydraulic radius, A_F is the flow cross-sectional area of the quarter circular channel section W_P and is its wetted perimeter.

Inserting the values of all these geometrical parameters from **Table 6. 9** and the inlet velocity value of 0.1 m s^{-1}, the value of inlet flow Reynolds number comes out to be 0.106. Therefore, the Stokes equation is an appropriate choice for representing the free flow phenomena in the coupled flow domain of the pleated cartridge filter module.

The development of pressure over the entire geometrical domain can be elaborated with the help of **Figure 6. 114**.
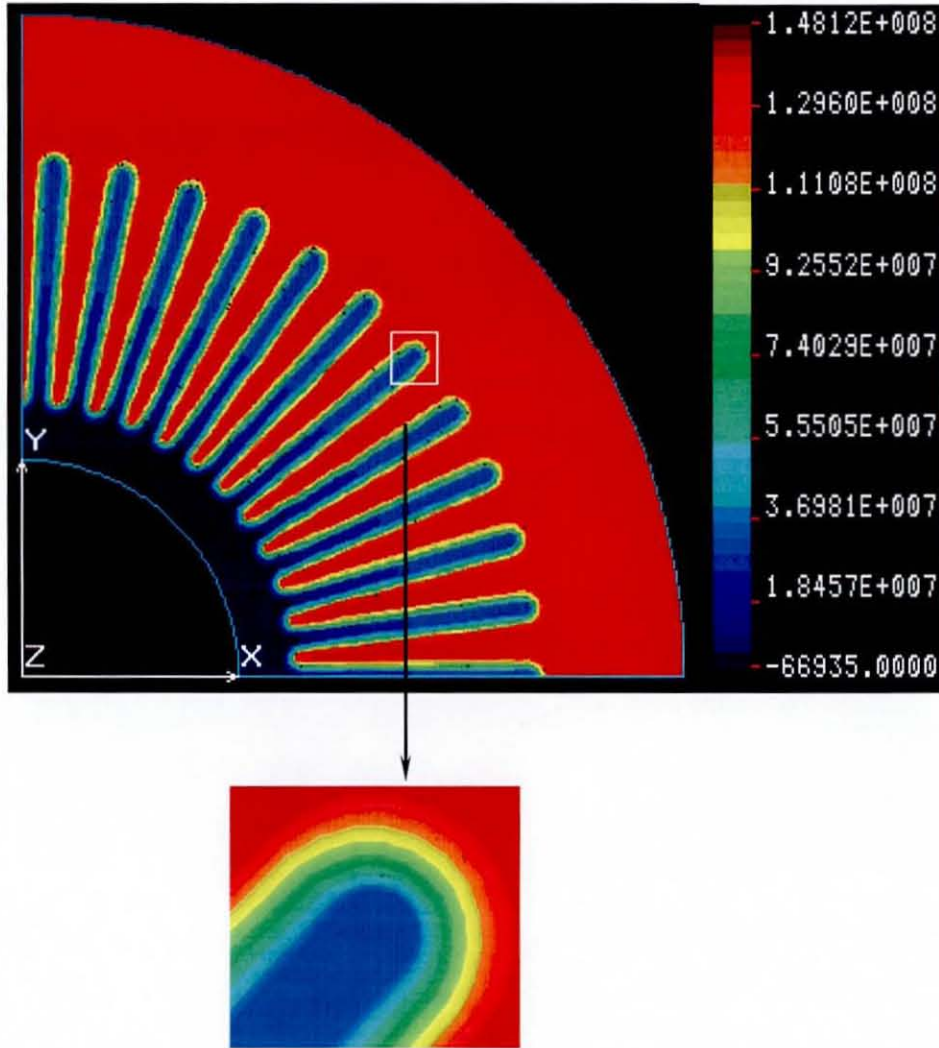
Figure 6. 114: Predicted pressure variations over quarter pleated domain

It is evident from **Figure 6. 114** that the nature of developed pressure field is the replicated version of the pressure variations observed in a single pleat domain shown in **Figure 6. 109**. The pressure drops in the exterior as well as the interior free flow regions are negligibly small. Considerable variations in the simulated pressure values are observed in the porous region. On the surface of the porous material, the fluid velocities are almost normal to the surface and hence a gradual variation in the pressure is visible across the porous medium which is magnified at the bottom of the plot.

In another experiment, the permeability of the pleated medium has been changed to 10^{-10} m². The physical properties of the fluid and the applied boundary conditions are kept intact. The predicted pressure variations obtained by simulation have been plotted over the quarter pleated domain in **Figure 6. 115**.
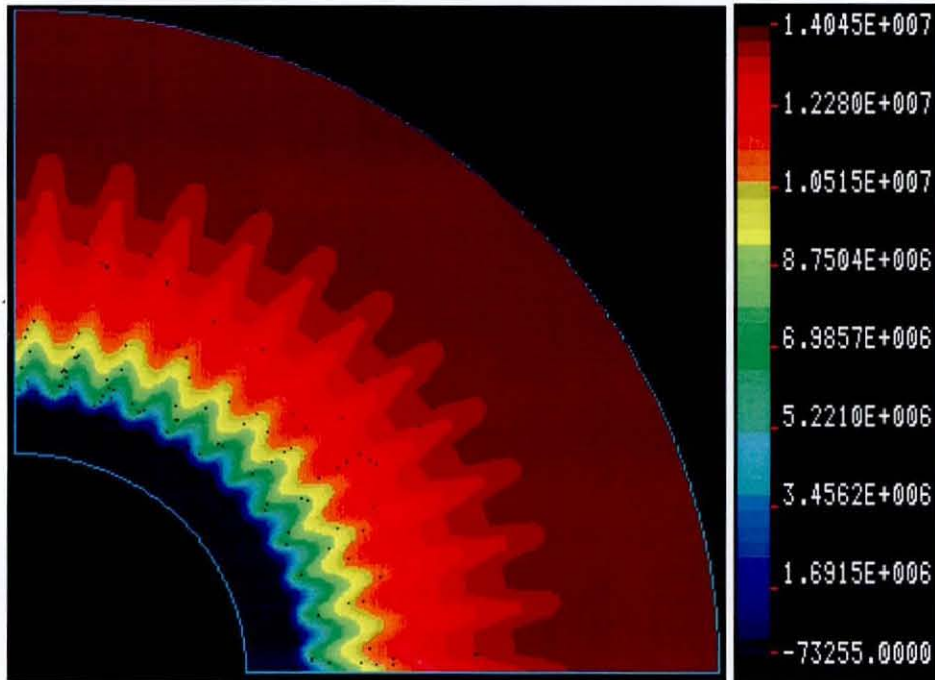
Figure 6. 115: Predicted pressure variations in the pleated Stokes/Darcy/Stokes quarter domain with permeability of porous medium of 10^{-10} m²

For the high permeability pleated porous medium, more and more amount of fluid finds its way through the bigger aperture pores present everywhere on the pleat surface as well as in the interior and not significant amount fluid choose to pass through the narrow pleat gaps. As a result, less hydrostatic pressure force is necessary physically to drive the same amount of fluid per unit time through the porous medium. Variations in pressure are completely radial in the direction of inlet flow and like the previous case, any significant fluctuations in the pressure values in both the free flow regimes are absent.

6.4.5 Flow through a tubular cross-flow membrane filtration module

As an example of axisymmetric flow situation, a tubular membrane filter element has been analysed for its coupled flow hydrodynamics. The filter module contains an outer cylindrical metal core which holds an annular cylindrical filter material which is made of wound fibre layers. The porous annular matrix is glued to a perforated cylindrical core to carry away the cleaned filtrate. The overall assembly of this filtration module could be understood from its cross-sectional view shown in **Figure 6. 116.**
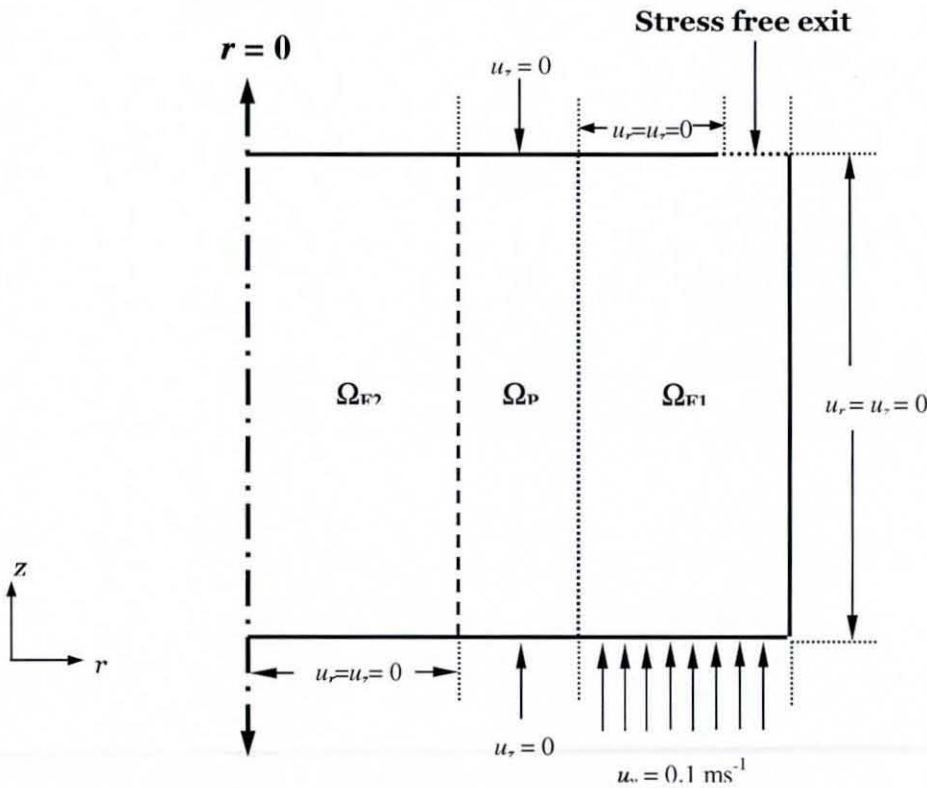
Figure 6. 116: Boundary constraints on the coupled free/porous/free regimes of cross-flow tubular membrane filter domain

All the three flow regimes are concentric and the filter element measures 0.05 m in length. The diameters of the outer metal casing and inner perforated core are 0.008 m and 0.02 m, respectively. The annular wounded porous region is 0.004 m thick. The fluid enters the filter through outer hollow casing and flows tangentially to the porous interface. The exit of the outer free flow region Ω_{F1} is

narrower than the entry section. The downstream end of the inner perforated core is closed and the cleaned filtrate is allowed to exit from upstream.

The porous medium is homogeneous and maintains rigidity throughout the course of filtration. The isotropic permeability of the medium is 10^{-9} m². The incompressible fluid to be cleaned is also supposed to be a homogeneous phase having density of 970 kg m^{-3} and viscosity for this purely Newtonian fluid is 80 Pa s. Within the bounds of these imposed constraints, the simulated flow field within the filter domain can be traced from the proportional velocity vectors in **Figure 6. 117.**
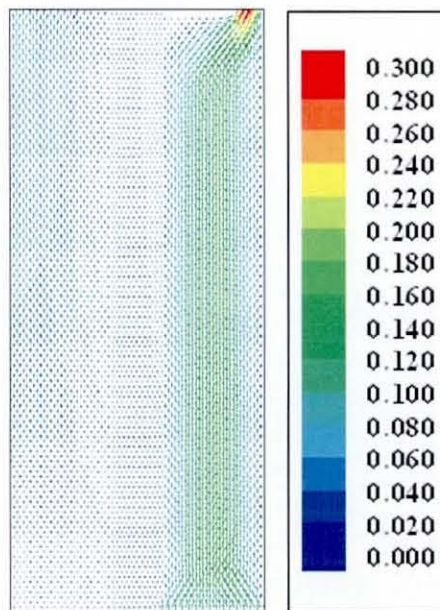
Figure 6. 117: Simulated flow field in the coupled free/porous/free axisymmetric regimes of cross-flow tubular membrane filter

The flow in the outer free flow region Ω_{F1} is developed at a certain distance from the entrance and the fluid penetrates gradually along the length of the porous matrix. Throughout the porous region, the fluid follows the plug flow profile according to the Darcy's law. After releasing into the inner most core, it follows the directions towards the upstream exit in the plug flow format attaining somewhat developed status near the exit boundary. Since the permeability of the filter medium lies in the upper bounds of applicability of the Darcy's law, a greater amount of fluid chooses to seep across the porous boundaries instead of escaping through the narrow exit of the outer metal casing straightaway.

The hydrostatic pressure developed due to the cross-flow of fluid in the permeable media is shown in **Figure 6. 118.**
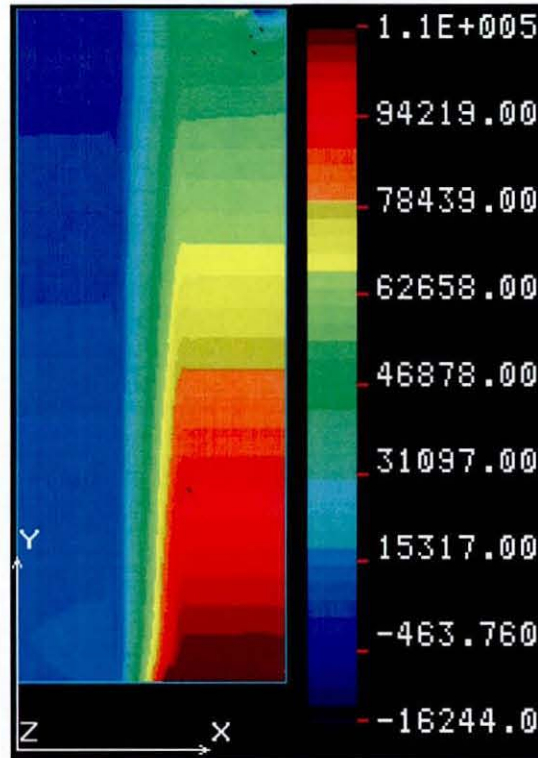
Figure 6. 118: Predicted pressure variations in the coupled free/porous/free flow regimes of tubular cross-flow membrane filtration module

As the fluid starts penetrating through the fine pores of the permeable medium, the pressure values are dropping in the direction of flow providing the necessary driving force. The simulated results have been validated by quantitative evaluations based on the global mass balance calculations which showed a positive discrepancy of 3% well within the tolerance bounds, however could be ameliorated by successive mesh refinements.

6.5 **Closure**

The C^0-continuous isoparametric elements are found to be highly versatile in approximating the curved geometrical features of domains with reduced domain approximation errors. Both the numerical schemes i.e. perturbed continuity method and Taylor-Hood method couples the free flow and porous flow

regimes in a considerably simpler way without applying any *ad-hoc* artificial boundary conditions at the free/porous interface. The finite element formulation based on the Taylor-Hood elements is found to be the most sophisticated approach due to absence of any mathematical complicacies related to stability and accuracy even for the highly irregular shaped domains.

7   Computational analysis of experimental data

As mentioned in the beginning of the discussion, the filter assembly is primarily composed of three distinct zones as shown in **Figure 7. 1**. Zone 1 is a free flow region between the housing and the inlet surface of the cartridge; zone 2 is the porous region (the filter medium and its supports); and zone 3 is the inner core (which is also a free flow region) downstream of the medium.
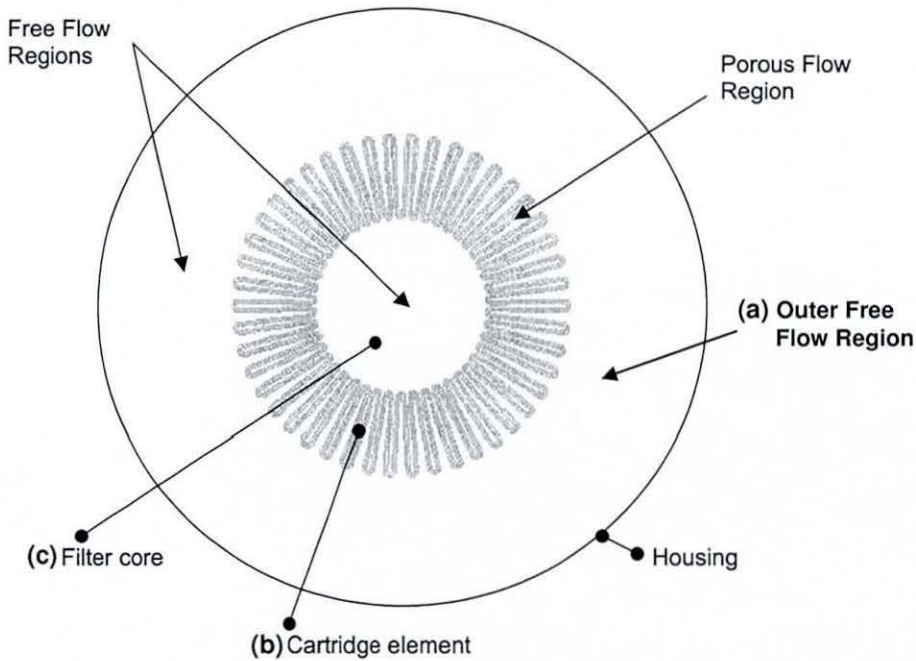
Figure 7. 1: Cross-sect ion of a pleated cartridge showing the three principle flow zones to be modelled: a) the region inside the housing and upstream of the medium; b) The filter cartridge; and c) the region downstream of the medium in the filter core.

From the computational results presented for the coupled free/porous flow dynamics in pleated cartridge filter domain, it has been concluded that the bulk of the pressure drop occurs within the porous filter medium and hence, the approach is primarily based on developing a porous flow model (Hanspal *et al*, 2005; Waghode *et al*., 2004; Ruziwa *et al*., 2003) for any quantitative analysis of cartridge permeation experimental data.

7.1   Modelling of pleated filter cartridge

Considering the complexity of the cartridge geometry, it is useful to investigate the possibility of a repetitive unit whose simulation is equivalent to the modelling of the whole domain. It could be used in the future to routinely speed up the simulations required in the design of new filters and would provide a more detailed analysis of hydrodynamics in cartridge filters. As the porous pleated cartridge is symmetric along both the coordinate axes, it's smallest unit which represents the overall cartridge domain can be selected for simulations to save the computational cost. With this aim, various sub-sections of the circular cartridge domain are testified, some of which are shown in **Figure 7. 2**.
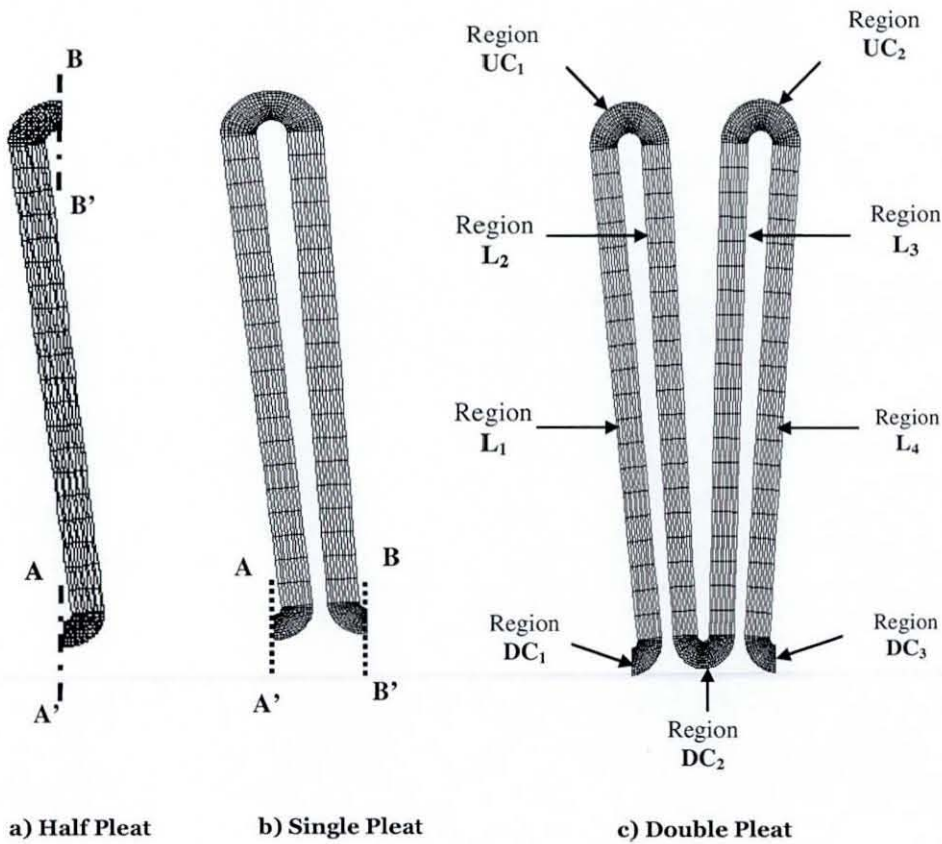
Figure 7. 2: Search for a repetitive unit of the pleated cartridge domain

All the pleated units in **Figure 7. 2(a), (b) and (c)** are taken from a larger symmetric cartridge domain and are accompanied by artificial or symmetrical boundaries such as AA' and BB'. The main idea behind this is to search for the

smallest unit of the symmetric cartridge which can represent it, in nature and geometry and the simulated fluid dynamics in this smallest sub-section would not be influenced by the constraints imposed on the so called prosthetic boundaries. Finally, a two-pleat domain presented in **Figure 7. 2(c)** is observed to be fulfilling this criterion and has been selected as a repetitive unit for performing further simulations to compute fluid dynamics in pleated cartridge domain.

The known input conditions are the constant volumetric flow rate to the cartridge housing and the pressure at the exit of the inner tube. As the filtration is carried out at constant throughput, flow velocity normal to the filtering surface is imposed at the inlet as shown in **Figure 7. 3**.
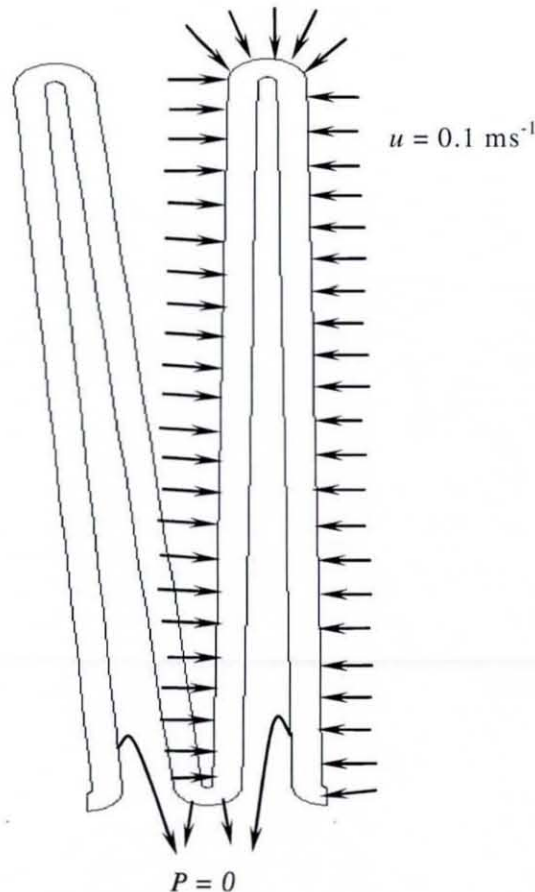
Figure 7. 3: Boundary conditions on double pleat repetitive domain

The pressure values at the exit surface are restricted by applying zero pressure datum. The imposition of no-slip velocity boundary condition is

incompatible with the Darcy's equation. At the artificial boundaries, the normal velocity is zero to imply symmetry along that surface. The geometrical characteristics, physical properties and rheological data of fluid and permeable media and cartridge are tabulated as in **Table 7. 1**. The units of measurements are according to the standards followed in aeronautics and filtration industries.

Table 7. 1: Geometrical characteristics and physical and rheological properties

Geometrical characteristics		
No.	**Property**	**Value**
1.	Number of pleats (N)	46
2.	Height of pleat (H)	17 mm
3.	Thickness of pleat (TH)	0.7 mm - 0.8 mm
4.	Height of filter element (L)	127 mm
5.	Diameter of inner core (ID)	34 mm
6.	Filtration area (Af)	0.218 m^2
7.	Volumetric flow rate (Q)	78 litres min^{-1}
Physical properties of fluid and porous media		
No.	**Property**	**Value**
1.	Density of fluid (ρ)	970 kg m^{-3}
2.	Permeability of porous medium K_x, K_y	10^{-12} m^2
Rheological properties of the fluid		
No.	**Property**	**Value**
1.	Power law index, n	1.3
2.	Consistency coefficient, η_0	0.08 Pa s

The computational mesh consists of 2400 elements with 10101 numbers of nodal points. The porous flow dynamics has been simulated by the UVP finite element method based on perturbed continuity scheme, described in Chapter 5. The value of speed of sound c used in the finite element simulations is chosen to be 1150 m s^{-1}. In finite difference approximations of temporal derivatives, the appropriate time-step value is found to be 0.1 in the implicit-θ formulations, the value of time-stepping parameter, θ is found to be 0.75. The stationary flow field obtained after 11 time steps is shown in **Figure 7. 4**.
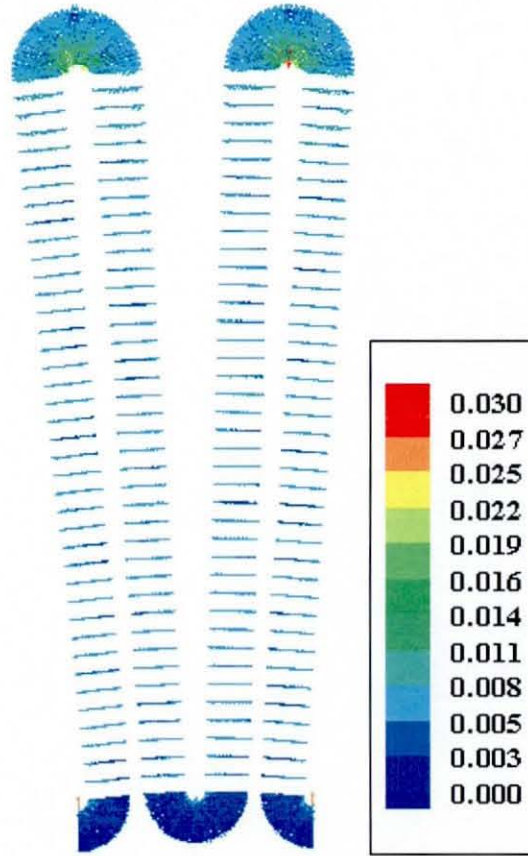
Figure 7. 4: Flow field over double pleat repetitive unit of the pleated cartridge

For clear visualisation of the values and orientation of velocity vectors, the flow fields in certain parts of the double pleat repetitive domain have been magnified in **Figure 7. 5.**

(a) UC_1 (b) UC_2
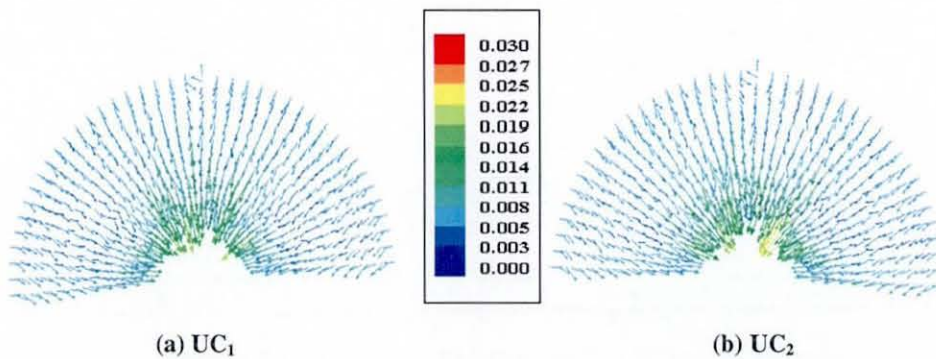
Figure 7. 5: Magnified flow filed in the top curved regions UC_1 and UC_2

Figure 7. 5 shows the magnified images of velocity profile in upstream top curved sections of the double pleat domains. As the fluid penetrates the porous matrix, the velocity increases due to reduction in effective cross-sectional area. The magnified view of velocity variations in straight sections of double pleat domain L_1 and L_3 is shown in **Figure 7. 6.**
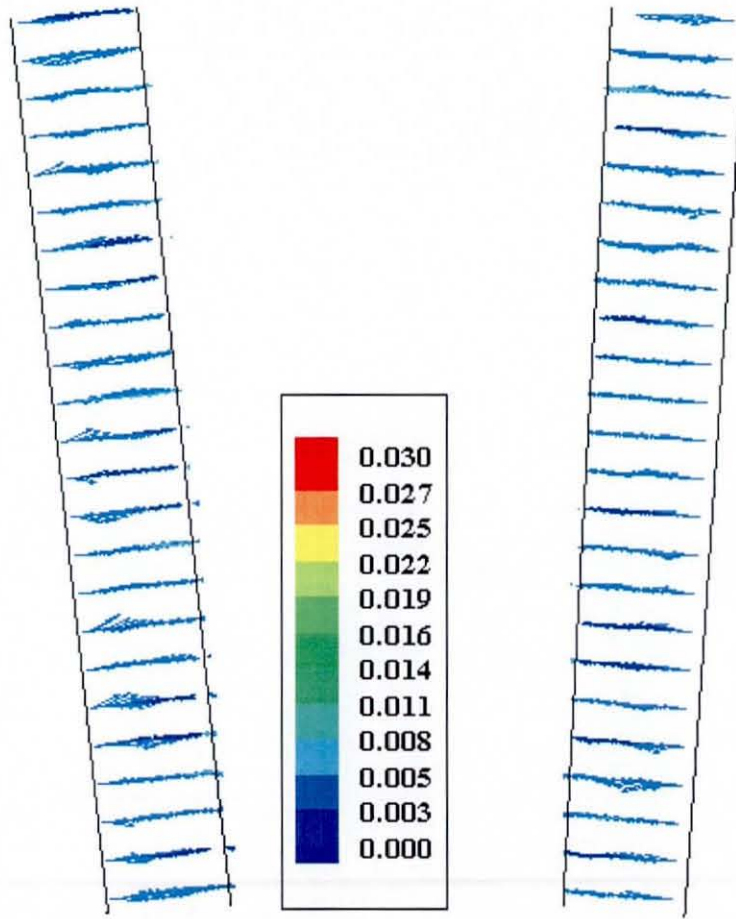
Figure 7. 6: Velocity profile in straight sections L_1 and L_3 of the double pleat repetitive domain

The flow in all the straight sections of the domain is almost constant. The flow profile in the curved regions at the downstream of the pleat is shown separately in **Figure 7. 7.**

(a) LC$_1$

(b) LC$_3$

(c) LC$_2$
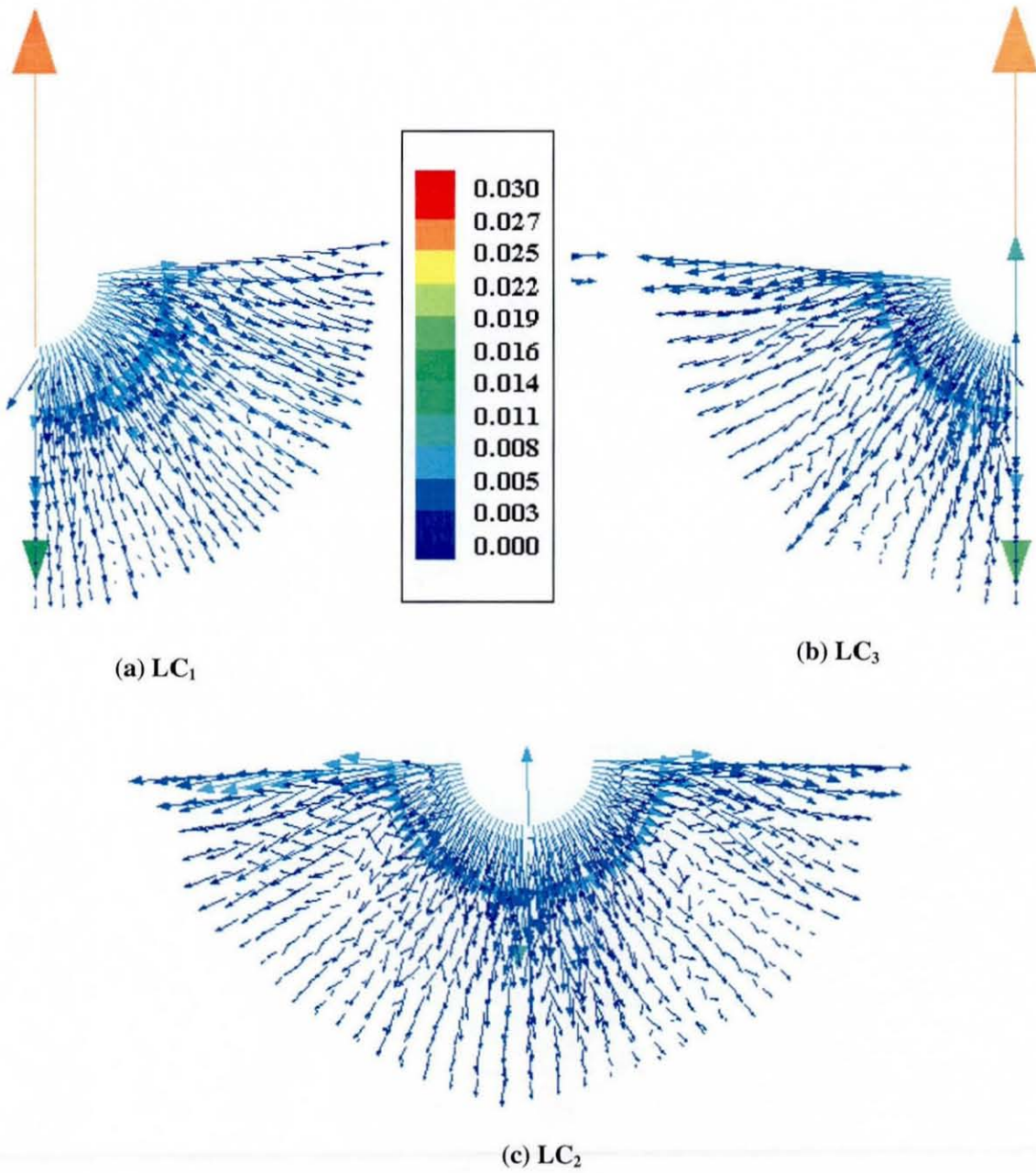
Figure 7. 7: Flow field developed in the curved regions in the downstream region of pleats

The flow experiences expansion from inlet to outlet as a result of increase in cross-sectional area normal to the flow direction. At the artificial boundaries where, the line of symmetry is specified, certain high velocity vectors are observed especially at corner points. This signifies a singularity at that point due to the ambiguity in the orientations.

The pressure distribution resulted from the constant volume filtration is plotted in **COSMOS Geostar** GUI as shown in **Figure 7. 8.**
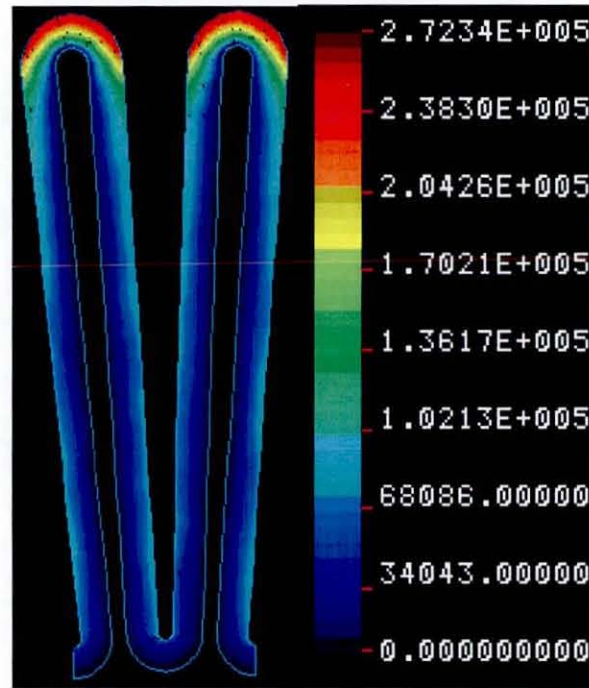
Figure 7. 8: Pressure variations in the double pleat repetitive domain

Maximum variations in pressure values are observed in the upstream curved sections of the pleat as the thickness of the pleat increases gradually from upstream towards downstream. The pressure field developed over the upstream curved section of the pleat has been magnified in **Figure 7. 9.**

(a) UC_1 (b) UC_2
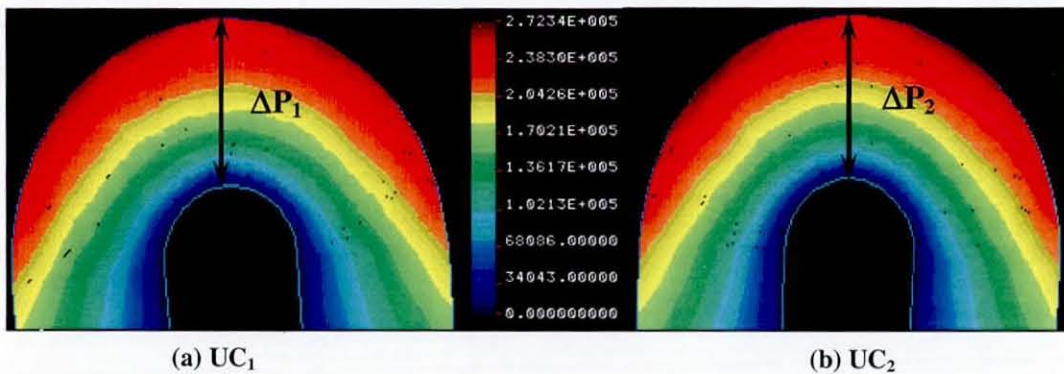
Figure 7. 9: Magnified view of pressure variations in upstream curved regions of pleat

Gradual variation in pressure has been observed in each elemental layer of the porous medium. The pressure differential developed over the thickness of the both the top curved porous regions UC_1 and UC_2, is almost equivalent to 2.7×10^5 Pa. An identical form of pressure variations have been observed in downstream curved regions of the pleats as presented in **Figure 7. 10**.

(a) DC_1 (b) DC_3

(c) DC_2
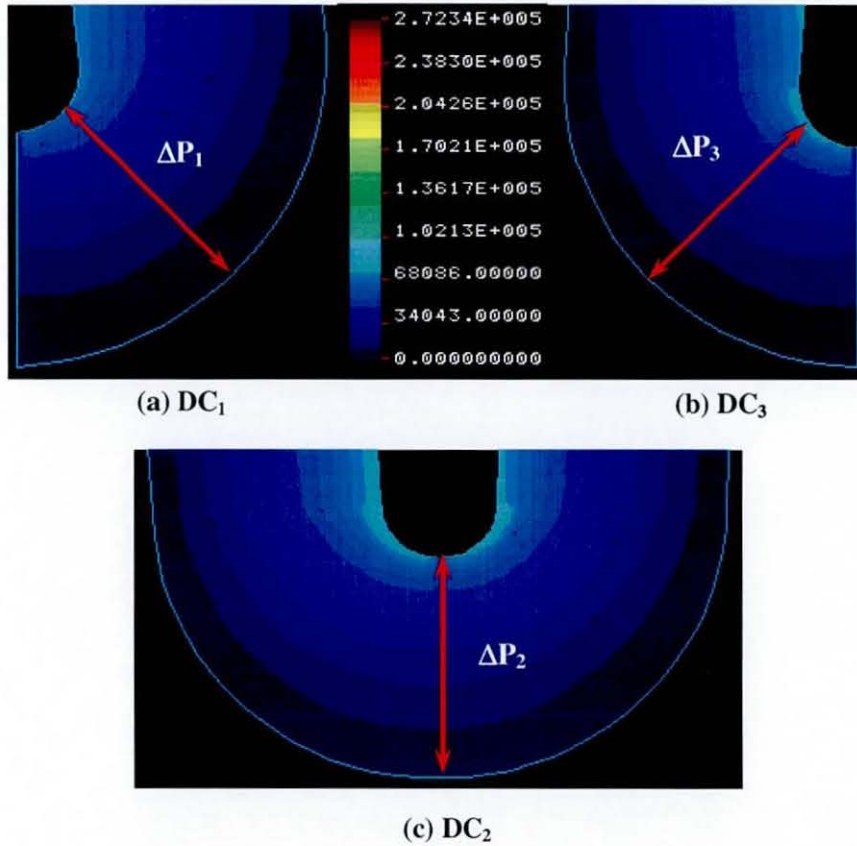
Figure 7. 10: Pressure variations in downstream curved regions of pleats

The pressure developed is found to be symmetrical in all the three curved region at downstream of the double pleated repetitive domain. The hydrostatic pressure drop developed across the medium in each case is around 1.0×10^5 Pa.

Table 7. 2 shows the mass balance figures for a repetitive unit. Since the repetitive unit has curved and straight regions, it is convenient to calculate mass flow through each region separately and add the values to give the cumulative amount of mass going in and out of the unit.

Table 7. 2: Mass balance for the repetitive unit

Regions	Mass$_{in}$ (kg)	Mass$_{out}$ (kg)
DC$_1$	2.53×10^{-4}	3.62×10^{-4}
DC$_3$	2.53×10^{-4}	5.36×10^{-4}
L$_1$	1.10×10^{-2}	1.15×10^{-2}
L$_4$	1.10×10^{-2}	1.12×10^{-2}
UC$_1$	2.99×10^{-3}	1.92×10^{-3}
UC$_2$	2.99×10^{-3}	1.92×10^{-3}
L$_2$	1.10×10^{-2}	1.15×10^{-2}
L$_3$	1.10×10^{-2}	1.15×10^{-2}
DC$_2$	5.06×10^{-4}	8.98×10^{-4}
Total	5.10×10^{-2}	5.15×10^{-2}
$\dfrac{Mass_{in} - Mass_{out}}{Mass_{in}} \times 100 \approx -1\%$		

7.2   Symmetric Domain

In order to provide validity for the results obtained from the repetitive unit, a computational grid for the 46 pleated symmetric domain, with 4968 number of elements with 23184 number of adjoining nodes, is used in further simulations. The resolution of the mesh in each pleat is necessarily lower than in the two pleat domain so that computational time should not be relatively large. The simulated pressure field developed over the cartridge domain is shown in flooded contours generated by **Geostar®** in **Figure 7. 11**.
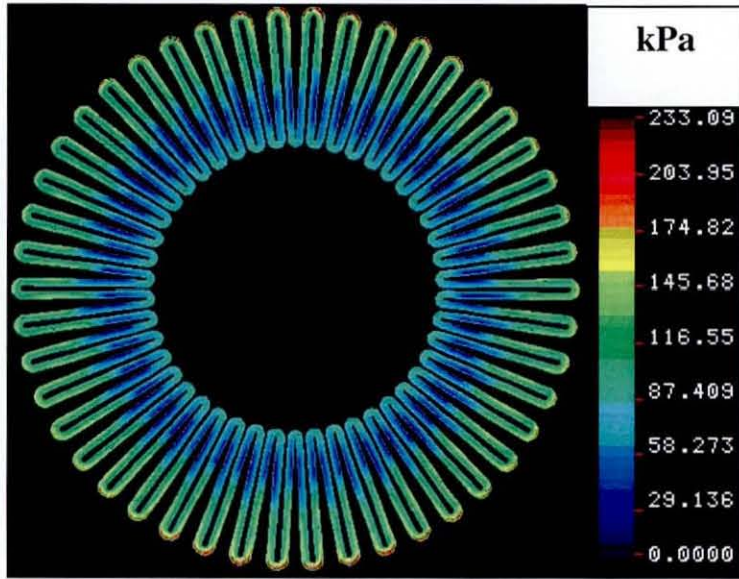
Figure 7. 11: Pressure field developed over full cartridge domain

A high pressure drop is developed at the outer curved boundary of the single individual pleat of the symmetric domain which decreases gradually, in the direction of flow through the porous domain. The pressure drop developed across the top curved region of the pleat was found to be around 230 kPa, which is in close agreement with the value obtained with the double pleat repetitive unit. A part of the cartridge domain has been magnified for improved visualisation of nature of pressure distribution in **Figure 7. 12.**
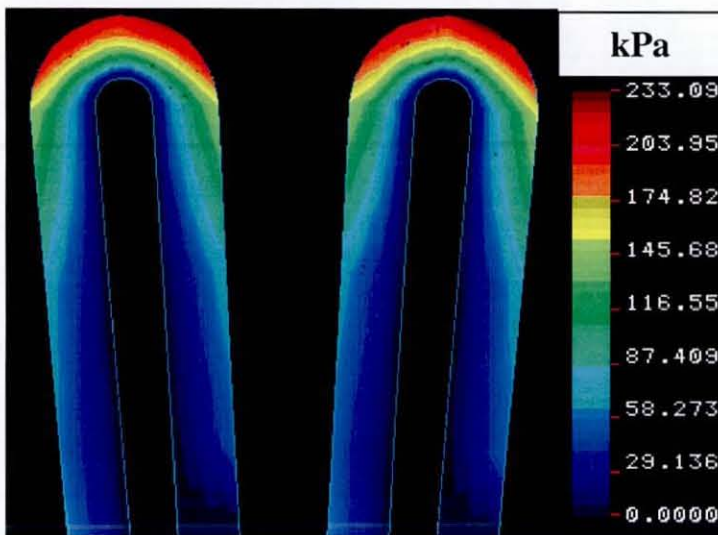
Figure 7. 12: Magnified view of pressure distribution shown in Figure 7. 11

The pressure variations over the bottom curved region of a typical individual pleat in the symmetric domain is similar in pattern to that in top curved region. The pressure values are decreasing towards zero in the direction of the flow. The pressure drop value is found to be around 95 kPa, which is in the vicinity of the value obtained with the double pleat repetitive unit.

In **Table** 7. 3, it is observed that the pressure drop values for the repetitive unit and the overall symmetric domain match closely. This data indicates that the "two pleat domain" is representative of the overall cartridge.

Table 7. 3: Comparison of results of repetitive unit and full cartridge domain

Region	Repetitive Unit (Δp in kPa)	Overall Domain (Δp in kPa)
Top Curved Region	270	230
Straight Region	100	100
Bottom Curved Region	100	95

7.3   Filter medium compression

Consider a flat sheet of a homogenous filter medium exposed to flow of a high velocity viscous fluid as shown in **Figure** 7. 13.
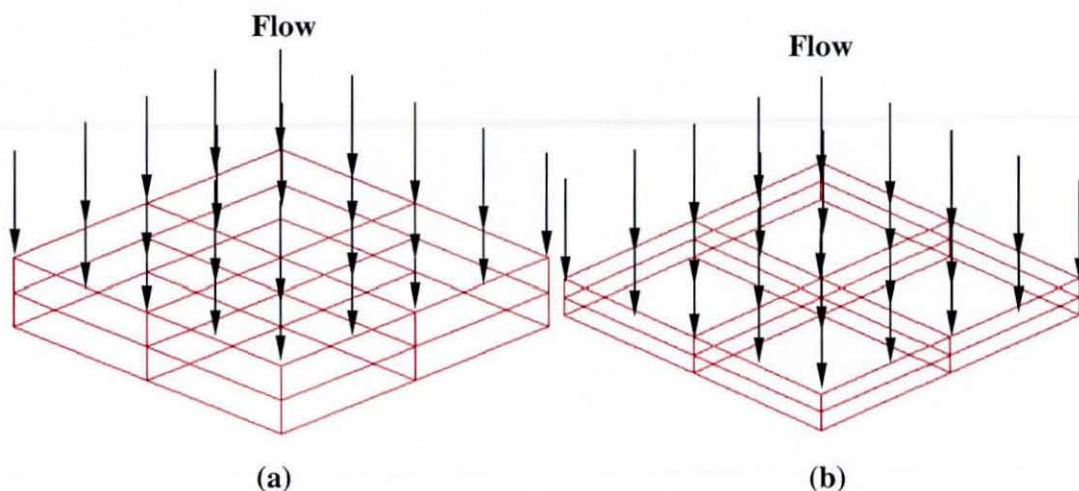
Figure 7. 13: (a) Flat filter medium before compression; (b) after compression

Due to the hydrostatic pressure exerted by the flowing fluid, the sheet gets compressed reducing the effective thickness of the medium. The compression thereby reduces the openness of pores and lowers down its permeability value than its parent dry or air permeability. The hydrostatic pressure drop developed across such a low permeability compressed filter medium then deviates significantly from its analytical value calculated from the Darcy's law as shown in **Figure** 7. 14.
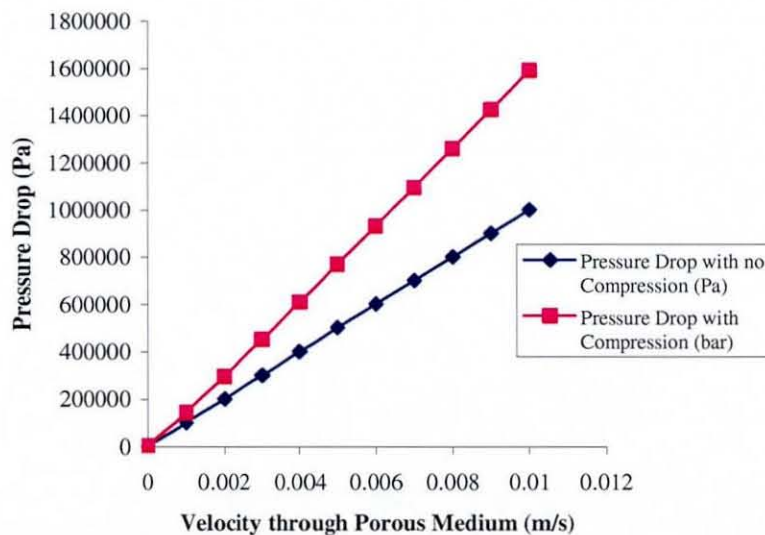
Figure 7. 14: Rise in pressure drop due to compression of porous medium

As the compression pressure drop is higher than the Darcy value and rises with the flow rate, it would have the severe influences on the mechanical and hydrodynamic designs of the filter cartridges as the pressure differential is a sole parameter of operational safety. Unfortunately, this point has not been addressed by the researchers and engineers working in the area of experimental analysis of cartridge filtration. The compression caused by the applied hydrodynamic forces alters the mechanical characteristics of the medium such as the bulk pore structure, tensile strength of the fibre etc. Since the fluid/solid interactions are not the topics of this discussion, the detailed analysis regarding the effect of compression on mechanical properties have been omitted.

In the case of pleated cartridges, the changes in fluid dynamical behaviour due to these media compression effects take place in slightly out of routine way as ,

- During the pleating process, tension occurs on the outer region of the folded filter medium where as the compression takes place on the inner region as shown in **Figure 7. 15,**
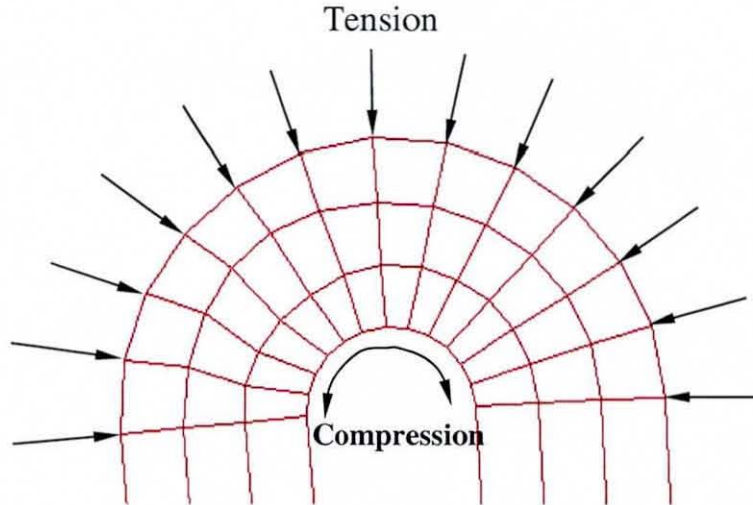
Figure 7. 15: Filter medium compression in pleated cartridge

- Hydrodynamic effects, when compression is due to the drag exerted by the flowing fluid on the surfaces of the particles or fibres forming the medium; compression of the medium increases with increasing stress acting on the fibre surfaces, resulting in a rise of the pressure drop over above what would otherwise be expected. **Figure 7. 14** shows the comparison of the flow rate versus pressure curves when the medium compresses with one where the medium is rigid and whose structure is unchanged at higher flow rates.

7.4   Pleat crowding and cartridge structure deformation

In pleated cartridge module, for a given inner core diameter, if the number of pleats surrounding the core is increased, it makes the adjacent pleats to narrow down their separating gap. In some cases, the adjacent pleats get merged thereby reducing the intrinsic filtration area. For a given value of volumetric flow rate, the reduced area incurs into drastic rise into inlet fluid velocity on the filter surface and henceforth, encourages the greater hydrostatic pressure drops. The geometric effects of increasing pleat density can be pictorially represented in **Figure 7. 16.**

| (a) Pleats = 75 | (b) Pleats = 100 | (c) Pleats = 125 |
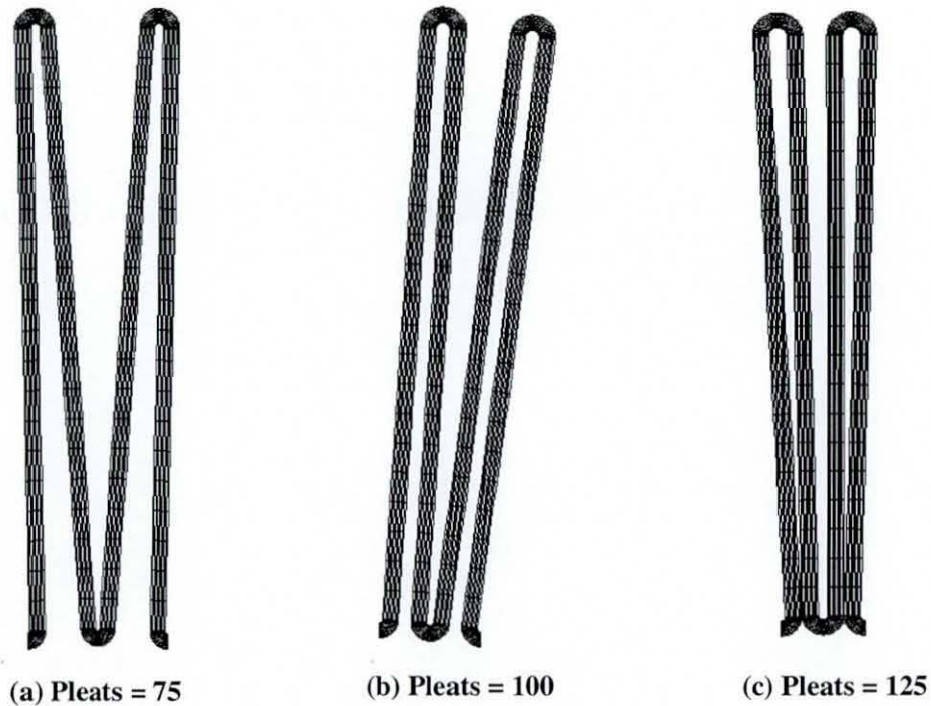
Figure 7. 16: Pleat closure due to increase in pleat density

Figure 7. 16 shows three different pleated cartridges having same geometrical dimensions except the number of filtering pleats. It can be observed that as the pleat numbers are increased, the pleat closure is enhanced.

In the case of porous medium having permeability of about 10^{-12} m^2 and greater and viscous shear-thickening fluid flow, the hydrodynamic drag on the pleat inflow surfaces is exceptionally high and causes the pleat faces to move towards one another, with the effect of closing up the pleat and reducing the effective filtration area. This effect is likely to be more pronounced at the leading and trailing edges of the pleat where the medium has been creased and pressure differences are at their greatest.

The assembly of pleats wound around the inner metal core is clamped at both the ends by flange heads. In certain cases, if the pleats are excessively high, these medium supports may prove to be inadequate to maintain the mechanical integrity of the pleated structure to withstand the fluid forces acting on the pleats.

The hydrodynamic forces caused by the inlet fluid at the filtering surface causes pleat deformation, "pushing" adjacent pleats apart. This effectively causes

two adjacent pleats to rotate slightly about the point where they contact the core, and makes gaps between neighbouring pleats on either side to be closed.

Pleat deformation due to long pleats in longer cartridge designs leads to either adjacent inner faces of a pleat or exterior faces of adjacent pleats coming together ("centre crowding") over the central regions of the pleat length. Some of these deformation effects are schematically drawn in **Figure 7. 17**.

Tension on the outer bend on the pleated medium causes compression.

Pleat closure due to fluid drag on medium fibres.

Region most influenced by too many pleats around the core, causing medium compression and pleat crowding.
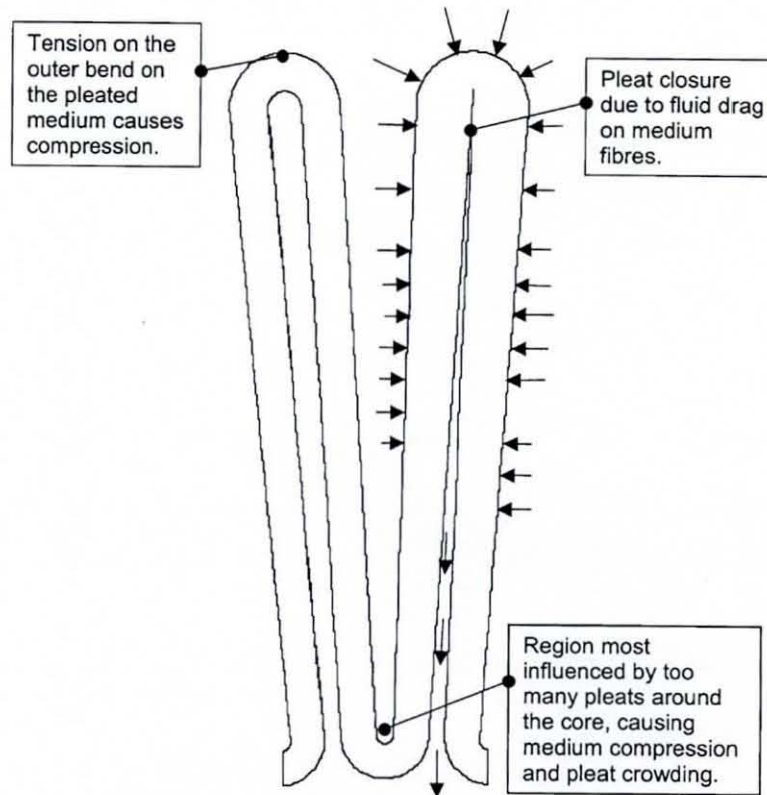
Figure 7. 17: Flat sheet media is pleated by bending, causing compression of the medium at the bends. Hydrodynamic drag closes the pleats, and too many pleats around the core cause pleat crowding. The left hand pleat illustrates one that is not affected by drag, the right hand one is closed near the pleat end due to drag and/or to tight pleating. The arrows show the general direction of fluid flow

In this work, we differentiate between medium compression and pleat crowding deformation in order to understand some specific aspects of cartridge performance.

7.5   Approach for the analysis of experimental data

The medium used in this study was **Fibre Glass** with an uncompressed thickness of 590 µm, which in the cartridge configuration were supported by wire meshes upstream and downstream with a combined thickness of 550 µm. The starting point for the work was the experimental determination of the flow rate versus pressure drop through flat sheets of the medium and through cartridges fabricated from the medium. These experiments were multi-pass tests carried out in accordance with ISO 16889 (1999), but without injection of contaminant into the fluid. That is, an oil having the technical name of MP 320 was permeated through the filter medium or cartridge at a constant flow rate and the resulting pressure losses were measured; the temperature was kept fairly constant (± 1°C), with a mean value of between 44 and 47°C, and measured at the same time as when a pressure measurement was taken.

From the flat sheet permeation data, a compression-permeability model was developed by simulation of flow through the medium. The resulting compression relationship was then used in a simulation of flow through the cartridge filter element made from the same media. In cases when a poor prediction of the flow rate versus pressure drop for the cartridge was obtained, flow through the cartridge was simulated with a reduced filtration area. In this way, effective area loss factors and degree of compression were determined for individual pleated filter elements. These factors accounted for the deviations between the simulated pressure drop based on conventional Darcy's law and the experimental pressure drop values.

7.5.1   Development of the permeability model

The flow rate-pressure drop variations for the flat sheet Fibre Glass medium (thickness 590 µm at 20 kPa, pore size 2.7 µm, 92 g m^{-2}) obtained by experiments are shown in **Figure 7. 18**. This experimental data was analysed to develop the permeability model for the medium. The permeating fluid used in the experiments was oil with a density of 880 kg m^{-3}, an average kinematic viscosity of

63 cSt, and a power law index of 1.0. The filtering area of the circular flat sheet of fibre glass medium used for carrying out the experiments was 28.3 cm².
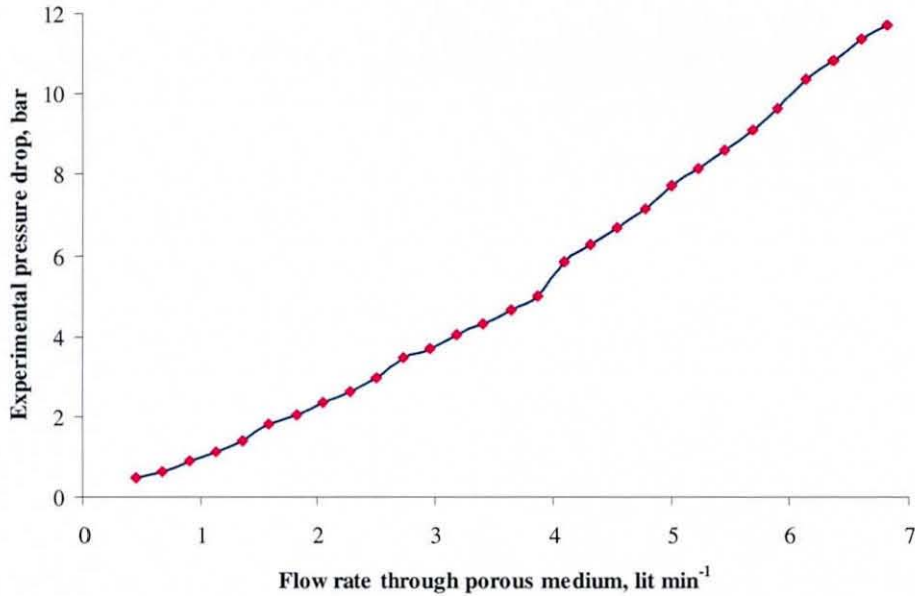
Figure 7. 18: Example of an experimentally measured curve of the velocity through a flat sheet dual fibre glass medium *vs.* pressure drop

The slope of the plot shown in **Figure 7. 18** was evaluated at each data point. Assuming that each flow rate on the plot obeys Darcy's law, the permeability of the medium was calculated for each point using

$$K_x = \frac{\eta}{slope} \Delta x \qquad\qquad (7.1)$$

where, Δx is the thickness of the flat sheet.

The permeability values for each flow rate were calculated. In these data, it was assumed that there was no compression for the first four data points and the compression effect reached a saturation limit at the last three flow rates (and remained constant for any higher flow rates). A linear relationship was then fitted to the first four points taking into account Darcy's law. It was therefore assumed that at low flow rates, the compression effect was negligible and only became significant as the flow rate is increased. As the degree of compression increased, a gradual decline in permeability values occurred.

Permeability equation for first four points in Figure 7. 18:

The first four points on the curve on **Figure** 7. 18 follow Darcy's Law without a compressive effect. The slope of the line drawn through these points gives a permeability value of 1.97×10^{-12} m². This approximates to the permeability of the uncompressed fibre glass medium, and has been used to simulate the pressure drop for the flat sheet medium when it was assumed that there were no compressive effects (see **Figure** 7. 20).

Mathematically, the uncompressed medium permeability can be written as:

$$K = K_x = K_y = 1.97 \times 10^{-12} \text{ m}^2 \text{ when } \Delta p < 1.13 \times 10^5 \text{ Pa} \tag{7. 2}$$

Permeability model for the 5th to 26th points in Figure 7. 18:

From the fifth data point (to the 26th), compression reduces the permeability value at each flow rate. The data was fitted with a power law expression as shown in **Figure** 7.19 and then the slope at each individual data point was calculated using equation **(7.1)**. The mathematical permeability model for the compression can be written as:

$$K = K_x = K_y = 3.26 \times 10^{-11} \Delta p^{-0.2397} \text{ m}^2 \text{ when } 1.13 \times 10^5 < \Delta p < 10.8 \times 10^5 \text{ Pa} \tag{7. 3}$$
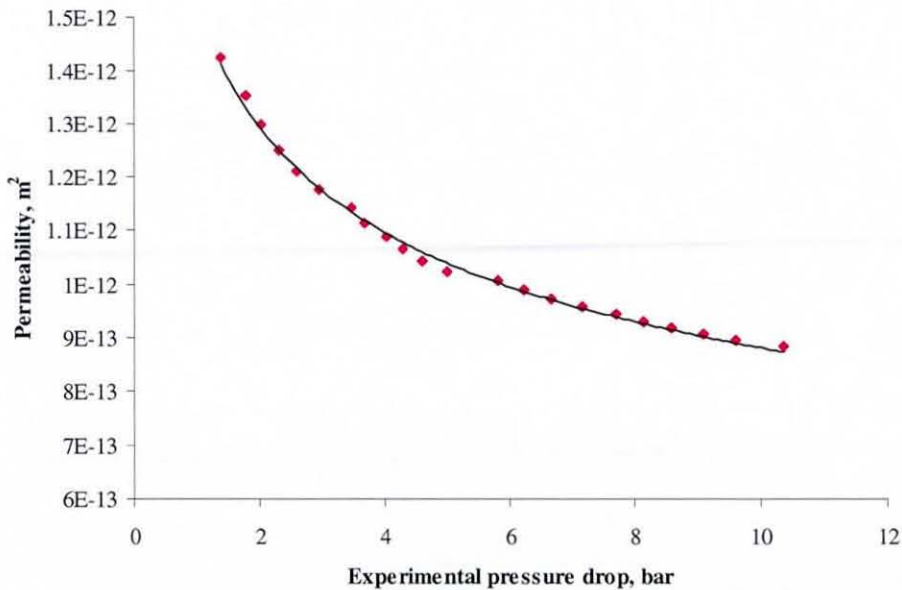
Figure 7. 19: Fitted curve for permeability *vs.* pressure drop for data points showing a compression effect (data from the flat sheet permeation test shown on Figure 7. 18)

Permeability model for last three points in Figure 7. 18:

It is assumed that at the 26th point (**Figure 7. 18**) compression has reached the saturation limit. Hence, the permeability value is constant for the last three data points and any higher flow rates. The last three data points were therefore represented by a straight line from which the permeability could be calculated. From the slope of this line the value of permeability corresponding to maximum compression was found to be:

$$K = K_x = K_y = 1.04 \times 10^{-12} \text{ m}^2 \text{ when } \Delta p > 10.8 \times 10^5 \text{ Pa}$$ **(7. 4)**

The variation of permeability with pressure for this filter medium is shown in **Figure 7. 20.**
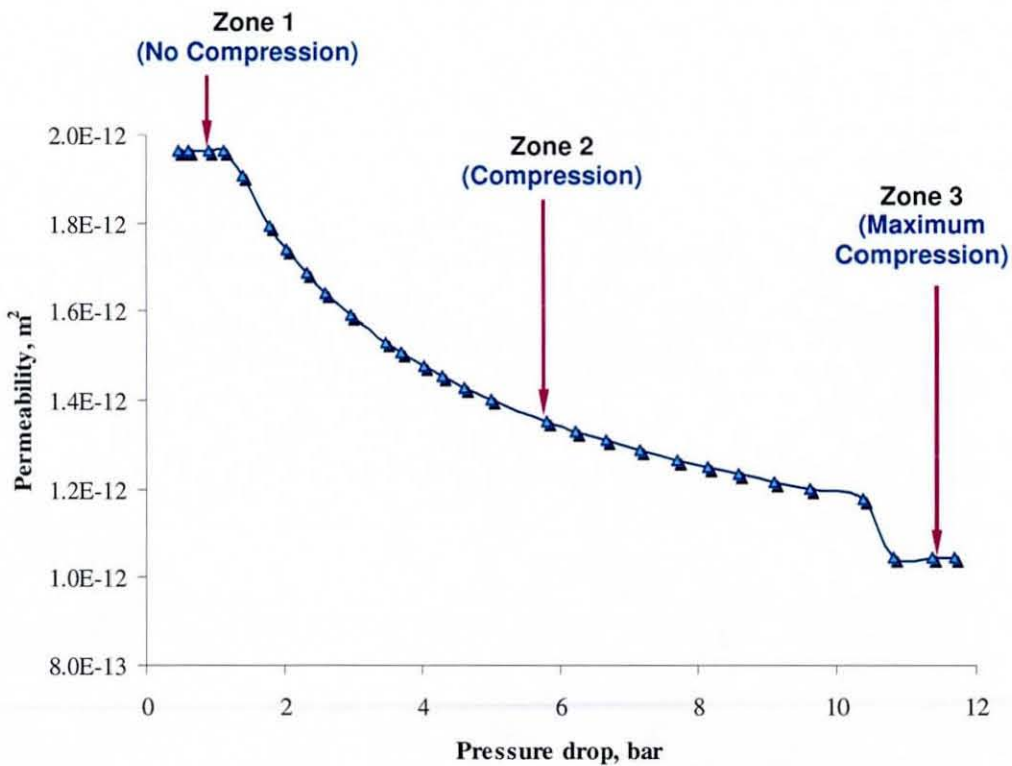
Figure 7. 20: Comparison of the experimental (data points) permeability – pressure drop data with the permeability model (equations (7.2), (7.3) and (7.4)) for the fibre glass medium

The permeability values corresponding to different flow rates, and represented by equations **(7.2)**, **(7.3)** and **(7.4)** were then incorporated into the main solution algorithms for simulation of flow behaviour in both the flat sheet and the cartridge. The simulated values of pressure losses across the flat sheet media were

found to agree well, as expected, with the experimentally determined values (see **Figure** 7. 21).
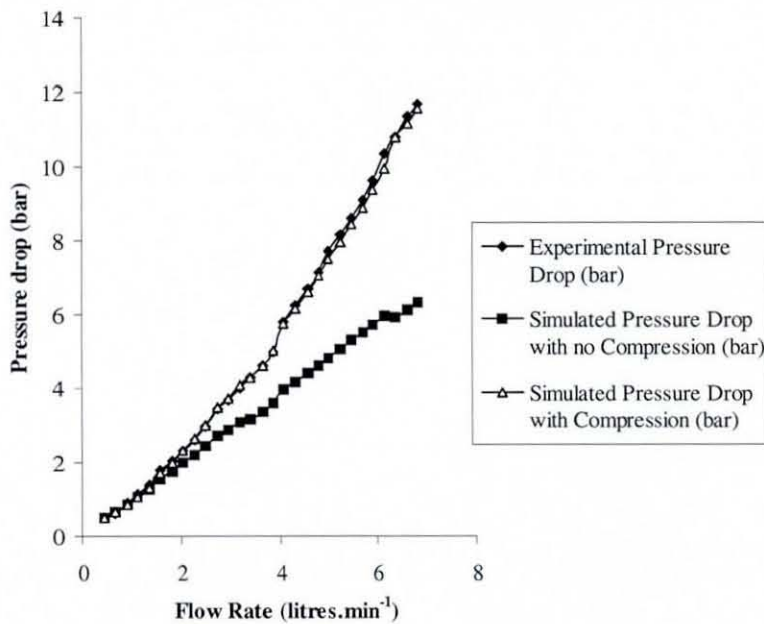
Figure 7. 21: Comparison of experimental and simulated pressure drop values for the flat sheet dual fibre glass medium

7.5.2   Compression and area loss in the cartridge

The degree of compression or the percentage compression for a given filter cartridge element under given flow conditions can be calculated using,

$$\% \text{ Compression} = \frac{K - K_c}{K} 100$$

(7. 5)

where, K_c is the permeability of the compressed medium (given by equations similar to (7.2), (7.3) and (7.4)), and K is the permeability of the medium without any compression (represented by equation (7.2)).

Estimation of losses of filtration area can be obtained using the pressure drop across the cartridge obtained from a permeation test, p_{exp}. The percentage loss in area can be evaluated using

$$\% \text{ Loss of Area} = \frac{p_{exp} - p_c}{p_c} 100$$

(7. 6)

where, p_c is the simulated pressure drop across the cartridge with the medium compression (that is, using the compressed medium permeability, K_c).

7.5.3   Computational results and discussions

A repetitive unit of the cartridge element shown in **Figure** 7. 3, whose simulation has been shown to be equivalent to the modelling of the whole filter domain (Ruziwa *et al.*, 2004), was used in the simulations to reduce the computational time. It has a replica of a single pleat unit within its geometry that is not affected by artificial boundary conditions that are required to be used in the simulations of a part of the whole domain. The dimensions of the repetitive units used were taken from the actual pleated cartridge filter geometries used in the field on-site experiments. The computational mesh (**Figure** 7. 2(c)) used in the simulations for the repetitive unit was generated using C^0-continuous 9-noded quadrilateral elements having bi-quadratic interpolation functions for velocity and pressure. The cartridge geometrical domain was tessellated with 2400 numbers of elements accompanied by 10101 numbers of nodal points.

In order to carry out the simulations and subsequent calculations related to medium compression and % losses in filtration area, the following operational, physical and geometrical data were measured,

- Filter medium thickness;
- Filter medium permeation test data (flow rate versus pressure drop) obtained from a flat sheet;
- Density of the permeating fluid;
- Zero shear rate viscosity and power law index for the permeating fluid;
- Total number of pleats;
- Length of the pleat (or of the filter element);

- Height of a pleat;
- Diameter of the inner core;
- Outer diameter of the cartridge geometry;
- Total filtration area of the cartridge;
- Cartridge permeation test data (using the same fluid as for the flat sheet experiment).

7.5.4 Analysis of the cartridge permeation data

The step-by-step procedure for analysis of the cartridge filter data was:

1. A simulation is performed for each flow rate used in an experiment to determine the permeation flow rate versus pressure drop data; then, using the compressed media permeability (K_c) obtained from analysis of the flat sheet medium experiment (see, for example, equations (7.2), (7.3) and (7.4), where Δp is the experimental pressure drop value corresponding to each flow rate), the degree of compression experienced by the media in the cartridge at each flow rate is calculated. The degree of compression (% compression) was then estimated using equation (7.5), where K is the uncompressed medium permeability. As the flow rate increases the degree of compression also increases and becomes relatively constant at higher flow rates (that is, as the limiting compression of the medium is reached).

2. Using the K_c values for each flow rate in the cartridge permeation test, new pressure drop values p_c were simulated at each flow rate. These pressure drop values are higher than those which would result from normal Darcy's law behaviour if the medium were not compressed, but may be lower than those measured in the cartridge permeation test. This simulated p_c takes into account the compression effects resulting into the lower permeability values of the medium. Some discrepancy may still be observed between the experimental values p_{exp} and simulated values p_c. The discrepancy is a result of loss in filtering area of the medium due to the effects of the cartridge structure deformation in the flow field and medium deformation in the pleating process.

3. The percentage losses in the filtering area were estimated using equation (7.6). It was generally observed that with an increase in fluid flow, the loss in area decreases and approaches a constant value at relatively higher flow rates. To incorporate the effects of area loss in the main simulation model, new average velocities were evaluated. These average velocities were based on the determined percentage area loss of the filtering area and the known flow rates. Using the K_c values and new average velocity figures, new pressure drop values for the cartridge were simulated. These pressure drop figures are denoted by p_{c+a}, which indicates the incorporation of both compression and area loss effects in the main model. The simulated pressure drop values corrected for medium compression (p_c) and for both compression and loss of area (p_{c+a}) are shown in **Table (7. 4)**, the latter values agree well with the experimentally determined pressure losses (p_{exp}). The complete numerical procedure can be understood with use from the flowchart in **Figure 7. 22.**
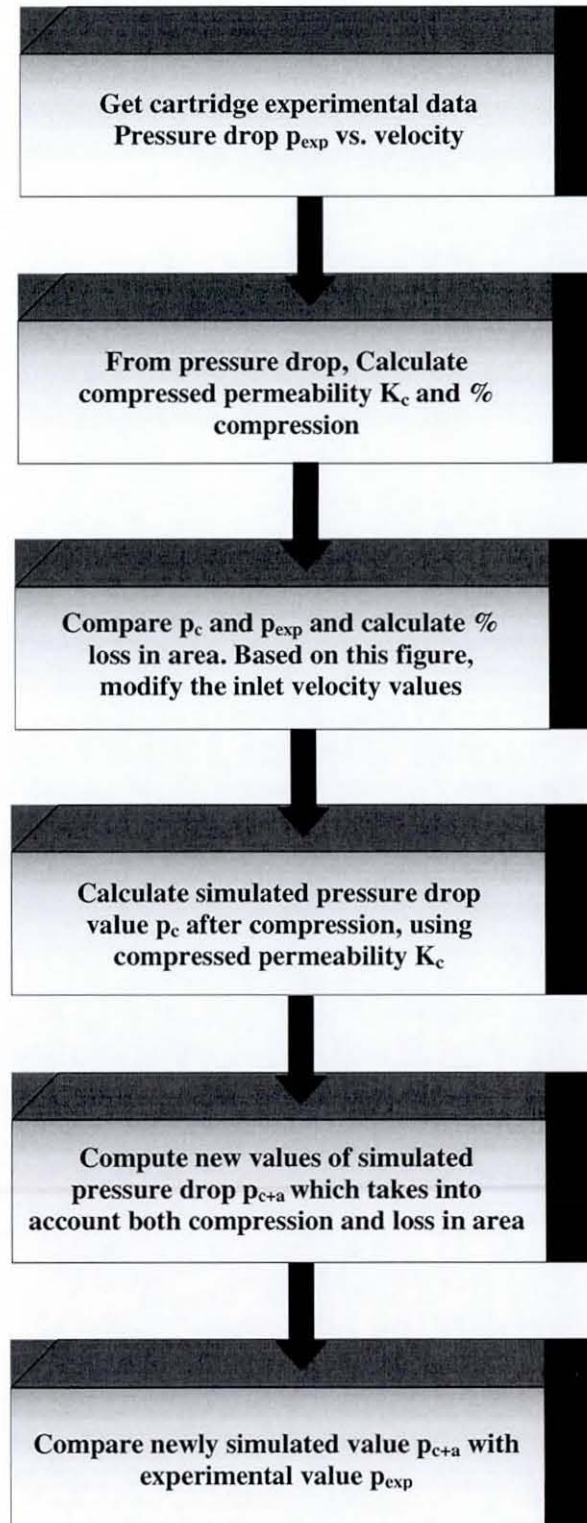
Figure 7. 22: Algorithm for the prediction of compression and loss in filtration area

Based on the computational algorithm shown in **Figure** 7. 22, a computer code has been developed to simulate the hydrodynamics and design parameters of pleated cartridge filters and has been named as **A**ircraft **C**artridge **F**ilter **A**nalysis **M**odelling **P**rogram (**ACFAMP**). It allows user to enter the cartridge filter specifications, filtration operating conditions, filter material and fluid physical properties in order to evaluate the critical operational parameters such as optimal pressure drop. **ACFAMP** quantifies the extent of compression and predicts losses in filtration area, which are of prime importance in cartridge design, sizing and manufacture. The components and sub-components of **ACFAMP** have been explained separately in a manual along with the detail listing of the computer code.

Simulated pressure drop values resulting from normal Darcy law behaviour (i.e. with no compression), values with compression, and values with compression and loss in area effects are compared with experimentally determined values on **Figure** 7. 23 for a cartridge clothed with glass fibre filter media. It is observed, when compression and loss in area effects are incorporated the simulated and experimentally determined values agree closely, thus indicating the validity of the developed model. It is expected that the methodology employed can be applied to any type of pleated cartridge geometry. However, it should be clearly noted that the simulations are sensitive to the pressure dependent permeability relationships that have been incorporated within the main hydrodynamic model. The accuracy of the CFD simulations is therefore dependent on the permeability and the material characterisation of the porous medium.
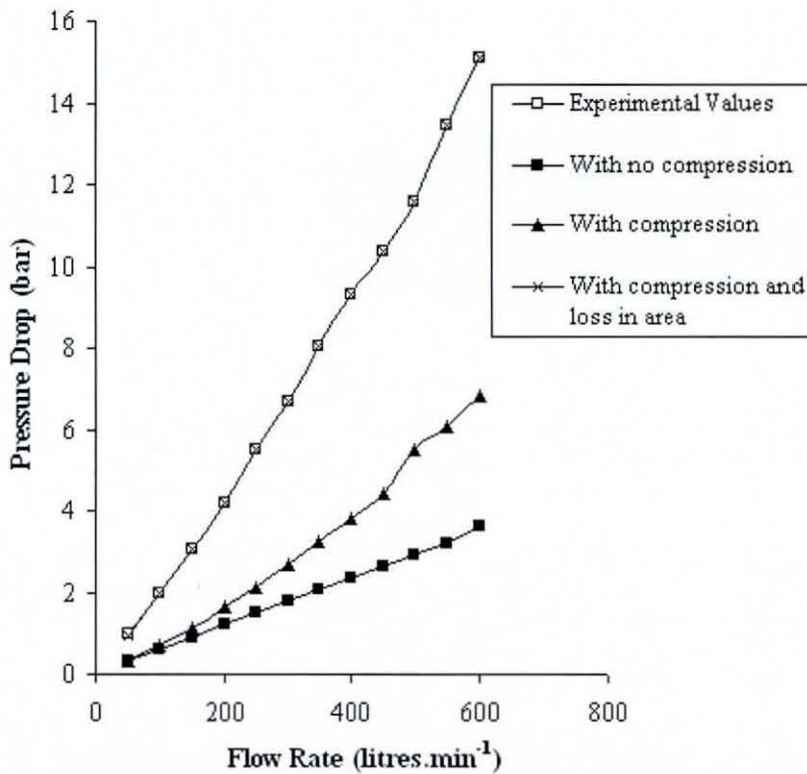
Figure 7. 23: Flow rate versus pressure drop for the whole cartridge with a glass fibre filter medium; the experimental values for the cartridge are compared with data from (a) the medium flat sheet experiment without allowing for compression, (b) after correcting for compression, and (c) after correcting for compression, and other contributors to area loss (pleat deformation and crowding)

Filter elements of varying number of pleats, height of the filter pleat, diameter of the core, and different filtering area were analysed using the developed model. Using the experimental data combined with the analytical procedures described above, the effects of pleat crowding and filter element length have also been investigated. The comparisons of the simulated results against the corresponding experimental data have been tabulated for each of the cartridge filter element in the Appendix **A2**. To gain a fair idea about the extent of compression of the permeable media and the effective losses in the filtration area occurring in the pleated cartridges for a range of flow rates, the analysis performed by the developed computational procedure have been presented for one representative cartridge element in **Table 7. 4.**

Table 7. 4: Example of comparison between the experimental and simulated pressure drops

Reference element	H24FDV80L
Filtering medium	Fibre Glass Medium β 3 μm >200 + square mesh aperture = 440 μm
Test fluid	MP 320
Density	880 kg m-3
Power law index	1.0
Number of pleats	80
Height of the filter element	211.5 mm
Height of the pleat	24.5 mm
Diameter of the inner core	59.0 mm
Filtering area	0.7783 m²
Outer diameter of the casing	120 mm

	Experimental data			Numerical analysis				
No	Flow Rate (lit min^{-1})	Viscosity (cSt)	Pressure drop p_{exp} (bar)	% Compn.	Pressure drop with compn. p_c (bar)	% Loss in area	Velocity corrected for loss in area (m s^{-1})	Pressure drop allowing for compression and loss in area p_{c+a} (bar)
1.	50	0.065	0.98	0	0.324	66.9	0.0032	0.982
2.	100	0.063	1.96	10.82	0.686	65.0	0.0061	1.961
3.	150	0.062	3.06	19.85	1.129	63.1	0.0087	3.061
4.	200	0.062	4.21	25.75	1.625	61.4	0.0111	4.211
5.	250	0.062	5.50	30.36	2.135	61.2	0.0138	5.500
6.	300	0.062	6.68	33.53	2.684	59.8	0.0160	6.681
7.	350	0.061	8.06	36.46	3.228	59.9	0.0187	8.060
8.	400	0.061	9.34	38.66	3.822	59.1	0.0209	9.340
9.	450	0.061	10.36	40.17	4.408	57.5	0.0226	10.36
10.	500	0.061	11.58	46.95	5.524	52.3	0.0224	11.58
11.	550	0.061	13.44	46.95	6.076	54.8	0.0261	13.44
12.	600	0.062	15.09	46.95	6.825	54.8	0.0284	15.09

7.6 Effects of medium compression and pleat crowding and/or deformation

Three filter elements having different number of pleats, i.e. 70, 75 and 80 were used for investigating the pleat crowding effect. All the elements have the same pleat height (24.5 mm), core diameter (59 mm) and filter element length (211.5 mm). Simulations were performed for different flow rates. It is observed that, at a given flow rate, as the number of pleats increase the losses in filtering area also increase (**Figure 7. 24**). This suggests that for a given pleat height, inner core diameter and filter element length, there is an optimum number of pleats that determines the utilisation efficiency of a given medium. It may seem odd that if **Figure 7. 24** were replotted as % loss of filtration area against pressure drop; the loss would decrease as the pressure drop increased. This results from each stage in the experiments being carried out at a constant flow rate. So, no matter what back-pressure resulted from the pleats fluid continued to be forced through them, causing the gap between or within the pleats to widen slightly.
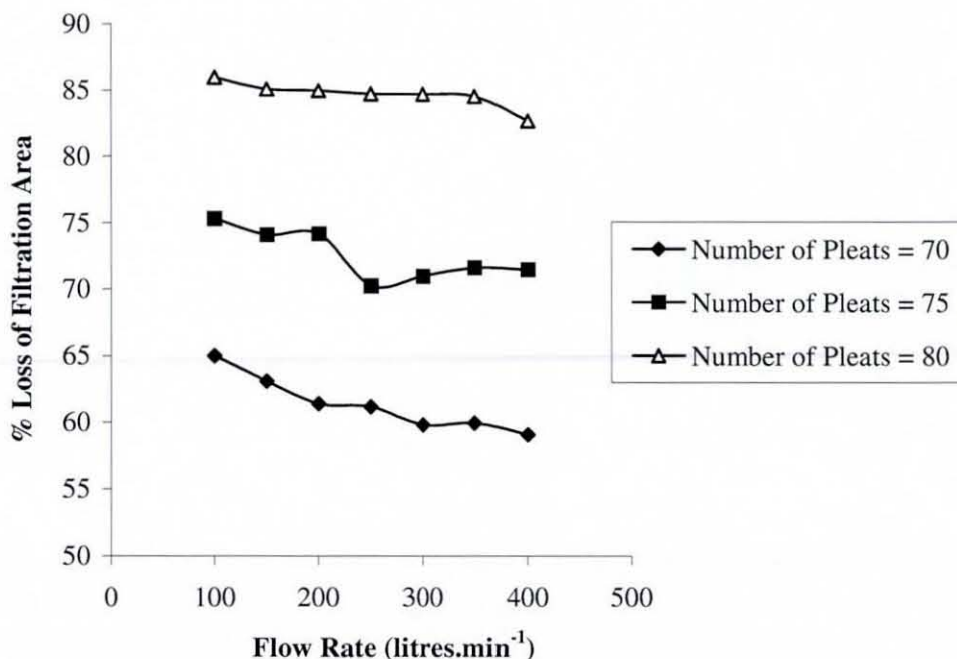
Figure 7. 24: Pleat crowding and/or pleat deformation effects on the performance of a fibre glass medium pleated cartridge filter (length of filter element 211.5 mm, height of pleat 24.5 mm, core diameter 59 mm)

Simulations were also performed for differing filter element lengths (97 and 211.5 mm). The elements have the same pleat height (24.5 mm), core diameter (59 mm) and number of pleats (70). It was observed that at a given flow rate, as the length of the element increased the losses in filtering area also increased (**Figure 7. 25**), thereby suggesting an optimum filter element length. If this area loss were due to deformation of the pleat near to the centre along its length, this points to a need to provide mechanical support of the pleat at this central point.
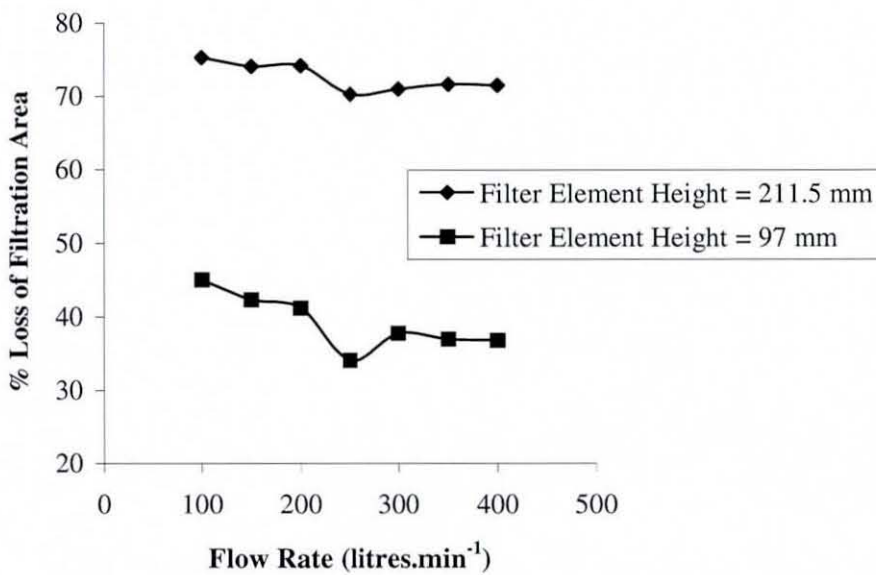
Figure 7. 25: Effect of pleat (or element) length on loss of filtration area of a glass fibre medium pleated cartridge filter.(number of pleats 70, height of pleat 24.5 mm, core diameter 59 mm)

Significant losses in filtration area suggest that a significant reduction in the amount of filter material used in the filter manufacture may be possible, or that the design of the cartridge could be changed to make better use of the medium in the element. In the former case, if the area is not required by the process an enhanced economy of the cartridge manufacturing process is possible. Further, less filter material being used in a given filter cartridge contributes to a reduction of mass of the filter element thereby enhancing the operational economy in those applications where filter weight is critical (for example, in aerospace applications).

7.7   Geometric considerations of pleat crowding

It would be tempting to develop a model for pleat crowding based on geometric considerations. Referring to **Figure** 7. 26, pleats with and without compression are shown in the top left part of the diagram; in the top right is shown an expanded diagram of a compressed pleat, with various dimension defined. If each inner fold of the pleat were perfectly sharp and the medium is not compressed by the pleating action, the number of pleats possible at the core diameter cannot exceed N_c, where

$$N_c = \frac{\pi D_c}{2(t + S_0)} \qquad\qquad (7.7)$$
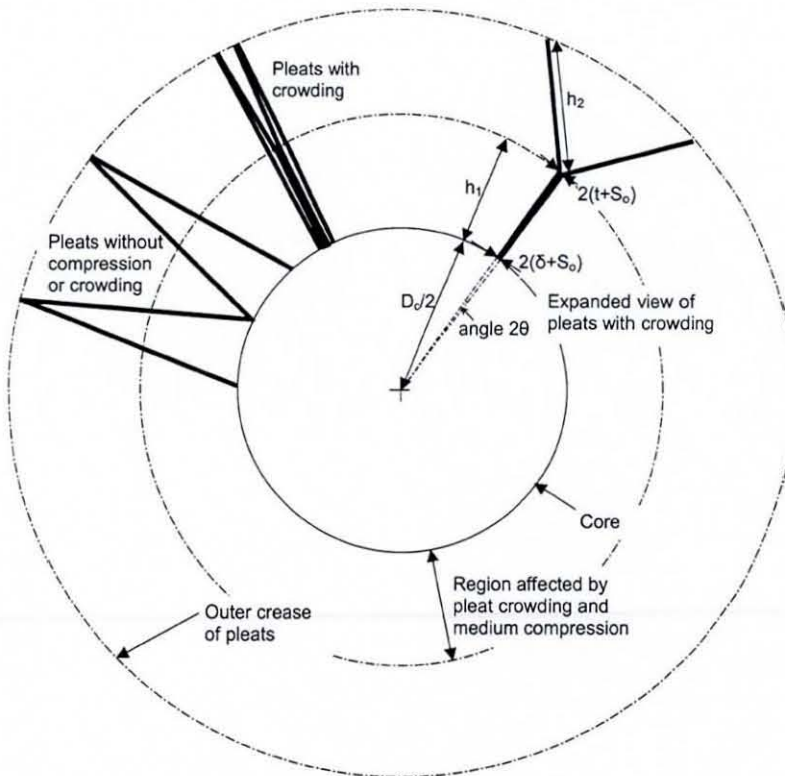
Figure 7. 26: Geometric modelling of pleat crowding effects. The top left quadrant shows pleats packed loosely around the core and pleats that are over-packed; the top right shows an expanded over-packed pleat and defines the terms used in the model

If the pleats are compressed at the core diameter due to pleat crowding, the number of pleats is greater than N_c and an effective loss of area close to the core results. If δ is the compressed thickness of the medium at the core, the number of pleats in the element is given as,

$$N = \frac{\pi D_c}{2(\delta + S_0)}$$

(7. 8)

If the percentage compression is denoted by X, then

$$\frac{X}{100} = 1 - \frac{\delta}{t} = \frac{1 - \dfrac{N_c}{N}}{1 - \dfrac{S_0}{t + S_0}}$$

(7. 9)

If we define the height of the pleat as $h_p \approx h_1 + h_2$, then the percentage loss of filtration area is given by

$$\% \text{ Loss in filtration area} = \frac{h_p - h_2}{h_p} 100 = \frac{h_1}{h_p} 100$$

(7. 10)

To estimate h_1 (or h_2), consider the compressed pleat shown in **Figure 7. 26**. Using the angle 2θ subtended by the pleat at the centre of the core, and noting that the pleat varies from a compressed state at the core diameter to an uncompressed one at distance h_1 from the core surface, h_1 is related to the core dimension and medium thickness by

$$h_1 = \frac{\dfrac{D_c}{2}\left(\dfrac{t}{\delta} - 1\right)}{\left(1 + \dfrac{S_0}{\delta}\right)}$$

(7. 11)

and to the compression of the medium by

$$h_1 = \frac{D_c}{2}\left(\frac{1}{\left(1 - \dfrac{X}{100}\right)} - 1\right)\frac{1}{\left(1 + \dfrac{S_0}{\delta}\right)}$$

(7. 12)

and the loss of filtration area is,

$$\% \, Loss \, in \, filtration \, area = \frac{D_c}{2h_p}\left(\frac{X/100}{1-(X/100)}\right)\left(\frac{1}{1+\dfrac{S_0}{\delta}}\right)\times100$$

(7. 13)

$$= \frac{D_c}{2h_p}\left(\frac{N}{N_c}-1\right)\times100$$

Although these equations show that a geometric model can indicate the same trend in the data as shown on **Figure** 7. 24, that is, that the loss of area increases as the number of pleats (N) increases, such models cannot account of the interactions between fluid flow and pleat construction. Without allowing for the radius of crimping at the pleat fold next to the core, equation (7. 7) suggests that it would be possible for there to be 81 uncompressed pleats in the elements used for the experiments in **Figure** 7. 24. If this were so, then none of the elements used in **Figure** 7. 24 would show any compression. Allowing for the radius of crimping by increasing S_0 to, say, $1.4S_0$ in equation (7. 7) leads to 68 uncompressed pleats. If this were so, equation (7. 13) suggests that the percentage loss of filtration area ranges from 35% to 100% for the cartridges used in **Figure** 7. 24.

The proposed approach of combining models of the hydrodynamics of flows in cartridges with industry standard tests is more realistic and more comprehensive than consideration of geometric factors alone. But, it is still recognized that even though compression effects on pressure losses can be accounted for, the precise reasons for area losses due to deformation and crowding (or other structural effects) still cannot be elucidated.

7.8   Closure

The cartridge permeation experimental data has been analysed for his theoretical consistency and validity against the simulated results generated by the developed computational program. The phenomena of medium deformation and pleat crowding have been identified with their possible consequences and evaluated their quantitative measures to show their severeness towards the current real life industrial situation.

8.   Conclusions

In broader perspective, the present work is comprised of two different application areas namely coupled flow hydrodynamics and numerical analysis of experimental permeation data of high performance pleated cartridge hydraulic filters employed in the aeronautical applications. In each individual case, the foundations of the quantitative appraisals rely on the weighted residual finite element scheme. The complex geometrical features of the solution domains have been taken care of by the isoparametric mappings. The developed computational algorithms have been evaluated for their accuracy, validity, consistency and flexibility towards a variety of practical situations. The numerical figures obtained from the simulations have received meaningful importance when compared against the experimental data wherever necessary. Though the inferences drawn from the numerical analysis have been described in detail at distinct places during the flow of discussion, it would be appropriate to present a summary of all the conclusions to close the description of the project.

8.1   Coupled free/porous hydrodynamics

Two different numerical schemes have been devised to obtain solutions for the coupled Stokes/Darcy flow problem encountered in pleated cartridge filtration. The Darcy equation is imposed as a boundary condition for the Stokes equations at the interface separating the free and porous flow regimes and continuity of the field variables is maintained across the interface naturally. The individual computational models for both free and porous flow situations generate stable results in a range of a variety of domain geometries and tally closely with their analytical values. Both the numerical schemes are based on the UVP mode of calculation of the primitive variables which are able to simulate flows of generalised Newtonian fluids ranging from pseudo plastics to dilatants.

The perturbed continuity scheme based on the equal order velocity and pressure approximations proves to the simplest method for its implementation with a slight compromise with the underlying physics of the incompressible flow phenomenon. The scheme generates physically sound and stable results for the combined flow situations in simplified domain geometries which are validated by

the overall mass balance calculations. Unfortunately, the scheme completely fails in simulating the coupled free/porous hydrodynamics in solution domains having irregular shaped free/porous interface. Moreover, the perturbed form of the continuity equation forces the momentum conservation equations to be transient which in turn requires a robust time-stepping method to attain temporal stability in the solutions. The accuracy of the simulated results relies to the greater extent on the geometrical characteristics and permeation properties of the interface separating the free and porous flow regimes.

The speed of sound is a key parameter in the numerical analysis carried out using the perturbed continuity scheme. Though its significance has been proved previously from a thermodynamic point of view, it has no direct influence on the fluid dynamical behaviour of incompressible viscous flow. However, the spatial, as well as, temporal stability of solutions depend primarily on this parameter which can only be chosen based on *ad-hoc* trial and errors. Although the values of time steps used in the perturbed continuity computations are extremely small, smallest variations in them drive the solution into oscillations. Therefore, this scheme exhibited its limitations in simulating the coupled fluid flow phenomena in relatively complicated flow domains such as pleated cartridge filters.

The Taylor-Hood scheme based on enriched velocity approximating spaces is highly compliant with the LBB stability criterion for the incompressible flow problems. The scheme produces highly stable, accurate and convergent solutions for distinct solution domains ranging from rectangular channel to pleated cartridge filters without any possible occurrences of numerical locking at the free/porous interface. Since the numerical scheme is based on purely steady state calculations, there are no mathematical complications related to the temporal instability unlike the perturbed continuity scheme. The mass continuity requirements are completely satisfies on the local i.e. elemental and global i.e. domain level. It could be presumed that with the Taylor-Hood scheme, the transient coupled flow calculations could be performed without using any advanced time-stepping method.

The simulated results lie in the close vicinity of their experimental counterparts. Any existing discrepancies between the inlet and outlet masses are found to be negligible affirming the validity of the results on theoretical grounds. In addition, for a case of Newtonian fluid flow, the permeability of the porous

medium and its pressure drop relationship is found to be perfectly linear as theoretically expected.

The variations in the field variables are found to be significant on either side of the free/porous interface mainly due to difference in the physics and the incompatibility of mathematical operators in the Stokes and the Darcy equations. As a result, the computational mesh is required to be highly refined in this region causing drastic rise in the computational costs especially if the scheme is extended to the three-dimensional problems. However, the Taylor-Hood element is the lowest member if the bubble element family. Therefore, it is expected that through the utilisation of more sophisticated and powerful members of the family, solutions having the same order of accuracy and convergence could be obtained using relatively coarser meshes.

The numerical algorithm is mainly developed taking into consideration the fact that most of the pleated cartridge aeronautical filters operate in dead-end filtration mode. However, the same methodology can be applied in a versatile way to the cross-flow filtration process to model the fluid flow tangential to the porous surface. However, in the cross-flow filtrations, the solutions to the coupled free/porous flow problem highly depend on the applicability range of Darcy's law for the porous regime. Though the developed algorithm has been developed for solving the fluid flow problems in Cartesian coordinate system, it has been successfully extended to the axisymmetric flow situations.

8.2 Numerical analysis of cartridge permeation data

The permeable medium deformations by the hydrodynamic effects have been figured out and has been evaluated by using the developed mathematical model which takes into account the changes in permeability by the hydrostatic fluid pressure drops. Though the greater numbers of pleats improve the filtration performance, excessive number of pleats may be detrimental due to the excess pressure drop over the value calculated by the Darcy's law and a concept such as the "optimum" number pleats comes into picture. Incorporation of the permeability model into the flow model accounts for the degree of compression of the medium and for filtration area losses in filter cartridges. When losses in area and degree of compression are taken into account, calculated and experimental pressure drop values for flow through pleated cartridges agree well.

The apparent losses in effective filtration area are found to be increasing with pleat density. These effects are also found to be proportional with the height of the filter element. The methodology presented here enables detailed analysis of the effects of cartridge filter design in different applications, enabling an "optimal" design configuration to be determined for each application. Significant over-use of media material or the need for changes to geometric or mechanical design can be identified using the procedures described. The detailed analysis and prediction of optimum geometrical factors for cartridge filter geometries is subject to availability of experimental data. Analogous procedures are being applied to the analysis of synthetic fibre media where other interactions between the fibre and the fluid such as medium swelling due to absorption of fluid may occur. Although the procedures developed are considered to be generic, the results are sensitive to the type and properties of the fluid being filtered, the properties of the filter medium, and the design configuration of the filter element. Further work is underway to check the non-specificity of the procedures.

Finally some critical outcomes of this work to be noted are,

- The developed numerical scheme for predicting flow behaviour in dead-end filtration system is generic and affirms its compatibility with any complex geometry such as pleated cartridge filter;

- The perturbed continuity scheme completely fails in simulating coupled free/porous flow when the domain geometries become relatively complex;

- The numerical schemes developed using elements that satisfy the LBB stability criterion and inf-sup conditions generate accurate results for incompressible combined flow problems;

- A new technology has been developed for design and analysis of aeronautical hydraulic and fuel oil filters;

- The novel designs would result into reduced weight and size of the cartridge filter and more importantly improved dirt holding capacity;

- Reduced weight of the filer housing with low fluid throughput have been predicted;

- Though the procedures developed are considered to be generic, the results are sensitive to properties of fluid to be filtered, properties of the filter medium and design configurations of the filter element.

9.   Future prospective

The core objective of the present work i.e. to develop the computational model for the coupled flow hydrodynamics in pleated cartridge aeronautical filter has been achieved which will assist in drawing its operational cost and life expectancy. Fundamentally, in filtration, the main aim lies in getting information on the number of particles deposited per unit length of fibre for a given flow rate, filter medium and fluid properties and particle characterisation. The particle tracking and capture is important equally to the hydrodynamic calculations to get the overall filter efficiency as the particle deposition influences the fluid pressure drop and changes in its operational characteristics. Therefore, it is highly essential to recalculate the flow field at any arbitrary level of deposition and to take into account the effect of particle accumulation both on flow field and on further deposition.

In this direction, the particle movement can be traced in the free flowing fluid medium before its deposition on the medium surface in case of the surface filtration mechanism which is the most common in the aeronautical filters. Numerical methods such as Lagrangian-Eularian (ALE) technique and the fictitious domain method for tracking the particle trajectories in the fluid medium are under consideration for their applicability and suitability towards the present problem. In case of depth filtration in the interior of the fine pores, probabilistic approach could be adopted to find out the active and passive nodes for the particle capture.

The effects of medium compression, cartridge deformations and pleat crowding have been addressed numerically by the permeability model. However, these effects can only be visualised in real sense when the solid-fluid interaction has been taken into account during the calculations. Moving mesh techniques such as the Arbitrary Lagrangian-Eularian framework can be deployed to tackle movement of the cartridge in each time step of the calculation.

In the present work, the filtration is assumed to be taking place in isothermal conditions at ambient temperatures. However, practically, the temperature during the operation changes drastically from the ground temperature to sub-cooled temperatures at greater altitudes in air. The solution of energy conservation equations in conjunction with the momentum conservation

equations becomes mandatory in these situations to develop a strategy about the optimal heat dissipation. The viscosity of the generalised Newtonian fluids changes exponentially with temperature in these non-isothermal operating conditions.

The core chemical engineering application of the coupled flow hydrodynamic modelling could be found in trickle bed catalytic reactors in which the gas-liquid reactions take place on the catalyst surface forming a porous bed. The porosity of the porous beds may alter depending on the sizes of the catalyst particles. In this situation, the convection-diffusion mass transport and energy transport equation containing the source/sink term of the reaction is solved with the equations of motion to calculate conversion of reactants over various parts of the reactor domain. One more application could be mentioned in catalytic converters of the automobiles where the exhaust gases consisting of CO_x, NO_x and VOCs can be reduced on the active sites of metal catalysts coated on ceramic porous structures.

The porous materials used in the construction of the pleated cartridges are homogeneous and isotropic. In some practical cases, composite porous media or media with varying permeability are used. In groundwater flows, the porosity of the soil subsurface changes in all possible directions, making it completely heterogeneous. In these situations, the permeability of the medium depends on many factors which need to be incorporated into the computational model. The subsurface reactions and transport could be studied in these heterogeneous soil media to access pollutant discharge and contamination from surface flows to subsurface water reserves, lakes and oceans.

In biomedical engineering, the coupled flow phenomena are found existence in arterial blood flows. Walls of the arteries are porous which allow molecules of definite sizes to pass from either side. These arterial walls are highly flexible towards deformations caused by fluctuating blood pressure levels which also changes the dimensions of their interior flow channels. The analysis of arterial blood coupled flow dynamics would be highly beneficial in developing new strategies for the treatment of blocked arteries. It would also assist in devising new drug delivery methods for intra-venous medicines.

References

Alazmi, B. and Vafai, K., 2001. Analysis of Fluid Flow and Heat Transfer Interfacial Conditions between a Porous Medium and a Fluid Layer. *International Journal of Heat and Mass Transfer,* **44**, pp. 1735-1749.

Alda, W., Dzwinel, W., Kitowski, J., Mocinski, J., Rybicki, J. and Boryeczko, K., 1999. Simulation of flow through porous media using particle models. *Computer Physics Communications,* **121**(9), pp. 594-595.

Anderson, J.D., 1999. *Computational Fluid Dynamics.* McGraw Hill, New York.

Aris, R., 1989. *Vectors, Tensors and the Basic Equations of Fluid Mechanics.* Dover Publications, New York.

Arnold, D.N., Fortin, M. and Brezzi, F., 1984. A stable finite element for the Stokes equations. *Calcolo,* **21**, pp. 337-344.

Babuska, I., 1970. Error-bounds for finite element method. *Numerische Mathematik,* **105**(1), pp. 125-141.

Baker, A.J., 1983. *Finite Element Computational Fluid Dynamics.* 1st Edition, McGraw Hill, New York.

Baléo, J.N., Subrenat, A. and Le Cloirec, P., 2000. Numerical simulation of flows in air treatment devices using activated carbon cloth filters. *Chemical Engineering Science,* **55**, pp. 1807-1816.

Basu, A.J. and Khalili, A., 1999. Computation of flow through a fluid-sediment interface in a benthic chamber. *The Physics of Fluids,* **11**(6), pp. 1395-1405.

Bathe, K.J., 1996. *Finite Element Procedure.* Prentice Hall, Englewood Cliff, New Jersey.

Bear, J., 1972. *Dynamics of Fluids in Porous Media.* America Elsevier, New York.

Beavers, G.S. and Joseph, D.D., 1967. Boundary conditions at a naturally permeable wall. *Journal of Fluid Mechanics,* **30**, pp. 197-207.

Beavers, G.S., Sparrow, E.M. and Rodenz, D.E., 1973. Influence of bed size on the flow characteristics and porosity of randomly packed bed of spheres. *Journal of Applied Mechanics,* **40**, pp. 655-660.

Beckerman, C., Ramadhyani, S. and **Viskanta, R.**, 1987. Natural convection flow and heat transfer between a fluid layer and a porous layer inside rectangular enclosure, *ASME Journal of Heat Transfer*, **109**, pp 363-370.

Beckerman, C., Ramadhyani, S. and **Viskanta, R.**, 1988. Natural convection in vertical enclosures containing simultaneously fluid and porous layer, *Journal of Fluid Mechanics*, **186**, pp 257-284.

Bercovier, M. and **Pironneau, O.**, 1979. Error estimates for finite element method solution of the Stokes problem in primitive variables. *Numerische Mathematik*, **33**, pp. 211-224.

Berman, A.S., 1953. Laminar flow in channels with porous walls. *Journal of Applied Physics*, **24**, pp. 1232-1237.

Binder, K., 1984. Application of Monte Carlo Method in Statistical Physics., 1st Edition, Springer-Verlag, Berlin.

Bird, R.B., Stewart, W.E. and **Lightfoot, E.N.**, 2000. *Transport Phenomena*, John Wiley and Sons., Singapore.

Brebbia, C.A., 1978. The Boundary Element Method for Engineers., 1st Edition, Pentech Press, London.

Brezzi, F., 1974. On the existence, uniqueness and approximation of saddle-point problems arising from Lagrangian Multipliers. *RAIRO Anal. Numer.*, 8(R-2), pp. 129-151.

Brezzi, F. and **Douglas, J.,** 1988. Stabilized mixed methods for the Stokes problem. *Numerische Mathematik*, **53**, pp. 225-235.

Brezzi, F. and **Falk, R. S.**, 1991. Stability of higher-order Taylor-Hood elements. *SIAM Journal on Numerical Analysis*, **28**, pp. 581-590.

Brezzi, F. and **Fortin, M.**, 1991. *Mixed and Hybrid Finite Element Methods..* Springer, Berlin.

Brinkman, H.C., 1947. Calculation of the viscous force exerted by a flowing fluid on a dense array of particles. *Applied Scientific Research*, **A1**, pp. 27-34.

Burman, E. and **Hansbo, P.**, 2002. A unified stabilized method for Stokes' and Darcy's equations. *Chalmers Finite Element Center*, Chalmers University of Technology, Gotteborg, Sweden.

Caeser, T. and **Schroth, T.,** 2002. The influence of pleat geometry on the pressure drop in deep-pleated cassette filters. *Filtration and Separation,* (11), pp. 49-54.

Chen, D.R., Pui, D.Y.H. and **Liu, B.Y.H.,** 1995. Optimization of pleated filter designs using a finite-element numerical model. *Aerosol Science and Technology,* **23**(4), pp. 579-590.

Chung, T.J., 2002. *Computational Fluid Dynamics.,* 1st Edition, Cambridge University Press, Cambridge, UK.

Conte, S.D. and de Boor, C., 1980. *Elementary Numerical Analysis.,* McGraw Hill, New York.

Coulaud, O., Morel, P. and **Caltagirone, J.P.,** 1988. Numerical modelling of nonlinear effects in laminar flow through a porous Medium. *Journal of Fluid Mechanics,* **190**, pp. 393-407.

Courant, R., 1943. Variational methods for solution of problem of equilibrium and vibration. *Bulletin of the American Mathematical Society,* **43**, pp. 1-43.

Crouzeix, M. and **Raviart, P.A.,** 1973. *Confirming and Non-confirming Finite Elements for Solving the Stationary Navier-Stokes Equations.,* 3rd Edition, RAIRO Serie Rouge.

Damak, K., Abdelmoneim, A., Schmitz, P. and **Zeghmati, B.,** 2004. Modelling of crossflow membrane separation processes under laminar flow conditions in tubular membrane. *Desalination,* **168**, pp. 231-239.

Damak, K., Ayadi, A., Zeghmati, B. and **Schmitz, P.,** 2004. A new Navier-Stokes and Darcy's law combined model for fluid flow in crossflow filtration tubular membranes. *Desalination,* **161**(1), pp. 67-77.

Darcy, H.P.G., 1856. Les Fontaines publiques de la ville de Dijon., Victor Dalmont, Paris.

Das, D.B. and **Nassehi, V.,** 2001. LANDFLOW: A 3D finite volume model of combined free and porous flow in contaminated land sites. *Water Science and Technology,* **43**(7), pp. 55-64.

De Sampaio, P.A.B. and **Moereira, M.L.,** 2000. A new finite element formulation for both compressible and nearly incompressible fluid

dynamics. *International Journal for Numerical Methods in Fluids*, 32, pp. 51-78.

Del Fabbro, L., Brun, P., Laborde, J.C., Lacan, J., Renoux, A. and **Ricciardi, L.,** 2000. Study of the clogging of industrial pleated filters by solid particles. *Journal of Aerosol Science*, 31(SUPPL 1), pp. 210-211.

Del Fabbro, L., Laborde, J.C., Merlin, P. and **Ricciardi, L.,** 2002. Air flows and pressure drop modelling for different pleated industrial filters. *Filtration and Separation*, 39(1), pp. 35-40.

Dickenson, T.C., 1997. *Filters and Filtration Handbook*, 4th Edition, Elsevier Science Limited, Oxford, UK.

Discacciati, M., Miglio, E. and **Quarteroni, A.,** 2002. Mathematical and numerical models for coupling surface and groundwater flows. *Applied Numerical Mathematics*, 43, pp. 57-74.

Discacciati, M. and **Quarteroni, A.,** 2003. Analysis of domain decomposition method for the coupling of Stokes and Darcy equations. In *Numerical Mathematics and Advanced Applications- ENUMATH 2001*, Edited by Brezzi, F. Buffa, S., Corsaro, S. And Murali, A., pp 3-20, Springer, Milan, Italy.

Discacciati, M. and **Quarteroni, A.,** 2004. Convergence analysis of a subdomain iterative method for the finite element approximation of the coupling of Stokes and Darcy equations. Computational Visualisation Science, 6, pp 93-103.

Discacciati, M., 2004. Iterative methods for Stokes/Darcy coupling, 15th International Conference on Domain Decomposition, 21st-25th July 2003, Berlin and Heidelberg, Germany, published in Domain Decomposition Methods in Science and Engineering, Edited by Kornhuber, R., Hoppe, R.H.W., Périaux, J., Pironneau, O., Widlund, O.B. and Xu, J., 40, pp 563-570, Springer, Berlin and Heidelberg, Germany.

Donea, J., 1984. A Taylor-Galerkin method for convective transport problems. *International Journal for Numerical Methods in Engineering*, 20(24), pp. 101-120.

Donea, J. and **Huerta, A.,** 2003. *Finite Element Methods for Flow Problems.*, John Wiley & Sons Limited, Chichester, UK.

Donea, J. and **Quartapelle, L.,** 1992. An introduction to finite element methods for transient advection problems. *Computer Methods in Applied Mechanics and Engineering,* 95(2), pp. 169-203.

Douglas, J. and **Wang, J.,** 1989. An absolutely stabilized finite element method for the Stokes problem. *Mathematics of Computation,* 52, pp. 495-508.

Dufreche, J., Prat, M., Schmitz, P. and **Sherwood, J.D.,** 2002. On the apparent permeability of porous layer backed by perforated plate. *Chemical Engineering Science,* 57, pp. 2933-2944.

Durlofski, L. and **Brady, J.F.,** 1987. Analysis of the Brinkman equation as a model for flow in porous media, *The Physics of Fluids,* 30, pp 3329-3341.

Ergatoudis, J., Irons, B.M. and **Zienkiewicz, O.C.,** 1968. Curved isoparametric, quadrilateral elements for finite element analysis. *International Journal of Solid Structures,* 4, pp. 31-42.

Farrah, S.L., Goyal, S.M., Gerba, C.P., Wallis, C. and **Shaffer, P.T.B.,** 1976. Characteristics of humic acid and organic compounds concentrated from tapwater using aquella virus concentrator. *Water Research,* 10(10), pp. 897-901.

Farrah, S.L., Goyal, S.M., Gerba, C.P., Wallis, C. and **Melnick, J.L.,** 1977. Concentration of enteroviruses from esturine water. *Applied and Environmental Microbiology,* 33(5), pp. 1192-1196.

Flippov, A., Starov, V.M., Lloyd, D.R., Chakravarti, S. and **Glaser, S,** 1994. Sieve mechanism of microfiltration. *Journal of Membrane Science,* 89, pp. 199-213.

Fochtman, E.G., 1973. Cartridge filtration: Technology and economics. *Proceedings of the Filtration Society,* (5-6), pp. 289-294.

Gartling, D.K., 1976. Recent developments in the use of finite element methods in fluid dynamics. *American Society of Mechanical Engineers,* 6 , pp. 65-81.

Gartling, D.K., Hickox, C.E. and **Givler, R.C.,** 1996. Simulation of coupled viscous and porous flow problems. *International Journal of Computational Fluid Dynamics,* 7, pp. 23-48.

Girault, V. and **Raviart, P.A.,** 1986. Finite Element Methods for Navier-Stokes Equations: Theory and Algorithms, Springer-Verlag, Berlin.

Givler, R.C. and **Atobelli, S.A.,** 1994. A determination of effective viscosity for the Brinkman-Forchheimer flow model. *Journal of Fluid Mechanics,* **258,** pp. 355-370.

Gollan, A. and **Parekh, B.S.,** 1985. Hydrodynamic aspects of semi-dense pleat designs in pleated cartridges. *Filtration and Separation,* **22**(5), pp. 326-329.

Gresho, P.M. and **Sani, R.L.,** 1999. *Incompressible Flows and Finite Element Method.,* John Wiley and Sons., New York.

Haber, S. and **Mauri, R.,** 1983. Boundary conditions for Darcy's Flow through porous media. *International Journal of Multiphase Flow,* **9,** pp. 561-574.

Hanspal, N.S., Ruziwa, W.R., Nassehi, V. and **Wakeman, R.J.,** 2004. Finite element modelling of flow of non-Newtonian fluids in pleated cartridge filters, *Proceedings of 9th World Filtration Congress,* New Orleans, Louisiana, USA, Paper 124-3 (CD ROM), 18-22 April.

Hanspal, N.S., Waghode, A.N., Nassehi, V. and **Wakeman, R.J.,** 2005. Numerical analysis of coupled Stokes/Darcy flows in industrial filtrations. *Transport in Porous Media* (In print).

Heinrich, J.C., Huyakorn, P.S., Zienkiewicz, O.C. and **Mitchell, A.R.,** 1977. An upwind finite element scheme for two-dimensional convective transport equation. *International Journal of Numerical Methods in Engineering,* **11**(1), pp. 131-144.

Heinrich, J.C. and **Pepper, D.W.,** 1999. *Intermediate Finite Element Methods, Fluid Flow and Heat Transfer Applications.,* Taylor and Francis Limited, London.

Hood, P., 1976. Frontal solution program for unsymmetric matrices. *International Journal of Numerical Methods in Engineering,* **10,** pp. 379-399.

Hood, P. and **Taylor, C.,** 1974. Navier-Stokes equation using mixed interpolation. In: J.T. ODEN, ed, *Finite element method in flow problems.* UAH Press, Croydon, UK.

Hsu, C.T. and **Cheng, P.,** 1985. The Brinkman model for natural convection about a semi-infinite vertical flat plate in porous medium, *International Journal of Heat and Mass Transfer,* 28(3), pp 683-697.

Hughes, T.J.R., Franca, L.P. and **Balestra, M.,** 1986. A new finite element formulation for computational fluid dynamics: V. Circumventing the Babuska-Brezzi condition: A stable Petrov-Galerkin formulation for the Stokes problem accomodating equal-order interpolations. *Computer Methods in Applied Mechanics and Engineering,* 59, pp. 85-99.

Huyakorn, P.S., Taylor, C., Lee, R.L. and **Gresho, P.M.,** 1978. A comparison of various mixed-interpolation finite elements for the Navier-Stokes equations. *Computers and Fluids,* 6, pp. 25-35.

Imadakm, A.O. and **Sahimi, M.,** Computer simulation of particle transfer processes in flow through porous media. *Chemical Engineering Science,* 46(8), pp. 1977-1993.

Irons, B.M., 1970. A frontal solution for finite element analysis. *International Journal for Numerical Methods in Engineering,* 2, pp. 5-32.

ISO 16889, 1999. *Hydraulic fluid power filters – multi-pass method for evaluating filtration performance of a filter element,* International Standards Organisation.

Itoh, G., Nakamura, J., Kino, K., Watambe, T., Ohashi, H., Chen, Y. and **Nagasaki, S.,** 2002. Pore-scale simulation for predicting material transport through porous media, *International Conference on Nuclear Engineering, Proceedings, ICONE,* 4,, pp 397-404.

Jager, W. and **Mikelić, A.,** 2000. On the interface boundary condition of Beavers, Joseph and Saffman. *SIAM Journal of Applied Mathematics,* 60, pp. 1111-1127.

Johnson, C., 1987. *Numerical Solution of Partial Differential Equations by the Finite Element Method.,* Cambridge University Press, Cambridge.

Jones, I.P., 1973. Low Reynolds number flow past a porous spherical shell. *Proceedings of Cambridge Philosophical Society,* 73, pp. 231-238.

Joseph, D.D., Nield, D.A. and **Papanicolaou, G.,** 1982. Nonlinear equation governing flow in a saturated porous medium., *Water Resources Research,* 18, pp 1049-1052.

Jurjenic, R., 1999. Modelling of two-dimensional laminar flow using finite element method. *International Journal for Numerical Methods in Fluids,* **31,** pp. 601-626.

Katto, Y. and **Masuoka, T.,** 1967. Criterion for the onset of convective flow in in a fluid in a porous medium. *International Journal of Heat and Mass Transfer,* **10,** pp. 297-309.

Kaviany, M., 1991. *Principles of Heat Transfer in Porous Media.,* Springer, New York.

Kim, S. and **Russell, W.B.,** 1985. Modelling of porous media by renormalization of the Stoke's equations. *Journal of Fluid Mechanics,* **154,** pp. 269-286.

Kosvintsev, S., Holdich, R.G., Cumming, I.W. and **Starov, V.M.,** 2002. Modelling of dead-end microfiltration with pore blocking and cake formation. *Journal of Membare Science,* 208(1-2), pp. 181-192.

Ladyzhenskaya, O.A., 1969. *The Mathematical Theory of Viscous Incompressible Flow.,* Gordon and Breach Science, New York.

Lage, J.L., 1998 The fundamental theory of flow through permeable media from Darcy to turbulence in *Transport Phenomena in Porous Media* - Edited by Ingham, D.B., and Pop, I., pp 1-30, Pergamon , Elsevier Science Limited, Oxford.

Lapidus, L. and **Pinder, G.F.,** 1982. *Numerical Solution of Partial Differential Equations in Science and Engineering.,* Wiley, New York.

Layton, W.J., Schiweck, F. and **Yotov, I.,** 2003. Coupling fluid flow with porous media flow. *SIAM Journal of Numerical Analysis,* 40(6), pp. 2195-2218.

Lücke, T. and **Fissan, H.,** 1996. The prediction of filtration performance of high efficiency gas filter elements. *Chemical Engineering Science,* 51(8), pp. 1199-1208.

Lundgren, T.S., 1972. Slow Flow through stationary random beds and suspensions of spheres. *Journal of Fluid Mechanics,* **51,** pp. 273-299.

Mardal, K.A., Tai, X. and **Winther, R.,** 2002. A robust finite element method for Darcy-Stokes flow. *SIAM Journal on Numerical Analysis,* 40(5), pp. 1605-1631.

Miglio, E., Quarteroni, A. and **Saleri, F.,** 2003. Coupling of free surface and groundwater flows. *Computers & Fluids,* 32(1), pp. 73-83.

Nassehi, V. and **Bikangaga, J.H.,** 1993. A mathematical model for the hydrodynamics and pollutants transport in long and narrow tidal rivers. *Applied Mathematical Modelling,* 17(8), pp. 415-422.

Nassehi, V. and **Petera, J.,** 1994. A new least-square finite element model for combined Navier-Stokes and Darcy flows in geometrically complicated domains with solid and porous boundaries. *International Journal for Numerical Methods in Engineering,* 37, pp. 1609-1620.

Nassehi, V. and **Petera, J.,** 1996. A new two-dimensional finite element model for shallow water equations using a Lagrangian framework constructed along fluid particle trajectories. *International Journal for Numerical Methods in Fluids,* 34, pp. 701-710.

Nassehi, V., 1998. Modelling of combined Navier-Stokes and Darcy flows in crossflow membrane filtration. *Chemical Engineering Science,* 53(6), pp. 1253-1265.

Nassehi, V., 2002. *Practical Aspects of Finite Element Modelling of Polymer Processing.,* John Wiley and Sons., Oxford, UK.

Nassehi, V., Hanspal, N.S., Waghode, A.N., Ruziwa, W.R. and **Wakeman, R.J.,** 2004. Finite element modelling of combined free/porous flow regimes: Simulation of flow through pleated cartridge filters, *Chemical Engineering Science,* 60(4), pp 995-1006.

Neale, G. and **Nader, W.,** 1974. Practical significance of Brinkman's extension of Darcy's Law: Coupled parallel flows within a channel and a bounding porous medium. *Canadian Journal of Chemical Engineering,* 52, pp. 475-478.

Neale, G., Epstein, N. and **Nader, W.,** 1973. Creeping flow relative to permeable spheres. 28(10), pp. 1865-1874.

Nickel, R.E., Tanner, R.I. and **Caswell, B.,** 1974. The solution of viscous incompressible jet and free surface flow using finite element method. *Journal of Fluid Mechanics,* 65, pp. 189-206.

Nickolaus, N., 1975. What, when and why of cartridge filters., *Filtration and Separation,* 12(2), pp. 7.

Nield, D.A., 1991. The limitations of the Brinkman-Forchheimer equation in modelling flow in a saturated porous medium and at the interface. *International Journal of Heat and Fluid Flow,* 12, pp. 269-272.

Nield, D.A. and **Bejan, A.,** 1992. *Convection in Porous Media,* 1st Edition, Springer-Verlag, London.

Noh, W.F., 1964. *A Time-dependent, Two-space Dimensional, Coupled Eulerian-Lagrange Code,* Academic Press, New York.

Ochoa-Tapia, J.A. and **Whitaker, S.,** 1995a. Momentum transfer at the boundary between a porous medium and a homogeneous fluid-I. Theoretical development. *International Journal of Heat and Mass Transfer,* 38(14), pp. 2635-2646.

Ochoa-Tapia, J.A. and **Whitaker, S.,** 1995b. Momentum transfer at the boundary between a porous medium and a homogeneous fluid-II. Comparison with experiment. *International Journal of Heat and Mass Transfer,* 38(14), pp. 2647-2655.

Oden, J.T. and **Weldford, L.C.J.,** 1972. Analysis of viscous flow by finite element method. *American Institute of Aeronautics and Astronautics,* 10, pp. 1590-1599.

Ostwald, W., 1925. In: Bird, R.B., Armstrong, R.C. and Hassager, O., Edited, *Dynamics of Polymeric Fluids,* Wiley, New York.

Oxarango, L., Schmitz, P. and **Quintard, M.,** 2004. Laminar flow in channels with wall suction or injection: A new model to study multi-channel filtration systems. *Chemical Engineering Science,* 59(5), pp. 1039-1051.

Papanastasiou, T.C., Malamataris, N. and **Ellwood, K.,** 1992. A new outflow boundary condition. *International Journal for Numerical Methods in Fluids,* 14, pp. 587-608.

Park, H., Park, S.J., Kim, S.D. and **Choi, H.K.,** 2003. Filtration characteristics of cartridge dust filters, *Proceedings of Filtech Europa Conference,* 1, pp 156-161, Düsseldorf, Germany.

Parvazinia, M., Nassehi, V., Wakeman, R.J. and **Ghoreishy, M.H.R.**, 2005. Finite element modelling of flow through a porous medium between two parallel plates using the Brinkman equation, *Transport in Porous Media* (submitted).

Patankar, S.V., 1980. *Numerical Heat Transfer and Fluid Flow*, Hemisphere/McGraw-Hill, New York.

Payne, L.E. and **Straughan, B.,** 1998. Analysis of the boundary condition at the interface between a viscous fluid and a porous medium and related modeling questions., *Journal De Mathématiques Pures Et Appliquées*, 77, pp 317-354.

Peyret, R. and **Taylor, T.D.,** 1983. *Computational Methods for Fluid Flow.*, Springer-Verlag, New York.

Pittman, J.F.T. and **Nakazawa, S.,** 1984. Finite element analysis of polymer processing operations. In: *Numerical Analysis of Forming Processes* – Edited by Pittman, J.F.T., Zienkiewicz, O.C., Wood, R.D. and Alexander, J.M., Wiley, Chichester, UK.

Pointon, C.W. and **Giles, J.W.,** 1974. Industrial screening filters with special reference to cartridge filters. *Proceedings of the Filtration Society*, (5-6), pp. 259-264.

Purchas, D.B., 1981. *Solid/Liquid Separation Technology.*, Uplands Press Limited, Croydon, UK.

Quarteroni, A. and **Valli, A.,** 1999. *Domain Decomposition Methods for Partial Differential Equations.*, Oxford University Press, Oxford, UK.

Reddy, J.N., 1993. *An Introduction to Finite Element Method.*, 2nd Edition, McGraw Hill, New York.

Reddy, J.N. and **Gartling, D.K.,** 2001. *The Finite Element Method in Heat Transfer and Fluid Dynamics.*, 2nd Edition, CRC Press LLC, Florida.

Renardy, M., 1997. Imposing 'no' boundary condition at outflow: Why does it work? *International Journal for Numerical Methods in Fluids,* 24, pp. 413-417.

Roorda, J.H., Poele, S. and **Van Der Graf, J.H.,** 2004. The role of microparticles in dead-end ultrafiltration of wwtp-effluent. *Water Science and Technology,* 50(12), pp. 87-94.

Rudraiah, N. and **Rao, S.B.**, 1982. Solution of nonlinear Brinkman equations of cellular convection and heat transport in a porous medium. *Applied and Scientific Research,* **39**, pp. 21-26.

Rushton, A., Ward, A.S. and **Holdich, R.G.,** 2000. *Solid-Liquid Filtration and Separation Technology.,* 2nd Edition, Wiley-VCH, Germany.

Ruziwa, W.R., Hanspal, N.S., Waghode, A.N., Nassehi, V. and **Wakeman, R.J.,** 2004. Computer modelling of pleated cartridge filters for viscous fluids. *Filtration,* 4(2), pp. 136-144.

Sabiri, N. and **Comiti, J.,** Pressure drop in non-Newtonian purely viscous fluid flow through porous media. *Chemical Engineering Science,* 50(7), pp. 1193-1201.

Saffman, P.G., 1971. The boundary condition at the surface of a porous medium. *Studies in Applied Mathematics,* **1**, pp. 93-101.

Sagerlind, L.J., 1984. *Applied Finite Element Analysis.,* 2nd Edition, John Wiley and Sons., New York

Sahraoui, M. and **Kaviany, M.,** 1992. Slip and no-slip velocity boundary conditions at the interface of porous plain media. *International Journal of Heat and Mass Transfer,* 35(4), pp. 927-933.

Salinger, A.G., Aris, R. and **Derby, J.J.,** 1994. Finite element formulations for large-scale, coupled flows in adjacent porous and open fluid domains. *International Journal for Numerical Methods in Fluids,* **18**, pp. 1185-1209.

Scanlon, M., 2004. Cartridge designed to optimize the sterile filtration of beer. *Filtration and Separation,* (7-8), pp. 26-27.

Seonghyeon, H., Jongdoo, J. and **Haecheon, C.,** 2002. Direct numerical simulation of turbulent channel flow with permeable walls. *Journal of Fluid Mechanics,* **450**, pp. 259-285.

Smit, G.J.F., Diedericks, G.P.J. and **Duplessis, J.P.,** 1998. Modelling procedure for prediction of flow through porous materials. *Advances in Fluid Mechanics,* **21**, pp. 232-240.

Sobsey, M.D. and **Glass, J.S.,** 1980. Poliovirus concentration from tapwater with electropositive adsorbent filters. *Applied and Environmental Microbiology,* 40(2), pp. 201-210.

Subrenat, A., Baleo, J. and **Le Cloirec, P.,** 2000. Analysis of pressure drops in pleated activated carbon cloth filters. *Journal of Environmental Engineering,* 126(6), pp. 562-568.

Subrenat, A., Bellettre, J. and **Le Cloirec, P.,** 2003. 3-D numerical simulations of flows in a cylindrical pleated filter packed with activated carbon cloth. *Chemical Engineering Science,* 58(22), pp. 4965-4973.

Suntherland, D.N. and **Goodarz-Nia, I.,** 1971. Floc simulation: The effect of collision sequence. *Chemical Engineering Science,* 26(12), pp. 2071-2085.

Taylor, C. and **Hood, P.,** 1973. A numerical solution of the Navier-Stokes equations using the finite element technique. *Computers and Fluids,* 1, pp. 73-100.

Thomas, J.R., 1980. Some current trends in finite element research. *Applied Mathematics Review,* 33(11), pp. 1467-1477.

Townsend, P. and **Webster, M.F.,** 1987. An algorithm for the three dimensional transient simulation of non-Newtonian fluid flow. In: *Transient Dynamic Analysis and Constitutive Laws for Engineering Materials.,* Edited By – Pande, G.N. and Middleton, J., Volume 2, T12, Nijhoff-Holland, Swansea, UK, pp 1-11.

Tronville, P. and **Sala, R.,** 2003. Minimization of resistance in pleated-media air filter designs: Empirical and CFD approaches. *HVAC&R Research,* 9(1), pp. 95-106.

Vafai, K. and **Thiyagaraja, R.,** 1987. Analysis of flow and heat transfer at the interface region of a porous medium. *International Journal of Heat and Mass Transfer,* 30, pp. 1391-1405.

Vafai, K. and **Kim, S.J.,** 1990. Fluid mechanics of the interface region between a porous medium and a fluid layer--an exact solution. *International Journal of Heat and Fluid Flow,* 11(3), pp. 254-256.

Vankan, W.J., Huyhge, J.M., Janssen, J.D., Huson, A., Hacking, W.J.G. and **Schreiner, W.,** 1997. Finite element analysis of blood flow through biological tissue. *International Journal of Engineering Science,* 35(4), pp. 375-385.

Versteeg, H.K. and **Malalasekera, W.,** 1995. *An Introduction to Computational Fluid Dynamics: The Finite Volume Method.*, 1st Edition, Longman Scientific and Technical, UK.

Waghode, A.N, Hanspal, N.S., Shigidi, I. M.T.A., Nassehi, V. and **Hellgardt, K.,** 2005. Computer modelling and numerical analysis of hydrodynamics and heat transfer in nonporous catalytic reactor for decomposition of ammonia, *Chemical Engineering Science,* 60(21), 5862-5877.

Wakeman, R.J. and **Tarleton, E.S.,** 1999. *Filtration: Equipment Selection Modelling and Process Simulation.*, 1st Edition, Elsevier Science Limited, Oxford, UK.

Wakeman, R.J. and **Harris, P.R.,** 1993. A methodology for modelling flow in pleated (star) filter cartridges, *Proceedings of Filtech EUROPA Conference,* 19-21 October, pp 335-343.

Wakeman, R.J., Hanspal N.S., Waghode, A.N. and **Nassehi, V.,** 2005. Analysis of pleat crowding and medium compression in pleated cartridge filters, *IChemE Transactions,* revised.

Ward, J.C., 1964. Turbulent flow in porous media., *American Society of Civil Engineers (ASCE) Hydraulics Division,* 90 (HY5), pp 1-12.

Wooding, R.A., 1957. Steady state free convection of liquid in a saturated porous medium. *Journal of Fluid Mechanics,* 2, pp. 273-285.

Yu, H.H.S. and **Goulding, C.H.,** 1992. Optimized ultra high efficiency filter for high-efficiency industrial combustion turbines, *International Gas Turbine and Aeroengine Congress and Exposition,* Cologne, Germany, 1-4 June 1992, published by American Society of Mechanical Engineers (ASME).

Zienkiewiez, O.C. and **Chueng, Y.K.,** 1965. Finite elements in the solution of field problems. *The Engineer,* pp. 507-510.

Zienkiewicz, O.C. and **Morgan, K.,** 1983. *Finite Elements and Approximation.*, Wiley, New York.

Zienkiewicz, O.C. and **Wu, J.,** 1991. Incompressibility without tears – How to avoid restrictions on mixed formulation. *International Journal of Numerical Methods in Engineering,* 32, pp. 1189-1203.

Zienkiewicz, O.C. and **Codina, R.,** 1995. A general algorithm for compressible and incompressible flow- Part I: Characteristics-based scheme. *International Journal of Numerical Method in Fluids,* **20,** pp. 869-885.

Zienkiewicz, O.C., Nithiarasu, P., Codina, R., Vázquez, M. and **Ortiz, P.,** 1999. The Characteristics-based-split procedure: An efficient and accurate algorithm for fluid problems., *International Journal of Numerical Method in Fluids,* **31,** pp. 359-392.

Zienkiewicz, O.C. and **Taylor, R.L.,** 2002. *The Finite Element Method.,* 5th Edition, Butterworth-Hienemann, Oxford, UK.

Zimmerman, W.B.J., 2004. *Process Modeling and Simulation with Finite Element Methods.,* World Scientific.

Appendix A1

Publications

Paper 1

Indian Chemical Engineer

Abstract

The aim of the present study is to analyse and visualize coupled free and porous flow phenomena. The practical application of this concept is found in designing of conventional filtration equipments for both cross flow and dead-end filtration techniques. The present work is an initiating step towards designing a novel design and analysis tool to the specific case of high performance pleated aeronautical cartridge filters. A two-dimensional computational code has been developed and is capable of modelling individual free flow, porous flow and coupled free/porous flow dynamics for Newtonian and non-Newtonian fluid flows. Results are presented for simple rectangular domains in form of pressure contours and velocity vector plots and the developed code has then been validated against curved geometries such as concentric circular domains. This proves the geometrical flexibility of the numerical scheme and its extension to highly complex geometry as found in pleated cartridge filters.

Paper 2

Filtration Journal (Transactions of Filtration Society)

Abstract

The primary aim of this study is to develop and validate a software package for the design of pleated cartridge filters for aeronautical applications. This package is intended to develop into a cost effective, robust and reliable design tool to enable engineers to appraise the operation of a filter. A 2-D computer code has been developed to simulate both Newtonian and non-Newtonian flows in the filter. The model is based on the flow and mass transport models described by the Continuity and Darcy equations and the Convective-Dispersion equation for the porous flow region. These equations are solved by the weighted residuals finite element method. First order Taylor-Galerkin and implicit time-stepping schemes were applied for temporal discretisation of the Darcy and the Convective-Dispersion equations, respectively. The streamline upwinding Petrov-Galerkin technique was chosen for the solution of the Convective-Dispersion equation to overcome the problem caused by high Peclet (convection dominated) transport. Preliminary numerical experiments were based on simple geometries and the domain complexity was increased in steps examine the model flexibility in dealing with various situations. The overall model was validated against experimental data. Domain variables of interest are velocity, pressure and concentration profiles, which are obtained through the solution of the governing equations taking into consideration the changes in the rheological properties of fluids being filtered.

Paper 3

Chemical Engineering Science

Abstract

Mathematical modelling of creeping incompressible Stokes flow and low permeability Darcy flow are well established and a number of reliable schemes for the simulation of these regimes are available in the literature. However, modelling of combined Stokes/Darcy regimes, such as those encountered in many types of industrial filters, still presents mathematical and practical challenges. In this paper we present a finite element model for the prediction and quantitative analyses of the hydrodynamic behaviour of deadend pleated cartridge filters. Elemental discretisation in this scheme is based on the use of unequal order approximation functions for velocity and pressure fields. We show that this discretisation generates unified stabilisation for both Stokes and Darcy equations and prevents 'numerical locking' whilst preserving the geometrical flexibility of the computational grid. Conducting a number of numerical tests, it is shown that the developed model is capable of yielding theoretically expected and accurate simulations for realistic industrially relevant problems. The model is tested for shear thickening non-Newtonian fluids, which represent fluids used in aeronautical applications. This study is part of a multi-disciplinary project undertaken by various investigators for the design and development of high performance deadend pleated cartridge filters for aeronautical applications. It has been demonstrated that the developed model presents a cost effective, robust and reliable design tool to enable engineers to appraise the operation of such filters.

Keywords: Pleated Cartridge, Hydrodynamics, Deadend Filter, Porous Media, Filtration, Finite Element Method

Paper 4

Chemical Engineering Science

Title: Computer modelling and numerical analysis of hydrodynamics and heat transfer in nonporous catalytic reactor for decomposition of ammonia

Citation: Waghode, A.N., Hanspal, N.S., Shigidi, I. M.T.A., Nassehi, V. and Hellgardt, K., 2005. Computer modelling and numerical analysis of hydrodynamics and heat transfer in nonporous catalytic reactor for decomposition of ammonia, *Chemical Engineering Science*, 60(21), 5862-5877.

Abstract

Chemical reactors exhibit very complex behaviours such as multiple steady states, oscillations, etc. resulting from complex linkage between the transport processes and the non-linear chemical kinetics. Ammonia is a potential hydrogen source for the many fuel cell applications for small scale power generation useful for portable equipments. In the present work, we analyse the fluid dynamics and heat-transfer in a catalytic microreactor systems for the decomposition of ammonia over a Ni/SiO$_2$/Al$_2$O$_3$ non-porous catalyst. The overall model for this convective-diffusive-reactive system consists of a flow model, a mass transport model, an energy conservation model and a reaction kinetics model for ammonia decomposition. The flow model is described by the Stokes equation for a creeping flow regime. The mass transport and energy conservation models are based on convective-diffusion equations. The rate of ammonia decomposition can be measured as a function of the catalyst activity and ammonia concentration. A standard Galerkin finite element technique has been applied for the solution of the flow equations. A slightly perturbed form of the mass continuity equation is used to satisfy the Ladyzhenskaya-Babuska-Brezzi stability criterion. For the solution of convective-diffusion equations, a streamline inconsistent upwind finite element

scheme has been chosen to avoid any spurious oscillations. C^o-continuous 9-noded Lagrangian biquadratic finite elements are used for the approximation of the field variables. A second-order Taylor-Galerkin time-stepping scheme has been chosen for the temporal discretisation of the flow equations whilst an implicit theta method has been used for convective-diffusion equations. The results are presented in the form of velocity vectors and concentration, temperature contours and are examined for stability, convergence and theoretical consistency.

Keywords: Ammonia Decomposition, Catalytic Reaction, Finite Element Modelling, Hydrodynamics, Heat Transfer

Paper 5

Transport in Porous Media

Abstract

Free flow channel confined by porous walls is a feature of many of the natural and industrial settings. Viscous flows adjacent to saturated porous medium occur in cross-flow and dead-end filtrations employed primarily in pharmaceutical and chemical industries for solid-liquid or gas-solid separations. Various mathematical models have been put forward to describe the conjugate flow dynamics based on theoretical grounds and experimental evidence. Despite this fact, there still exists a wide scope for extensive research in numerical solutions of these coupled models when applied to problems with industrial relevance. The present work aims towards the numerical analysis of coupled free/porous flow dynamics in the context of industrial filtration systems. The free flow dynamics has been expressed by the Stokes equations for the creeping, laminar flow regime whereas the flow behaviour in very low permeability porous media has been represented by the conventional Darcy equation. The combined free/porous fluid dynamical behaviour has been simulated using a mixed finite element formulation based on the standard Galerkin technique. A nodal replacement technique has been developed for the direct linking of Stokes and Darcy flow regimes which alleviates specification of any additional constraint at the free/porous interface. The simulated flow and pressure fields have been found for flow domains with different geometries which represent prototypes of actual

industrial filtration equipment. Results have been obtained for varying values of permeability of the porous medium for generalised Newtonian fluids obeying the power law model. A series of numerical experiments has been performed in order to validate the coupled flow model. The developed model has been examined for its flexibility in dealing with complex geometrical domains and found to be generic in delivering convergent, stable and theoretically consistent results. The validity and accuracy of the simulated results has been affirmed by comparing with available experimental data.

Keywords: Coupled flow, porous media, dead-end filter, cross-flow filter, finite element method

Paper 6

IChemE Transactions

Abstract

A simulation code that can model fluid hydrodynamics in permeable media and pleated filter cartridges has been developed and used to evaluate the performance and design of pleated cartridge filter elements. The effects of medium compression, pleat deformation and pleat crowding are analysed. A permeability model that interprets medium compression effects and which is based on data obtained from flat sheets of the filter material used in the fabrication of filter cartridges is incorporated into the main model. During pleating, bending and creasing of the medium deforms it and leads to a loss of permeability and/or effective filtering area. The combined effects of compression and reduction in filtration area cause deviations from Darcy's law. The present work is directed towards the prediction of accurate values of compression factors and percentage losses in the filtration area, which assist in designing pleated cartridge filter elements. The simulated results have been compared against the experimental data for purposes of validation.

Conference Proceedings 1

ICFD Conference on Numerical Methods for Fluid Dynamics

29th March - 1st April, 2004, Oxford, UK.

Title: Comparison of the Darcy and the Brinkman models in the simulation of flow through porous media

Status: Presented and published in conference proceedings

Citation: Parvazinia, M., Waghode, A.N., Hanspal N.S., Ruziwa, W.R., and Nassehi, V., 2004. Comparison of the Darcy and the Brinkman models in the simulation of flow through porous media, *ICFD Conference on Numerical Methods in Fluid Dynamics*, 29th March-1st .April, Oxford, UK.

Abstract

Despite the widespread use of the Darcy equation to model porous flow, there are some cases where this equation is inconsistent. For example, no slip conditions at flow domain walls or interfaces between different sections. Therefore, in cases where the boundary effects on flow regime are expected to be significant, the use of the Darcy equation can cause difficulties and alternate models such as the Brinkman need to be considered. This paper is devoted to the study of the flow of a Newtonian fluid in a porous medium between two impermeable parallel walls at different Darcy parameters (Da) to compare the Darcy and the Brinkman equations results. The flow regime is considered to be isothermal and steady state. In the present work, a finite element scheme is used to solve both the Darcy and the Brinkman equations. The range of applicability of the Darcy and the Brinkman equations are shown.

Keywords: Porous medium, Permeability, Darcy equation, Brinkman equation, Finite element method

Conference Proceedings 2

13th European Conference on Mathematics in Industry (ECMI)

21st - 25th July 2004, Eindhoven, The Netherlands

Title: Mathematical modelling of flow through pleated cartridge filters

Status: Presented as an abstract and contributed as a full length paper to the conference proceedings published by Springer-Verlag, Germany

Citation: Nassehi, V., Waghode, A.N., Hanspal N.S., and Wakeman R.J., 2004. Mathematical modelling of flow through pleated cartridge filters, *13th European Conference on Mathematics in Industry*, 21st – 29th .July, Eindhoven, The Netherlands.

Abstract

Mathematical modelling of creeping incompressible Stokes flow and low permeability Darcy flow are well established and a number of reliable schemes for simulation of these regimes are available in the published literature. However, modelling of combined Stokes/Darcy regimes are available in the published literature. However, modelling of combined Stokes/Darcy regimes, such as those encountered in many types of industrial filters, still presents mathematical and practical challenges. In this paper, we present a finite element model for the prediction and quantitative analyses of the hydrodynamic behaviour of dead-end pleated cartridge filters. Elemental discretisation in this scheme is based on using unequal order approximation functions for velocity and pressure fields. We show that the used discretisation is able to generate unified stabilisation for both the Stokes and the Darcy equations, avoid 'numerical locking' and preserve geometrical flexibility of the computational grid. Conducting a number of numerical tests, it is shown that the developed model is capable of yielding theoretically expected and accurate simulations for realistic industrially relevant problems. The model is tested for both Newtonian and shear thickening non-

Newtonian fluids which represent type of fluids used in aeronautical applications. It has been demonstrated that the developed model presents a cost effective, robust and reliable design tool to enable engineers to appraise the operation of dead-end pleated cartridge filters.

Conference Proceedings 3

54th Canadian Chemical Engineering Conference

3rd - 6th October 2004, Calgary, Alberta, Canada

Title: Development of a predictive mathematical model for coupled Stokes and Darcy flows in cross-flow membrane filtration

Status: Presented and published in the proceedings as an abstract

Citation: Hanspal N.S., Waghode, A.N., Nassehi, V. and Wakeman R.J., 2004. Development of a predictive mathematical model for coupled Stokes and Darcy flows in cross-flow membrane filtration, *54th Canadian Chemical Engineering Conference*, 3rd – 6th .October, Calgary, Alberta, Canada.

Abstract

Free flow regimes bounded by porous walls are a common feature of many important processes such as cross-flow filtration. This process is used in a variety of industrial applications ranging from medical to oil and reservoir engineering. To provide a theoretical support for the physics behind the coupled flow phenomenon, a mathematically sound model is required which can reliably represent the interfacial boundary whilst maintaining the continuity of flow field variables across the interface between free and porous flow regimes. Though various attempts have been reported in the literature, the development of a general analysis of the coupled flows have been prohibited by the complexities of interactions between the free and the porous flow systems. The present work is directed towards developing a two-dimensional mathematical model to gain a deeper understanding of interfacial phenomena in the coupled free and porous flow regimes of a cross-flow filtration system. The free flow dynamics can be easily represented by the well-known Stokes equation in the creeping flow regime. The non-isothermal, non-inertial, incompressible flow in a low permeability porous

medium can be expressed by the Darcy equation. The model becomes a basis for a computer code which is shown to yield stable and convergent solutions to the governing equations. The system of coupled partial differential equations is solved using a Galerkin weighted residual finite element scheme with unequal order basis functions for velocity and pressure fields. The Stokes and the Darcy equations are combined using a novel nodal replacement technique. A series of numerical experiments have been performed to examine the susceptibility of the developed model towards complex and irregular shaped geometries. The developed flow fields and pressure distributions are presented for flow through a rectangular channel confined by a porous membrane wall for a range of permeability values. The developed model has been validated for theoretical consistency by quantitative evaluations based on overall mass balance calculations.

Conference Proceedings 4

American Institute of Chemical Enginners (AIChE) Annual Meeting

7th - 12th November 2004, Austin, Texas, USA

Title: Numerical analysis of medium compression and losses in filtration area in pleated cartridge membrane filters

Status: Presented and contributed as a full length paper to the conference proceedings

Citation: Waghode, A.N., Hanspal, N.S., Nassehi, V. and Wakeman, R.J., 2004 Numerical analysis of medium compression and losses in filtration area in pleated cartridge membrane filters, *American Institute of Chemical Engineers (AIChE) Annual Meeting*, 7th-12th November, Austin, Texas, USA.

Abstract

A computer model has been developed to simulate the fluid flow in pleated filter cartridges. This model has been used to evaluate the performance and design of pleated cartridge membrane filters. The effects of medium compression, pleat deformation and pleat crowding are analysed. At higher flow rates due to the exerted fluid pressure the medium gets deformed which leads to a reduction in the material permeability. Further, due to pleating and bending leads to a loss in effective filtration area. The combined effects of compression and reduction in filtration area cause deviations from Darcy's law. To interpret such deviations, permeability models based on the data obtained from the flat sheets of the filter material used in cartridge fabrication, have been developed. The incorporation of the permeability model within the main hydrodynamic model determines the percentage losses is filtration area, percentage medium compression and the pressure drop across the filters. Results in this paper have been presented for fibre glass medium. The simulated results have been compared against the

experimental industrial data for purposes of model validation. The developed simulation tool offers a robust, cost-effective and user friendly design and analysis tool for pleated cartridge membrane filters, which can be easily used by engineers in industry.

Conference Proceedings 5

Filtech Europa Conference

11th - 13th October 2005, Wiesbaden, Germany

Title: Analysis of pleat crowding and medium compression in pleated cartridge filters

Status: Will be presented and published in the proceedings as a full length paper

Citation: Wakeman R.J., Hanspal N.S., Waghode, A.N., and Nassehi, V., 2005. Analysis of pleat crowding and medium compression in pleated cartridge filters, *Filtech Europa Conference*, 11th – 13th .October, Wiesbaden, Germany.

Abstract

A simulation code that can model fluid hydrodynamics in permeable media and pleated filter cartridges has been developed and used to evaluate the performance and design of pleated cartridge filter elements. The effects of medium compression, pleat deformation and pleat crowding are analysed. A permeability model that interprets medium compression effects and which is based on data obtained from flat sheets of the filter material used in the fabrication of filter cartridges is incorporated into the main model. During pleating, bending and creasing of the medium deforms it and leads to a loss of permeability and/or effective filtering area. The combined effects of compression and reduction in filtration area cause deviations from Darcy's law. The present work is directed towards the prediction of accurate values of compression factors and percentage losses in the filtration area, which assist in designing pleated cartridge filter elements. The simulated results have been compared against the experimental data for purposes of validation.

Keywords: Cartridge filter, CFD simulation, compressible porous media, modelling, nonwovens, pressure loss.

Conference Proceedings 6

American Institute of Chemical Enginners (AIChE) Annual Meeting

31ᵗʰ October - 6ᵗʰ November 2005, Cincinnati, Ohio, USA

Title: Numerical modelling of injection moulding: Comparisons using the Phan Thien-Tanner & Criminale-Erickson-Fibley models

Status: Will be presented and published as a full length paper in the conference proceedings

Citation: Hanspal, N.S., Kulkarni, A., Waghode, A.N., and Nassehi, V., 2005. Numerical modelling of injection moulding: Comparisons using the Phan-Than-Teinner & Criminale-Erickson-Fibley models, *American Institute of Chemical Engineers (AIChE) Annual Meeting*, 31ˢᵗ October -6ᵗʰ November, Cincinnati, Ohio, USA.

Abstract

Finite element technique is used to model the free surface flow regime representing injection mould filling of elastomeric material such as rubber compounds. The most distinct feature of the constitutive behaviour of elastomers, is the influence of material elasticity on the elongation and shear deformation suffered by the fluid during flow. In the present paper we tackle this effect by the use of Phan-Than-Teinner (P-T/T) and Criminale-Erickson-Fibley (CEF) models. For the simple geometry used in the current work, the 2-D model for the representation of the flow is based on the Cauchy's and the continuity equation for an incompressible fluid. A continuous penalty/Galerkin finite element scheme is used for the solution of governing equations of the flow model. A scheme based on the Volume of Fluid technique is developed for free surface tracking. The solution of the free surface equation, which mainly represents the convection of free surface boundary in line with the flow, is based on the Stream Line Upwind Petrov

Galerkin Scheme (SUPG). Time stepping used in conjunction with all these schemes is based on the well known Implicit-Theta method. Comparisons are made between the results obtained from both the models and their applicability to industrially relevant situations has been evaluated. The models can be further used to investigate the influence of effects such as change in the material properties at the advancing front surfaces.

Key Words: Injection Moulding, CEF model, P-T/T model, Front Tracking, VOF Technique, Finite Element method

Conference Proceedings 7

American Institute of Chemical Enginners (AIChE) Annual Meeting

31st October - 6th November 2005, Cincinnati, Ohio, USA

Title: Medium swelling and pleat crowding effects in cartridge filters

Status: Will be presented and published as a full length paper in the conference proceedings

Citation: Waghode, A.N., Hanspal, N.S., Kulkarni, A., Nassehi, V. Wakeman, R.J., 2005. Medium swelling and pleat crowding effects in cartridge filters, *American Institute of Chemical Engineers (AIChE) Annual Meeting*, 31st October -6th November, Cincinnati, Ohio, USA.

Abstract

A two-dimensional mathematical model has been developed describing hydrodynamics in pleated cartridge membrane filters to evaluate design and operating characteristics. The fluid dynamical behaviour of creeping non-inertial porous flow regime has been represented by the Darcy's law. The absorption of the filtering fluid by the porous structure results into the medium swelling increasing its intrinsic permeability. In a pleated cartridge, an apparent loss in the filtration area is observed due the high pleat density and medium deformation due to hydrostatic force exerted by the fluid. The combined effects of medium swelling and losses in effective filtration area causes deviations from the Darcy's law. To interpret these effects, permeability-pressure drop models have been developed based on experimental data obtained from a flat sheet of synthetic membrane used in cartridge fabrication. The inclusion of these permeability models into the hydrodynamic model reveals percentage losses in filtration area and increase in the permeability of the medium. The simulated results have been validated by comparing against the known experimental data.

Keywords: Pleated cartridge, absorptive swelling, pleat crowding, filtration area, Darcy's law

Book Contribution

The Encyclopaedia of Water

Title: Finite element modelling of coupled free and porous flow in the
             subsurface

Status: Accepted for publication

Citation: Waghode, A.N., Hanspal, N.S. and Das, D.B., 2005. Finite element
             modelling of coupled free and porous flow in the subsurface, in The
             Encyclopaedia of Water, Edited by: Lehr, J., John Wiley and Sons,
             Oxford.

Finite Element Modelling of Coupled Free and Porous Flow in the Subsurface

A.N.Waghode[1], N.S. Hanspal[1], D.B. Das[2]

[1]Advanced Separation Technologies Group,

Department of Chemical Engineering,

Loughborough University,

Loughborough, Leicestershire,

LE11 3TU, United Kingdom

[2]Department of Engineering Science,

University of Oxford

OX1 3PJ, United Kingdom

Introduction:

The present article concerns with the finite element modelling (FEM) of groundwater flow in coupled free and porous domains, in the subsurface. In general, free flow regime can be viewed as if the flow were in a layer of fluid or a pipe and it needs only the fluid dynamical characterisation of the domain, e.g., Reynolds number. On the other hand, porous flow regime indicates flow through a porous medium and it needs the characterisation for both the fluid dynamics and the medium, e.g., permeability, porosity, etc. The flow on the ground surface is termed as free surface flow. Some of the water from this surface flow seeps in the bulk of the underground soil which is made of fine tiny pores. This flow is called as subsurface or porous flow. As well as the expected media heterogeneity, e.g., presence of layers, laminations, etc, the subsurface also contain non-porous sections, e.g., conduits, fissures, buried structures that are often damaged, macro-pores, vugular inclusions and fractures, etc. The hydrodynamics of groundwater flow in the non-porous (e.g. vugs) and porous sections are fundamentally governed by the Navier-Stokes and Darcy equations, respectively (Zimmerman and Yeo, 2000; Das and Nassehi, 2003; Abrogast *et al.*, 2004) although simplified forms of Navier-Stokes equations are often used in practice for the non-porous

domains. The overall flow behaviour in the non-porous and porous region can be modelled with an approach that couples Navier-Stokes and Darcy equations with suitable interfacial and boundary conditions. However, the complexity of the subsurface regions is such that it is usually not possible to predict the coupled flow behaviour with confidence using the traditional analytical methods or experiments. FEM is powerful method that can be used to validate results from experiments and/or analytical method. In other cases where such results are not available, FEM modelling can also be used independently to predict the flow in the subsurface. The FEM method is based on the initial approximations which guide the numerical procedure towards the exact solution of the problem and the basis of the FEM is on minimization of errors introduced due to these initial approximations made. The versatility of FEM lies in its ability to cope with complex and irregular geometries of the flow domain.

In this article, the finite element method has been discussed in the context of solving the Navier-Stokes and Darcy equations in accordance with appropriately chosen boundary conditions.

Appendix A2

Numerical Analysis of Cartridge Permeation Data

Reference element	H24FDV70L
Filtering medium	Fibre Glass Medium β 3 μm >200 + square mesh aperture = 440 μm
Test fluid	MP 320
Density	880 kgm-3
Power law index	1.0
Number of pleats	70
Height of the filter element	211.5 mm
Height of the pleat	24.5 mm
Diameter of the inner core	59 mm
Filtering area	0.681 m²
Outer diameter of the casing	120 mm

Experimental data				Numerical analysis			
No	Flow Rate (lit min⁻¹)	Viscosity (cSt)	Pressure drop p_{exp} (bar)	% Compn.	Pressure drop with no compn. and no loss in area P (bar)	Pressure drop with compn. p_c (bar)	% Loss in area	Pressure drop allowing for compression and loss in area p_{c+a} (bar)
1.	100	72	3.79	23.86	0.71	0.936	75.30	3.790
2.	150	70	5.84	31.36	1.04	1.513	74.09	5.840
3.	200	69	8.39	37.07	1.36	2.168	74.16	8.390
4.	250	69	10.81	46.95	1.71	3.215	70.26	10.811
5.	300	69	13.29	46.95	2.05	3.858	70.97	13.291
6.	350	69	15.85	46.95	2.39	4.501	71.60	15.852
7.	400	70	18.30	46.95	2.77	5.221	71.47	18.300

Reference element	H19FDV88L
Filtering medium	Fibre Glass Medium β 3 µm >200 + square mesh aperture = 440 µm
Test fluid	MP 320
Density	880 kgm^{-3}
Power law index	1.0
Number of pleats	88
Height of the filter element	211.5 mm
Height of the pleat	19 mm
Diameter of the inner core	70 mm
Filtering area	0.651 m²
Outer diameter of the casing	120 mm

Experimental data				Numerical analysis			
No	Flow Rate (lit min^{-1})	Viscosity (cSt)	Pressure drop p_{exp} (bar)	% Compn.	Pressure drop with no compn. and no loss in area P (bar)	Pressure drop with compn. p_c (bar)	% Loss in area	Pressure drop allowing for compression and loss in area p_{c+a} (bar)
1.	50	76	0.91	0	0.55	0.55	39.09	0.909
2.	100	75	1.88	9.93	1.09	1.21	35.42	1.880
3.	150	74	2.91	18.88	1.62	1.99	31.45	2.910
4.	200	73	3.98	24.75	2.13	2.83	28.96	3.979
5.	250	72	5.20	29.42	2.63	3.72	28.44	5.200
6.	300	72	6.45	32.97	3.15	4.70	27.10	6.449
7.	350	71	7.67	35.70	3.62	5.64	26.51	7.67
8.	400	71	8.93	38.00	4.14	6.68	25.18	8.93
9.	450	72	9.94	39.57	4.73	7.82	21.30	9.94
10.	500	72	11.12	46.95	5.25	9.90	10.95	11.12
11.	550	73	12.92	46.95	5.85	11.02	14.63	12.92
12.	600	75	14.52	46.95	6.56	12.37	14.81	14.52

Reference element	H24FDV75L
Filtering medium	Fibre Glass Medium β 3 μm >200 + square mesh aperture = 440 μm
Test fluid	MP 320
Density	880 kgm-3
Power law index	1.0
Number of pleats	75
Height of the filter element	211.5 mm
Height of the pleat	24.5 mm
Diameter of the inner core	59 mm
Filtering area	0.73 m²
Outer diameter of the casing	120 mm

	Experimental data			Numerical analysis				
No	Flow Rate (lit min⁻¹)	Viscosity (cSt)	Pressure drop p_{exp} (bar)	% Compn.	Pressure drop with no compn. and no loss in area P (bar)	Pressure drop with compn. p_c (bar)	% Loss in area	Pressure drop allowing for compression and loss in area p_{c+a} (bar)
1.	100	71	2.28	14.00	0.27	0.32	85.98	2.280
2.	150	69	3.45	22.13	0.40	0.51	85.09	3.450
3.	200	69	4.98	28.68	0.53	0.75	84.96	4.977
4.	250	68	6.41	32.87	0.66	0.98	84.72	6.409
5.	300	67	7.98	36.31	0.78	1.22	84.68	7.980
6.	350	67	9.65	39.14	0.91	1.49	84.53	9.646
7.	400	66	11.13	46.95	1.02	1.93	82.68	11.131
8.	450	66	12.30	46.95	1.15	2.17	82.37	12.305
9.	500	66	13.97	46.95	1.28	2.41	82.75	13.970
10.	550	67	16.07	46.95	1.43	2.69	83.25	16.070
11.	600	68	17.77	46.95	1.58	2.97	83.25	17.770

Reference element	H24FDV70C
Filtering medium	Fibre Glass Medium β 3 μm >200 + square mesh aperture = 440 μm
Test fluid	MP 320
Density	880 kgm^{-3}
Power law index	1.0
Number of pleats	70
Height of the filter element	97 mm
Height of the pleat	24.5 mm
Diameter of the inner core	59 mm
Filtering area	0.312 m²
Outer diameter of the casing	120 mm

Experimental data				Numerical analysis				
No	Flow Rate (lit min^{-1})	Viscosity (cSt)	Pressure drop p_{exp} (bar)	% Compn.	Pressure drop with no compn. and no loss in area P (bar)	Pressure drop with compn. p_c (bar)	% Loss in area	Pressure drop allowing for compression and loss in area p_{c+a} (bar)
1.	100	78	4.09	24.24	1.68	2.25	45.01	4.089
2.	150	76	6.34	32.69	2.46	3.65	42.36	6.340
3.	200	75	8.86	37.88	3.23	5.21	41.22	8.860
4.	250	74	11.41	46.95	3.99	7.52	34.10	11.410
5.	300	74	14.50	46.95	4.79	9.02	37.77	14.500
6.	350	74	16.70	46.95	5.58	10.53	36.96	16.700
7.	400	75	19.30	46.95	6.47	12.20	36.80	19.300

Reference element	H19FDV82L
Filtering medium	Fibre Glass Medium β 3 μm >200 + square mesh aperture = 440 μm
Test fluid	MP 320
Density	880 kgm⁻³
Power law index	1.0
Number of pleats	82
Height of the filter element	211.5 mm
Height of the pleat	19 mm
Diameter of the inner core	70 mm
Filtering area	0.607 m²
Outer diameter of the casing	120 mm

Experimental data				Numerical analysis			
No	Flow Rate (lit min⁻¹)	Viscosity (cSt)	Pressure drop p_{exp} (bar)	% Compn.	Pressure drop with no compn. and no loss in area P (bar)	Pressure drop with compn. p_c (bar)	% Loss in area	Pressure drop allowing for compression and loss in area p_{c+a} (bar)
1.	50	72	0.89	0	0.60	0.60	32.27	0.89
2.	100	71	1.93	10.49	1.19	1.33	31.20	1.93
3.	150	70	3.05	19.79	1.76	2.19	28.17	3.05
4.	200	69	4.19	25.67	2.31	3.10	25.87	4.19
5.	250	69	5.60	30.66	2.88	4.16	25.68	5.60
6.	300	69	6.94	34.14	3.46	5.26	24.24	6.94
7.	350	68	8.33	36.96	3.98	6.31	24.20	8.33
8.	400	68	9.66	39.16	4.55	7.48	22.60	9.66
9.	450	69	10.81	40.77	5.19	8.77	18.86	10.81
10.	500	69	12.17	46.95	5.77	10.88	10.59	12.17
11.	550	71	14.04	46.95	6.54	12.32	12.22	14.04
12.	600	72	15.56	46.95	7.23	13.64	12.35	15.56

Reference element	H24FDV75L
Filtering medium	Fibre Glass Medium β 3 μm >200 + square mesh aperture = 440 μm
Test fluid	MP 320
Density	880 kgm-3
Power law index	1.0
Number of pleats	75
Height of the filter element	211.5 mm
Height of the pleat	24.5 mm
Diameter of the inner core	59 mm
Filtering area	0.73 m²
Outer diameter of the casing	120 mm

Experimental data				Numerical analysis			
No	Flow Rate (lit min^{-1})	Viscosity (cSt)	Pressure drop p_{exp} (bar)	% Compn.	Pressure drop with no compn. and no loss in area P (bar)	Pressure drop with compn. p_c (bar)	% Loss in area	Pressure drop allowing for compression and loss in area p_{c+a} (bar)
1.	50	80	2.29	14.09	0.15	0.18	92.13	2.29
2.	100	79	4.56	27.16	0.30	0.42	90.79	4.56
3.	150	79	6.90	30.05	0.46	0.69	89.92	6.90
4.	200	79	9.20	38.44	0.61	0.99	89.20	9.20
5.	250	79	11.80	46.95	0.76	1.44	87.79	11.80
6.	300	79	14.30	46.95	0.92	1.73	87.91	14.30
7.	312	80	15.01	46.95	0.97	1.82	87.86	15.01

Reference element	H15FDV93L20
Filtering medium	Dual Fibre Glass Medium β 3 μm >200 + square mesh aperture = 440 μm
Special characteristics	2 circular straps along the length of cartridge
Test fluid	MP 320
Density	880 kgm^{-3}
Power law index	1.0
Number of pleats	93
Height of the filter element	231.5 mm
Height of the pleat	15 mm
Diameter of the inner core	78 mm
Filtering area	0.58 m^2
Outer diameter of the casing	120 mm

Experimental data				Numerical analysis			
No	Flow Rate (lit min^{-1})	Viscosity (cSt)	Pressure drop p_{exp} (bar)	% Compn.	Pressure drop with no compn. and no loss in area P (bar)	Pressure drop with compn. p_c (bar)	% Loss in area	Pressure drop allowing for compression and loss in area p_{c+a} (bar)
1.	101	72.4	1.29	1.42	0.18	0.18	86.15	1.29
2.	150	71.7	1.94	10.6	0.26	0.29	85.07	1.94
3.	201	70.7	2.61	16.74	0.34	0.41	84.25	2.61
4.	250	69.4	3.24	20.95	0.42	0.53	83.69	3.24
5.	301	68.1	4.05	25.06	0.49	0.66	83.74	4.05
6.	350	67.1	4.87	28.3	0.56	0.79	83.8	4.87
7.	400	66.2	5.78	31.19	0.64	0.93	83.97	5.78
8.	454	64.9	6.63	33.41	0.71	1.07	83.93	6.63
9.	504	64.0	7.42	35.19	0.78	1.20	83.85	7.42

Reference element	H15FDV82L40
Filtering medium	Dual Fibre Glass Medium β 3 μm >200 + square mesh aperture = 440 μm
Special characteristics	2 circular straps along the length of cartridge
Test fluid	MP 320
Density	880 kgm^{-3}
Power law index	1.0
Number of pleats	82
Height of the filter element	251.5 mm
Height of the pleat	15 mm
Diameter of the inner core	78 mm
Filtering area	0.56 m²
Outer diameter of the casing	120 mm

Experimental data				Numerical analysis			
No	Flow Rate (lit min^{-1})	Viscosity (cSt)	Pressure drop p_{exp} (bar)	% Compn.	Pressure drop with no compn. and no loss in area P (bar)	Pressure drop with compn. p_c (bar)	% Loss in area	Pressure drop allowing for compression and loss in area p_{c+a} (bar)
1.	101	71.7	1.24	1.42	0.87	0.88	31.80	1.29
2.	150	71.4	1.89	10.6	1.28	1.43	26.45	1.94
3.	201	70.7	2.55	16.74	1.68	2.02	22.44	2.61
4.	250	69.4	3.37	20.95	2.06	2.60	19.66	3.24
5.	301	68.4	4.34	25.06	2.43	3.24	19.90	4.05
6.	350	67.1	5.31	28.3	2.78	3.88	20.23	4.87
7.	400	66.2	6.43	31.19	3.14	4.56	21.04	5.78
8.	454	65.2	7.38	33.41	3.49	5.25	20.84	6.63
9.	504	64.0	8.18	35.19	3.83	5.90	20.45	7.42

Reference element	H15FDV98L00
Filtering medium	Dual Fibre Glass Medium β 3 μm >200 + square mesh aperture = 440 μm
Test fluid	MP 320
Density	880 kgm^{-3}
Power law index	1.0
Number of pleats	98
Height of the filter element	211.5 mm
Height of the pleat	15 mm
Diameter of the inner core	78 mm
Filtering area	0.56 m²
Outer diameter of the casing	120 mm

Experimental data				Numerical analysis			
No	Flow Rate (lit min^{-1})	Viscosity (cSt)	Pressure drop p_{exp} (bar)	% Compn.	Pressure drop with no compn. and no loss in area P (bar)	Pressure drop with compn. p_c (bar)	% Loss in area	Pressure drop allowing for compression and loss in area p_{c+a} (bar)
1.	100	73.8	1.92	10.38	0.86	0.96	50.06	1.92
2.	150	73.8	2.89	18.75	1.29	1.59	45.11	2.89
3.	200	73.8	3.95	24.61	1.72	2.28	42.29	3.95
4.	250	73.1	5.16	29.29	2.13	3.01	41.68	5.16
5.	300	72.1	6.46	33.00	2.52	3.76	41.81	6.46
6.	350	71.0	7.75	35.86	2.89	4.51	41.79	7.75
7.	400	69.7	8.97	38.07	3.25	5.24	41.57	8.97
8.	450	68.7	10.08	39.78	3.60	5.98	40.70	10.08
9.	500	67.4	10.94	46.95	3.92	7.40	32.38	10.94

Reference element	H15FDV82C (2×48)
Filtering medium	Bilayer Fibre Glass Medium β 3 μm >200 + square mesh aperture = 440 μm
Special characteristics	Filter element in two pieces
Test fluid	MP 320
Density	880 kgm^{-3}
Power law index	1.0
Number of pleats	82
Height of the filter element	306.5 mm
Height of the pleat	15 mm
Diameter of the inner core	78 mm
Filtering area	0.68 m²
Outer diameter of the casing	120 mm

Experimental data				Numerical analysis			
No	Flow Rate (lit min^{-1})	Viscosity (cSt)	Pressure drop p_{exp} (bar)	% Compn.	Pressure drop with no compn. and no loss in area P (bar)	Pressure drop with compn. p_c (bar)	% Loss in area	Pressure drop allowing for compression and loss in area p_{c+a} (bar)
1.	102	74.5	1.21	0	0.64	0.64	47.07	1.21
2.	150	74.9	1.78	8.74	0.95	1.04	41.64	1.78
3.	200	74.9	2.40	15.05	1.26	1.49	38.01	2.40
4.	251	74.2	3.10	20.10	1.57	1.97	36.55	3.10
5.	302	73.5	3.85	24.15	1.87	2.47	35.87	3.85
6.	351	72.8	4.70	27.69	2.16	2.98	36.56	4.70
7.	401	71.7	5.64	30.78	2.43	3.50	37.86	5.64
8.	449	70.7	6.50	33.10	2.68	4.00	38.41	6.50
9.	500	69.7	7.22	34.76	2.94	4.51	37.57	7.22

Reference element	H12FDV96L70
Filtering medium	Dual Fibre Glass Medium β 3 μm >200 + square mesh aperture = 440 μm
Special characteristics	2 circular straps along the length of cartridge
Test fluid	MP 320
Density	880 kgm-3
Power law index	1.0
Number of pleats	96
Height of the filter element	281.5 mm
Height of the pleat	12 mm
Diameter of the inner core	78 mm
Filtering area	0.57 m²
Outer diameter of the casing	120 mm

Experimental data				Numerical analysis				
No	Flow Rate (lit min⁻¹)	Viscosity (cSt)	Pressure drop p_{exp} (bar)	% Compn.	Pressure drop with no compn. and no loss in area P (bar)	Pressure drop with compn. p_c (bar)	% Loss in area	Pressure drop allowing for compression and loss in area p_{c+a} (bar)
1.	103	71.4	1.01	0	0.73	0.73	27.70	1.01
2.	150	70.4	1.54	5.52	1.05	1.11	27.94	1.54
3.	200	69.7	2.07	11.98	1.38	1.57	24.03	2.07
4.	252	68.4	2.66	17.12	1.71	2.06	22.37	2.66
5.	302	67.1	3.32	21.41	2.01	2.56	22.89	3.32
6.	352	65.5	4.08	25.19	2.29	3.06	24.99	4.08
7.	401	64.6	4.93	28.51	2.57	3.60	27.02	4.93
8.	457	63.7	5.70	30.96	2.89	4.19	26.55	5.70
9.	504	62.8	6.39	32.82	3.14	4.68	26.79	6.39

Reference element	H12FDV100L50
Filtering medium	Dual Fibre Glass Medium β 3 μm >200 + square mesh aperture = 440 μm
Test fluid	MP 320
Density	880 kgm-3
Power law index	1.0
Number of pleats	100
Height of the filter element	261.5 mm
Height of the pleat	12 mm
Diameter of the inner core	84 mm
Filtering area	0.55 m²
Outer diameter of the casing	120 mm

Experimental data				Numerical analysis			
No	Flow Rate (lit min⁻¹)	Viscosity (cSt)	Pressure drop p_{exp} (bar)	% Compn.	Pressure drop with no compn. and no loss in area P (bar)	Pressure drop with compn. p_c (bar)	% Loss in area	Pressure drop allowing for compression and loss in area p_{c+a} (bar)
1.	102.5	72.4	1.12	0	0.71	0.71	36.81	1.12
2.	149	70.4	1.69	7.60	1.00	1.08	35.94	1.69
3.	198	69.0	2.33	14.44	1.30	1.52	34.64	2.33
4.	251	67.4	3.04	19.73	1.61	2.01	33.88	3.04
5.	302	65.8	3.89	24.33	1.89	2.50	35.61	3.89
6.	351	64.9	4.76	27.91	2.17	3.01	36.69	4.76
7.	400	64.0	5.75	31.10	2.44	3.54	38.37	5.75
8.	454	63.1	6.66	33.49	2.73	4.11	38.33	6.66
9.	505	61.7	7.44	35.23	2.97	4.59	38.34	7.44

Reference element	H12FDV82C (2×48)
Filtering medium	Bilayer Fibre Glass Medium β 3 μm >200 + square mesh aperture = 440 μm
Special characteristics	Filter element in two pieces
Test fluid	MP 320
Density	880 kgm⁻³
Power law index	1.0
Number of pleats	96
Height of the filter element	306.5 mm
Height of the pleat	12 mm
Diameter of the inner core	78 mm
Filtering area	0.62 m²
Outer diameter of the casing	120 mm

	Experimental data			Numerical analysis				
No	Flow Rate (lit min⁻¹)	Viscosity (cSt)	Pressure drop p_{exp} (bar)	% Compn.	Pressure drop with no compn. and no loss in area P (bar)	Pressure drop with compn. p_c (bar)	% Loss in area	Pressure drop allowing for compression and loss in area p_{c+a} (bar)
1.	101	73.5	1.12	0	0.68	0.68	39.56	1.12
2.	150	73.5	1.67	7.33	1.00	1.08	35.03	1.67
3.	200	73.5	2.27	13.91	1.34	1.56	31.41	2.27
4.	251.4	72.8	2.92	18.95	1.67	2.06	29.48	2.92
5.	303	72.4	3.67	23.27	2.00	2.61	28.96	3.67
6.	352	71.4	4.48	26.85	2.29	3.13	30.06	4.48
7.	400	70.0	5.33	29.84	2.55	3.64	31.72	5.33
8.	450	69.0	6.2	32.33	2.83	4.18	32.51	6.20
9.	503	67.7	6.91	34.07	3.10	4.71	31.83	6.91

Reference element	H17FDV91L00
Filtering medium	Dual Fibre Glass Medium β 3 μm >200 + square mesh aperture = 440 μm
Special characteristics	2 circular straps along the length of cartridge
Test fluid	MP 320
Density	880 kgm-3
Power law index	1.0
Number of pleats	91
Height of the filter element	211.5 mm
Height of the pleat	17 mm
Diameter of the inner core	74 mm
Filtering area	0.60 m²
Outer diameter of the casing	120 mm

Experimental data				Numerical analysis			
No	Flow Rate (lit min⁻¹)	Viscosity (cSt)	Pressure drop p_{exp} (bar)	% Compn.	Pressure drop with no compn. and no loss in area P (bar)	Pressure drop with compn. p_c (bar)	% Loss in area	Pressure drop allowing for compression and loss in area p_{c+a} (bar)
1.	100	72.4	1.62	6.66	0.60	0.65	60.06	1.62
2.	150	72.4	2.44	15.38	0.90	1.07	56.12	2.44
3.	200	71.0	3.41	21.91	1.18	1.52	55.52	3.41
4.	250	69.0	4.49	26.89	1.44	1.97	56.16	4.49
5.	300	67.7	5.76	31.13	1.69	2.46	57.29	5.76
6.	350	66.8	7.13	34.56	1.95	2.98	58.20	7.13
7.	400	65.8	8.47	37.21	2.20	3.50	58.72	8.47
8.	450	65.2	9.49	38.90	2.45	4.01	57.79	9.49
9.	500	63.7	10.26	40.03	2.66	4.43	56.82	10.26

Reference element	CA1148AD
Filtering medium	Dual Fibre Glass Medium β 3 μm >200 + square mesh aperture = 440 μm
Special characteristics	2 circular straps along the length of cartridge
Test fluid	MP 320
Density	880 kgm^{-3}
Power law index	1.0
Number of pleats	91
Height of the filter element	211.5 mm
Height of the pleat	24.5 mm
Diameter of the inner core	58.8 mm
Filtering area	0.78 m^2
Outer diameter of the casing	120 mm

Experimental data				Numerical analysis				
No	Flow Rate (lit min^{-1})	Viscosity (cSt)	Pressure drop p_{exp} (bar)	% Compn.	Pressure drop with no compn. and no loss in area P (bar)	Pressure drop with compn. p_c (bar)	% Loss in area	Pressure drop allowing for compression and loss in area p_{c+a} (bar)
1.	100	72.4	2.40	15.05	0.36	0.42	82.48	2.40
2.	150	69.7	3.51	22.45	0.52	0.66	81.05	3.51
3.	200	68.4	4.75	27.87	0.67	0.94	80.29	4.75
4.	250	67.1	5.88	31.47	0.83	1.21	79.46	5.88
5.	300	65.5	6.79	33.79	0.97	1.46	78.43	6.79
6.	350	63.7	7.56	35.48	1.10	1.70	77.44	7.56
7.	400	62.2	8.42	37.12	1.23	1.95	76.81	8.42
8.	450	61.4	8.91	37.97	1.36	2.20	75.33	8.91
9.	500	60.3	9.59	39.05	1.49	2.44	74.54	9.59

Reference element	H17FDV94L(-20)
Filtering medium	Dual Fibre Glass Medium β 3 μm >200 + square mesh aperture = 440 μm
Special characteristics	2 circular straps along the length of cartridge
Test fluid	MP 320
Density	880 kgm^{-3}
Power law index	1.0
Number of pleats	94
Height of the filter element	191.5 mm
Height of the pleat	17 mm
Diameter of the inner core	74 mm
Filtering area	0.56 m²
Outer diameter of the casing	120 mm

	Experimental data			Numerical analysis				
No	Flow Rate (lit min^{-1})	Viscosity (cSt)	Pressure drop p_{exp} (bar)	% Compn.	Pressure drop with no compn. and no loss in area P (bar)	Pressure drop with compn. p_c (bar)	% Loss in area	Pressure drop allowing for compression and loss in area p_{c+a} (bar)
1.	100	73.1	1.62	6.66	0.63	0.68	58.25	1.62
2.	150	73.5	2.44	15.38	0.95	1.12	54.13	2.44
3.	200	73.1	3.41	21.91	1.24	1.59	53.50	3.41
4.	250	72.4	4.49	26.89	1.50	2.06	54.17	4.49
5.	300	71.7	5.76	31.13	1.77	2.57	55.35	5.76
6.	350	70.4	7.13	34.56	2.04	3.12	56.3	7.13
7.	400	69.4	8.47	37.21	2.29	3.65	56.84	8.47
8.	450	68.4	9.49	38.90	2.56	4.19	55.88	9.49
9.	500	67.7	10.26	40.03	2.78	4.63	54.86	10.26